The Reactivity and Cation Exchange of MOF-5

by

Carl Kavanaugh Brozek

S.B., University of Chicago (2010)

Submitted to the Department of Chemistry
in partial fulfillment of the requirements for the degree of

Doctor of Philosophy in Inorganic Chemistry

at the

MASSACHUSETTS INSTITUTE OF TECHNOLOGY

June 2015

Signature redacted

Author .....
Department of Chemistry
April 2, 2015

Signature redacted

Certified by ....
Mircea Dincă
Assistant Professor
Thesis Supervisor

Signature redacted

Accepted by .....
Robert W. Field
Chairman, Department Committee on Graduate Theses

The Reactivity and Cation Exchange of MOF-5

by

Carl Kavanaugh Brozek

Submitted to the Department of Chemistry
on April 2, 2015, in partial fulfillment of the
requirements for the degree of
Doctor of Philosophy in Inorganic Chemistry

Abstract

The aim of this thesis is to demonstrate that the inorganic clusters within MOF-5 can be derivatized with redox-active cations for subsequent use in coordination chemistry and small-molecule activation. Rather than reproduce known metal species, this work harnesses the intrinsic properties of the MOF-5 lattice to isolate species that are difficult or impossible to achieve with solution-phase molecules or even other materials. Most of these MOF-5 variants are synthesized through a technique known as cation exchange—a process not well understood.

Part 1, chapters 1-6, is devoted to studying the parameters that govern this phenomenon and how they may be manipulated. The first chapter surveys the known examples of cation exchange at the secondary building units of MOFs and poses questions to guide future studies. Chapter 2 reports the isolation of a Ni^{2+}-exchanged variant of this material and demonstrates that this unusual species and changes to its coordination environment can be monitored by conventional methods. Chapter 3 establishes that the original Zn^{2+} in MOF-5 also interact with coordinating ligands, but with no more than one Zn^{2+} in each cluster interacting at a time. Chapter 4 proposes that this observation explains why only one Zn^{2+} is replaceable by O_h cations and provides a strategy for replacing the remaining Zn^{2+} ions. In chapter 5, methods for analyzing crystallographic data are presented for locating and quantifying the occupancy of cations inserted into a MOF. Finally, Chapter 6 describes the solvent dependence of the kinetics and thermodynamics of cation exchange.

Part 2, chapters 7-9, describes the reactivity of MOF-5 after replacement with redox-active cations. Chapter 7 provides evidence that the Fe^{2+} sites in Fe-MOF-5 possess the flexibility and reactivity to interact with N_2. In Chapter 8, Ti^{3+}, V^{3+}, V^{2+}, Cr^{3+}, Cr^{2+}, Mn^{2+}, and Fe^{2+} variants are shown to undergo electron transfer. Finally, we conclude with evidence that Fe-MOF-5 promotes the disproportionation of NO. Together, these chapters lay the foundation for the eventual goal of heterogeneous catalysis at well-defined metal sites in MOFs.

Thesis Supervisor: Mircea Dincă
Title: Assistant Professor

This doctoral thesis has been examined by a Committee of the Department of Chemistry as follows:

Signature redacted

Professor Christopher C. Cummins .....
Chairman, Thesis Committee
Professor of Chemistry

Signature redacted

Professor Mircea Dincă .....
Thesis Supervisor
Assistant Professor of Chemistry

Signature redacted

Professor Stephen J. Lippard .....
Member, Thesis Committee
Arthur Amos Noyes Professor of Chemistry

Contents

I Cation Exchange in MOF-5 **23**

1 Cation Exchange in MOFs **25**

1.1 Motivation 25

1.2 Background 27

1.3 Which SBUs Undergo Cation Exchange? 29

1.4 Which Ions Exchange into SBUs? 35

1.5 How Does the Framework Influence the Exchange? 38

1.6 What Role Does the Solvent Play in Cation Exchange? 40

1.7 Applications 41

1.8 Outlook 45

2 MOF-5 Stabilizes an Unusual Pseudo-T_d Ni^{2+} Species **49**

2.1 Abstract 49

2.2 Introduction 50

2.3 Results and Discussion 50

2.4 Conclusion 57

2.5 Methods 57

2.5.1 Materials 57

2.5.2 X-ray Crystal Structure Determination 61

2.5.3 Physical Measurements 61

2.5.4 Calculations 62

2.5.5 Preparation of $Ni_xZn_{4-x}O(BDC)_3$ 64

2.5.6 Preparation of $(MesCNO)Ni_xZn_{4-x}O(BDC)_3$ 66

3 MOF-5 Contains Unsaturated Zn Centers **73**

3.1 Abstract . . . 73

3.2 Introduction . . . 74

3.3 Results . . . 75

3.4 Discussion . . . 85

3.5 Conclusion and Outlook . . . 89

3.6 Methods . . . 89

3.6.1 Materials . . . 89

3.6.2 Experimental Conditions for Solid-state Nuclear Magnetic Resonance . . . 90

3.6.3 Born-Oppenheimer Molecular Dynamics . . . 91

3.6.4 Preparation of ^{67}Zn-enriched $Zn(NO_3)_2{\cdot}xH_2O$ . . . 92

3.6.5 Preparation of ^{67}Zn-enriched MOF-5 . . . 93

3.6.6 Sample Preparation for Nuclear Magnetic Resonance . . . 94

3.6.7 Solid-state Nuclear Magnetic Resonance Analysis of Activated MOF-5 . . . 94

3.6.8 Solid-state Nuclear Magnetic Resonance Analysis of DMF-Solvated ^{67}Zn Enriched MOF-5 . . . 95

3.6.9 Other Physical Measurements . . . 96

3.6.10 Sample Preparation for Calorimetry Studies . . . 96

4 Extending Co^{2+} Exchange in MOF-5 by Sidestepping Lattice Strain **97**

4.1 Abstract . . . 97

4.2 Introduction . . . 97

4.3 Results and Discussion . . . 99

4.4 Conclusion . . . 104

4.5 Methods . . . 104

4.5.1 Physical Measurements . . . 105

4.5.2 $Zn_{4-x}M_{4-x}O(C_8H_4O_4)_3$ (M = Ni or Co). . . . 105

4.5.3 Calculations . . . 105

5 Quantifying and Locating Cation Exchange within MOFs through Multi-wavelength Anomalous Dispersion **115**

5.1 Abstract . . . 115

5.2 Introduction . . . 116

5.3 Methods . . . 117

5.3.1 Materials . . . 117

5.3.2 Preparation of MnMnBTT . . . 118

5.3.3 Metal exchange in MnMnBTT . . . 118

5.3.4 Elemental analysis . . . 118

5.3.5 X-ray Absorption Spectroscopy . . . 119

5.3.6 Multi-wavelength Anomalous Dispersion . . . 119

5.3.7 Data Reduction . . . 120

5.3.8 Data Analysis . . . 120

5.4 Results and Discussion . . . 122

5.5 Conclusion . . . 126

6 The Solvent Dependence of Cation Exchange in MOFs **131**

6.1 Abstract . . . 131

6.2 Introduction . . . 131

6.3 Results and Discussion . . . 132

6.4 Conclusion . . . 145

6.5 Methods . . . 145

6.5.1 Materials . . . 145

6.5.2 Synthetic Aspects of Co^{2+} Exchange in MFU-4*l* . . . 146

6.5.3 Synthetic Aspects of Ni^{2+} Exchange in MOF-5 . . . 146

6.5.4 Physical Measurements . . . 146

6.5.5 Computational Details . . . 147

II Reactivity of MOF-5 **148**

7 Dynamic Structural Flexibility of Fe^{2+} Centers in MOF-5 **149**

7.1 Abstract . . . 149
7.2 Introduction . . . 150
7.3 Results . . . 151
7.4 Discussion . . . 161
7.5 Conclusion . . . 165
7.6 Methods . . . 165
7.6.1 Materials . . . 166
7.6.2 Physical Measurements . . . 166
7.6.3 $Zn_{4-x}Fe_xO_{13}C_{24}H_{12}$ (Fe-MOF-5) . . . 168
7.6.4 Partial Oxidation of Fe-MOF-5 by O_2 . . . 168
7.6.5 Calculations . . . 168

8 Redox-active Cations within MOF-5 171
8.1 Abstract . . . 171
8.2 Introduction . . . 172
8.3 Results and Discussion . . . 173
8.4 Conclusion . . . 194
8.5 Methods . . . 195
8.5.1 Materials . . . 196
8.5.2 Physical Measurements . . . 196
8.5.3 $Zn_{4-x}M_xCl_xO_{13}C_{24}H_{12}$ (ClM-MOF-5, M = Ti, V, Cr) . . . 198
8.5.4 $Zn_{4-x}M_xO_{13}C_{24}H_{12}$ (M-MOF-5, M = V, Cr, Mn, Fe) . . . 199
8.5.5 In Situ DRIFTS of NO + Fe-MOF-5 . . . 199
8.5.6 Reduction of ClV-MOF-5 by $[(THF)_3Na^+(TEMPO^-)]_4$ . . . 199
8.5.7 Calculations . . . 200
8.5.8 EPR Simulation . . . 200

9 Nitric Oxide Disproportionation Promoted by Fe-MOF-5 205
9.1 Abstract . . . 205
9.2 Introduction . . . 206
9.3 Results . . . 207

9.4 Discussion 217
9.5 Conclusion 226
9.6 Methods 228
9.6.1 Materials 228
9.6.2 Physical Measurements 228
9.6.3 Calculations 231
9.6.4 $Zn_{4-x}Fe_xO_{13}C_{24}H_{12}$ (Fe-MOF-5) 231
9.6.5 Synthesis of ^{15}NO 232

List of abbreviations **239**

Acknowledgements **259**

Curriculum Vitae **260**

List of Figures

1-1 MOF SBUs known to undergo cation exchange 31

1-2 Depiction of mechanistic pathways for cation exchange. 42

2-1 The MOF-5 node as a tripodal ligand 50

2-2 Powder X-ray diffraction pattern of Ni-MOF-5 51

2-3 Amount of Ni^{2+} incorporated into MOF-5 as a function of Ni:Zn molar ratio in solution 53

2-4 TGA plot of unactivated Ni-MOF-5 54

2-5 Portion of crystal structure of Ni-MOF-5 55

2-6 N_2 adsorption isotherm for Ni-MOF-5 at 77 K 56

2-7 FT-IR spectrum of as-synthesized Ni-MOF-5 58

2-8 In situ diffuse reflectance UV-Vis-IR of Ni-MOF-5 during activation . 59

2-9 The temperature dependence of $\chi_m T$ of evacuated Ni-MOF-5 59

2-10 diffuse reflectance UV-Vis-NIR spectra of (DMF)Ni-MOF-5 and of (MesCNO)Ni-MOF-5. 60

2-11 FT-IR spectrum of fully activated Ni-MOF-5 and (MesCNO)Ni-MOF-5 60

2-12 Sequential loss of DMF molecules from a $(DMF)_2NiZn_3O(carboxylate)_6$ cluster and isolation of a MesCNO adduct 61

2-13 Experimental and theoretical UV-Vis traces of six-, five-, and four-coordinate Ni-MOF-5. 63

2-14 The experimental and theoretical UV-Vis traces of $(DMF)_2$Ni-MOF-5 65

2-15 Two views of the geometry-optimized cluster $NiZn_3O(O_2C\text{-}C_6H_5)_6$ . . 66

2-16 Two stereoisomers of (DMF)$NiZn_3O(O_2C\text{-}C_6H_5)_6$ after geometry optimization 67
2-17 The geometry-optimized cluster $(DMF)_2NiZn_3O(O_2C\text{-}C_6H_5)_6$ 67

3-1 FT-IR spectrum and TGA plot of solvated MOF-5 with RGA-MS of exhaust gas 76
3-2 ^{67}Zn and ^{13}C NMR spectra of solvated MOF-5 79
3-3 ^{67}Zn NMR spectra of natural abundance desolvated MOF-5 acquired at 21.1 T under spinning and non-spinning conditions 80
3-4 Comparison of ^{67}Zn NMR spectra of natural abundance and ^{67}Zn-enriched MOF-5 81
3-5 ^{13}C NMR spectra of solvated MOF-5 83
3-6 Variable temperature non-spinning ^2H NMR spectra of d_7-DMF bound to MOF-5. 84
3-7 Dynamic changes in coordination number of Zn sites in MOF-5, as determined by molecular dynamics simulation 86
3-8 Summary of the BOMD simulated trajectories corresponding to the pseudo-octahedral Zn site, Zn_8, for the first 6 ps 87
3-9 PXRD patterns of ^{67}Zn-enriched MOF-5 used for ^{67}Zn NMR experiments 93
3-10 ^{67}Zn NMR spectrum of natural abundance desolvated Zn-MOF acquired at 21.1 T compared to simulated quadrupolar and chemical shift anisotropy 95

4-1 MOF-5 clusters relevant to Co^{2+}-exchange with the corresponding nomenclature 98
4-2 Optical photographs of Co-MOF-5 after different periods of cation exchange 100
4-3 Diffuse reflectance visible spectra of MOF-5 after soaking in $CoCl_2$-DMF solutions for specified lengths of time 101
4-4 Amount of Co^{2+}-exchanged into each MOF-5 cluster as determined from ICP-AES analysis when using $CoCl_2$ 102

4-5 Amount of Co^{2+}-exchanged into each MOF-5 cluster as determined from ICP-AES analysis when using $Co(NO_3)_2 \cdot xH_2O$ 102
4-6 Amount of Ni^{2+}-exchanged into each MOF-5 cluster as determined from ICP-AES analysis when using $Ni(NO_3)_2 \cdot xH_2O$ 103

5-1 Illustration of exchangeable metal sites in M_1M_2BTT. 116
5-2 The f' and f'' curves shown with the incident wavelengths delineated by vertical lines. 123

6-1 The SBUs of MOF-5 (left) and MFU-4*l* (right). 132
6-2 Ni:Zn molar ratio in Ni-MOF-5 plotted against Dq 133
6-3 Ni:Zn molar ratio in Ni-MOF-5 plotted against calculated Ni–solvent interactions 134
6-4 Ni:Zn molar ratio in Ni-MOF-5 plotted against calculated Zn–solvent interactions 135
6-5 Ni:Zn molar ratio in Ni-MOF-5 plotted against Gutmann donor numbers of the various solvents. 135
6-6 Ni:Zn molar ratio in Ni-MOF-5 plotted against the polarity index of each solvent. 136
6-7 Ni:Zn molar ratio in Ni-MOF-5 plotted against the static dielectric constants of the various solvents. 137
6-8 Co:Zn molarnratio of Co-MFU-4*l* plotted against ligand field parameter Dq. 138
6-9 Co:Zn molar ratio of Co-MOF-5 plotted against ligand field parameter Dq 138
6-10 Co:Zn molar ratio of Co-MFU-4*l* plotted against Gutmann donor numbers of the various solvents 139
6-11 Co:Zn molar ratio of Co-MFU-4*l* plotted against the computed Co–solvent interaction of each solvent 140
6-12 Co:Zn molar ratio of Co-MFU-4*l* plotted against the computed Zn–solvent interaction of each solvent 140

6-13 Co:Zn molar ratio of Co-MFU-4*l* plotted against Snyder polarity indices 141
6-14 Co:Zn molar ratio of Co-MFU-4*l* plotted against the Hansen δ_H solubility parameter 142
6-15 Co:Zn molar ratio of Co-MFU-4*l* plotted against the static dielectric constants of the various solvents 143
6-16 Approximate $\ln K_{eq}$ versus 1/T. 144

7-1 An illustration of the metal cluster of Fe^{2+}-MOF-5 151
7-2 PXRD pattern of Fe^{2+}-MOF-5 152
7-3 N_2 isotherm at 77 K of Fe^{2+}-MOF-5 152
7-4 The temperature-dependent magnetic susceptibility Fe^{2+}-MOF-5 . . . 153
7-5 Temperature-dependence of the zero-field Mössbauer spectra recorded for a non-evacuated Fe-MOF-5 sample 155
7-6 The temperature-dependence of the quadrupole splitting fit from Mössbauer of non-evacuated Fe-MOF-5 156
7-7 The magnetic Mössbauer spectra of Fe-MOF-5 under N_2 157
7-8 The Mössbauer spectra of Fe-MOF-5 after exposure to O_2 158
7-9 Temperature dependence of the zero-field Mössbauer spectra recorded for the evacuated Fe-MOF-5 sample 159
7-10 Comparison of the zero-field Mössbauer spectra recorded at 4.2 (top) and 70 K (bottom) of the evacuated (right) and non-evacuated (left) Fe-MOF-5 samples 160
7-11 Plot of measured ΔE_Q versus temperature for evacuated Fe-MOF-5 under Ar with fit 163
7-12 The field-dependent Mössbauer spectra of evacuated Fe-MOF-5 under Ar and Paratone® N oil 164

8-1 Illustration of MOF-5 as a tripodal ligand 172
8-2 PXRD patters of (Cl)M-MOF-5 173
8-3 Optical microscope photographs and SEM-EDX data of a single crystal of ClTi-MOF-5 175

8-4 Optical microscope photographs and SEM-EDX data of a single crystal of ClCr-MOF-5 176
8-5 Optical microscope photographs and SEM-EDX data of a single crystal of Mn-MOF-5 177
8-6 Optical microscope photographs and SEM-EDX data of a single crystal of Fe-MOF-5 178
8-7 Optical microscope photographs of a single crystal of V-MOF-5 . . . 179
8-8 Optical microscope photographs of a single crystal of ClV-MOF-5 . . 179
8-9 Optical microscope photographs of a single crystal of Cr-MOF-5 . . . 179
8-10 Diffuse reflectance UV-Vis-NIR spectrum of ClTi-MOF-5. 180
8-11 Diffuse reflectance UV-Vis-NIR spectra of ClCr-MOF-5, Cr-MOF-5, and Cr-MOF-5 after treatment with $NOBF_4$ to afford BF_4Cr-MOF-5 181
8-12 Continuous-wave X-band EPR spectrum of ClTi-MOF-5 at 77 K . . . 182
8-13 Continuous-wave X-band EPR spectrum of Mn-MOF-5 at 77 K . . . 182
8-14 Continuous-wave X-band EPR spectrum of ClCr-MOF-5 at 77 K . . 183
8-15 Continuous-wave X-band EPR spectrum of V-MOF-5 at 77 K and a simulated trace 183
8-16 The N_2 uptake at 77 K of (Cl)M-MOF-5 184
8-17 Diffuse reflectance UV-Vis-NIR spectrum of Cr-MOF-5 with TD-DFT-predicted transitions 186
8-18 Diffuse reflectance UV-Vis-NIR spectrum of ClCr-MOF-5 with TD-DFT transitions predicted from a model compound without pendant Cl atom 187
8-19 Diffuse reflectance UV-Vis-NIR spectrum of ClCr-MOF-5 with TD-DFT transitions predicted from a model compound without pendant Cl atom 188
8-20 Diffuse reflectance UV-Vis-NIR spectrum of BF_4Cr-MOF-5 shown in green with TD-DFT transitions predicted from a model compound without pendant Cl atom 189

8-21 PXRD patterns of (BF_4)Cr-MOF-5 and (NO)Fe-MOF-5 compared to that simulated for MOF-5 190
8-22 N_2 isotherms of Cr-MOF-5 and (BF_4)Cr-MOF-5 190
8-23 DRIFTS spectra of Fe-MOF-5 before and after exposure to NO . . . 192
8-24 DRIFTS spectra of fully activated MOF-5 before and after exposure to NO. 193
8-25 Diffuse reflectance UV-Vis-NIR of FeMOF-5 before and after treatment with NO gas at room temperature 194
8-26 Continuous-wave X-band EPR spectrum of (NO)Fe-MOF-5 at 77 K . 195
8-27 Continuous-wave X-band EPR spectrum of ClV-MOF-5 after treatment with $[(THF)_3Na^+(TEMPO^-)]_4$ collected at 77 K. 196

9-1 The crystal structure of MOF-5 with proposed Fe^{2+} site 206
9-2 The UV-Vis spectra Fe^{2+}-MOF-5 after exposure to NO 208
9-3 Selected in situ DRIFTS of Fe-MOF-5 during NO disproportionation 210
9-4 Complete in situ DRIFTS collected on Fe-MOF-5 during NO disproportionation 211
9-5 Powder X-ray diffraction pattern of NO_2Fe-MOF-5 212
9-6 N_2 isotherm of NO_2Fe-MOF-5 213
9-7 RGA-MS after NO disproportionation 213
9-8 XAS spectra of of Fe-MOF-5, species NO_2Fe-MOF-5, and species N_2O_2Fe-MOF-5 214
9-9 Mössbauer spectra of Fe-MOF-5 and NO_2-FeMOF-5 215
9-10 EPR spectrum of NO_2Fe-MOF-5 216
9-11 EPR spectrum of N_2O_2Fe-MOF-5 216
9-12 Selected DRIFTS spectra of NO disproportionation when using ^{15}NO 218
9-13 Transient DRIFTS spectra of Fe-MOF-5 under ^{15}NO 219
9-14 RGA-MS detection of $^{15}N^{15}NO$ 220
9-15 Geometry-optimized structure of ONNO– 221
9-16 Geometry-optimized structure of ONN–O 222

9-17 Geometry-optimized structure of –ONNO– 223
9-18 Geometry-optimized structure of –NO2 224
9-19 Geometry-optimized structure of –ONO– 225
9-20 Apparatus for the synthesis of ^{15}NO 233

List of Tables

1.1 Summary of known examples of cation exchange 47

1.2 Summary of known examples of cation exchange, continued 48

2.1 Calculated Racah and ligand field parameters of various tetrahedral Ni^{2+} species based on observed transitions ν_2 and ν_3. 54

2.2 Crystallographic data for crystals of $Ni_{0.36}Zn_{3.64}O_{13}C_{24}H_{12}$. 68

2.3 Optimized atomic coordinates for $NiZn_3O(C_8H_4O_4)_6$ 69

2.4 Optimized atomic coordinates for $(DMF)_2NiZn_3O(C_8H_4O_4)_6$ 70

2.5 Optimized coordinates of the equatorial isomer $(DMF)NiZn_3O(C_8H_4O_4)_6$ 71

2.6 Optimized coordinates for axial isomer of $(DMF)NiZn_3O(C_8H_4O_4)_6$. 72

3.1 Thermodynamic cycle used to determine ΔH_f of solvated MOF-5 . . 77

3.2 Thermodynamic data used to determine ΔH_f of solvated MOF-5 . . 77

4.1 Calculated ΔG_{rxn} of different Co-MOF-5 clusters 103

4.2 Optimized atomic coordinates for $Co(DMF)_4{}^{2+}$ 108

4.3 Optimized atomic coordinates for $Co(DMF)_6{}^{2+}$ 109

4.4 Optimized atomic coordinates for $Zn(DMF)_6{}^{2+}$ 110

4.5 Optimized atomic coordinates for $(DMF)_2Zn_4O(C_7H_5O_2)_6$ 111

4.6 Optimized atomic coordinates for $(DMF)_2CoZn_3O(C_7H_5O_2)_6$ 112

4.7 Optimized atomic coordinates for $CoZn_3O(C_7H_5O_2)_6$ 113

4.8 Optimized atomic coordinates for $(DMF)_2ZnCoZn_3O(C_7H_5O_2)_6$ . . . 114

5.1 Unit cell parameters and C_{4v} metal site occupancy data for MnMnBTT-7d collected at Fe, Cu and Zn edges shown as M%. 124

5.2 Unit cell parameters and C_{4v} metal site occupancy data for MMnBTT-7d (M = Fe, Cu and Zn) shown as M% [M% corrected for baseline from MnMnBTT]. 125
5.3 Crystallographic data for crystals of $C_{41}H_{12}Cl_{1.50}Fe_{1.11}Mn_{5.64}N_{48}O_5$. . 127
5.4 Crystallographic data for crystals of $C_{41}H_{12}Cl_{1.38}Cu_{6.02}Mn_{0.67}N_{48}O_5$. . 128
5.5 Crystallographic data for crystals of $C_{41}H_{12}Cl_{1.50}Zn_{4.85}Mn_{1.90}N_{48}O_5$. . 129

7.1 Comparison of Mössbauer parameters determined at 4.3 K for the evacuated and non-evacuated Fe-MOF-5 161

8.1 Molecular formulas of (Cl)M-MOF-5 based on ICP-AES results and C, H, N, Cl elemental analysis 173
8.2 Comparison of ν_{N-O} and λ_{max} values for the nitrosyl-to-iron charge transfer band in (NO)Fe-MOF-5 with relevant $\{Fe\text{-}NO\}^7$ complexes and other MOFs 193
8.3 Optimized atomic coordinates for $ClTiZn_3O(C_8H_4O_4)_6$ 201
8.4 Optimized atomic coordinates for $ClCrZn_3O(C_8H_4O_4)_6$ 202
8.5 Optimized atomic coordinates for $Cr^{3+}Zn_3O(C_8H_4O_4)_6$ 203
8.6 Optimized atomic coordinates for $Cr^{2+}Zn_3O(C_8H_4O_4)_6$ 204

9.1 Summary of transient DRIFTS bands in **B** – **D** 209
9.2 Summary calculated frequencies of model compounds 227
9.3 Optimized atomic coordinates for the ONNO– isomer 234
9.4 Optimized atomic coordinates for the ONN–O isomer 235
9.5 Optimized atomic coordinates for the –ONNO– isomer 236
9.6 Optimized atomic coordinates for the $–NO_2$ isomer 237
9.7 Optimized atomic coordinates for the –ONO– isomer 238

Part I

Cation Exchange in MOF-5

Chapter 1

Cation Exchange in MOFs

1.1 Motivation

The chemical transformation of reactant molecules into products often requires electron transfer from transition-metal species. The role that they play may be catalytic, where the metal species remains unchanged at the end of numerous transformations, or stoichiometric, where it is consumed after just a single transformation. If the reactant and metal species share the same phase, their interaction is called homogeneous and typically involves molecules in the liquid phase. Often, in industrially relevant catalysis, the metal species is in the solid state, reacting with liquid- or gas-phase molecules, in which case the interaction is heterogeneous. When employing homogeneous or heterogeneous systems, each enjoys distinct advantages. For example, the active metal species in homogeneous reactions can be studied through precise characterization methods and, once identified, can be equated with the bulk material. This precision translates into great control over the properties and, hence, reactivity of the metal species. In heterogeneous systems, on the other hand, the metal species remains active at high temperatures and pressures, and the material is often inexpensive. Despite this appeal, the active sites in heterogeneous systems may arise as defects, rendering them difficult to characterize and control. However well-defined metal species are in homogeneous reactions, they are constrained to milder reaction conditions, may deactivate through mechanisms like bimolecular deactivation,[1] and

are often expensive to synthesize and recover from reaction mixtures. The focus of this thesis is to bridge these two classes of reactivity and combine their advantages by using the class of materials known as metal-organic frameworks (MOFs). In particular, this thesis will demonstrate that the metal clusters comprising MOFs can be viewed as well-defined molecules that are endowed with the unique ligand field of the MOF lattice and that they can undergo redox chemistry with small molecules.

MOFs are coordination polymers with permanent porosity after evacuation. They consist of metal cations or inorganic clusters tethered together by organic molecules that contain multiple functional groups capable of ligating to metal sites. The inorganic clusters are often referred to as metal nodes or secondary building units (SBUs). Over the past two decades, MOFs have been tested for many applications, but the SBUs are almost always treated as structural supports, thought to be too rigid for further chemistry—at least without compromising the integrity of the material. We noticed, however, that on occasion the resulting SBUs are unusual metal species when viewed from the perspective of classical inorganic synthesis. For example, the material known as MnMn-BTT contains a four-coordinate Mn^{2+} with C_{4v} symmetry in the asymmetric unit and another with C_s symmetry and only two coordinate geometry.[2] Inspired by these cases, we sought to prove that the SBUs of MOFs can be used as novel platforms for coordination chemistry and small-molecule activation.

For the SBUs to be employed for reactivity studies we had to demonstrate that they met several criteria. For this task, we focused on the iconic example known as MOF-5 since it is often employed in seminal findings about MOFs in general. In the following chapters, the SBUs of MOF-5 are shown to support metal species that are difficult or impossible to achieve in other materials or as molecules. Furthermore, we show they can undergo significant geometrical distortions while dynamically interacting with molecules as benign as N_2. Without disrupting the crystallinity or porosity of MOF-5, transition-metal cations mediate both outer-sphere and inner-sphere electron transfer during transformations that can be well-understood by spectroscopy and other characterization methods. As a proof that the SBUs can be used for small molecule activation, we present evidence that Fe^{2+} ions within MOF-5 promote the

disproportionation of NO.

MOF-5 does not normally contain unusual metal species or cations that can facilitate redox transformations. Instead, we employed a technique known as cation exchange to replace a portion of the original Zn^{2+} ions with Ti^{3+}, V^{3+}, V^{2+}, Cr^{3+}, Cr^{2+}, Mn^{2+}, Fe^{2+}, Co^{2+}, or Ni^{2+}. That this process can occur without destroying the material is at least as fascinating as the subsequent reactivity studies discussed in Part 2. Because the resulting materials were often isolable only through cation exchange, we devoted much effort to understanding the factors that govern the exchange process so that it might be used as a general and rational tool. Part 1 of this thesis presents our foundational studies into this area, and, as in the case of Chapter 3, our findings guided our understanding of how to then conduct reactivity studies. The following chapter surveys the known examples of cation exchange at the SBUs of MOFs through a series of questions such as, "Which SBUs can undergo cation exchange?" By directing future studies toward answering these questions, the community will reveal deep insight into this fascinating phenomenon.[1]

1.2 Background

Cation exchange is a powerful tool for designing new materials. Broadly defined, it is the partial or complete substitution of a metal ion at the site of another. This process offers an alternative, typically milder, route for accessing materials when conventional synthesis at high temperature fails. For decades, it has been employed to tailor the composition of zeolites and, more recently, nanocrystals. MOFs emerged decades ago, but cation exchange was only first demonstrated with them in 2007.[3] In these materials, the exchange occurs at the SBUs. Although these clusters are integral to the MOF structure, the metal ions can be replaced, sometimes entirely and in a matter of hours, without compromising the structure. The details of this fascinating transformation are unknown, and the bounty of MOF structures that

[1] A portion of the following chapter appeared previously in Brozek, C. K.; Dincă, M. *Chem. Soc. Rev.* **2014**, *43*, 5456 and is reproduced here with permission from the Royal Society of Chemistry.

undergo metal-ion substitution presents a host of curiosities to explain.

Geochemists have long known cation exchange as diadochy.[4] Minerals are rarely pure phases because minor amounts of foreign ions of similar charge and size often incorporate into the structure. The replacement of an ion for another at a particular crystalline lattice position is a diadochic transformation, and often requires high temperatures and pressures. For instance, the volcanic rocks known as the olivine series, $(Mg^{2+}, Fe^{2+})SiO_4$, differ by their relative composition of Mg^{2+} or Fe^{2+}, which results from diadochic transformations in magma.[5] Meanwhile, the substitution of Na^+ into porous leucite, $KAlSi_2O_6$, occurs at temperatures as low as 150 °C, illustrating the role of porosity in facilitating the exchange process.[6] V. M. Goldschmidt developed a set of rules to explain the mutual replacement of ions in magmatic minerals.[7] This contends that ions undergo diadochy if they possess similar charge and radii. Ions with greater charge or smaller radii incorporate to a great degree because they will form stronger, more ionic bonds. To account for the covalent component of these bonds, Ringwood's rule states that ions with similar electronegativity replace each other.[8] The ion with the lower value will exchange more because it will form bonds with greater ionic character. These trends are useful for assessing the cation-exchange behavior of MOFs, though they derive from observations with minerals, which are typically densely packed structures.

Cation exchange is also employed with nanocrystals to finely tune their band structures by inserting specific ions into well-defined environments.[9] Unlike in bulk CdSe, Cu_2S, or similar extended materials, cation exchange in nanocrystals occurs at room temperature at sub-second rates due to enhanced surface area and low atomic counts. The small size of these particles also facilitates atomic reorganization and diminishes lattice strain. This technique enables the synthesis of metastable phases that are not achievable by conventional "hot injection" synthesis, such as Cu_2S particles with turn-on plasmon resonance.[10] Cation exchange also enables complexity to be engineered into a nanocrysal device. For instance, templating CdSe on PbSe nanorods for fixed amounts of time generates CdSe/PbSe core/shell heterostructures so that electron and hole carriers confine within the lower band-gap PbSe core, resulting in

high quantum yield excitonic emission.[11]

In solution, metallo-cluster compounds and mononuclear complexes are also known to substitute for other cations. For decades, transmetallation has been used to replace cations in mononuclear compounds featuring multidentate ligands. The mechanism of these exchanges often involves the transfer of a ligand to a new metal ion.[12] Cation substitution at a molecular cluster that left the anionic framework intact was first documented in 1982 for the adamantane-like cage compounds, $[M_{4-n},M'_n,(SC_6H_5)]_{2-}$ (M, M′ = Fe^{2+}, Co^{2+}, Zn^{2+}, Cd^{2+}).[13] Metal exchange in these compounds was believed to involve free ions exiting the cage before the inserting species associated. However, mechanistic studies of the simpler case of Co^{2+} incorporating into $[M_4(SPh)_{10}]^{2-}$ (M = Zn or Fe) revealed a process that was quite complex.[14] Few other reports have attempted to understand cation exchange in molecules, though metallothioneins are thought to mediate detoxification of trace metal through some version of metal ion substitution.[15]

This chapter outlines the available observations of cation exchange at MOF SBUs so that general trends and future studies can be sketched. We organize data around questions that need to be answered to endow this technique with predictive capabilities. All known examples of metal-ion substitution at MOF SBUs and relevant details are listed in Table 1.1 with pictorial representations of the SBUs in Figure 1-1. This discussion is confined to substitution that occurs at SBUs and not in the pores or when metal ions are part of the ligands, in so-called metalloligands. Cation exchange has already yielded some surprising results and new materials that have not been accessible otherwise, but the extent of its use for designing new MOFs in a systematic and predictive manner depends on understanding its mechanism.

1.3 Which SBUs Undergo Cation Exchange?

If we can predict which MOFs are susceptible to cation exchange, it will become a rational tool for synthesizing new materials with intended properties. After elucidating the factors that make an SBU exchangeable, specific materials could be selected

for cation exchange from among the thousands of reported MOFs, and their exact compositions could be designed beforehand. These factors are yet unknown, but surveying the reported examples of cation exchange in MOFs reveals several common features among their SBUs.

A foremost observation is that the exchangeable metal ions in an SBU are often capable of higher coordination numbers than those observed in the X-ray crystal structures. For example, the series of materials known as (Cl)M-MOF-5 arise from Ti^{3+}, V^{3+}, V^{2+}, Cr^{3+}, Cr^{2+}, Mn^{2+}, Fe^{2+}, or Ni^{2+} replacing a four-coordinate Zn^{2+} cation in each cluster of MOF-5 ($Zn_4O(BDC)_3$).[16,17] Similarly, the tetrahedral Zn^{2+} sites in ZIF-8 (Zn-(MeIm)) and ZIF-71 (Zn-(Cl_2Im)) can be replaced by Mn^{2+} ions,[18] while the four-coordinate Zn^{2+} sites in MFU-4*l* ($ZnZn_4Cl_4(BTDD_6)$) can be replaced by Co^{2+} ions.[19] Furthermore, one of the two replaceable Zn^{2+} sites in JUC-118 ($[Zn_4(TIAPy)\cdot(H_2O)_4\cdot(EGME)_2]$) is four-coordinate,[20] as are two of the four unique Zn^{2+} sites in Zn_4-$(DCPP)_2(DMF)_3(H_2O)_2$,[21] while one of the two exchangeable Zn^{2+} sites in $Zn_3(CBAI)_2(DMF)_2]$ is five-coordinate.[22]

In several examples, the exchangeable metal ions contain open sites when fully evacuated, but become partially solvated when immersed in solution. The family of MOFs known as MM-BTT ($M_3[(M_4Cl)_3(BTT)_8]_2$), begin with a two-coordinate C_s-symmetric Mn^{2+} site and five-coordinate Mn^{2+} site with C_{4v} symmetry.[2] When in methanol, the latter gains a solvent ligand to become six-coordinate, while the former becomes fully solvated in the cavities of the structure. Either the fully solvated or both Mn^{2+} sites exchange for Fe^{2+}, Co^{2+}, Ni^{2+}, Cu^{2+}, or Zn^{2+}.[3] An isostructural material known as $Cd_3[(Cd_4Cl)_3(BTT)_8]_2$ contains Cd^{2+} that demonstrates similar coordinative changes upon solvation and replaces for Co^{2+} or Ni^{2+}.[23]

Not all structures can be desolvated as MM-BTT, but the metal sites in many other SBUs typically feature bound solvent molecules. The materials known as Zn-HKUST-1 ($[Zn_3(BTC)_2(H_2O)_3]$),[24] PMOF-2 ($Zn_{24}(TDCPEB)_8(H_2O)_{12}$),[24] PCN-921 ($Zn_4(ETTB)\cdot 4DMF$),[25] and $Zn_7(BODPDI)_3(H_2O)_7]_n[Zn_5((BODPDI))_3(H_2O)_5]_n$[26] contain SBUs with "paddlewheel" structures. Each of the metal sites in these clusters is bound to four carboxylates from the framework and one solvent molecule

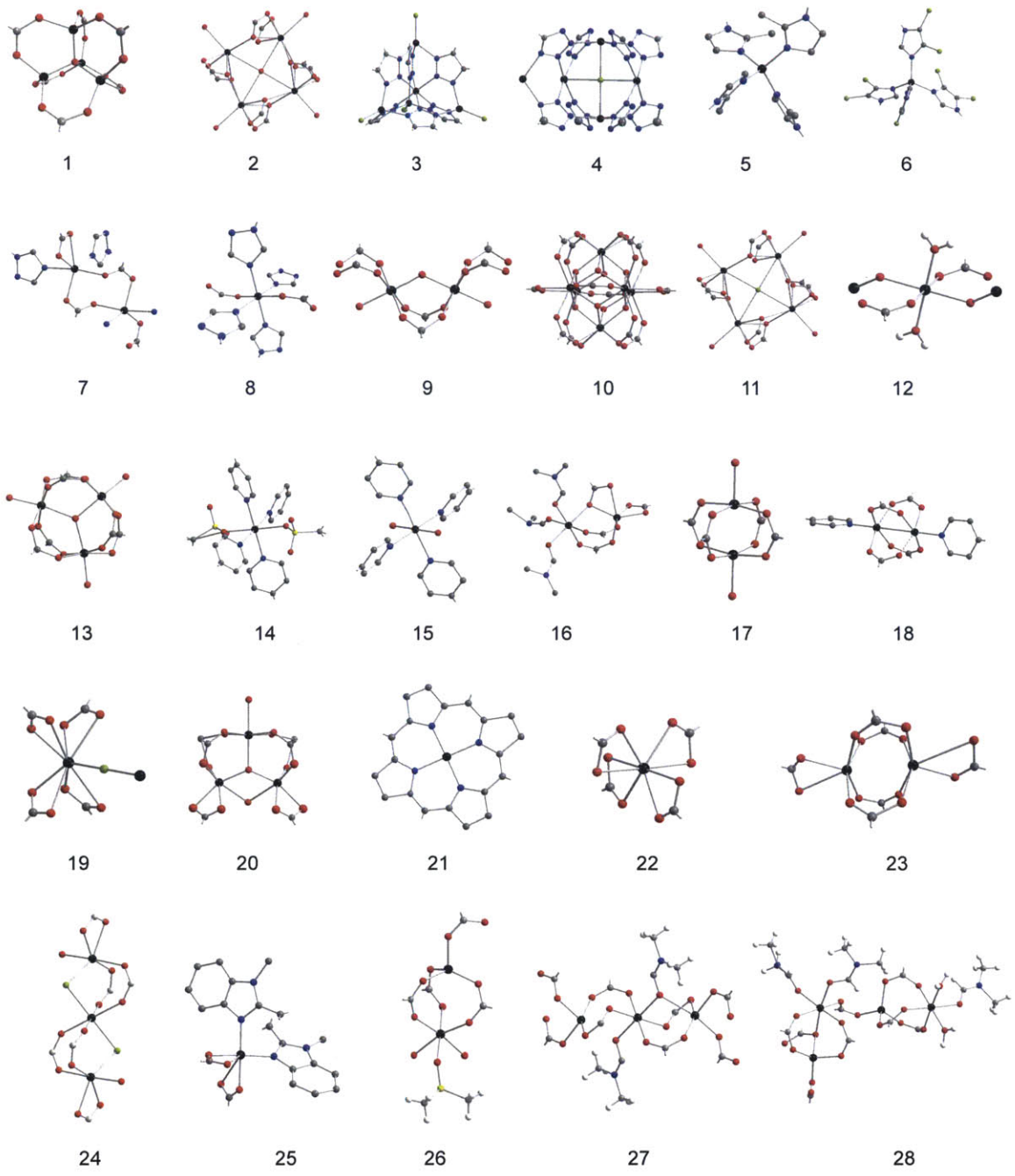

Figure 1-1: The known examples of MOF SBUs that undergo cation exchange. Black, green, red, blue, and gray spheres denote metal, chloride, oxygen, nitrogen, and carbon atoms, respectively.

at the axial position. $Cd_{1.5}(H_3O)_3[(Cd_4O)_3(HETT)_8]_2{\cdot}6H_2O$[27] and POST-65(Mn) ($Mn(H_3O)[(Mn_4Cl)_3(HMTT)_8]_2$)[28] have the sodalite topology, like MM-BTT, with similar partially solvated SBUs. The metal sites in the planar Cd_4O clusters of $Cd_{1.5}(H_3O)_3[(Cd_4O)_3(HETT)_8]{\cdot}6H_2O$ are each bound to a solvent molecule and exchange for Pb^{2+}. The Mn_4Cl clusters of POST-65(Mn) are partially solvated, as in MM-BTT, and can be replaced by Fe^{3+}, Co^{2+}, Ni^{2+}, Cu^{2+}. In the case of Fe^{3+} exchange, the $[M_4Cl]^{7+}$ SBU transforms to $[Fe_4OH]^{11+}$, with two μ_2-O providing additional charge balance. Similar to the metal sites in the "paddlewheel" and the planar MCl/O clusters, the exchangeable Cr^{3+} sites in MIL-101(Cr)[29] ($Cr_3F(H_2O)_2O(BDC)_3$) would be coordinatively unsaturated if not for a pendent solvent ligand in the axial position. Similarly, the SBU of the series $[Co_3O(BTB)_2(H_2O)_x(DMF)_y]{\cdot}z\text{DMF}{\cdot}nH_2O$ ($x = y = 1$, $z = 7.5$, $n = 12$; $x = 2, y = 0, z = 8.5$, $n = 8$; $x = 2$, $y = 1$, $z = 7$, $n = 8$) contains a cobalt site with a bound solvent molecule, and all three Co^{2+} sites exchange to form an entirely new structure.[30] In another case of partial solvation, the exchangeable di-zinc sites in NTU-101-Zn[31] ($Zn_2(TDP)(DMF)_3$) and $Zn_2(BDCPPI)(DMF)_3$ contain a Zn^{2+} ion held to the framework by only three bonds, with its remaining coordination sphere filled by three solvent molecules.[32] The material $Zn(OOCClH_3C_6Fc)_2(H_2O)_3$ features $[\text{–}Zn^{2+}\text{–}O^{2-}\text{–}Zn^{2+}\text{–}]_\infty$ chains with each Zn^{2+} site bound to two bridging carboxylates that are oriented trans from each other.[33] These otherwise four-coordinate Zn^{2+} ions include two ligated water molecules and can be replaced by Pb^{2+}, Cd^{2+}, Cu^{2+}, Ni^{2+}, Co^{2+}, Mn^{2+}, or Cr^{2+}. DMSO occupies a coordination site of the 6-coordinate Zn^{2+} in JUC-118,[20] two DMF molecules are bound to a Zn^{2+} atom in the asymmetric unit of $Zn_3(CBAI)_2(DMF)_2$,[22] and two of the four Zn^{2+} sites in Zn_4-$(DCPP)_2(DMF)_3(H_2O)$[21] are ligated by DMF or H_2O. In one of the most complete mechanistic reports of cation exchange in a MOF, magnetic measurements revealed that the first Zn^{2+} to exchange in this material is the one with most bound solvent.

Conversely, SBUs with metal sites that are octahedrally coordinated by the framework ligands and have no terminal solvento species typically do not undergo cation exchange. For instance, of the two crystallographically distinct Zn^{2+} sites in MFU-4*l*,

the ion attached through six bonds to the framework does not exchange for Co^{2+}.[19] In the MOF known as porph@MOM-10-Cd ($[Cd_6(BPT)_4Cl_4(H_2O)_4]\cdot[C_{44}H_{36}N_8CdCl]$), one Cd^{2+} is coordinatively saturated in octahedral fashion by framework ligands, while the other site contains a solvent ligand.[34] Cu^{2+} only exchanges the latter completely. Unlike the previous two examples where the extent of cation exchange could be compared between two types of coordination environments within the same MOF, we do not have this vantage point in analyzing $[(CH_3)_2NH_2]_{15}[(Cd_2Cl)_3(TATPT)_4]$, where a single nine-coordinate Cd^{2+} ion is present in the asymmetric unit.[35] Consistent with the generally small degree of exchange for more highly coordinated ions, Cd^{2+} centers in this structure exchange with Cu^{2+}, Co^{2+}, Ni^{2+}, and Zn^{2+}, but only to a small degree. Finally, the MOFs known as UiO-66[36] ($Zr_6O_4(OH)_4(BDC)_{12}$) and MIL-53(Al)-Br[36] (Al(OH)(BDC-Br)) also contain SBUs with metals bound to the framework in high coordination and do not exchange for other ions completely. Given that Zr^{4+} and Al^{3+} form some of the strongest metal-oxygen bonds among the metals incorporated in MOFs, it is remarkable that they undergo any extent of cation exchange.

Metal sites that are coordinately saturated by the framework and undergo complete cation exchange might do so because their weak-field ligands readily dissociate from the metal. A ligand-field analysis of Ni-MOF-5 indicates that the MOF-5 framework is a stronger ligand than halides, but is significantly weaker than coordinating solvents such as DMSO or DMF. Considering that in MOF-5 the ligand field is weak despite the presence of an O^{2-} in the coordination sphere, this study suggests that SBUs comprised of only carboxylates form weak bonds with late transition metal ions. For example, the metal sites in both $Na_{0.25}[(CH_3)_2NH_2]_{1.75}[M(HMBM)_2]$[37] ($M = Cd^{2+}$ or Cu^{2+}) and porph@MOM-11-Cd[34] ($[Cd_4(BPT)_4]\cdot[Cd(C_{44}H_{36}N_8)]$ are bound to six carboxylate ligands, yet exchange for Cu^{2+} at 96% of the sites, virtually quantitatively. Here, the weak-field carboxylates might dissociate and permit cation exchange despite the metal sites being octahedrally coordinated. The almost complete exchange of seemingly coordinatively saturated ions is also observed with ligands other than carboxylates. Unlike $[(CH_3)_2NH_2]_{15}[(Cd_2Cl)_3(TATPT)_4]$ or MIL-53(Al)-Br, which

exchange partially, the environments of these SBUs typically do not contain single atom μ_2 ligands, such as O^{2-} or Cl^-. The "paddlewheel" SBUs of PCN-921, SUMOF-1-Zn ($Zn_6(BTB)_4(BP)_3$),[38] and $M_6(BTB)_4(BP)_3$ (M = Co, Cu, Ni) contain 4,4′-bipyridine bridging to an adjacent SBU, rather than a solvent molecule at the axial position.[39] Despite lacking solvent ligands, the metal sites in these materials exchange for Cu^{2+} completely. Metal ions in the SBUs of $Co_3(BTX)_4(BDC)_3(H_2O)_4$,[40] Zn(4,4′-BP)$_2$-$(FcphSO_3)_2$,[41] $Cd(BP)_2(FcSO_3)$,[42] and $[M(BTTN)_2(H_2O)_2]_2(PF_6)$pyrene$_2$[43] (M = Cd^{2+}, Zn^{2+}) can be entirely replaced by Cu^{2+}, despite being bound to four 4,4′-bipyridine ligands and two carboxylates. Similarly, the six-coordinate Cd^{2+} sites in $Cd_2(BTX)_2(BDC)_2$ can be replaced by Cu^{2+}, even though they are bound to bridging carboxylates and triazole ligands. None of these examples contain chains bridged by single atom μ_2 ligands, and undergo complete exchange despite being coordinatively saturated by framework ligands. It is important to note that the family of MOFs known as M-MOF-74 feature SBUs with $[-M^{2+}-O^{2-}-M^{2+}-]_\infty$ chains and is conspicuously absent from the known examples of cation exchange.

Taken together, these observations begin to reveal the factors that enable cation exchange at certain SBUs. The pervasiveness of partially solvated SBUs among these examples and the coordination changes that MM-BTT undergoes upon solvation call into question whether the metal sites in MOF-5, ZIF-8, and MFU-4*l* are indeed unsaturated when surrounded by solvent. If geometric flexibility and the ability of metal sites to interact with the solvent are requisites for cation exchange, then we can begin to sketch a mechanism for this process (see Figure 1-2). Perhaps the metal ion does not readily leave from the cluster as a dissociated cation. Instead, solvent molecules might associate step-wise to the exiting metal ion as it remains partially bound to the cluster. Furthermore, since cation exchange occurs in "paddlewheel" structures with either a solvent or 4,4′-bipyridine at the axial position of the metal site, the clusters must be flexible enough to accommodate the inserting metal ions or, alternatively, the carboxylates and 4,4′-bipyridine must readily dissociate without compromising the framework. Alternatively, we may consider a model where the MOF ligands dynamically dissociate from metal sites in the presence of coordinating solvents and

thereby enable cation exchange. The ability of coordinatively saturated metal sites to exchange when surrounded by weak-field carboxylates, but not bridging O^{2-} ligands, suggests that cation exchange might become a predictable tool by quantifying the interaction of the SBU with the metal ions. If future studies measured the ligand field strength of the exchangeable SBUs, then general trends might emerge and aid our understanding of the cation-exchange process. This might be achieved by UV-Vis spectroscopy, for instance, in a manner analogous to classic solution studies of homoleptic complexes.[44]

1.4 Which Ions Exchange into SBUs?

To program physical properties into a SBU through cation exchange, we must be able to predict whether a particular cation will replace another and to what extent. By controlling the initial concentration of the inserting cation solution, the thermodynamic equilibria of the exchange processes could be controlled to furnish heterometallic SBUs for specific catalytic applications. Clusters with unusual magnetic and electronic properties could be assembled through judicious cation exchange that might be otherwise impossible through direct synthesis. Attaining this depth of understanding can be achieved by comparing how a wide variety of cations replace SBUs in a particular MOF structure. Unfortunately, few studies report the results of more than one exchange, and almost none report unsuccessful attempts, which in the context of mechanistic investigations can be equally informative.

Most examples of cation exchange at SBUs involve Cu^{2+} replacing Zn^{2+} or Cd^{2+}. The Zn^{2+} ions in porph@MOM-11-Zn, PCN-921, NTU-101-Zn, and PMOF-2 are known to undergo a high degree of substitution for Cu^{2+}, with no reported attempts to exchange with other ions.[24,25,31,45] Similarly, the Cd^{2+} ions in $Cd_2(BTX)_2(BDC)_2$ and $Cd(BTX)_2Cl_2$ can be totally replaced by Cu^{2+}, but their exchange with other ions is unknown.[40] In the isostructural variants of $M_2(BDCPPI)(DMF)_3$ (M = Cd^{2+} or Zn^{2+}) both Cd^{2+} and Zn^{2+} are fully replaced by Cu^{2+}.[32] The Zn^{2+} ions in Zn-HKUST-1[24] and Zn^{2+} or Cd^{2+} ion in $M(BP)_2(FcSO_3)$ (M= Zn^{2+} or Cd^{2+}) both

exchange for Cu^{2+},[41,42] though not to completion. These reports do not always test whether the cation exchange is reversible, but the reversibility of a process lends insight into the relative thermodynamic stability of the exchanged variants. We do know, however, that reversible Zn^{2+} exchange into NTU-101-Cu[31] or Cu-PMOF-2[24] is impossible, while Zn^{2+} can partially replace Cu^{2+} in the framework of porph@MOM-11-Cu, but not at the porphyrin metalloligand.[45] Cu^{2+} replaces the Zn^{2+} atoms in these MOFs completely and, in the case of JUC-118[20] and $Zn_3(CBAI)_2(DMF)_2$,[22] does so irreversibly. While Ni^{2+} and Co^{2+} do not exchange at all into $Zn_3(CBAI)_2(DMF)_2$, they insert only into the six-coordinate sites of Zn_4-$(DCPP)_2(DMF)_3(H_2O)_2$, due to the preference for these geometries.[45]

When information is available for Cu^{2+} as well as other transition metals exchanging in the same host structure, Cu^{2+} typically inserts to the greatest extent and is the least reversible. In $Zn_2(BDCPPI)(DMF)_3$, 97% of the Zn^{2+} sites are exchangeable for Cu^{2+}, but none can be replaced by Ni^{2+}, Co^{2+}, or Cd^{2+}.[32] Similarly, Cu^{2+} exchanges Zn^{2+} in $Zn_7((BODPDI))_3(H_2O)_7]_n[Zn_5((BODPDI))_3(H_2O)_5]_n$[26] and Cd^{2+} in $Na_{0.25}[(CH_3)_2NH_2]_{1.75}[Cd(HMBM)_2]$,[37] but Ni^{2+} or Co^{2+} do not. Cu^{2+}, Co^{2+}, and Ni^{2+} replace Zn^{2+} in SUMOF-1-Zn, but only Cu^{2+} replaces all the sites, while Co^{2+} replaces 35% and Ni replaces 38% after identical times.[38] In the reverse process, the all-Zn^{2+} material can be regenerated from the Co^{2+} or Ni^{2+} variants after 7 days, but Zn^{2+} can replace only 38% of the Cu^{2+} sites in SUMOF-1-Cu. Furthermore, the Co^{2+}, Ni^{2+}, and Zn^{2+} materials are all interchangeable through reversible cation exchange, while their replacement for Cu^{2+} is irreversible. Similarly, the isostructural series $M_6(BTB)_4(BP)_3$ ($M = Zn^{2+}$, Co^{2+}, or Ni^{2+}) generate a Cu^{2+} analogue through irreversible cation exchange, while the Co^{2+} and Zn^{2+} variants are completely interchangeable.[39] Despite the overall low degree of cation exchange in $[(CH_3)_2NH_2]_{15}[(Cd_2Cl)_3(TATPT)_4]$, Cu^{2+} still replaced Cd^{2+} more than Co^{2+}, Ni^{2+}, or Zn^{2+}.[35] Among all known examples, there is only one instance in which Cu^{2+} is replaced by other transition metal ions: Zn^{2+} and Co^{2+} both exchange the Cu^{2+} sites in $Cu_8(BIM)_{16}$, ($M = Cu^{2+}$, Zn^{2+}, or Co^{2+} and $x = 0$, 0.21, or 15, respectively) albeit only 21% and 15% of the Cu^{2+} sites are replaced, respectively.[46]

SBUs that exchange a variety of cations but are not fully exchangeable by Cu^{2+} still demonstrate preference for Cu^{2+}. All the Mn^{2+} sites of POST-65(Mn) can be replaced by Co^{2+}, and Ni^{2+} but not Cu^{2+}. Nevertheless, Mn^{2+} can replace only 34% of the Cu^{2+}, whereas the Co^{2+} and Ni^{2+} processes are fully reversible.[28] The Mn^{2+} ions in the SBU of the material known as MnMn-BTT are exchangeable for Cu^{2+} and Zn^{2+}, with Cu^{2+} replacing Mn^{2+} to the fullest extent.[47] A notable exception to the apparent dominance of Cu^{2+} is porph@MOM-10-Cd, where Mn^{2+} replaces all Cd^{2+} sites, while Cu^{2+} replaces 76%.[34]

Outside the first transition series, Pb^{2+} and Cd^{2+} tend to exchange preferentially into SBUs over Cu^{2+} and other transition metals. The extent that Zn^{2+} sites can be exchanged in $Zn(OOCClH_3C_6Fc)_2(H_2O)_3$ follows the order $Pb^{2+} > Cd^{2+} > Cu^{2+} > Mn^{2+} > Ni^{2+} > Co^{2+} > Cr^{2+}$.[33] In a related system, Pb^{2+} replaces 75% of the Zn^{2+} sites of $Zn_{1-x}M_x(4,4'\text{-BP})_2\text{-}(FcphSO_3)_2$, whereas Cu^{2+} replaces just 50%.[41]

Although little rigorous work has been done to interrogate the kinetics of cation exchange in MOFs, the present studies indicate that the rate of substitution into a particular SBU depends on the identity of the metal ions. For (Cl)M-MOF-5, Ni^{2+} requires up to a year to replace 25% of the original Zn^{2+} sites, whereas Cr^{2+} and Fe^{2+} reach that extent in a week. Furthermore, the exchange with Mn^{2+} is so rapid at room temperature that the process destroys the crystals and only proceeds in a controlled fashion when conducted at 35 °C.[17] Though the resulting materials are isostructural, Cu^{2+} fully exchanges $Zn_6(BTB)_4(BP)_3$ in 2 days, $Co_6(BTB)_4(BP)_3$ in 1 day, and $Ni_6(BTB)_4(BP)_3$ in 15 days.[39] Pb^{2+} replaces Cd^{2+} in 7 days for $Cd_{1.5}(H_3O)_3[(Cd_4O)_3(HETT)_8]\cdot 6H_2O$, yet Co^{2+}, Ni^{2+}, and Cu^{2+} require 12 days to replace Mn^{2+} in a similar structure.[27]

The dominance of Cu^{2+} among these examples and the preference for Cd^{2+} and Pb^{2+} over Cu^{2+} might be explained by differences in electronegativity. Calculations suggest that Pb^{2+} has the lowest electronegativity among the cations that undergo exchange, followed by Mn^{2+} and Cd^{2+}. Cu^{2+}, on the other hand, has the highest electronegativity.[48] Perhaps Pb^{2+}, Mn^{2+}, and Cd^{2+} ions form labile ionic bonds, allowing them to perform cation exchange faster. This kinetic argument might explain

why Pb^{2+} and Cd^{2+} exchange more sites than Cu^{2+} in $Zn(OOCClH_3C_6Fc)_2(H_2O)_3$[33] ($x = 1$, 0.92, and 0.76 for Pb^{2+}, Cd^{2+}, and Cu^{2+}, respectively) and why Mn^{2+} replaces more sites than Cu^{2+} in porph@MOM-10-Cd.[34] If these experiments were allowed to go longer, Cu^{2+} might have exchanged completely. The high electronegativity of Cu^{2+} would enable it to form bonds that are more covalent and thermodynamically stable. A greater thermodynamic driving force would be consistent with the irreversibility and high degree of substitution of Cu^{2+} exchanges. This trend in electronegativity is also consistent with cation preference following the Irving-Williams series,[49] since labile Mn^{2+} species and thermodynamically stable Cu^{2+} bonds constitute either end of the series.

Even with the general trends exposed above, we cannot yet predict whether a particular cation will replace another and to what extent. In the absence of more experimental and empirical evidence, quantum chemical calculations could prove useful in predicting which cations form more thermodynamically stable complexes in a given SBU. With the computed energy values, thermodynamic equilibria could be manipulated to engineer SBUs with certain mixed-metal compositions. The mechanism of cation exchange, on the other hand, will need to be studied on a case-by-case basis. With a more detailed understanding of how the process depends on the identity of the cation, one might control the kinetics and harness cation exchange as a synthetic tool.

1.5 How Does the Framework Influence the Exchange?

To rationalize how cation exchange occurs at SBUs, one must remember that SBUs are embedded in the lattice of a MOF. Although they often resemble molecular clusters, they do not possess the degrees of freedom of molecules in solution. Thus, the lattice limits the geometrical distortions available to an SBU. We must also understand that the cation exchange process must occur in the MOF pores. The process is therefore likely influenced by diffusion and pore size effects. We do not know how these intrinsic features of MOFs impact cation exchange, but any mechanistic understanding must

account for them. The scant observations already suggest the MOF lattice impacts the cation exchange and vice versa.

An important evidence for this co-dependency is that certain cation exchanges can compromise the structural integrity of a framework. For instance, the crystals are known to crack after Cu^{2+} replacement of Zn^{2+} sites in $Zn_2(BDCPPI)(DMF)_3$,[32] and the material known as $[Zn(BTTN)_2(H_2O)_2]_2(PF_6)pyrene_2$.[43] As mentioned above, especially fast exchanges into MOF-5, such as Mn^{2+}, also deteriorate the crystals, which is evidenced both optically and especially through surface area measurements. For example, synthesizing Fe-MOF-5 using a solution of anhydrous $FeCl_2$ is rapid and leads to inferior quality powder, whereas the exchange from $Fe(BF_4)_2 \cdot xH_2O$ is slow and gives a superior material.[17] Among the cations that substitute into MOF-5, Ni^{2+} is the slowest and has the highest apparent surface area. Similarly, after Co^{2+} exchanges Cd^{2+} in MMPF-5(Cd), the surface area decreases, possibly due to collapsed pores.[50]

Observations suggest that the framework itself limits the extent of cation exchange. The replacement of Zn^{2+} by Co^{2+} in $Zn_6(BTB)_4(BP)_3$ occurs initially at the exterior of the crystals and replaces interior sites after approximately a day. The authors contend that this time dependence is the result of the lattice being more flexible at the exterior, not of diffusion limitations in the framework pores.[39] When rationalizing why Cu^{2+} exchanges 53% of the Zn^{2+} sites in Zn-HKUST-1 but all sites in PMOF-2, the authors invoked a similar argument: the longer linkers in PMOF-2 endow the lattice with greater flexibility, even though its SBUs are the same as in Zn-HKUST-1.[24] Perhaps this reasoning might explain why the extent of cation exchange in $Zn_{1-x}M_x$(4,4′-BP)$_2$-(FcphSO$_3$)$_2$ (x = 0.5, 0.75, and 0.5 for Cd^{2+}, Pb^{2+}, and Cu^{2+}, respectively) is lower for a powder material than for single crystals.[41] Larger particles might better accommodate distortions and defects introduced by the exchange process than small ones. As will be discussed in later chapters and especially in Chapter 4, the substitution of cations in the SBU of MOF-5 is almost universally capped at 25% (i.e. only one Zn^{2+} ion in every Zn_4O cluster). In fact, it may be surprising that the MOF-5 lattice, which has seemingly saturated pseudo-tetrahedral Zn^{2+} ions,

enables cation exchange at all. Attempting to substitute Ni^{2+} into basic zinc acetate, a molecular analogue of the MOF-5 SBUs, is not possible with retention of the cluster geometry.[16] Perhaps the M-MOF-74 class of materials do not undergo cation exchange because any distortion to the $[-M^{2+}-O^{2+}-M^{2+}-]_{\infty}$ SBUs would require a large activation energy imposed by the lattice.

Predicting how a MOF framework influences the cation-exchange process will become a general tool by first proceeding on a case-by-case basis. Still, knowing how a lattice inhibits or enables substitution at a SBU would allow us to design the composition of a material with greater precision.

1.6 What Role Does the Solvent Play in Cation Exchange?

Solvents differ along a wide variety of parameters that might be relevant to the mechanism of cation exchange at SBUs. The solvent dielectric constant, highest occupied molecular orbital (HOMO) level, molecular size, or ligand field strength might dictate how substitution occurs. When we develop a deeper understanding of this process, careful selection of the solvent might become a powerful handle on the rate and extent of cation exchange. Studies on the effect of employing different solvents are rarest for cation exchange in MOFs, but the available observations are still useful.

$Zn_2(BDCPPI)(DMF)_3$ was one of the first exchangeable materials to be tested against several solvents. The results suggest that the size of the solvation sphere impacts the rate of substitution. While the exchange is fast in methanol, it is slow in acetone and does not occur in larger solvents such as DMF or 1-pentanol.[32] Yet, solvents appear to play a mechanistic role aside from shuttling solvated cations through pores. Given that most SBUs feature coordinatively unsaturated metal sites or solvent ligands, it is significant that all exchanges involve coordinating solvents. Most use methanol, DMF, or H_2O—all strongly donating ligands with relatively high ligand field strengths. The Cu^{2+} substitution into Zn-HKUST-1 occurs more slowly

in DMF than in the weaker Lewis-base methanol.[24] Perhaps the Co^{2+} exchange into MMPF-5(Cd) does not go to completion because the strongly donating solvent, DMSO, was used.[50] Cu^{2+} inserts into $Zn_4(TIAPy)\cdot(H_2O)_4\cdot(EGME)_2$ in the presence of 2-methoxyethanol but not common solvents such as DMF, MeOH, or acetone.[20] Since 2-methoxyethanol also induces a single crystal-to-single crystal transformation, perhaps it allows cation exchange by facilitating bond rupture between the Zn^{2+} and carboxylate ligands in the MOF. Based on the ligand-field analysis of Ni-MOF-5,[16] the lattice is a far weaker ligand than solvents used for cation exchange. If solvents act as ligands during the exchange mechanism, then they might associate to SBUs and weaken the bonds between the exiting metal ion and the framework. They might also stabilize reactive intermediates or dictate the rate at which the inserting metal ion desolvates and subsequently enters the SBU.

Systematic studies will be needed to elucidate how solvents influence the mechanistic details. Future reports should attempt their synthesis procedures with multiple solvents and plot the extent of exchange versus relevant solvent parameters. Finding a single parameter that correlates well with exchange rate would shed light on the crucial steps of the exchange process. For an example, if substitution rate in a particular MOF correlates with dielectric constant, then perhaps the role of the solvent is to stabilize an intermediate with a large dipole moment. Each system will need to be studied individually, but with many thorough solvent investigations we could learn about the cation exchange mechanism in general. We will present in Chapter 6 our work with MOF-5 and MFU-4*l* to demonstrate these sorts of studies are possible and informative.[51]

1.7 Applications

As a research direction, cation exchange at MOF SBUs is still in its infancy, but the exchange process already has applications that are impossible to achieve through conventional synthetic routes. Most of the materials covered in this chapter can only be made through cation exchange. Isolating Ni-MOF-5 is possible by solvothermal

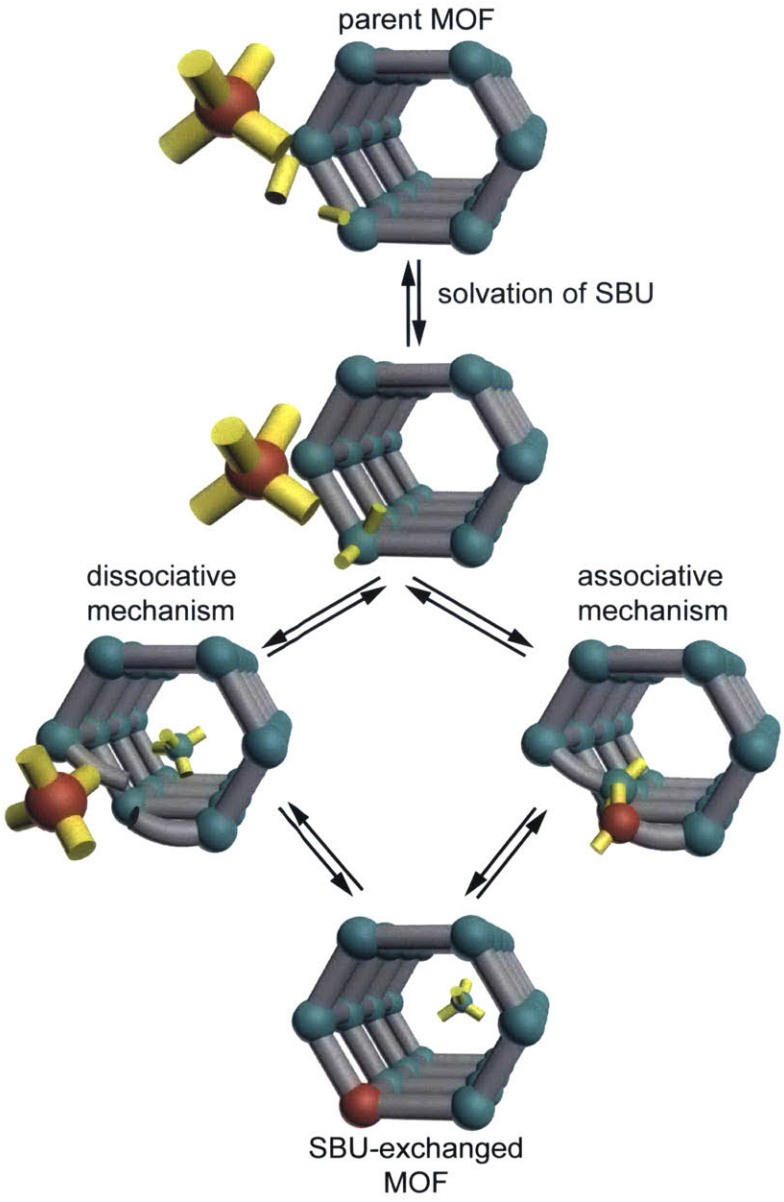

Figure 1-2: Simplified mechanistic pathways for cation exchange at MOF SBUs. Green and red spheres represent exiting and inserting metal ions, respectively. Organic linkers are shown in gray and solvent is depicted in yellow.

synthesis, but all other variants in the (Cl)M-MOF-5 family are not. M-HKUST-1 (M = Zn^{2+} or Cu^{2+}), M-PMOF-2 (M = Zn^{2+} or Cu^{2+}), MIL-53(Fe)-Br, MIL-53(Al)-Br, MIL-101(Fe), MIL-101(Al), and the class of MOFs known as $M_6(BTB)_4(BP)_3$ (M = Co^{2+}, Ni^{2+}, Cu^{2+}, or Zn^{2+}) are accessible through direct synthesis, but the mixed-metal derivatives have only been accessed by cation exchange. The Mn^{2+},[2] Fe^{2+},[52] and Cu^{2+}[53] variants of MM-BTT can be made directly, but cation exchange remains the only route to the Zn^{2+}, Co^{2+}, Ni^{2+}-based materials.[3,23]

The most common application for cation exchanged-MOFs is in gas storage. Installing cations with open coordination sites and open-shell electronic structures enhances the adsorption interaction between the SBU and guest molecule to increase the overall gas uptake. Whether starting from CdCd-BTT[23] or MnMn-BTT,[3] altering the cation identity leads to tunable apparent surface areas, H_2 uptake, and H_2 adsorption enthalpies. So far accessible only by cation exchange, the partially exchanged Co^{2+} derivative exhibited an unprecedented initial enthalpy of adsorption, ΔH, of 10.5 kJ/mol. Calculations suggest that ZnZn-BTT should exhibit the largest enthalpy of adsorption. Although only a partially substituted Zn analogue has been reported, the all-Zn material may be accessible through cation exchange.[54] Soaking POST-65(Mn) in a solution of Fe^{2+}, Co^{2+}, Ni^{2+}, or Cu^{2+} leads to isostructural analogues with enhanced H_2 uptake when measured in mole of gas per mole of material. Most show greater ΔH than the initial 5.21 kJ/mol of POST-65(Mn), with POST-65(Fe) displaying a ΔH of 6.60 kJ/mol. Each variant also displays distinct magnetic properties, with the Co^{2+}, Ni^{2+}, and Cu^{2+} materials showing antiferromagnetic coupling while the Fe^{2+} version exhibits ferromagnetic coupling.[28] The Zn^{2+}-variants of HKUST-1 and PMOF-2 do not show appreciable gas uptake since they are not stable to complete desolvation. The Cu^{2+} analogue of HKUST-1 is, on the other hand, stable to desolvation, and greater amounts of Cu^{2+} substitution into the Zn^{2+} parent material lead to significant N_2 uptake indicative of greater porosity and stability.[24] Similarly, the ability of $M_6(BTB)_4(BP)_3$ (M = Co^{2+}, Ni^{2+}, or Zn^{2+}) to adsorb N_2 can be tailored by altering the ratio of any two of these cations in the structure.[39] Finally, while NTU-101-Zn exhibits a BET surface area of just 37 m^2/g, the Cu^{2+}

variant adsorbs significant amounts of H_2, CO_2, and N_2 to give a BET value of 2017 m^2/g.[31]

The application of cation exchange that will be the focus of this thesis in the nascent area of small molecule reactivity and catalysis in MOFs. Even in these examples, most reports focus on simply demonstrating reactivity or catalysis; it is unfortunately not yet common practice to show how the new SBUs compare with the state-of-the-art (heterogeneous) catalysts for a given transformation. For instance, after replacing the Cd^{2+} ions in porph@MOM-10-Cd with Mn^{2+} or Cu^{2+}, the MOFs are capable of catalyzing the oxidation of trans-stilbene to stilbene oxide and benzaldehyde in the presence of tert-butyl hydroperoxide.[34] Here, the conversion and turnover number compare well to molecular Mn^{3+}[TMPyP] under similar conditions. The Cu^{2+}, Zn^{2+}, and Co^{2+} variants of the helical framework known as $M_xCu_{1-x}(BIM)_{16}$ catalyze the self-coupling of 2,6-di-tert-butylphenol under ambient conditions to afford 3,3′,5,5′-tetra-tert-butyl-4,4′-diphenoquinone.[46] After replacing the four exterior Zn^{2+} sites in the SBU of MFU-4*l* with Co^{2+}, Co-MFU-4*l* becomes catalytically active in oxidizing CO to CO_2.

As will be discussed later, cation exchange builds a fundamentally new platform for reactivity studies because the resultant metal clusters of SBUs are often unusual coordination motifs that are difficult or impossible to achieve as solution-phase molecules. For example, no molecule is known to stabilize Ni^{2+} or Co^{2+} in the two-coordinate environment conferred by MM-BTT. The metal species in the (Cl)M-MOF-5 family are without precedent in either materials or molecules because of the unusual all-oxygen, dianionic, and tripodal ligand field in the MOF-5 SBU. These sites are some of the few examples of divalent metal ions in three-fold symmetric tetradentate environments. A ligand-field analysis of Ni-MOF-5 indicates that MOF-5 is by far the strongest ligand to stabilize Ni^{2+} in a pseudo-tetrahedral geometry, which is remarkable because ligand fields of similar strength coerce Ni^{2+} to assume a square planar configuration. Preliminary studies demonstrate that these unusual species perform small-molecule activation without compromising the integrity of the lattice. The Fe^{2+} centers in Fe-MOF-5 react with NO to generate an unusual ferric nitrosyl, which is

the only example of electron transfer to NO in a MOF and the only example of a ferric nitrosyl in an all-oxygen environment.

Viewing the cation exchanged SBUs as molecular entities will be a useful perspective for conceiving new applications in reactivity and catalysis. Reimagining SBUs as coordination environments for various transition metal ions constructs an entirely new platform for coordination and redox chemistry. SBUs will act as superior catalysts only by treating the SBU as an unusual ligand environment. This viewpoint inspired the use of open-coordination and open-shell metal ions to enhance H_2 uptake. Novel porous magnets might result from installing particular metal ions into desirable molecular entities. Only a few reports have investigated the applications of cation exchange, but the ability to insert reactive metal ions into specific geometries should enable chemistry that is otherwise impossible to achieve.

1.8 Outlook

Being able to substitute specific metal ions into predefined environments is a level of control uncommon to solid-state synthetic chemistry. Cation exchange into the SBUs of MOFs is already unlocking materials with unprecedented properties that cannot be achieved otherwise. However, harnessing this process as a predictive synthetic tool will require understanding its mechanistic details. The available experimental observations are insufficient to draw meaningful conclusions about how the process transpires in even a particular material. Future studies, including those we proposed here, will uncover trends that will make this technique predictive. We recommend that if a MOF appears active for cation exchange, then the substitution should be attempted for a variety of metal species and solvents to tease out trends. The rate and extent of exchange under these different conditions could be compared against various chemical properties of the metal ions and solvents to find parameters that are most relevant to the mechanism. Chapter 6 describes our early attempts at this approach. Future studies should also report exchange conditions that did not work along with those that did. Such detailed, seemingly obscure, observations might prove

critical in uncovering a deeper understanding of cation exchange.

Discovering how SBUs undergo cation exchange will teach us about MOF chemistry and dynamics in general. For example, if coordinating solvents enable the exchange process by binding to metal sites in SBUs, perhaps this will reveal that MOFs dynamically interact with solvents and are not as rigid as commonly assumed or as portrayed by X-ray crystal structures. This is the conclusion we draw in Chapter 3 when studying MOF-5. Elucidating these sorts of fundamentals about MOFs will have profound consequences for any of their applications. Understanding how the lattice flexibility or the symmetry of the SBU limits the geometrical distortions of the metal site will shape future catalytic studies of MOFs. The reactivity of metal sites could be controlled with the fine level of control we enjoy with molecular catalysts, but with the unexplored solid-state ligand environment of MOFs. Cation exchange at the SBUs of MOFs promises a new landscape of materials chemistry and our investigations have only just begun.

Molecular Formula	SBU	Common Name	Inserted cation	Extent	Conditions	Reference
Al(OH)(BDC-Br)	9	MIL-53(Al)-Br	Fe^{3+}	undertermined	H_2O, 85 °C, 5 d	[36]
Co$(H_3O)[(\mathbf{Co}_4Cl)_3(HMTT)_8]_2$	11	POST-65(Co)	Mn^{2+}	complete	DMF, RT, 1 mo	[28]
$\mathbf{Co}_6(BTB)_4(BP)_3$	18		Ni^{2+}, Cu^{2+}, Zn^{2+}	complete	DMF, RT, 1 d, 1 d, 2 d	[39]
$\mathbf{Co}_3(BTX)_4(BDC)_3(H_2O)_4$	8		Cd^{2+}	complete	H_2O, RT, 7 d	[40]
$\mathbf{Co}_3O(BTB)_2(H_2O)_x(DMF)_y{\cdot}zDMF{\cdot}nH_2O$	20		Co^{3+}	complete	DMF/EtOH, RT, 1 wk – 3 wk	[30]
$Zn_{2.5}\mathbf{Co}_{1.5}(DCPP)_2(DMF)_3(H_2O)_2$	28		Zn^{2+}	complete	MeCN, 80 °C, 3 h	[21]
$Zn_{3.9}\mathbf{Co}_{2.1}(BTB)_4(BP)_3$	18	SUMOF-1(Co:2Zn)	Zn^{2+}	complete	DMF, RT, 7 d	[38]
$\mathbf{Cd}_{1.5}(H_3O)_3[(\mathbf{Cd}_4O)_3(HETT)_8]{\cdot}6H_2O$	2		Pb^{2+}, Dy^{3+}, Nd^{3+}	complete	H_2O, RT, 7 d	[27]
$\mathbf{Cd}(BTX)_2Cl_2$			Cu^{2+}	complete	H_2O, RT, 7 d	[40]
$\mathbf{Cd}_2(BTX)_2(BDC)_2$	7		Cu^{2+}	complete	H_2O, RT, 7 d	[40]
$\mathbf{Cd}_3[\mathbf{Cd}_4Cl](BTT)_8]_2$	4	CdCd-BTT	Co^{2+}, Ni^{2+} *not* Mn^{2+}, Fe^{2+}, Cu^{2+}, *or* Zn^{2+}	complete	MeOH, 80 °C, 30 d	[23]
$\mathbf{Cd}(BTTN)_2(H_2O)_2]_2(PF_6)$pyrene$_2$	15		Cu^{2+}	complete	MeOH, RT 30 d	[43]
$\mathbf{Cd}(BP)_2(O_3SFcSO_3){\cdot}(CH_3OH)_4$	14		Cu^{2+}	50%	MeOH, RT, 30 d	[42]
$[(CH_3)_2NH_2]_{15}[(\mathbf{Cd}_2Cl)_3(TATPT)_4]$	19		Cu^{2+}, Co^{2+}, Ni^{2+},Zn^{2+}	Cu^{2+} 7.7%, Co^{2+} 6.2%, Ni^{2+} 4.3%, Zn 4.6%	DMF, RT, 5 d	[35]
$C_{156}H_{60}\mathbf{Cd}_{11}N_{12}O_{51}$	21	MMPF-5(Cd)	Co^{2+}	complete at porphyrin	DMSO, 85 °C, 2 d	[50]
$[\mathbf{Cd}_4(BPT)_4] \cdot [\mathbf{Cd}(C_{44}H_{36}N_8)] \cdot [$ MeOH,H_2O $]$	23	porph@MOM-11-Cd	Cu^{2+}	complete	MeOH, RT, 10 d	[45]
$[\mathbf{Cd}_6(BPT)_4Cl_4(H_2O)_4] \cdot [C_{44}H_{36}N_8\mathbf{Cd}Cl]$	24	porph@MOM-10	Mn^{2+}, Cu^{2+}	Mn complete, Cu 76%	MeOH, RT, 1 mo	[37]
$Na_{0.25}[(CH_3)_2NH_2]_{1.75}[\mathbf{Cd}(HMBM)_2]$	22		Cu^{2+}not Ni^{2+} or Co^{2+}	96%	MeOH, RT, 7 d	[37]
$\mathbf{Cr}_3F(H_2O)_2O(BDC)_3$	13	MIL-101(Cr)	Al^{3+}, Fe^{3+}	Al^{3+} 10%, Fe^{3+} 5.8%	H_2O, 100 °C, 3 d	[29]
$\mathbf{Cu}_{2/3}Mn_{1/3}(H_3O)[(\mathbf{Cu}_{8/3}Mn_{4/3}Cl)_3(HMTT)_8]_2$	11	POST-65(Cu)	Mn^{2+}	34%	DMF, RT, 1 mo	[28]
$[\mathbf{Cu}(BTTN)_2(H_2O)_2]_2(PF_6)$pyrene$_2$	15		Cd^{2+}	complete	MeOH, RT, 10 d	[43]
$\mathbf{Cu}_6(BTB)_4(BP)_3$	18	SUMOF-1-Cu	Zn^{2+}	38%	DMF, RT, 3 mo	[38]
$\mathbf{Cu}(BIM)_{16}$	25		Zn^{2+}, Co^{2+}	Zn 20.81%, Co 14.97%	H_2O, RT, 5 d	[46]
$\mathbf{Cu}_4(DCPP)_2(DMF)_3(H_2O)_2$	28		Zn^{2+}	complete	MeCN, 80 °C, 6 h	[21]
Fe(OH)(BDC-Br)	9	MIL-53(Fe)-Br	Al^{3+}	undetermined	H_2O, 85 °C, 5 d	[36]

Table 1.1: The known examples of MOF SBUs that undergo cation exchange. SBU numbers refer to structures depicted in Figure 1-1. The exchangeable metal sites are shown in bold and presented alphabetically.

Molecular Formula	SBU	Common Name	Inserted cation	Extent	Conditions	Reference
$\mathbf{Mn}_3[(\mathbf{Mn}_4Cl)_3(BTT)_8]_2$	4	MnMn-BTT	Li^+, Fe^{2+}, Co^{2+}, Ni^{2+}, Cu^{2+}, Zn^{2+}	Li^+ 21%, Fe^{2+} 20%, Co^{2+} 20%, Ni^{2+} 18%, Cu^{2+} 92%, Zn^{2+} 80%	MeOH, RT, 1 mo	2,3,47
$\mathbf{Mn}(H_3O)[(\mathbf{Mn}_4Cl)_3(HMTT)_8]_2$	11	POST-65(Mn)	Fe^{3+}, Co^{2+}, Ni^{2+}, Cu^{2+}	Fe^{3+}, Co^{2+}, Ni^{2+} 100%, Cu^{2+} 66%	DMF, RT, 12 d	28
$\mathbf{Ni}_6(BTB)_4(BP)_3$	18		Cu^{2+}	complete	DMF, RT, 15 d	39
$Zn_{3.72}\mathbf{Ni}_{2.28}(BTB)_4(BP)_3$	18	SUMOF-1-(Ni:2Zn)	Zn^{2+}	complete	DMF, RT, 7 d	38
$\mathbf{Ni}(H_3O)[(\mathbf{Ni}_4Cl)_3(HMTT)_8]_2$	11	POST-65(Ni)	Mn^{2+}	complete	DMF, RT, 1 mo	28
$Zn_2\mathbf{Ni}_2(DCPP)_2(DMF)_3(H_2O)_2$	28		Zn^{2+}	complete	MeCN, 80 °C, 4 h	21
$\mathbf{Pb}_{1.5}(H_3O)_3[(\mathbf{Pb}_4O)_3(HETT)_8]\cdot 6H_2O$	2		Cd^{2+}	complete	H_2O, RT, 3 wk	27
$\mathbf{Zn}OOCClH_3C_6Fc)_2(H_2O)_3$	12		Pb^{2+}, Cd^{2+}, Cu^{2+}, Ni^{2+}, Co^{2+}, Mn^{2+}, Cr^{2+}	Pb^{2+} 100%, Cd^{2+} 92%, Cu^{2+} 76%	H_2O, RT, 5 d	33
$\mathbf{Zn}(4,4'\text{-}BP)_2\text{-}(FcphSO_3)_2$	14		Cd^{2+}, Pb^{2+}, Cu^{2+}	Cd^{2+} 40%, Pb^{2+} 75%, Cu^{2+} 50%	MeOH, RT, 30 d	41
$[\mathbf{Zn}(BTTN)_2(H_2O)_2]_2(PF_6)pyrene_2$	15		Cu^{2+}	complete	MeOH, RT, 6 h	43
$\mathbf{Zn}_2(BDCPPI)(DMF)_3O$	16		Cu^{2+} Not Co^{2+}, Ni^{2+}, Cd^{2+}	97%	MeOH, RT, 4 d	32
$\mathbf{Zn}_3(BTC)_2(H_2O)_3$	17	Zn-HKUST-1	Cu^{2+}	53%	MeOH, RT, 3 mo	24
$\mathbf{Zn}_{24}(TDCPEB)_8(H_2O)_{12}$	17	PMOF-2	Cu^{2+}	complete	MeOH, RT, 3 d	24
$\mathbf{Zn}_6(BTB)_4(BP)_3$	18		Ni^{2+}, Cu^{2+}, Co^{2+}	complete	DMF, RT, 2 d	39
$\mathbf{Zn}_2(TDP)(DMF)_3$	16	NTU-101-Zn	Cu^{2+}	80%	DMF, RT, 14 d	31
$\mathbf{Zn}_4(ETTB)\cdot 4DMF\cdot x$Solvent	17	PCN-921	Cu^{2+}	complete	DMF, RT, 4 d	25
$\mathbf{Zn}_6(BTB)_4(BP)_3$	18	SUMOF-1-Zn	Cu^{2+}, Co^{2+}, Ni^{2+}	Cu 100%, Co 35%, Ni 38%	DMF, RT, 3 mo	38
$[\mathbf{Zn}_7(BODPDI)_3(H_2O)_7]_n[\mathbf{Zn}_5(BODPDI)_3(H_2O)_5]_n$	17		Cu^{2+} not Ni^{2+} or Co^{2+}	87%	MeOH, RT, 7 d	26
$\mathbf{Zn}_4(TIAPy)\cdot(H_2O)_4\cdot(EGME)_2$	26	JUC-118	Cu^{2+}	98.8%	2-methoxyethanol, RT, 3 d	20
$\mathbf{Zn}_3(CBAI)_2(DMF)_2$	27		Cu^{2+}, not Co^{2+} or Ni^{2+}	Complete	DMF-H_2O, RT, 5 d	22
$\mathbf{Zn}_4(DCPP)_2(DMF)_3(H_2O)_2$	28		Cu^{2+}, Co^{2+}, Ni^{2+}	Cu^{2+} 100%, Co^{2+} and Ni^{2+} only O_h sites	MeCN, 80 °C, 4 h	21
$Zn\mathbf{Zn}_4Cl_4(BTDD)_6$	3	MFU-4*l*	Co^{2+}	80% (not Zn_2)	DMF, 140 °C, 20 h	19
$\mathbf{Zn}$-(MeIm)	5	ZIF-8	Mn^{2+}	12%	MeOH, 55 °C, 24 h	18
$\mathbf{Zn}$-(Cl_2Im)	6	ZIF-71	Mn^{2+}	10%	MeOH, 55 °C, 24 h	18
$\mathbf{Zn}_4O(BDC)_3$	1	MOF-5	Ti^{3+}, V^{3+}, V^{2+}, Cr^{3+}, Cr^{2+}, Mn^{2+}, Fe^{2+}, Ni^{2+}	Ti^{3+} 2.3%, V^{3+} 5%, V^{2+} 4.3%, Cr^{3+} 35%, Cr^{2+} 24%, Mn^{2+} 11%, Fe^{2+} 24%, Ni^{2+} 25%	DMF, RT, 7 d	16,17
$\mathbf{Zr}_6O_4(OH)_4(BDC)_{12}$	10	UiO-66	Ti^{4+}, Hf^{4+}	Ti^{4+} 94%, Hf^{4+} 18%	DMF, 85 °C, 5 d	36

Table 1.2: Continuation of Table 1.1.

Chapter 2

MOF-5 Stabilizes an Unusual Pseudo-T_d Ni^{2+} Species

2.1 Abstract

In this chapter, we demonstrate that inorganic clusters in $Zn_4O(BDC)_3$ (MOF-5) can be employed as tripodal ligands to enforce an unusual pseudo-tetrahedral oxygen ligand field around Ni^{2+}. The Ni^{2+} variant of MOF-5 is characterized by porosity measurements and a suite of electronic structure spectroscopies. Classical ligand field analysis of the Ni^{2+} ion isolated in MOF-5 depicts the $Zn_3O(carboxylate)_6$ tripodal ligand as an unusual, stronger field ligand than halides and other oxygen donor ligands. This chapter also establishes that that the inserted Ni^{2+} can undergo geometrical transformations without disrupting the MOF lattice. These changes can be monitored by spectroscopy and manipulated using by invoking the same steric arguments employed by molecular chemists.[1]

[1] A portion of this work appeared previously in Brozek, C. K.; Dincă, M. *Chem. Sci.* **2012**, *3*, 2110 and is reproduced here with permission from the Royal Society of Chemistry.

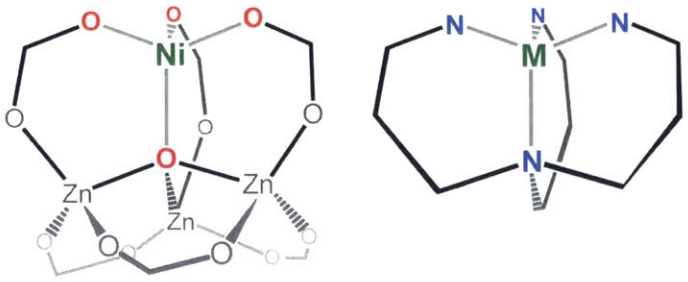

Figure 2-1: Illustration of the $Zn_3O(carboxylate)_6$ SBU of MOF-5 as a tripodal support that enforces a tetrahedral oxygen ligand field, akin to standard chelating ligands such as the tetra-amine on the right.

2.2 Introduction

In molecular inorganic synthesis, ligands are used to tune the environment around metal ions. This fine level of control is uncommon in the solid state. As a proof-of-concept, we reconceived the SBU of MOF-5[55] as a tripodal ligand for metals that are typically incompatible with tetrahedral oxygen ligand fields, such as Ni^{2+} (see Figure 2-1). Normally, Ni^{2+} (d^8) prefers octahedral or square planar coordination in oxygen ligand fields because the ligand field splitting outweighs the spin pairing energy. It assumes tetrahedral geometry only when trapped in condensed lattices such as ZnO,[56,57] or when surrounded by bulky supporting ligands.[58–62] The resulting pseudo-T_d species is site-isolated, allowing its unusual properties and its interaction with donating ligands to be monitored by UV-Vis-NIR spectroscopy and magnetic measurements.

2.3 Results and Discussion

Colorless crystals of MOF-5 were soaked in a saturated solution of $Ni(NO_3)_2{\cdot}xH_2O$. The resulting yellow crystals were washed repeatedly with DMF and CH_2Cl_2 without loss of color until the solvent no longer showed UV-Vis absorption profiles characteristic of solvated Ni^{2+} ions. Powder X-ray diffraction and elemental analysis of these yellow crystals revealed a pattern nearly identical to that of MOF-5 (Figure

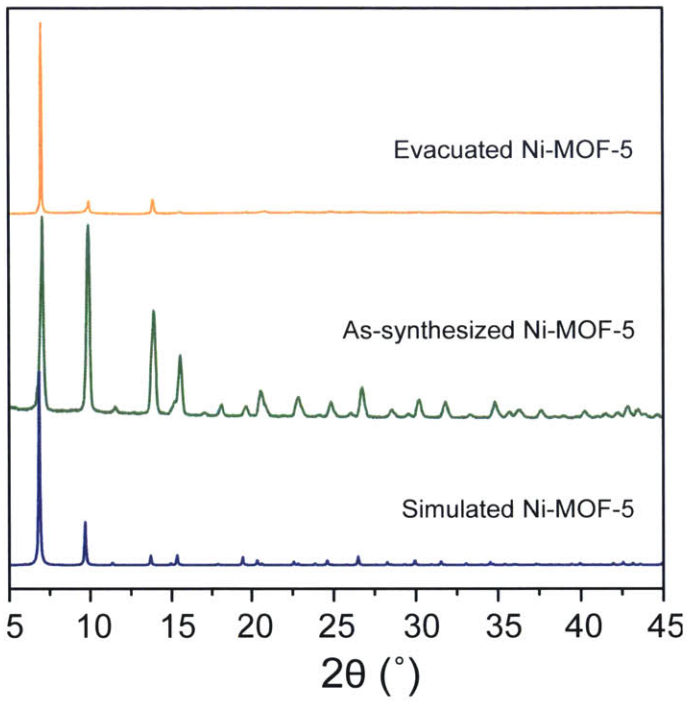

Figure 2-2: Powder X-ray diffraction patterns of Ni-MOF-5. Differences in intensity between the as-synthesized and evacuated Ni-MOF-5 are due to orientation effects. These occurred because the samples were prepared without grinding to avoid decomposition in the presence of moisture.

2-2) and a Ni:Zn ratio of 1:3. Shorter soaking times engendered lower levels of Ni^{2+} substitution, with Ni:Zn ratios of 1:10 achievable after two weeks. Alternatively, the material could be isolated directly, through solvothermal synthesis. Heating mixtures of $Zn(NO_3)_2{\cdot}xH_2O$, $Ni(NO_3)_2{\cdot}xH_2O$, and H_2BDC in DMF afforded cubic yellow crystals whose diffraction pattern matched that of MOF-5. We observed that the Ni:Zn ratio in these samples depended on the relative concentrations of $Ni(NO_3)_2{\cdot}xH_2O$ and $Zn(NO_3)_2{\cdot}xH_2O$ yet never exceeded 1:3 (Figure 2-3). In fact, increasing the Ni:Zn ratio in the reactant mixture above 6:1 led to selective formation of a yet unidentified crystalline green powder that did not match the X-ray diffraction pattern of any known Ni^{2+}-BDC or Zn^{2+}-BDC phases. The upper limit of the Ni^{2+} content was similar to what had previously been reported as a curiosity in Co^{2+}-substituted MOF-5 materials.[63] Based on these observations, we hypothesized that the yellow color of as-synthesized Ni^{2+}-substituted MOF-5 was indicative of octahedral Ni^{2+} and that the MOF-5 SBU accommodates only one such distortion. Additional Ni^{2+} substitution into the ensuing $NiZn_3O$ cluster is prevented by a large kinetic barrier as it would exert debilitating strain on the lattice. The presence and identity of the two additional ligands that complete the coordination sphere of octahedral Ni^{2+} was confirmed by thermogravimetric analysis, which showed that two DMF molecules per Ni center are lost by heating the yellow crystals between 70 and 150 °C (Figure 2-4). $Zn_4O(carboxylate)_6$ SBUs wherein one Zn^{2+} is hexa-coordinate and binds two DMF molecules have been reported,[64–71] offering precedent for the formulation of Ni-substituted MOF-5 as $(DMF)_{2x}Ni_xZn_{4-x}O(BDC)_3$ ($0 < x < 1$), ($(DMF)_2$Ni-MOF-5).

Remarkably, heating $(DMF)_2$Ni-MOF-5 under vacuum afforded indigo crystals. Further characterization revealed this material to have the formula $Ni_xZn_{4-x}O(BDC)_3$, which we term Ni-MOF-5, and that it contained pseudo-tetrahedral Ni^{2+} supported only by oxygen ligands, shown in Figure 2-5. Single-crystal X-ray diffraction analysis revealed that the asymmetric unit of Ni-MOF-5 features a single metal site, indicating that Ni^{2+} substitutes Zn^{2+} inside the SBU of a structure otherwise identical to MOF-5 (see 2.2). Functional similarity to MOF-5 was also established by porosity measurements. The indigo Ni-MOF-5 adsorbed 825 cm^3 of N_2/g at 1 atm and 77 K

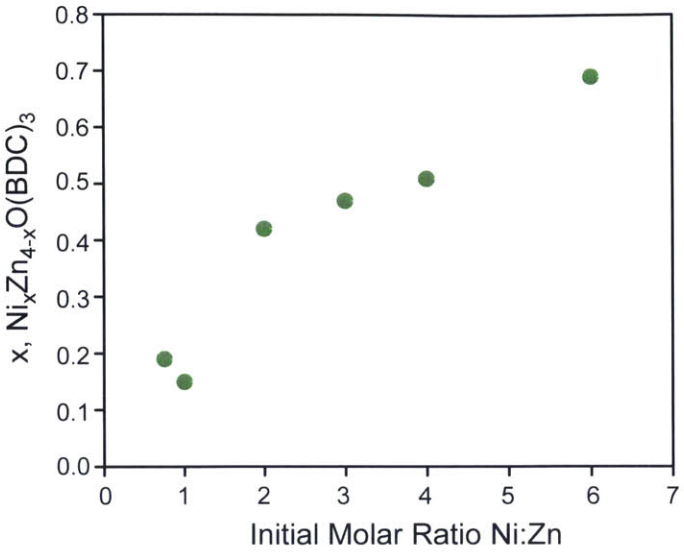

Figure 2-3: Formula of Ni-MOF-5 as a function of the initial molar ratio of Ni:Zn used in the preparation. Higher initial ratios of Ni:Zn leads to phase segregation and isolation of a yet unidentified green crystalline powder that does not match that of MOF-5 or any known Ni-BDC or Zn-BDC phases.

and exhibited a BET surface area of 3300(100) m^2/g, analogous to original MOF-5 (Figure 2-6).[72] FT-IR analysis of Ni-MOF-5 confirmed the absence of a C=O stretch at 1660 cm^{-1} that would be expected if DMF were still coordinated to Ni^{2+} (Figure 2-7). In contrast to Be^{2+} and Co^{2+} analogues of MOF-5,[73] Ni-MOF-5 is built from SBUs that do not have molecular analogues, highlighting the importance of the lattice in stabilizing otherwise inaccessible molecular species. Soaking basic zinc acetate crystals, $Zn_4O(O_2C\text{-}CH_3)_6$,[74] in an anhydrous DMF solution of $Ni(NO_3)_2{\cdot}6H_2O$ for up to three weeks led to the decomposition of the metal cluster, not the incorporation of Ni^{2+}.

The pseudo-tetrahedral geometry around the Ni^{2+} was quantified by diffuse reflectance UV-Vis-NIR spectroscopy (blue trace in Figure 2-8), and magnetic measurements. Despite the slight deviation from tetrahedral geometry around Ni^{2+}, Ni-MOF-5 exhibited a spectrum that resembled solution-phase spectra of strictly tetrahedral Ni^{2+} complexes.[75–81] A peak at 1020 nm (9803 cm^{-1}) can be assigned to the $^3T_1(F) \rightarrow {}^3A_2$ transition of a d^8 tetrahedral ion (ν_2), while the doublet of peaks at 540 nm (18,500 cm^{-1}) and 608 nm (16,400 cm^{-1}) can be assigned to the $^3T_1(F) \rightarrow {}^3T_1(P)$

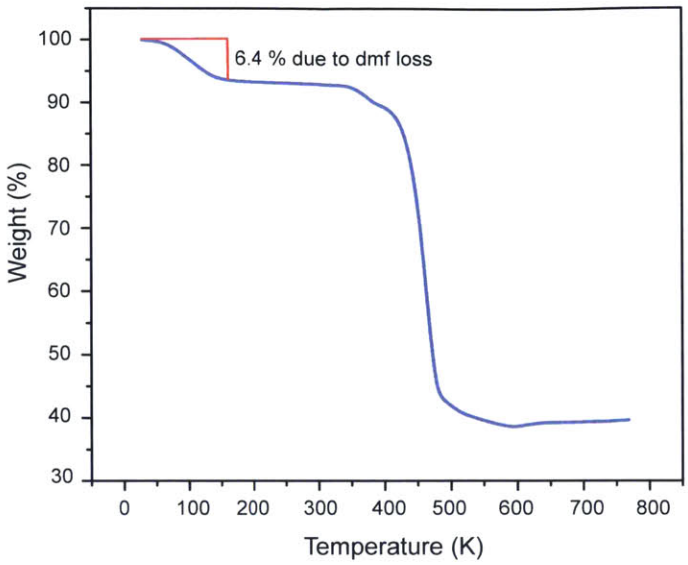

Figure 2-4: Thermogravimetric analysis plot of $(DMF)_{0.72}Ni_{0.36}Zn_{3.64}O(BDC)_3$

Species	ν_3 (cm^{-1})	ν_2 (cm^{-1})	B (cm^{-1})	Dq
$^{82}[NiBr_4]^{2-}$	13320	6995	379	201
$^{82}NiCl_4]^{2-}$	14760	7470	405	206
$^{82}Ni(NCO)_4]^{2-}$	16200	9460	511	311
$^{57}CdS{:}Ni^{2+}$	12395	7840	570	400
$^{57}ZnO{:}Ni^{2+}$	15720	8340	770	420
$^{57}ZnS{:}Ni^{2+}$	12790	9750	560	475
$^{61}Ni(OAr)_4]^{2-}$	16820	10000	867	540
Ni-MOF-5	17406	9803	**1045**	**753**

Table 2.1: Calculated Racah and ligand field parameters of various tetrahedral Ni^{2+} species based on observed transitions ν_2 and ν_3.

transition (ν_3), where ^3P is split by spin-orbit coupling into $^3P_0$ (A_1), $^3P_1$ (T_1), $^3P_2$ ($E + T_2$) respectively.[56] A ligand field analysis of this spectrum using a system of equations originally derived by Ballhausen revealed Racah and Dq parameters of 1045 cm^{-1} and 753 cm^{-1}. As shown in Table 2.1, these are notably higher than those common for tetrahedral Ni^{2+} and suggest that spin-spin repulsion is almost as large as in unperturbed Ni^{2+} ions, thereby preserving a large spin-orbit coupling interaction.

The presence of significant spin-orbit coupling was also evidenced by magnetic measurements. A $\chi_m T$ vs. T plot of Ni-MOF-5, shown in Figure 2-9, revealed the

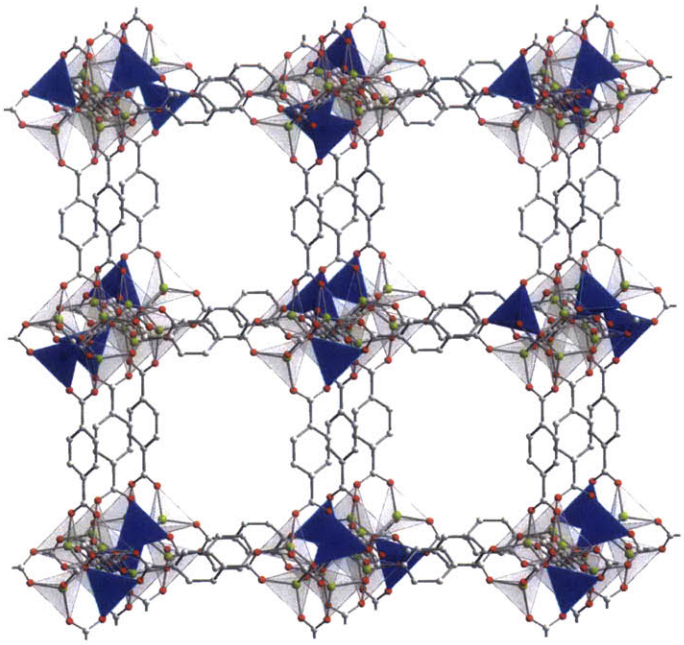

Figure 2-5: Part of the crystal structure of $Ni_xZn_{4-x}O(BDC)_3$ ($x = 1$). Due to crystallographically-imposed symmetry, the position of Ni^{2+} centers (blue tetrahedra) within individual $NiZn_3$ clusters cannot be identified unambiguously, and these are depicted at random. Green, red, and grey spheres represent Zn, O, and C atoms, respectively. Hydrogen atoms are omitted for clarity.

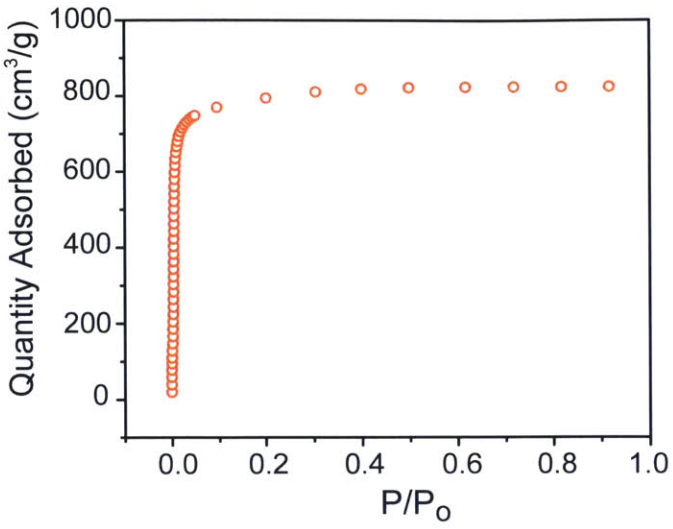

Figure 2-6: N_2 adsorption isotherm for Ni-MOF-5 at 77 K. The BET apparent surface area is 3300(100) m^2/g. Eleven relative pressure points between 0.01 and 0.05 were chosen for the fit, giving a C value of 869.

presence of magnetically dilute Ni^{2+} ions and a room-temperature magnetic moment of 4.21 μ_B per Ni^{2+} ion. This value is higher than the spin-only value expected for Ni^{2+}, but is expected for tetrahedral d^8 ions subject to unquenched orbital angular momentum.[83–85] The value of μ_{eff} is further elevated by a temperature independent paramagnetism value of 0.2×10^{-6} cm^3/mol as determined by a fit of the susceptibility data using julX.[2]

We could monitor the evacuation of the as-synthesized crystals by in situ UV-Vis-NIR spectroscopy and confirm that the Ni^{2+} sites were undergoing step-wise changes to its coordination sphere. These experiments, plotted in Figure 2-8, evidenced an isosbestic point around 700 nm, which suggested that DMF loss occurred in two kinetically independent processes via a well-defined five-coordinate Ni^{2+} species. The identity of this species was probed by treating Ni-MOF-5 with various nucleophiles. Although the reaction of Ni-MOF-5 with small ligands such as PMe_3, THF, and MeCN rapidly produced octahedral Ni^{2+}, indicated by a color reversal to yellow, sterically demanding MesCNO afforded an orange adduct, whose spectrum matched that of the

[2]E. Bill, Max Planck Institute for Chemical Energy Conversion in Muelheim, Germany, 2013. Available from the author by e-mail to ebill@gwdg.de.

putative pentacoordinate (DMF)Ni-MOF-5 adduct (Figure 2-10). An FT-IR spectrum of these crystals confirmed the presence of MesCNO (Figure 2-11). Figure 2-8 depicts a consecutive six-(O_h) to five-(C_{4v}) to four-(pseudo-T_d) coordinate conversion of Ni in a 2+ formal oxidation state. These transformations, illustrated in Figure 2-12, are supported by computational modeling of $(DMF)_yNiZn_3O(benzoate)_6$ (y = 0, 1, 2) clusters containing six-, five-, and four-coordinate Ni^{2+} ions with two, one, or no bound DMF molecules. As shown in Figure 2-13, time-dependent DFT calculations using optimized geometries of these clusters (see 2.3–2.6) predicted electronic absorption spectra that agreed well with the assigned yellow, red, and blue traces in Figure 2-8.

2.4 Conclusion

This chapter establishes that MOF SBUs meet several requirements if they are to be used for small-molecule activation. Not only do they stabilize unusual coordination compounds, but they also permit significant geometrical transformations without compromising the material. Furthermore, the resulting species can be monitored by conventional methods and treated as site-isolated cations. Finally, chemistry at the unusual metal site can be manipulated by invoking the steric arguments employed by molecular synthetic chemists. Later chapters will build upon these results to show that the SBUs of MOFs meet other criteria for their use in small-molecule activation.

2.5 Methods

2.5.1 Materials

Dichloromethane (DCM, HPLC grade, Honeywell), *N*,*N*-dimethylformamide (DMF, 99.8%, VWR), $Ni(NO_3)_2{\cdot}6H_2O$ (99.9%, Strem), and $Zn(NO_3)_2{\cdot}6H_2O$ (99%, Alfa Aesar) were used as received. Mesityl nitrile oxide was prepared according to published procedures.[86]

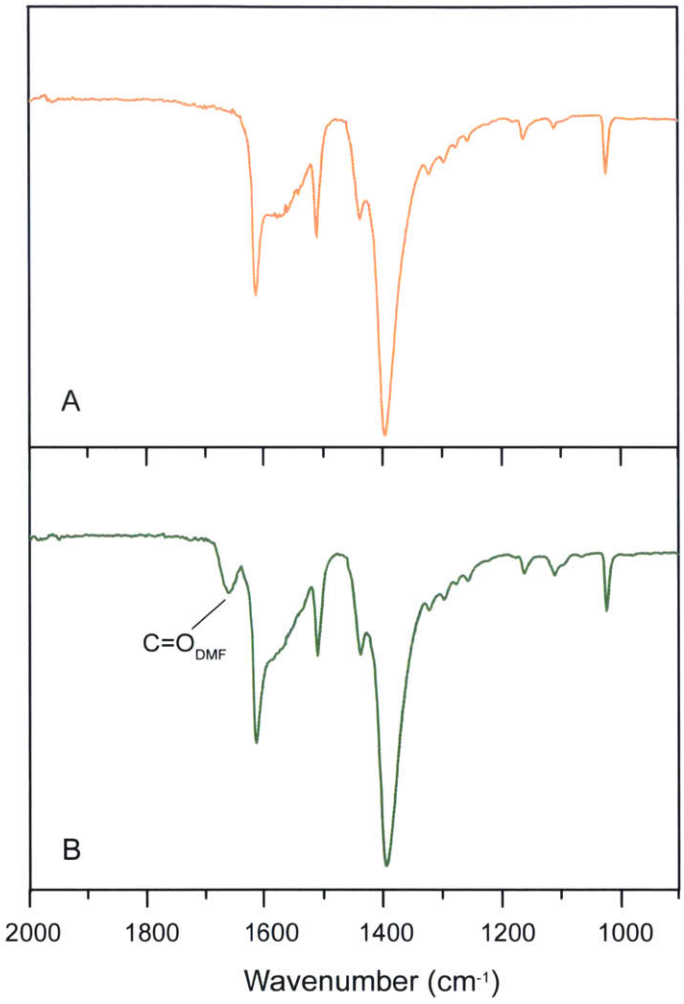

Figure 2-7: FT-IR spectrum of as-synthesized Ni-MOF-5 after washing with DMF and CH_2Cl_2 (A) and after evacuation (B), confirming the disappearance of the DMF carbonyl stretch.

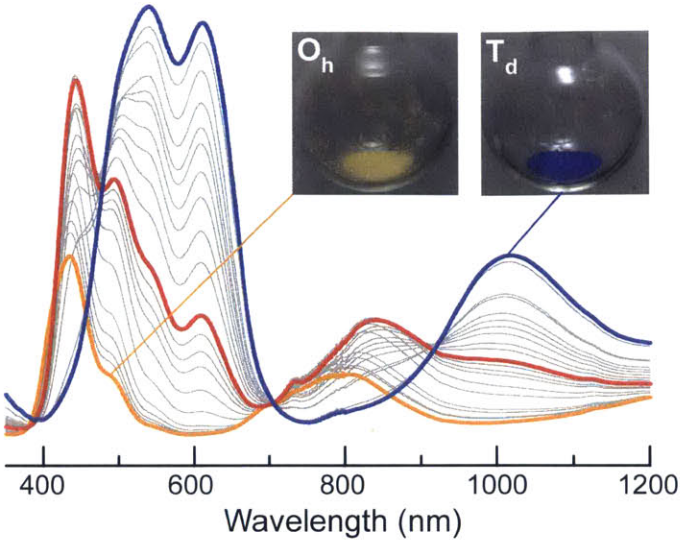

Figure 2-8: In situ diffuse reflectance spectra depicting the color progression from yellow $(DMF)_2$Ni-MOF-5 to blue Ni-MOF-5 via a putative penta-coordinated Ni_{2+} intermediate (red trace). The inset shows optical images of the yellow and blue crystals.

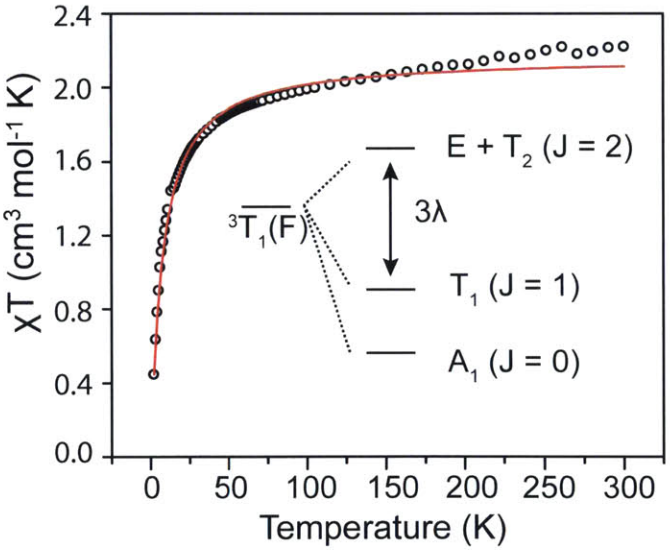

Figure 2-9: The temperature dependence of $\chi_m T$ of evacuated Ni-MOF-5 (circles). The red trace represents a fit obtained using julX. The relevant energy splittings are superimposed as an inset.

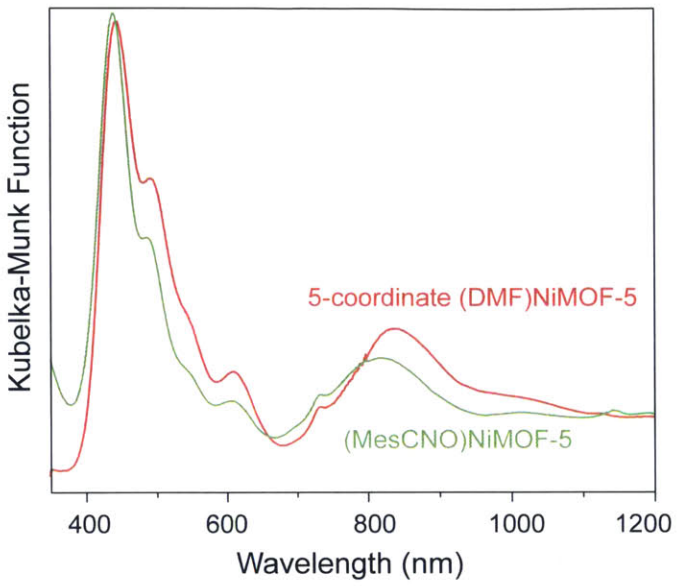

Figure 2-10: diffuse reflectance UV-Vis-NIR spectra of (DMF)Ni-MOF-5 and of (MesCNO)Ni-MOF-5.

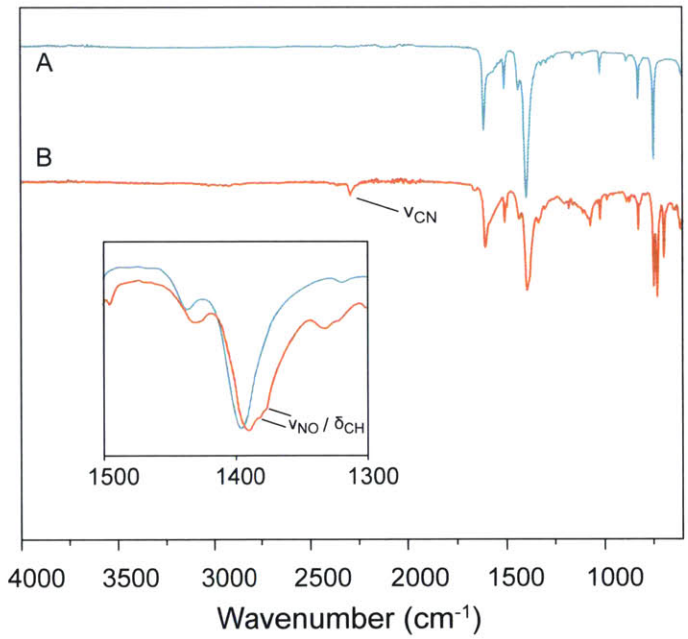

Figure 2-11: FT-IR spectrum of fully activated Ni-MOF-5 (A) and (MesCNO)Ni-MOF-5 (B). The CN stretch of the adduct is highlighted at 2293 cm^{-1}. Inset: Magnification of the region between 1500 cm^{-1} and 1300 cm^{-1} to emphasize the peaks at 1380 cm^{-1} and at 1376 cm^{-1}. These appear as shoulders on the asymmetric carboxylate stretch and correspond to the C–H bend of the mesityl methyl groups and the N–O stretch of MesCNO.

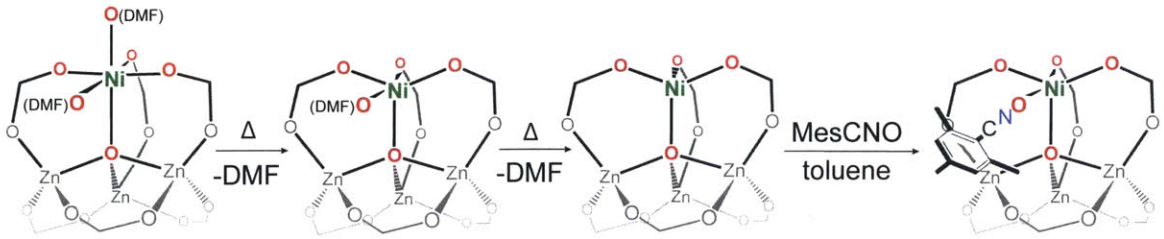

Figure 2-12: Sequential loss of DMF molecules from a $(DMF)_2NiZn_3O(carboxylate)_6$ cluster and isolation of a MesCNO adduct.

2.5.2 X-ray Crystal Structure Determination

A diffraction-quality single crystal of $Ni_{0.36}Zn_{3.64}O(BDC)_3$ was mounted on Kapton loops using paratone-N® oil. Low temperature (100 K) diffraction data (ϕ- and ω-scans) were collected on a Bruker-AXS X8 Kapp Duo diffractometer coupled to a Smart APEX II CCD detector with Mo-Kα radiation (λ = 0.71073 Å) from a IμS-micro source. Absorption and other corrections were applied using SADABS.[87] The structures were solved by direct methods using SHELXS and refined against F^2 on all data by full-matrix least squares as implemented in SHELXL-97.[88] All non-hydrogen atoms were refined anisotropically. The Ni/Zn ratio was fixed and refined as 1:10. Hydrogen atoms were included at geometrically calculated positions using a riding model. The crystallographic data for $Ni_{0.36}Zn_{3.64}O_{13}C_{24}H_{12}$ is shown in 2.2.

2.5.3 Physical Measurements

Thermogravimetric analysis (TGA) was performed on a TA Instruments Q500 Thermogravimetric Analyzer at a heating rate of 0.5 °C/min under a nitrogen gas flow of 9 mL/min. Infrared spectra were obtained on a Perkin Elmer Spectrum 400 FT-IR/FT-FIR Spectrometer equipped with a Pike Technologies GladiATR accessory with a diamond single-bounce crystal. Powder X-ray diffraction (PXRD) patterns were recorded on PANalytical X'Pert Pro and Bruker Advance II diffractometers equipped with $\theta/2\theta$ Bragg-Brentano geometry and Ni-filtered Cu-Kα radiation (Kα_1 = 1.5406 Å). The tube voltage and current were 45 kV and 40 mA, respectively. Samples for PXRD were prepared by placing a thin layer of samples on a zero-background

silicon crystal plate. Solution UV-Vis spectra were obtained at room temperature on an Agilent 8453 spectrophotometer. Diffuse reflectance UV-Vis spectra were collected on a Varian Cary 5000 UV-Vis-NIR spectrometer equipped with a Praying Mantis diffuse reflectance accessory and an environmental chamber (Harrick Scientific Products) and referenced to Spectralon® or $BaSO_4$.

A Micromeritics ASAP 2020 Surface Area and Porosity Analyzer was used to measure nitrogen adsorption isotherms. Oven-dried sample tubes equipped with TranSeals™(Micrometrics) were evacuated and tared. Samples were transferred to the sample tubes, heated to the appropriate temperatures (as determined by TGA analysis), and held at those temperatures until the outgas rate was less than 2 mtorr/minute. The evacuated sample tubes were weighed again and the sample mass was determined by subtracting the mass of the previously tared tube. N_2 isotherms were measured using liquid nitrogen baths (77 K). UHP grade (99.999% purity) N_2 and He, oil-free valves and gas regulators were used for all free space corrections and measurements.

Magnetic data were collected using a Quantum Design MPMS-XL SQUID magnetometer. A gelatin capsule was filled with evacuated crystals of $Ni_{0.36}Zn_{3.64}O(BDC)_3$ to obtain susceptibility data. DC susceptibility measurements were obtained under a DC field of 100 Oe between 5 K – 300 K. All data were corrected for diamagnetic contributions from the capsule and the sample using Pascal's constants.[89]

Nickel and zinc analyses were conducted at the MIT Center for Materials Science and Engineering Shared Experimental Facility (CMSE-SEF) using a HORIBA Jobin ACTIVA inductively coupled plasma atomic emission spectrometer (ICP-AES). Standards were prepared from solutions purchased from ULTRA Scientific©, designated suitable for ICP analysis.

2.5.4 Calculations

All time-dependent density functional theory (TD-DFT) calculations and geometry optimizations were performed at the spin-unrestricted level using the Becke-Perdew (BP) functional,[90,91] with the ORCA 2.8.0 software package.[92] For each TD-DFT

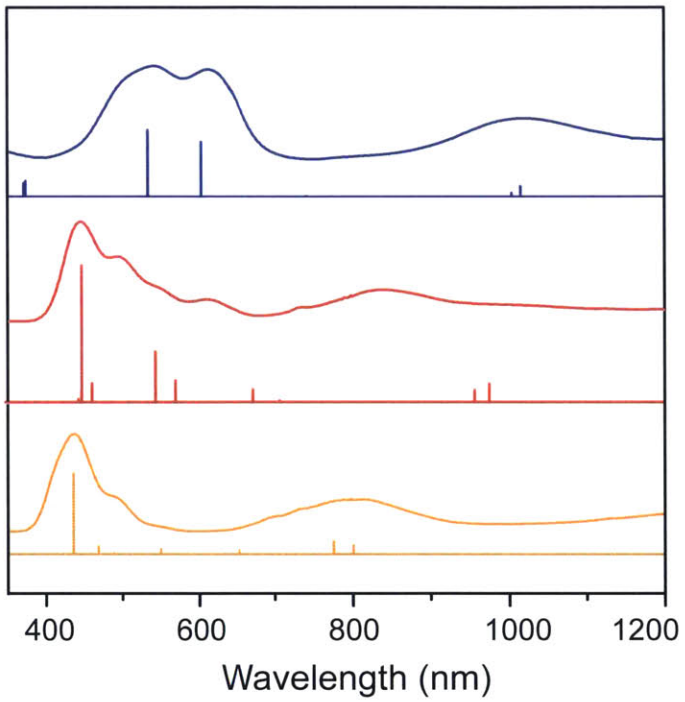

Figure 2-13: Experimental diffuse reflectance traces of the six-(yellow), five-(red), and four-(indigo)-coordinate nickel(II) species are compared to the calculated transitions of their corresponding model compounds, shown in Figures 2-15 – 2-17.

calculation, 10 excited states were included using one-electron transitions. All geometry optimizations began from crystallographically determined structures, where all atomic positions were optimized.

The all-electron Gaussian basis sets developed by the Ahlrichs group were employed in all calculations.[93,94] The standard basis sets TZV(p) (for H), TZV(2d) (for C, N, and O), and TZV(2pf) (for Zn and Ni) were employed. The resolution of the identity (RI) approach was taken for geometry optimizations, though not for TD-DFT calculations. The zeroth-order regular approximation (ZORA) method was implemented for all calculations involving Ni.[95–97] All calculations were performed with triplet spin multiplicities.

Figure 2-13 invokes the calculated transitions of a model compound where the pendant DMF molecule is in an equatorial position, as shown on the right side of Figure 2-16. However, both possible structural isomers gave rise to spectra that agreed with the experimental red trace, as shown in Figure 2-14.

2.5.5 Preparation of $Ni_xZn_{4-x}O(BDC)_3$

Method A. $Zn(NO_3)_2{\cdot}6H_2O$ (446 mg, 1.50 mmol), $Ni(NO_3)_2{\cdot}6H_2O$ (327 mg, 1.13 mmol), and terephthalic acid (H_2BDC, 83 mg, 0.50 mmol) were combined in a 100 mL jar with a Teflon-lined lid. The contents were dissolved in 49 mL of anhydrous DMF and 1 mL of deionized H_2O. The solution was heated for 7 h at 100 °C to afford yellow cubic crystals. The reaction container was allowed to cool to room temperature, then transferred to a nitrogen-filled glove bag, with oven-dried glassware and dry solvents. The crystals were collected by gravity filtration and washed with anhydrous DMF (6 × 20 mL), soaking for 8 h each time. The DMF was decanted and the resulting solid was washed with CH_2Cl_2(6 × 20 mL), again soaking for 8 h after each wash. A UV-Vis spectrum was taken of the final DMF wash to verify the removal of free metal ions. After the final CH_2Cl_2 wash, the solvent was decanted and the crystals were heated under vacuum for 12 h (4 mtorr, 200 °C) to yield indigo crystals. ICP-AES and elemental microanalysis for $C_{24}H_{12}O_{13}Ni_{0.36}Zn_{3.64}$: Calculated: C% 37.60, H% 1.60, N% 0.00; Ni/Zn, 0.10. Found: C% 37.40, H% 1.80, N% 0.00; Ni/Zn, 0.10.

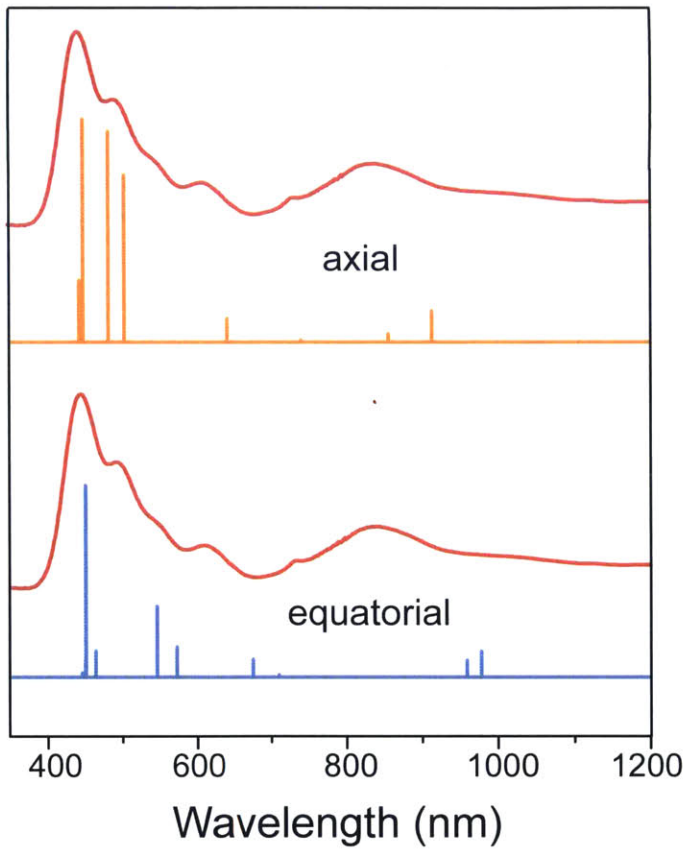

Figure 2-14: The experimental red trace of the purported $(DMF)_xNi_xZn_{4-x}O(BDC)_3$ is compared to two model compounds, where the nickel center is five-coordinate with a DMF bound axially or equatorially with respect to the carboxylate oxygens around nickel. See Figure 2-16 for depictions of the model structures.

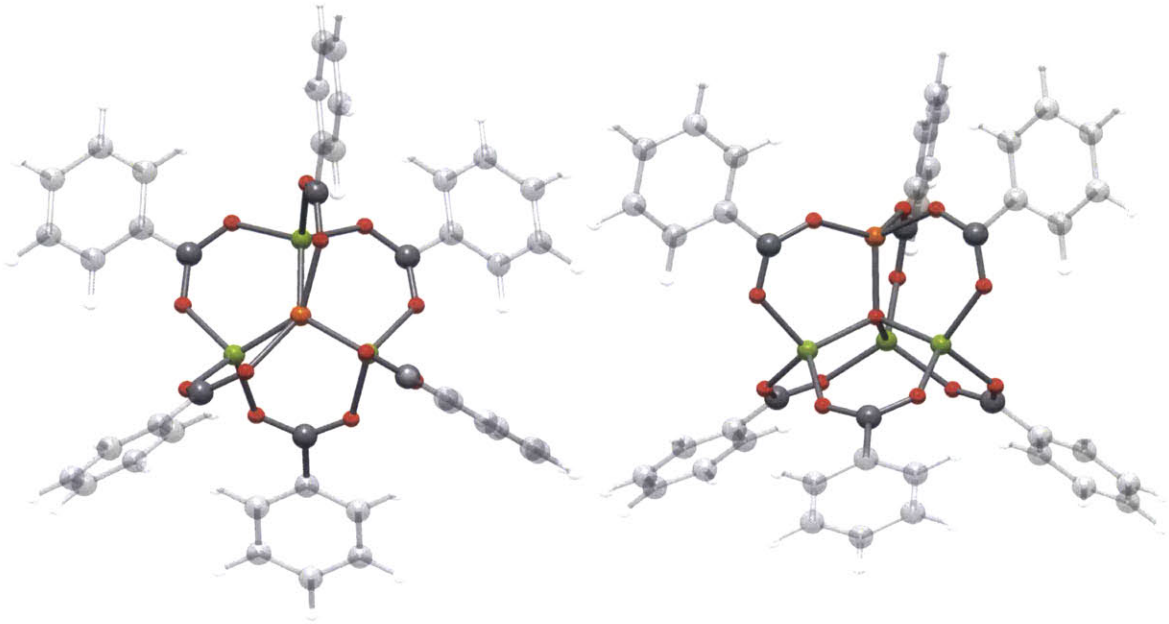

Figure 2-15: Two views of the geometry-optimized cluster $NiZn_3O(O_2C\text{-}C_6H_5)_6$. Orange, green, red, grey, and white atoms represent Ni, Zn, O, C, H respectively.

Method B. A sample of $Ni_xZn_{4-x}O(BDC)_3$ ($x = 1$) was obtained by soaking colorless MOF-5 crystals prepared in a manner described by Kaye et al.[72] in a 20 mL solution of anhydrous DMF and 5.00 g $Ni(NO_3)_2{\cdot}6H_2O$ for 1 year. Yellow cubic crystals were collected by decanting the solution. These were washed with DMF and CH_2Cl_2 in a manner identical to Method A. Ni-MOF-5 was obtained alternatively by soaking MOF-5 crystals for 2 weeks, but the Ni:Zn content never reached 1:3.

2.5.6 Preparation of (MesCNO)$Ni_xZn_{4-x}O(BDC)_3$

A 15 mL toluene solution of MesCNO (11.4 mg, 70.5 μmol) was added dropwise to a suspension of activated single crystals of Ni-MOF-5 ($Ni_{0.23}Zn_{3.77}O_{13}C_{24}H_{12}$) (150 mg, 0.196 mmol) in 5 mL of toluene while stirring at 35 °C. After combining, the mixture was allowed to warm to room temperature, whereupon the indigo crystals turned orange. Toluene was removed under reduced pressure. Elemental microanalysis for $(C_{10}H_{11}NO)_{0.23}Ni_{0.23}Zn_{3.77}O_{13}C_{24}H_{12}(C_7H_8)_{3.5}$: Calculated: C% 54.10 H% 3.81 N% 0.29. Found: C% 54.72 H% 4.32 N% 0.10.

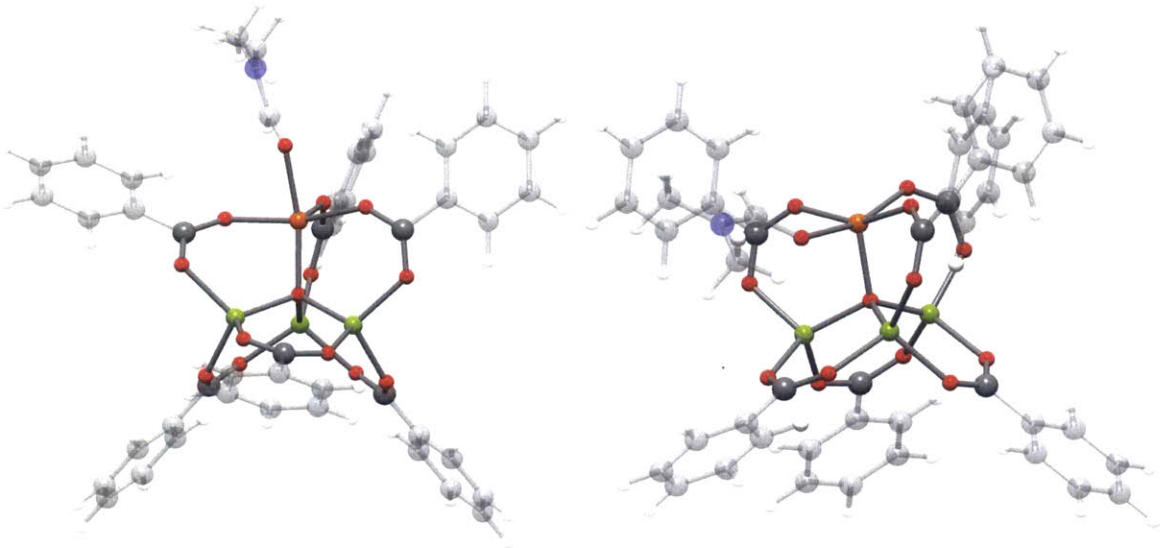

Figure 2-16: Two stereoisomers of (DMF)$NiZn_3O(O_2C\text{-}C_6H_5)_6$ after geometry optimization. Orange, green, red, blue, grey, and white atoms represent Ni, Zn, O, N, C, and H respectively. The axial (left) and equatorial (right) geometries were juxtaposed the red experimental trace in figure S8. Scheme 1 and figure S7 employ the equatorial isomer as the better suited model for (DMF)Ni-MOF-5.

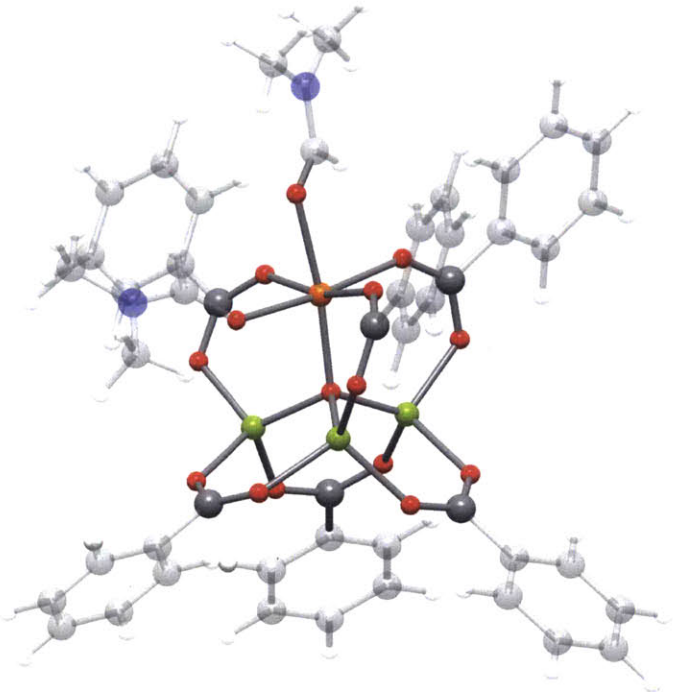

Figure 2-17: The geometry-optimized cluster $(DMF)_2NiZn_3O(O_2C\text{-}C_6H_5)_6$ that was used as a model for $(DMF)_2$Ni-MOF-5. Orange, green, red, blue, grey, and white atoms represent Ni, Zn, O, N, C, and H respectively.

	Ni-MOF-5
Formula	$Ni_{0.36}Zn_{3.64}O_{13}C_{24}H_{12}$
FW	247.91
T, K	100(2)
group	$Fm\bar{3}m$
Z	32
a, Å	25.8380(2)
V, Å^3	17249.5
d_{calc}, g/cm^3	0.784
μ, mm^{-1}	1.220
F(000)	3930
crystal size, mm	0.2 × 0.2 × 0.2
theta range	1.37 to 26.82
index ranges	$-32 \leq h \leq 32$
	$-32 \leq k \leq 32$
	$-32 \leq l \leq 32$
refl. collected	80165
data/restr./param.	991/0/34
GOF on F^2	1.571
largest peak/hole, e/Å^3	2.05/−0.45
R_1 (wR_2), % [I>2sigma(I)]	9.05(34.24)

Table 2.2: Crystallographic data for crystals of $Ni_{0.36}Zn_{3.64}O_{13}C_{24}H_{12}$.

atom	x	y	z	atom	x	y	z	atom	x	y	z
C	19.378500	24.450500	19.378500	C	20.355572	25.133837	20.104233	C	18.396376	25.135525	18.661690
Zn	20.499661	31.187010	20.521545	Zn	20.480604	33.419535	18.279675	Zn	18.255551	31.186895	18.275639
Ni	18.231043	33.459319	20.595411	O	19.331370	32.334757	19.438162	O	19.915034	31.291732	22.388219
O	22.401958	31.650762	20.321387	O	20.306087	29.286561	20.036737	O	20.072151	33.197912	16.365251
O	22.387134	32.944292	18.448130	O	20.287239	35.320966	8.686533	O	18.678439	31.400038	16.366864
O	16.350529	31.464295	18.594371	O	18.466395	29.278161	18.69780	O	19.012783	33.376823	22.393063
O	16.376605	33.174726	20.091825	O	18.482995	35.308511	20.077689	C	19.378500	32.297500	22.969980
C	22.969980	32.297500	19.378500	C	19.378500	28.706020	19.378500	C	19.378500	32.297500	15.787020
C	19.378500	35.888980	19.378500	C	15.787020	32.297500	19.378500	C	19.202146	32.179251	24.437535
C	24.469045	32.294756	19.366318	C	19.373282	27.219527	19.390041	C	19.380662	32.294310	14.301252
C	19.366254	37.375412	19.376465	C	19.378500	32.297500	11.531500	C	19.378500	40.144500	19.378500
C	14.304963	32.265565	19.407824	C	11.531500	32.297500	19.378500	C	19.569342	30.995186	25.096888
C	25.182722	31.590865	20.348762	C	20.353697	26.524905	20.111655	C	20.132149	33.253167	13.607499
C	25.167862	32.996736	18.371881	C	20.129513	33.254013	12.216561	C	20.329751	39.457135	18.623927
C	18.629033	31.336223	13.606750	C	13.606883	31.389693	18.560574	C	18.393255	26.526300	18.665921
C	18.629549	31.338663	12.215704	C	12.216227	31.407886	18.543852	C	18.679941	33.256188	25.159045
C	13.612335	33.141540	20.246155	C	18.411948	38.072052	20.130514	C	18.419229	39.463083	20.129675
C	12.223960	33.141880	20.222890	C	18.893841	31.966049	27.198959	C	19.411991	30.887610	26.476941
C	18.534110	33.141880	26.533040	C	27.269107	32.291005	19.342564	C	26.577239	31.590529	20.335943
C	26.562380	32.993330	18.361003	C	20.324344	38.066369	18.621268	H	19.382075	23.358218	19.372636
H	21.114166	24.579725	20.658787	H	17.640418	24.583135	18.101856	H	19.377163	32.298967	10.439245
H	19.383399	41.236746	19.380909	H	10.439849	32.317760	19.365368	H	19.975415	30.172538	24.509949
H	24.629036	31.049760	21.115445	H	21.102049	27.091986	20.663820	H	20.705861	33.984324	14.175508
H	24.602480	33.539094	17.614646	H	20.708692	33.995086	11.663986	H	21.070991	40.007127	18.042507
H	18.055588	30.604107	14.173833	H	14.173323	30.716260	17.918982	H	17.645272	27.095117	18.115217
H	18.049514	30.598841	11.662354	H	11.665002	30.738200	17.882279	H	18.402897	34.168231	24.631737
H	14.170783	33.815394	20.894260	H	17.679351	37.508796	20.707101	H	17.683066	40.018873	20.712041
H	11.674367	33.825892	20.872889	H	18.769810	31.893670	28.280743	H	19.694637	29.966679	26.989152
H	18.131658	33.979841	27.105754	H	28.360510	32.289541	19.333330	H	27.127567	31.04239	21.102267
H	27.101130	33.539982	17.585445	H	21.052259	37.496134	18.045974				

Table 2.3: Optimized atomic coordinates for $NiZn_3O(C_8H_4O_4)_6$

atom	x	y	z	atom	x	y	z	atom	x	y	z
Zn	1.305441	0.416011	1.950299	Zn	1.894097	0.629380	-1.153936	Zn	-0.568919	2.083254	0.059001
Ni	-0.658761	-1.176642	-0.236998	O	0.486739	0.453778	0.185598	O	3.292425	0.513869	1.872816
O	3.655398	1.044799	-0.310963	O	0.876139	-1.160533	3.027187	O	-0.366946	-2.285511	1.481553
O	0.817110	1.992356	3.068420	O	-0.191294	3.355309	1.550237	C	8.220289	1.381758	1.719973
C	7.736963	1.558940	0.419671	C	6.379400	1.386983	0.149699	C	5.494334	1.037007	1.180382
C	5.984005	0.860804	2.483204	C	7.342087	1.032476	2.750734	C	4.031993	0.850636	0.890745
C	-0.016595	-5.508573	5.315035	C	-0.312135	-5.688283	3.959961	C	-0.245648	-4.606257	3.081009
C	0.132738	-3.338366	3.545435	C	0.444524	-3.168470	4.902348	C	0.359855	-4.246516	5.784169
C	0.216691	-2.168899	2.597195	C	0.233060	6.272649	5.599008	C	-0.316599	6.474200	4.328940
C	-0.294755	5.445634	3.387124	C	0.278493	4.206484	3.709685	C	0.829124	4.009467	4.984931
C	0.805686	5.039242	5.925330	C	0.304112	3.097652	2.696663	N	-3.373105	-4.493531	-0.328011
O	-1.970752	-2.776464	-0.910813	C	-2.572990	-3.440872	-0.048721	C	-4.057628	-5.218805	0.731822
C	-3.580488	-4.937988	-1.699632	N	-2.372060	0.250044	-3.887310	O	-1.023172	-0.268370	-2.114330
C	-2.146948	-0.227043	-2.649773	C	-1.278053	0.757659	-4.709686	C	-3.719377	0.321880	-4.432427
O	-2.421834	-0.426718	0.608545	O	-2.518345	1.802700	0.158685	O	1.635173	2.176483	-2.389696
O	-0.226881	3.188763	-1.5550717	O	2.222198	-0.937091	-2.283984	O	0.829440	-2.303927	-1.108824
C	-7.144889	0.832314	1.791344	C	-6.520264	1.981696	1.297775	C	-5.182428	1.936490	0.904026
C	-4.458283	0.737826	0.993219	C	-5.090515	-0.410638	1.491222	C	-6.426358	-0.363516	1.890908
C	-3.014837	0.690186	0.559393	C	0.923094	6.019526	-5.519198	C	1.872907	4.994418	-5.464415
C	1.813196	4.040101	-4.448591	C	0.800232	4.103650	-3.479806	C	-0.148741	5.135725	-3.537873
C	-0.086895	6.089269	-4.554287	C	0.733794	3.074021	-2.385131	C	3.266851	-5.463561	-4.147405
C	2.250338	-5.640810	-3.2029897	C	1.750006	-4.544235	-2.500478	C	2.262900	-3.260326	-2.735627
C	3.284359	-3.088624	-3.681640	C	3.782806	-4.185916	-4.385009	C	1.719457	-2.078369	-1.975839
H	9.282961	1.516169	1.930349	H	8.421570	1.831493	-0.385306	H	5.984306	1.519955	-0.857097
H	5.284652	0.588419	3.273196	H	7.718342	0.893945	3.765702	H	-0.072388	-6.353812	6.003392
H	-0.588237	-6.676972	3.588596	H	-0.459062	-4.731848	2.019303	H	0.752261	-2.182158	5.248627
H	0.594964	-4.104311	6.840333	H	0.215912	7.078351	6.335290	H	-0.762669	7.436797	4.073227
H	-0.717180	5.584169	2.392238	H	1.272111	3.042124	5.220312	H	1.235905	4.881449	6.915729
H	-2.471824	-3.212398	1.025405	H	-3.784481	-4.789952	1.703608	H	-3.769486	-6.281553	0.721458
H	-5.150095	-5.152905	0.607426	H	-4.637821	-4.825384	-1.986623	H	-3.301398	-5.997825	-1.800630
H	-2.952435	-4.329858	-2.358853	H	-3.050053	-0.594470	-2.131853	H	-1.271038	0.238383	-5.679552
H	-0.332679	0.577817	-4.188311	H	-1.399890	1.836933	-4.884543	H	-4.431991	-0.087772	-3.706092
H	-3.788461	-0.256273	-5.366892	H	-3.994334	1.366341	-4.645596	H	-8.189713	0.869558	2.104909
H	-7.076972	2.917607	1.226009	H	-4.676233	2.824984	0.527609	H	-4.511758	-1.330671	1.568878
H	-6.909785	-1.258605	2.286470	H	0.972488	6.767505	-6.312642	H	2.664252	4.942291	-6.214027
H	2.547499	3.237218	-4.386317	H	-0.924323	5.177246	-2.773355	H	-0.824659	6.892519	-4.592752
H	3.659433	-6.322140	-4.695490	H	1.850659	-6.638743	-3.013198	H	0.960345	-4.658344	-1.758079
H	3.677874	-2.086466	-3.849834	H	4.578979	-4.046185	-5.118365				

Table 2.4: Optimized atomic coordinates for $(DMF)_2NiZn_3O(C_8H_4O_4)_6$

atom	x	y	z	atom	x	y	z	atom	x	y	z
Zn	11.603012	-5.910506	-8.207048	Zn	14.786785	-5.845586	-7.854292	Zn	13.419909	-4.288477	-10.281963
Ni	13.749095	-7.343178	-10.354886	O	13.314660	-5.831322	-9.120071	O	11.864727	-5.804877	-6.242525
O	14.123168	-5.581629	-6.010995	O	10.616928	-7.537336	-8.616683	O	12.036269	-8.391978	-10.204073
O	10.491478	-4.343456	-8.711800	O	11.870672	-3.091962	-10.028289	C	12.454686	-5.222196	-1.305597
C	13.731254	-5.176264	-1.874697	C	13.886731	-5.310785	-3.253955	C	12.764203	-5.491714	-4.075946
C	11.485468	-5.536800	-3.500269	C	11.332865	-5.402699	-2.120596	C	12.928423	-5.637509	-5.560765
C	8.270981	-11.688779	-10.120542	C	9.464555	-11.616354	-10.845388	C	10.340935	-10.550611	-10.643504
C	10.031758	-9.545609	-9.714081	C	8.833094	-9.623458	-8.990096	C	7.957836	-10.690412	-9.193043
C	10.987037	-8.396231	-9.501434	C	7.800409	-0.212913	-9.583055	C	9.017357	-0.052467	-10.253104
C	9.985265	-1.054640	-10.194250	C	9.742731	-2.226448	-9.461972	C	8.520284	-2.382700	-8.790931
C	7.553695	-1.379442	-8.852511	C	10.781209	-3.307102	-9.393043	N	17.685617	-6.440733	-11.716115
O	15.669123	-6.401983	-10.626756	C	16.371137	-6.699385	-11.614784	C	18.420067	-5.802418	-10.628127
C	18.425807	-6.784027	-12.922621	O	13.447263	-7.101199	-12.305153	O	13.352604	-4.814181	-12.201941
O	16.036071	-4.335349	-8.191421	O	15.038496	-3.207487	-9.910635	O	15.729898	-7.589912	-7.830842
O	14.790438	-8.821872	-9.517689	C	12.326165	-5.788434	-17.003810	C	12.467554	-4.603373	-16.275244
C	12.770537	-4.649169	-14.914515	C	12.938698	-5.884483	-14.271284	C	12.793953	-7.072007	-15.007151
C	12.487948	-7.022762	-16.366854	C	13.269076	-5.941658	-12.806153	C	19.058288	-0.405853	-8.896261
C	19.052101	-1.454664	-7.971263	C	18.044411	-2.418211	-8.014001	C	17.032372	-2.339307	-8.983045
C	17.041013	-1.282356	-9.906059	C	18.051164	-0.321620	-9.862924	C	15.946290	-3.376598	-9.029439
C	17.739303	-12.130205	-7.192211	C	16.903896	-12.211975	-8.310495	C	16.192367	-11.089684	-8.734287
C	16.311108	-9.874343	-8.041172	C	17.147974	-9.798883	-6.917915	C	17.858984	-10.922765	-6.497094
C	15.546840	-8.667219	-8.505632	H	12.333965	-5.117315	-0.225983	H	14.607639	-5.035524	-1.240083
H	14.873950	-5.277711	-3.713566	H	10.622187	-5.678560	-4.149636	H	10.336174	-5.439099	-1.678137
H	7.585161	-12.523079	-10.278155	H	9.711487	-12.394349	-11.569802	H	11.276382	-10.475496	-11.197348
H	8.603100	-8.838074	-8.270945	H	7.027121	-10.744639	-8.625867	H	7.043573	0.572014	-9.630193
H	9.211129	0.857478	-10.823204	H	10.938503	-0.945534	-10.710338	H	8.345112	-3.297832	-8.226221
H	6.604684	-1.506346	-8.329314	H	15.940150	-7.211625	-12.493076	H	19.271312	-6.435071	-10.336574
H	17.747805	-5.673189	-9.774230	H	18.800105	-4.820663	-10.947332	H	17.752176	-7.261712	-13.644174
H	19.245136	-7.479374	-12.684811	H	18.854348	-5.880088	-13.381471	H	12.085118	-5.749988	-18.067531
H	12.336592	-3.639735	-16.770131	H	12.876830	-3.734822	-14.331811	H	12.915351	-8.023753	-14.490626
H	12.370520	-7.948818	-16.931940	H	19.846124	0.348546	-8.861133	H	19.833405	-1.518275	-7.212264
H	18.021817	-3.238283	-7.296791	H	16.245292	-1.227467	-10.648351	H	18.051710	0.498673	-10.582415
H	18.294489	-13.008942	-6.859312	H	16.804866	-13.154800	-8.850884	H	15.530838	-11.134153	-9.598904
H	17.226356	-8.852520	-6.383881	H	18.506634	-10.859331	-5.621148				

Table 2.5: Optimized coordinates of the equatorial isomer $(DMF)NiZn_3O(C_8H_4O_4)_6$

atom	x	y	z	atom	x	y	z	atom	x	y	z
Zn	1.036619	0.384695	1.459538	Zn	1.770304	0.639862	-1.601023	Zn	-0.796517	2.042231	-0.464329
Ni	-0.835855	-1.199401	-0.550651	O	0.291903	0.415996	-0.346623	O	3.015409	0.560898	1.454268
O	3.487991	1.054218	-0.717020	O	0.692019	-1.277799	2.440150	O	-0.339658	-2.534385	0.841730
O	0.450142	1.908105	2.577449	O	-0.350563	3.325905	0.988162	C	7.926133	1.538930	1.550160
C	7.510563	1.675961	0.221928	C	6.174261	1.466421	-0.117467	C	5.242244	1.118146	0.871832
C	5.663767	0.981863	2.203124	C	7.000807	1.191549	2.539484	C	3.804339	0.893681	0.508880
C	0.391541	-5.792269	4.577678	C	-0.010169	-5.945034	3.246827	C	-0.078097	-4.834563	2.405446
C	0.264828	-3.561713	2.885992	C	0.677479	-3.415553	4.218756	C	0.734137	-4.525917	5.061321
C	0.199217	-2.362415	1.982061	C	-0.069595	6.225705	5.063039	C	-0.508152	6.454796	3.755023
C	-0.475886	5.423874	2.816545	C	-0.002182	4.154263	3.180664	C	0.437513	3.929267	4.494024
C	0.402711	4.961772	5.430671	C	0.035159	3.045734	2.172238	N	-4.122711	-3.808440	-0.884406
O	-2.365912	-2.401388	-1.292202	C	-3.038122	-3.103565	-0.511261	C	-4.866826	-4.610295	0.076055
C	-4.606440	-3.772937	-2.259927	O	-2.312799	-0.445063	0.675686	O	-2.701207	1.625151	-0.178865
O	1.444255	2.164109	-2.834517	O	-0.553461	3.016861	-2.150472	O	2.068890	-0.941938	-2.703823
O	0.224776	-2.095700	-2.020232	C	-6.864001	0.715006	2.456780	C	-6.508583	1.713590	1.544862
C	-5.261831	1.679488	0.919811	C	-4.365308	0.634653	1.189828	C	-4.727695	-0.365408	2.104672
C	-5.968778	-0.321704	2.739770	C	-3.023944	0.595052	0.514599	C	0.455290	5.659314	-6.281016
C	1.504214	4.749273	-6.115776	C	1.503037	3.870631	-5.032911	C	0.450096	3.896320	-4.105850
C	-0.600168	4.811199	-4.275568	C	-0.596212	5.688602	-5.359507	C	0.449401	2.951681	-2.941511
C	2.347245	-5.183416	-5.345392	C	1.198486	-5.275614	-4.552947	C	0.852450	-4.228561	-3.698988
C	1.653336	-3.079117	-3.630436	C	2.804299	-2.990930	-4.427614	C	3.148791	-4.039572	-5.280776
C	1.279685	-1.952859	-2.706342	H	8.972237	1.703252	1.814581	H	8.231513	1.947082	-0.550938
H	5.833162	1.569122	-1.147131	H	4.929317	0.710845	2.960906	H	7.323742	1.084481	3.576248
H	0.443213	-6.661142	5.236051	H	-0.265984	-6.934452	2.863946	H	-0.378011	-4.938877	1.362911
H	0.950452	-2.423539	4.577139	H	1.051616	-4.404712	6.098201	H	-0.095194	7.033429	5.796635
H	-0.875953	7.440813	3.466841	H	-0.813007	5.584655	1.792995	H	0.803900	2.938877	4.762385
H	0.745934	4.782206	6.450740	H	-2.768850	-3.198579	0.553598	H	-4.386182	-4.543741	1.059405
H	-4.888849	-5.665309	-0.237675	H	-5.902626	-4.247719	0.161850	H	-5.627635	-3.364185	-2.292198
H	-4.618728	-4.788651	-2.682994	H	-3.937284	-3.137300	-2.848207	H	-7.835755	0.748335	2.952465
H	-7.203592	2.525903	1.326356	H	-4.963831	2.456800	0.216819	H	-4.013611	-1.159762	2.321180
H	-6.238486	-1.093739	3.462479	H	0.457455	6.346730	-7.128757	H	2.325292	4.725493	-6.833962
H	2.311998	3.155184	-4.888609	H	-1.411210	4.820940	-3.548097	H	-1.414909	6.398572	-5.487056
H	2.618155	-6.003363	-6.012929	H	0.572470	-6.168315	-4.601913	H	-0.037763	-4.279637	-3.072622
H	3.418453	-2.093203	-4.364578	H	4.045913	-3.965747	-5.897638				

Table 2.6: Optimized coordinates for axial isomer of (DMF)$NiZn_3O(C_8H_4O_4)_6$

Chapter 3

MOF-5 Contains Unsaturated Zn Centers

3.1 Abstract

A growing number of reports are incompatible with the prevailing assumption that MOFs are rigid materials. In this chapter, we report multinuclear solid-state NMR, mass spectrometry, molecular dynamics simulations, and other complementary evidence indicating that MOF-5 interacts dynamically with surrounding molecules. Contrary to how this material has been viewed for 15 years, these data reveal that the zinc ions, like the inserted Ni^{2+} in Ni-MOF-5, are not rigid. They bind solvent molecules, thereby increasing their coordination number, and dynamically dissociate from the framework itself. We find that, on average, one zinc ion in each cluster has at least one coordinated DMF molecule, such that the formula of as-synthesized MOF-5 is defined as $Zn_4O(BDC)_3(DMF)_x$ (x = 1-2). Given the relevance of MOF-5, this dynamic behavior will help explain current phenomena and inspire new applications.[1]

[1]At the time of writing this thesis, the work presented in this chapter was unpublished. NMR experiments and analyses were conducted in collaboration with Vlad K. Michaelis, Ta-Chung Ong and Professor Robert G. Griffin. Molecular dynamics simulations were performed in collaboration with Luca Bellarosa and Professor Núria López.

3.2 Introduction

Designing applications for metal-organic frameworks (MOFs) rests on the premise that the materials are accurately represented by their crystal structures. Unlike the random sprawl of many polymers, the repeating units of MOFs are depicted with perfect long-range order. Viewing them as periodic lattices simplifies the investigation of their properties and the design of their composition. For over 15 years, MOF chemistry has been viewed largely through this lens, their properties often interpreted on the basis of rigid X-ray crystal structures. There are, nevertheless, important examples of MOFs behaving dynamically and exhibiting properties that are inconsistent with a static view of their structure. For instance, the organic ligands and SBUs can be exchanged in numerous MOFs by simply soaking them in solutions of the inserting components.[98,99] In another body of literature, catalysis occurs within MOFs where the metal center has no available binding sites, yet the catalytic transformation involves inner-sphere reactivity and must proceed through bond formation between the substrate and the metal center.[100–104] Defects notwithstanding, for these and other phenomena to occur, the metal–ligand bonds in MOFs must dissociate. Although such dynamic behavior is sometimes implied in such studies, we hereby report evidence that the Zn_4O SBUs of MOF-5, an iconic example in this class of materials, interact dynamically with coordinating molecules, thereby distorting its lattice. In the presence of coordinating solvents, MOF-5 contains not just tetrahedral Zn^{2+} ions, as previously thought, but also octahedral metals.

Due to its ubiquity in the field, demonstrating that MOF-5 is a dynamic structure capable of additional coordination at the Zn^{2+} ions suggests that the SBUs in other MOFs may also be less rigid than previously believed. Several seminal findings for MOFs were established by first demonstrating they were true for MOF-5. When published 1999,[55] the discovery of MOF-5 concluded that materials in this class could be permanently porous and provided design principles for the emerging field. Early studies on modifying the composition of MOF-5 inspired the now-common notion that the pore size and physicochemical properties of a material might be tailored

systematically while preserving the overall topology, through reticular synthesis.[105] Gas storage in these materials has become a large area of sustainable energy research and is rooted in the early reports on hydrogen and methane sorption in MOF-5.[106] When the binding sites of N_2 and Ar within a MOF were first established by single-crystal X-ray diffraction[107] and when Monte Carlo simulations were employed to evaluate the accuracy of the Brunauer-Emmett-Teller (BET) theory in calculating apparent internal surface areas,[108] MOF-5 was again the material of choice. These reports indicate that MOF-5 maintains its iconic status because it has historically opened new avenues of research in this area and continues to offer critical insight into porous frameworks in general.

3.3 Results

We first suspected that Zn ions of MOF-5 interact with solvent molecules during a routine characterization of the sample. We followed a previously reported procedure that was optimized to remove excess solvent molecules from the pores and to maximize surface area.[72] $Zn(NO_3)_2 \cdot 6H_2O$ and 1,4-benzenedicarboxylate were dissolved in DMF containing 2% deionized water and heated for 7 h at 100 °C. The crystals were collected and washed with fresh DMF every 8 h for two days, then soaked in CH_2Cl_2 with similar repetitions. Surprisingly, although this treatment was reported to remove excess DMF, a FT-IR spectrum of a sample that had been fully washed with CH_2Cl_2, but not evacuated, showed a resonance at 1665 cm^{-1} corresponding to the C=O stretch of DMF (inset of Figure 3-1). Furthermore, a thermogravimetric (TGA) profile of the same sample exhibited a well-defined mass loss at approximately 50 °C (shown in Figure 3-1).[109,110] Because of its unambiguous and reproducible "step-like" change, we were able to quantify this mass loss and discovered that it corresponds to exactly two molecules of DMF per Zn_4O cluster. The mass loss was further identified as DMF by measuring a TGA of DMF-soaked MOF-5 in-line with a mass spectrometer. This confirmed that the weight loss step between 50 and 150 °C corresponds to the release of DMF (Figure 3-1). Together, the FT-IR and TGA-MS data suggested

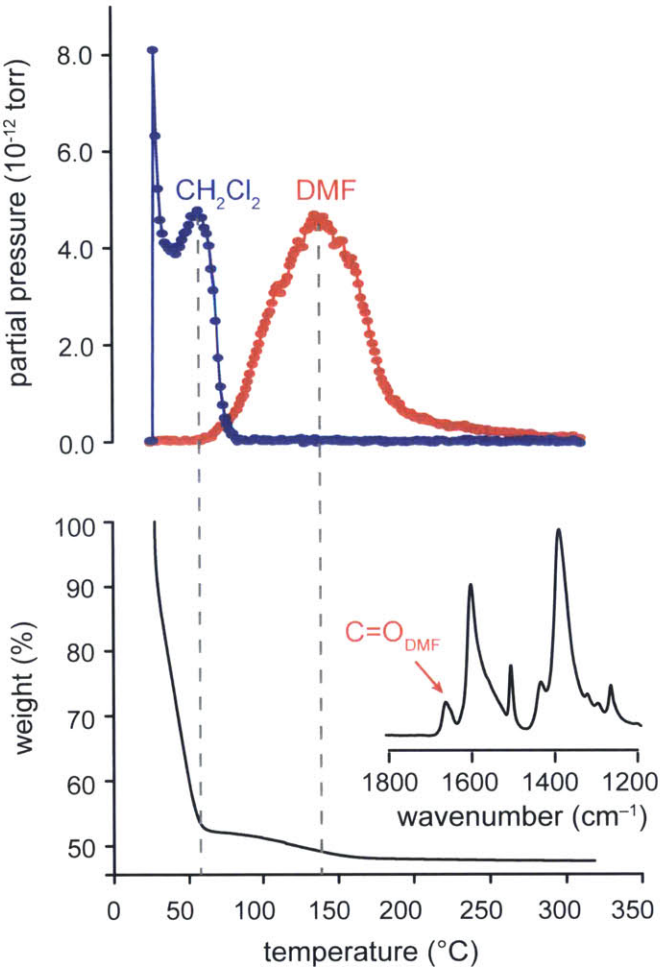

Figure 3-1: A TGA analysis (bottom) shown alongside mass spectrometry (top) of CH_2Cl_2 and DMF-soaked MOF-5. A selected portion of the FT-IR spectrum of this sample is shown as an inset.

that solvent was binding to the SBUs of MOF-5. In other words, unactivated or as-synthesized MOF-5 contained up to two bound DMF molecules per Zn_4O cluster.

We sought to quantify the interaction between DMF and the Zn_4O clusters using calorimetric measurements of solvated MOF-5. In collaboration with the research group of Prof. Alexandra Navrotsky we employed the thermodynamic cycle shown in Table 3.1, based on solution enthalpies (ΔH_s) of zinc oxide, 1,4-benzenedicarboxylic acid, and DMF (Table 3.2). The enthalpy of formation (ΔH_f) was determined to be 4.0 $\pm$ 0.28 kcal/mol per cluster. Using a previously reported formation enthalpy of desolvated MOF-5,[111] the interaction energy between DMF and each cluster is –19.19

reaction scheme	enthalpy measurement
$4Zn^{2+}(aq) + 3BDC^{2-}(aq) + DMF(aq) + 2OH^{-}(aq) \rightarrow Zn_4O(BDC)_3{\cdot}DMF(cr) + H_2O(l)$	$\Delta H_1 = \Delta H_s(\text{MOF-5})$
$4\times[ZnO(cr) + H_2O(aq) \rightarrow Zn^{2+}(aq) + 2OH^{-}(aq)]$	$\Delta H_2 = \Delta H_s(\text{ZnO})$
$3\times[H_2BDC(cr) + 2OH^{-}(aq) \rightarrow BDC^{2-}(aq) + 2H_2O(aq)]$	$\Delta H_3 = \Delta H_s(\text{ZnO})$
$DMF(l) \rightarrow DMF(aq)$	$\Delta H_4 = \Delta H_s(\text{DMF})$
$3\times[H_2O(aq) \rightarrow H_2O(l)]$	$\Delta H_5 = \Delta H_s(H_2O)$
$4ZnO(cr) + 3H_2BDC(cr) + x\text{DMF}(l) \rightarrow Zn_4O(BDC)_3DMF + 3H_2O(l)$	$\Delta H_f = \Delta H_1 + \Delta H_2 + \Delta H_3 + \Delta H_4 + \Delta H_5$

Table 3.1: Thermodynamic cycle used to measure the formation enthalpy of solvated MOF-5 via solution calorimetry in 5 M NaOH at 298.15 K.

compound	formula	ΔH_s (kcal/mol)	ΔH_{rxn} (kcal/mol)	ΔH_f (kcal/mol of Zn_4O)
ZnO	ZnO	-0.81 ± 0.67		
H_2BDC	$C_8H_6O_4$	-16.75 ± 0.029		
DMF	C_3H_7NO	-0.11 ± 0.1		
H_2O	H_2O	0.12		
solvated MOF-5	$(C_3H_7NO)Zn_4O(C_8H_4O_4)_3$	-54.312 ± 0.251	3.989 ± 0.289	4.00 ± 0.288
MOF-5	$Zn_4O(C_8H_4O_4)_3$	-73.984 ± 1.22	23.77 ± 0.865	23.78 ± 0.88

Table 3.2: Thermodynamic data used in and derived from 5 M NaOH at 298.15 K.

$\pm$ 1.16 kcal/mol. This value is quite similar to the measured bond dissociation energy of *N*-methylacetamide (NMA) from $Zn^{2+}(NMA)_6$ at –22.9 kcal/mol and acetone $Zn^{2+}(acetone)_6$ at –17.4 kcal/mol.[112]

With these data in hand, we sought structural evidence for DMF interacting with the Zn sites of MOF-5, and turned to solid-state ^{67}Zn nuclear magnetic resonance spectroscopy (^{67}Zn NMR).[113–115] An earlier ^{67}Zn NMR study of MOF-5 yielded high-quality spectra, but focused only on the fully evacuated samples or samples that were first fully evacuated then subsequently soaked in non-coordinating solvents such as chloroform.[116] Our NMR examination of a sample of DMF-soaked MOF-5 with natural abundance of ^{67}Zn (4.1 %) for 20 hours at 21.1 T and under magic-angle spinning (MAS) conditions revealed no discernable NMR signal (Figure 3-2A (bottom)). However, a fully evacuated sample produced a well-resolved signal under otherwise identical conditions (Figure 3-2A (top) and Figure 3-3). This comparison clearly indicated that the presence of DMF affected the ^{67}Zn NMR parameters in MOF-5, but further experiments were needed to identify the exact nature of the MOF-5 interaction with DMF in the solvated sample, requiring a significantly improved signal-to-noise

ratio.

To increase the sensitivity of the ^{67}Zn NMR signal, we synthesized MOF-5 from 97%-enriched ^{67}Zn metal. A new spectrum of DMF-solvated and ^{67}Zn-enriched MOF-5, acquired at 21.1 T, revealed a strong resonance with some finer structural details at the edges. Careful examination between the non-spinning and MAS spectra (Figure 3-4) suggests a secondary zinc. As a first approximation this spectrum (Figure 3-4A and Figure 3-2A, middle) can be described using a two-site model: a resonance centered at approximately 100 ppm with a full width at half maximum (FWHM) of 14 kHz, and a second site with a larger quadrupolar interaction (CQ $\approx$ 6 MHz, $\eta < 0.15$, to assist the reader a simulation (blue inset) of this larger site has been inserted into Figure 3-2A). Since the first site has the smaller quadrupolar coupling constant and is similar to what we observe with evacuated MOF-5, we refer to it as the "unsolvated site", i.e., pseudo-tetrahedral. Consequently, the second site, quite different from the evacuated MOF-5 signal, is named the "solvated site".

To confirm our two-site model and deconvolute the NMR parameters for each Zn site, we repeated the ^{67}Zn NMR measurements at a lower magnetic field because the linewidth due to second-order quadrupolar interactions scales inversely with magnetic field (i.e., the solvated-site would become more apparent as the broadening would become more obvious at 500 MHz vs. 900 MHz). Non-spinning experiments for the ^{67}Zn-enriched solvated sample, performed at 11.7 T, revealed two distinguishable Zn sites with second-order quadrupolar dominated lineshapes as shown in Figure 3-2B. Using collectively the 11.7 and 21.1 T data, the unsolvated site was simulated with CQ $\sim$ 4 MHz, $\eta \leq 0.65$ and δ_{iso} = 100 (50) ppm and the solvated site with C_Q = 5.90 (0.25) MHz, $\eta \leq 0.1$ and δ_{iso} = 165 (10) ppm. Due to the lack in resolution between the sites and unsuccessful attempts with quantum chemical methods due to non-favorable nuclear spin-spin relaxation further constraints regarding the NMR parameters cannot be obtained. The parameters fitting these data suggest that the unsolvated and solvated sites exist in a ratio of 70(8):30(8). In other words, DMF molecules bind to one of the four Zn sites in each Zn_4O cluster of MOF-5, as suggested by the TGA-MS and FT-IR data.

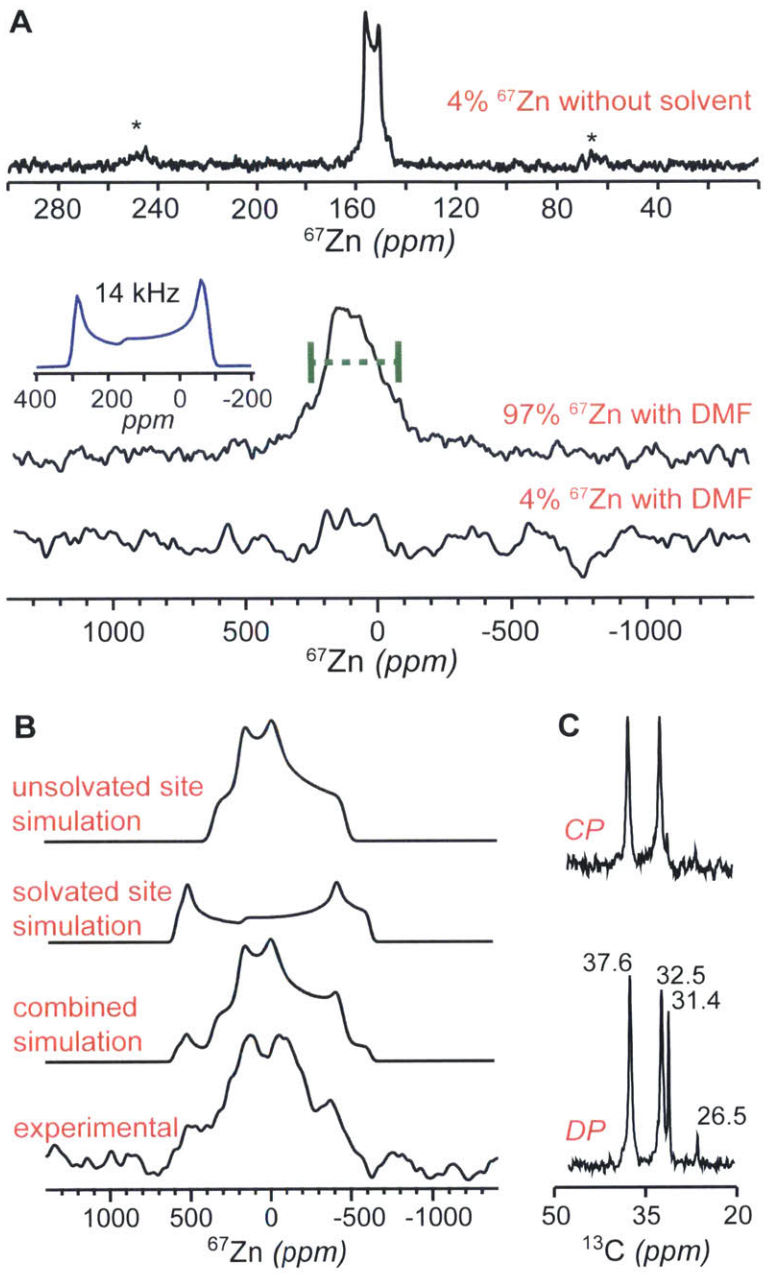

Figure 3-2: **A** ^{67}Zn NMR spectra MOF-5 taken under magic-angle spinning conditions at 21.1 T: fully evacuated (top) and when solvated with DMF using enriched (middle) and natural abundant (bottom) zinc. Asterisks denote spinning side bands. The spectral inset (blue) illustrates the secondary site present within the solvated system. **B** ^{67}Zn non-spinning NMR spectra of experimental 97% enriched sample soaked in DMF alongside spectra for two simulated sites collected at 11.7 T. **C** ^{13}C NMR spectra taken of CH_2Cl_2 and DMF-soaked MOF-5 with only the methyl region displayed using direct-polarization (DP) and $^{13}C\{^1H\}$ cross-polarization (CP).

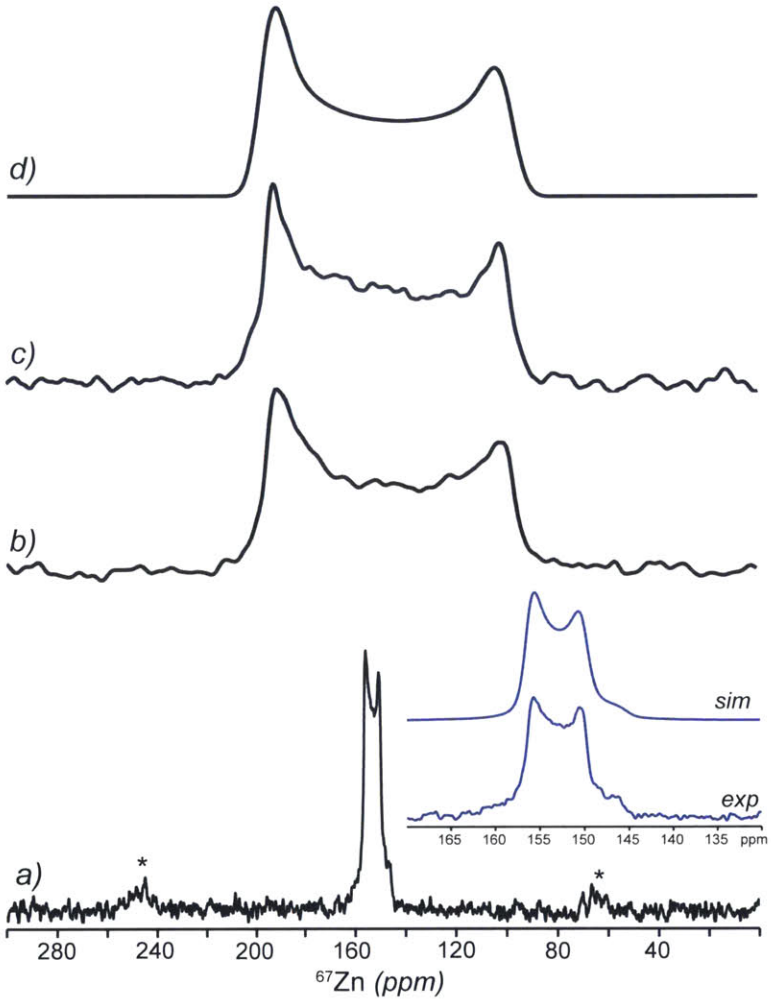

Figure 3-3: ^{67}Zn NMR spectra of natural abundance desolvated MOF-5 acquired at 21.1 T (900 MHz, ^{1}H). (a) MAS spectrum (inset (blue) – expanded region of the experimental (exp) MAS NMR spectrum and simulation (sim) using the following parameters, $\delta_{iso} = 158$ ppm, $C_Q = 1.65$ MHz and $\eta = 0$, (b) non-spinning spectrum, (c) non-spinning with ^{1}H decoupling, and (d) complete spectral simulation using the following parameters, $C_Q = 1.65$ MHz, $\eta = 0$, $\delta_{iso} = 158$ ppm, $\Omega = 87$ ppm and $\kappa = 1$.

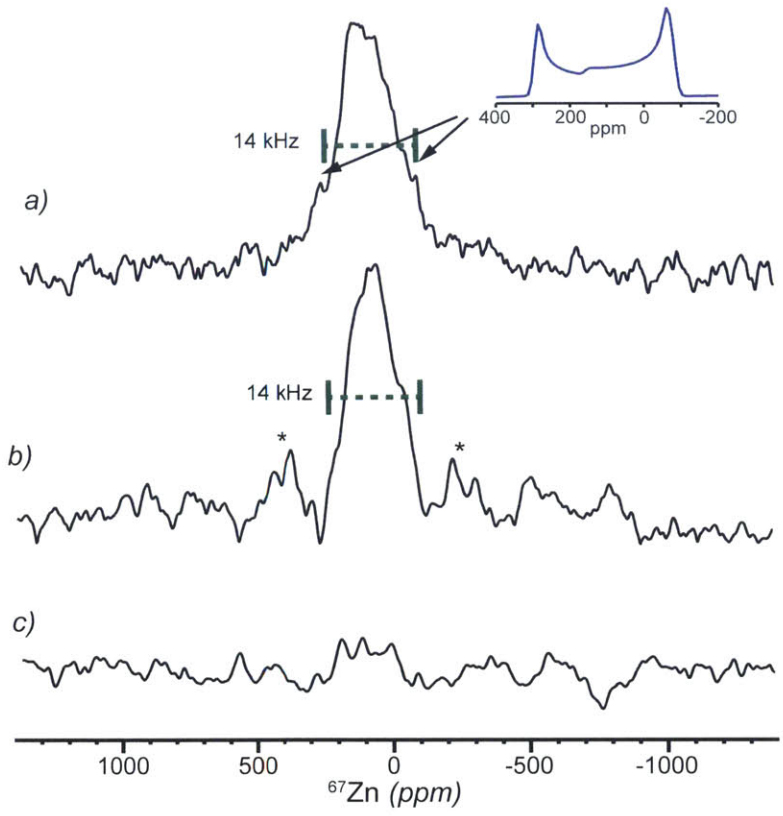

Figure 3-4: ^{67}Zn NMR spectra acquired at 21.1 T (900 MHz, 1H) using (a) ^{67}Zn isotopically labeled DMF-solvated MOF-5 under non-spinning (a) and MAS (b) conditions ("*" denotes the location of the spinning sidebands). Natural-abundant DMF solvated MOF-5 gave spectrum (c), under non-spinning conditions. The spectral inset (blue) illustrates the secondary site present within the solvated system.

As a complement to our structural information obtained from the ^{67}Zn NMR data, we probed the Zn–DMF interaction from the perspective of DMF by performing MAS ^{13}C NMR. Solvated MOF-5 was examined by a Bloch decay experiment to observe all ^{13}C resonances within the sample. The resulting spectrum, shown in Figure 3-5, displays resonances between 130 and 140 ppm and at 175 ppm, corresponding to aromatic and carboxylate carbons, respectively. Additional resonances between 30 and 40 ppm suggested that at least two DMF species exist in the sample. To test whether these signals result from bound and unbound solvent, we performed a ^{13}C{^{1}H} cross-polarization experiment, intended to reveal only rigid species, i.e., terephthalate and bound DMF. Indeed, Figure 3-5 and 3-2C indicate that the signal at 31.4 ppm, likely stemming from unbound DMF, drops out under cross-polarization conditions, leaving the two inequivalent methyl groups at 32.5 ppm and 37.6 ppm locked in position, as would be expected for bound DMF. We also attempted a solution-based refocused-INEPT experiment (Figure 3-5) and temperature-dependent ^{2}H NMR (Figure 3-6) using d_7-DMF in the hope of probing the dynamics of the Zn–DMF interaction. Due to the time scale of these measurements, however, they were sensitive only to the internal dynamics of methyl rotation of the bound DMF. Nevertheless, the spectra acquired from the ^{2}H NMR confirm that the DMF molecules were bound since they depict a Pake doublet below 255 K, which is only observed for rigid powder-type species.

With experimental evidence that the Zn_4O clusters interact with coordinating solvent, we employed density functional theory to explore how this interaction might occur. Several previous reports used molecular dynamics simulations to understand the water-induced degradation of MOF-5.[117–119] Inspired by these studies, we used Born-Oppenheimer Molecular Dynamics (BOMD) to take into consideration bond formation and configurational contributions from the interaction between MOF-5 and DMF. We employed a cell containing two rotated $Zn_4(\mu_4\text{-O})$(1,4-benzenedicarboxylate)$_3$ units in the presence of 15 DMF molecules, equivalent to the concentration in liquid DMF (see Figure 3-7A). The trajectory of the 15 DMF molecules was calculated over 25 ps using 1 fs steps and conducted at 300 K. Starting from an optimized

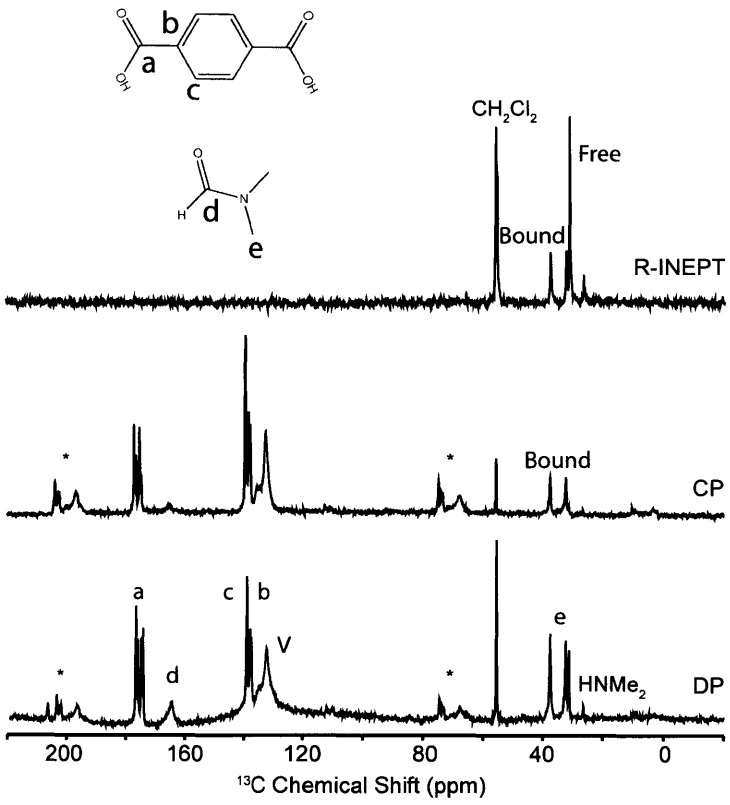

Figure 3-5: ^{13}C MAS NMR of DMF-solvated MOF-5 at 303 K using Bloch (DP), cross-polarization (CP) and refocused-INEPT (R-INEPT). Lower case letters denote the identity of the resonances according to the species illustrated at the top. V corresponds to Vespel present within the rotor and stator housing and * denotes spinning sidebands. Dimethylamine and dichloromethane impurities are assigned as well

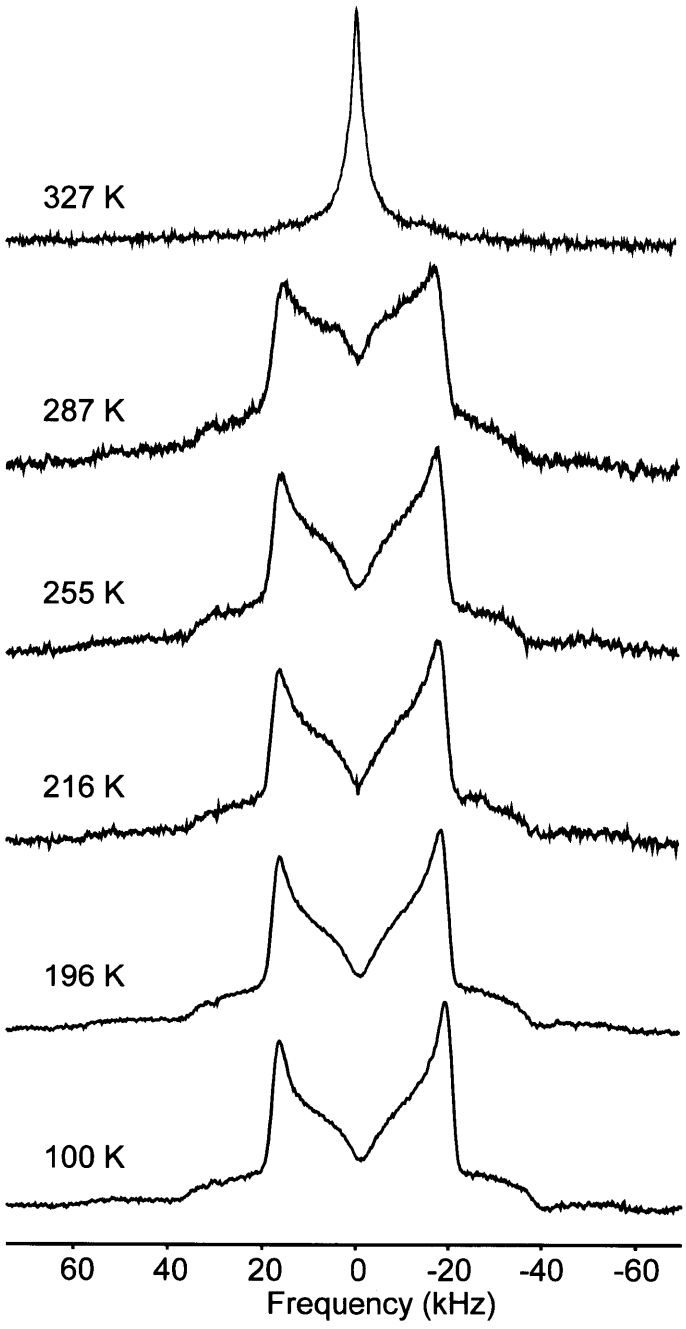

Figure 3-6: Variable temperature non-spinning ^{2}H NMR spectra of d_7-DMF bound to MOF-5.

structure, we explored two scenarios: one Zn_4O node (Core 1 containing Zn atoms Zn_1 through Zn_4) was constructed without bound DMF molecules, whereas a second Zn_4O node (Core 2, containing Zn atoms Zn_5 through Zn_8) was specified with one pseudo-octahedral site (Zn_8) with two bound DMF molecules at the onset.

In line with our experimental observations, our simulations predict that the MOF-5 SBUs dynamically bind and release DMF molecules without compromising the structural integrity of the framework within the 25 ps time frame of our simulation. Although Core 1 is initially unsolvated, its Zn ions repeatedly exchange DMF molecules after the first 5 ps (Zn_1 through Zn_4 in Figure 3-7). All Zn atoms participate in DMF binding events over the simulated time frame, but just one site at a time interacts with solvent. Overall, this node spends 28% of the simulation time with coordinated DMF. Even more striking, our simulations illustrate that the Zn ions in Core 2 (Zn_5 through Zn_8) not only dynamically coordinate DMF, but also release the organic linker (shown in red in Figure 3-8). The Zn ion that begins with two solvent ligands, Zn_8, quickly releases one DMF to solution and after only 2.5 ps a framework carboxylate detaches. Yet, by 5 ps the Zn_8 site regains both DMF molecules and the organic linker, thereby assuming its original pseudo-octahedral geometry, and then finally releases the DMF back to solution (right panel of Figure 3-8). The carboxylate group initially bound to the pseudo-octahedral Zn_8 ion starts coordinated in η^2 fashion to Zn_8 and Zn_6 atoms, then detaches and coordinates η^1 only to Zn_6, and ends as η^2-bound to the same. Overall, Core 2 spends 53% of the simulation time with a Zn site bound to DMF. Most significantly, these simulations show that DMF binding to the Zn_4O clusters is favorable and occurs dynamically in liquid DMF at a rate faster than 109 Hz (1 ns).

3.4 Discussion

Although MOF-5 has previously been depicted as a coordinatively saturated and rigid MOF even in its solvated form, our observation that DMF binds to MOF-5 is consistent with crystal structures of molecules and other MOFs with Zn_4O clus-

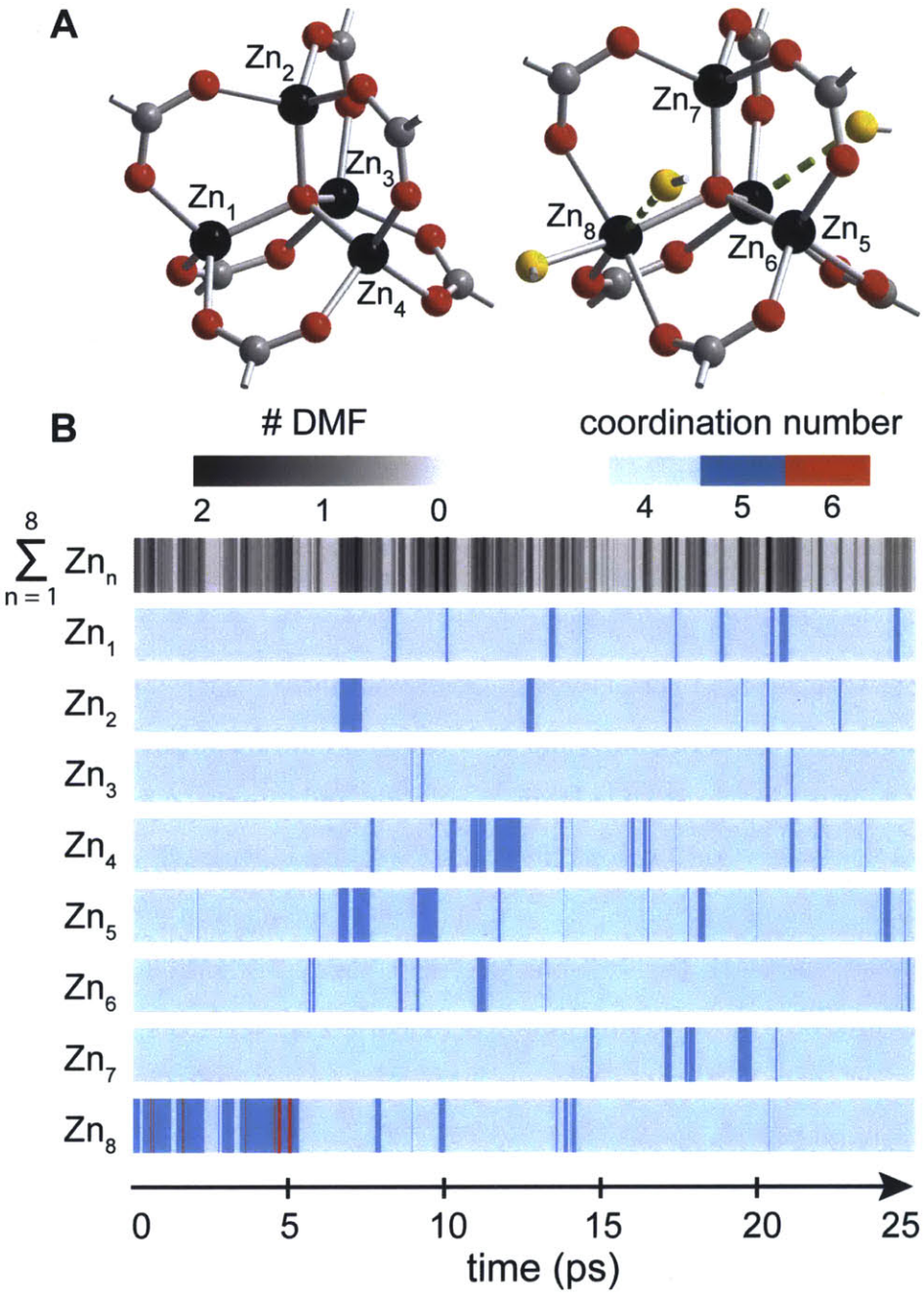

Figure 3-7: **A** Cluster 1 (left) and cluster 2 (right) of the two $Zn_4(\mu_4\text{-O})$(1,4-benzenedicarboxylate)$_3$ units employed for the simulation as they appear at time = 0 ps. Carbonyl oxygen atoms from DMF solvent are depicted in yellow. **B** Coordination number for individual Zn sites (Zn_1 through Zn_8) along the BOMD 25 ps simulation. Light blue denotes a coordination number of 4, dark blue denotes 5, and red denotes 6. The total number of DMF molecules bound to any of the eight Zn sites, Zn_1 through Zn_8, is shown at the top on a spectrum from zero to two, denoted by white to black, respectively.

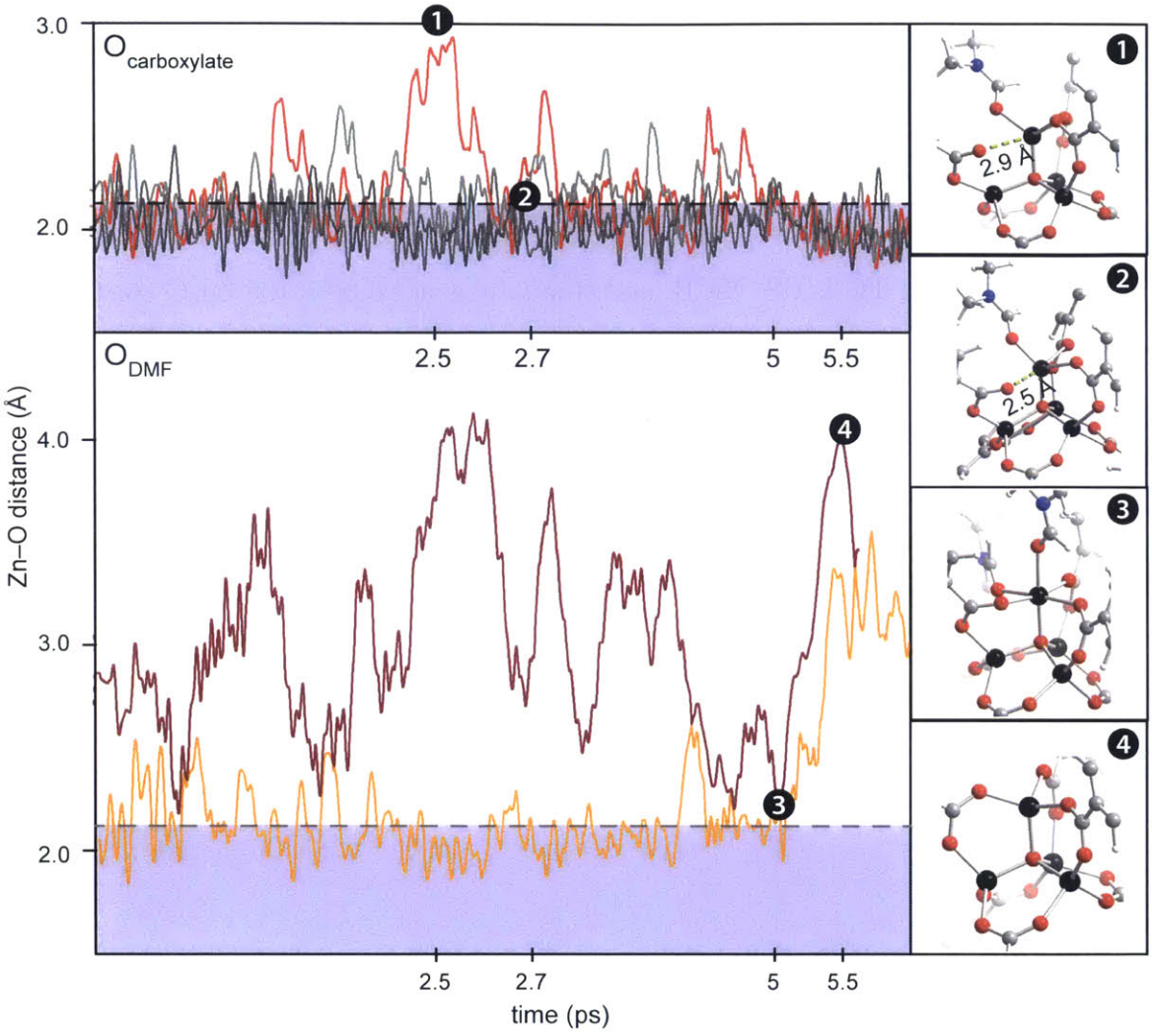

Figure 3-8: Summary of the BOMD simulated trajectories corresponding to the pseudo-octahedral Zn site, Zn_8, for the first 6 ps. Zn–O distances are plotted at the top for the framework carboxylates and at the bottom for the two nearest DMF molecules. Snapshots of the simulation are shown at time points (ps) on the right. The carboxylate oxygen that dissociates completely is shown as the red trace in the $O_{carboxylate}$ panel. The two colored traces in the O_{DMF} panel represent the positions of the oxygen atoms of two DMF molecules in the vicinity of Zn_8. The Zn–O bonding regions are defined by the colored rectangular regions starting at 2.2 Å for both carboxylate and DMF oxygen atoms.

ters where at least one Zn site features pendant solvent molecules. For instance, Bury *et al.* reported crystal structures of molecular Zn_4O clusters with benzoate or 9-anthracenecarboxylate ligands and a Zn site featuring additional bonds to tetrahydrofuran or water.[120] A number of MOFs with Zn_4O clusters also exhibit bound solvent molecules, but no reports exist describing MOF-5 itself with bound solvent molecules. The most relevant is a structure that is analogous to MOF-5 and includes a zinc site with two bound water molecules, but is made from naphthalene linkers.[67] Consistent with our TGA-MS, NMR, and simulations of MOF-5, the Zn_4O clusters in these crystal structures accommodate only one six-coordinate Zn site.[65,66,68–71,121–127] This evidence suggests that while the MOF-5 node undergoes dynamic interactions, the number of Zn sites that can bind DMF in each Zn_4O cluster is limited by how much the framework lattice can distort. That the MOF-5 SBUs can dynamically detach from the framework and support a limited amount of geometric distortion is also in line with reports that Ni^{2+} and other cations can replace up to a single Zn^{2+} per node.[16,17]

The ability of Zn sites in MOF-5 to alter their coordination environment and detach from ligands may explain other interesting phenomena observed in MOFs. Of the materials reported to undergo cation exchange, many contain metal ions that are coordinatively saturated and are integral to the framework integrity. It is likely that cation exchange preserves the crystallinity in these systems because their SBUs reversibly bind solvent molecules, as in MOF-5. The dynamic behavior of the MOF-5 SBUs revealed in this study could also explain the growing body of literature describing redox catalysis at coordinatively saturated metal sites. Although defect sites can never be discounted in heterogeneous catalysis, it is possible that MOFs able to catalyze reactions at metal sites that are seemingly coordinatively saturated do so by distorting their SBUs when binding substrates.[100–102,104]

3.5 Conclusion and Outlook

This chapter establishes that the Zn_4O clusters in MOF-5 interact with coordinating ligands, but that no more than 2 will bind at a time. Coupled with the results of the preceding chapter, this behavior appears to be general of any metal ion in the MOF-5 SBU. Simulations also suggest that these interactions are dynamic and involve detachment of MOF-based ligands themselves.

Viewing all MOF SBUs as dynamic entities will inform the design principles used for future reactivity studies, thus possibly enabling new applications for these materials. Using this perspective to review even mature fields, such as gas storage and separation in MOFs, may uncover new insights into how guest molecules adsorb onto pore surfaces. How MOFs are formed, how they interact with their guest molecules, and other fundamental questions might be answered from viewing even the more classically rigid SBUs as dynamic and potentially coordinatively unsaturated molecular entities.

3.6 Methods

3.6.1 Materials

Dry, deaerated CH_2Cl_2 (HPLC grade, Honeywell) and *N*,*N*-dimethylformamide (DMF, 99.8%, VWR) were obtained by degassing with a flow of argon gas for 30 min and by passing the solvent through two silica columns in a Glass Contour Solvent System. 70% HNO_3 (ICP-AES grade, EMD), zinc nitrate hexahydrate (99%, Alfa Aesar), ^{67}Zn metal (97% enriched, Trace Sciences International), and terephthalic acid (Sigma-Aldrich) were used without further modification. Natural abundance MOF-5 was prepared according to literature.[72]

3.6.2 Experimental Conditions for Solid-state Nuclear Magnetic Resonance

High-field ^{67}Zn nuclear magnetic resonance (NMR) spectra were acquired using a Bruker Avance III 500 (11.7 T) equipped with a 4 mm magic-angle spinning (MAS) single resonance low-gamma Bruker probe using a quadrupolar echo experiment.[128] Pulses were calibrated using a 2 M aqueous solution of $Zn(NO_3)_2$ (2.3 μs, $\pi/2$ pulses, $\omega_1/2\pi$ = 36 kHz), an echo delay of 60 μs, an optimized recycle delay of 1 seconds, and 512,000 co-added transients. The frequency axis is referenced to 0 ppm using 1 M solution of $Zn(NO_3)_2$.[129]

Ultrahigh field ^{67}Zn NMR spectra were acquired using a Bruker Avance II 900 (21.1 T) spectrometer. Spectra were acquired using various probes including a 4 mm MAS double resonance (H/X), a home-built single resonance solenoid 5-mm low-gamma non-spinning, a 7-mm MAS double resonance (H/X), and a 7-mm solenoid-coil single resonance non-spinning probes. Spectra were acquired using either the Bloch decay,[130] the quadrupole echo,[128] or the CPMG16 (Quadrupolar CPMG) pulse sequence. Pulses were calibrated using a 1-M aqueous solution of $Zn(NO_3)_2$ for the 4-mm (3 μ s, $\pi/2$ pulses, $\omega_1/2\pi$ = 28 kHz), the 5-mm (2 μs, $\pi/2$ pulses, $\omega_1/2\pi$ = 42 kHz), and the 7-mm probes (5 μs, $\pi/2$ pulses, $\omega_1/2\pi$ = 17 kHz (H/X) and 3 μs, $\pi/2$ pulses, $\omega_1/2\pi$ = 28 kHz (X)). Experiments were acquired using either a 0.5- or 1-s recycle delay, between 8,192 and 128,000 co-added transients, and an echo delay between 60 and 100 μs. MAS NMR spectra were acquired using a spinning frequency between 5 and 10 kHz. The frequency axis is referenced to 0 ppm using 1-M solution of $Zn(NO_3)_2$.[129] Spectral parameters were simulated using the WSOLIDS software package.[131]

^{13}C MAS NMR data were acquired using a home-built 500 MHz (11.7 T) spectrometer (courtesy of Dr. D. Ruben, FBML-MIT) equipped with a Magnex superconducting magnet. Spectra were acquired using a 4-mm MAS Chemagnetics triple resonance (H/C/N) probe. Variable temperature ^{13}C MAS NMR data were acquired using Bloch,[130] cross polarization (CP),[132] and refocused-INEPT[133] experiments. A

1.5-ms contact time was used for the CP experiment, and all experiments were collected with high-power ($\omega_1/2\pi$ = 100 kHz) TPPM[134] ^{1}H decoupling during acquisition. Spectra were acquired using 3 to 20 s recycle delays, between 8,192 and 32,768 co-added transients, temperatures between 273 and 308 K, and a spinning frequency, $\omega r/2\pi$ = 8,000 (2) Hz. The ^{13}C chemical shift axis was referenced to 40.[135] ppm using solid adamantane with respect to DSS (4,4-dimethyl-4-silapentane-1-sulfonic acid, 0 ppm.

Non-spinning ^{2}H NMR experiments were acquired on a custom-built 400 MHz spectrometer (courtesy of Dr. D. Ruben, FBML-MIT) using a custom-built single channel trans-mission line probe equipped with cryogenic temperature capabilities. All ^{2}H NMR spectra were obtained using the quadrupolar echo sequence[136] with 8-step phase cycling4[137] using a $\pi/2$ pulse of 2.0 μs and a delay of 30 μs between the two pulses. The recycle delay was 30 s for all experiments and the number of co-added transients was between 4,000 and 20,000 depending on the signal-to-noise.

3.6.3 Born-Oppenheimer Molecular Dynamics

A rhombohedral cell was used to model the MOF-5 lattice, consisting of two rotated $Zn_4(\mu_4\text{-O})(\mu\text{-BDC})_3$ units. This corresponds to 25% of the cubic crystallographic cell, $[Zn_4(\mu_4\text{-O})(\mu\text{-BDC})_3]_8$ and has been successfully employed in previous studies.[135]

Static calculations (optimization) were performed using density functional theory (DFT) as implemented in the Vienna Ab Initio Simulation Package (VASP) plane wave code, version 5.2.[138,139] We employed the Perdew-Burke-Ernzerhof (PBE) exchange-correlation functional[140] that was shown to reproduce binding energies well,[141,142] with dispersion corrections added via the Grimme DFT-D2 semi-empirical approach.[143] Inner electrons were replaced by all-electron frozen cores (projector augmented wave) PAW method,[144,145] whereas monoelectronic valence electrons were expanded in plane waves with a kinetic cut-off energy of 350 eV. The threshold for the geometry optimizations was set to 0.015 eV/Å. All the calculations were performed at the Γ point.

This cell was then employed in a first-principles Molecular Dynamics calculation,

since it is the only method capable of describing the electronic structure and the dynamics simultaneously. In particular, we used Born-Oppenheimer Molecular Dynamics (BOMD) to investigate the dynamics of the cage in the presence of DMF, with a liquid phase density. For the BOMD, the convergence criterion in the electronic density of each minimization was set to 10^{-7} eV. This setup minimizes the energy drift of the extended system including ions, electrons, and the thermostat, for an average value smaller than 0.003 eV/ps per unit cell. The runs were performed in the NVT canonical ensemble; the temperature was controlled using a Nosé thermostat, mass parameter 0.01 a.m.u, and set to 300 K. Each equilibration step was performed over 1 ps, whereas each production run was 24 ps long with a time step of 1 fs.

To address the issue of DMF coordination to the metal centers in the MOF-5 structure we employed a continuous coordination number, c. We define two atoms being bonded, $c = 1$, when their distance is smaller or equal to the sum of the ionic radii of the cation and anion. The coordination is then calculated through a Gaussian function that follows the harmonic potential between the two atoms and set to zero for distances longer than the sum of the radii plus 0.9 Å (i.e., longer than the van der Waals corresponding distances). The values rounded to the closest integer were then plotted in Figure 3-7.

3.6.4 Preparation of ^{67}Zn-enriched $Zn(NO_3)_2{\cdot}xH_2O$

^{67}Zn metal flakes (0.100 g, 1.5 mmol) were suspended in 1 mL of deionized water in a glass vial and placed in a −20 °C fridge for 15 min. This vial was then held in an ice bath and 1.00 mL of 70% aqueous HNO_3 that was cooled to −20 °C was added dropwise in two portions. After adding 600 μL the reaction suspension and remaining HNO_3 was placed back into the freezer. After 20 min, the remaining acid was added dropwise. The solution was then kept at 10^{-6} torr on a Schlenk line overnight and 370 mg of white powder was recovered and used without further purification for the synthesis of enriched MOF-5.

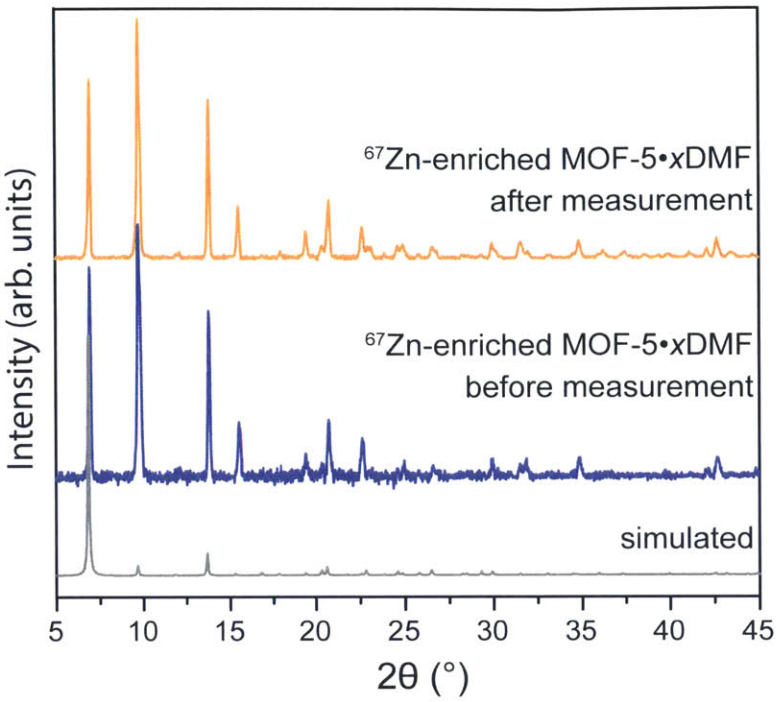

Figure 3-9: Powder X-ray diffraction pattern of the ^{67}Zn-enriched DMF-solvated MOF-5 sample that was used for ^{67}Zn NMR experiments before (middle) and after (top) measurements compared to the simulated pattern of evacuated MOF-5 (bottom). Note that discrepancies in peak intensities are due to the sample being solvated.

3.6.5 Preparation of ^{67}Zn-enriched MOF-5

This preparation followed the procedure reported for natural-abundance MOF-5.[72] The white powder described above was dissolved in 41 mL of anhydrous DMF and 500 μL of deionized water in a 100 mL Teflon-capped glass jar. Terephthalic acid (69 mg, 0.42 mmol) was added and sonicated until completely dissolved and two glass slides were added to increase the surface area available for crystallization. After heating at 100 °C for 7 h, cubic crystals were collected by gravity filtration in an N_2-filled bench-top glovebox. These were washed in fresh DMF for 8 h, repeated six times, and soaked in CH_2Cl_2 following directions as indicated for natural abundance MOF-5.1 The phase purity of this material, partially solvated by DMF and CH_2Cl_2, was confirmed by PXRD (Figure 3-9).

3.6.6 Sample Preparation for Nuclear Magnetic Resonance

Zn-MOF samples were prepared as described above using natural abundant ^{67}Zn (4.1 %) for MOF solvated with DMF or desolvated without DMF. Enriched solvated Zn-MOF sample was prepared using 97 % enriched ^{67}Zn. Samples were packed in a glovebox under dry Ar or N_2 gas into zirconia (ZrO_2) magic angle spinning (MAS) rotors with outer diameters of either 4 mm or 7 mm (100 or 400 μl, respectively). The enriched sample was sealed using epoxy to inhibit any reaction with the atmosphere. For the solvated sample, desolvated Zn-MOF was packed into ZrO_2 rotors and solvated in situ using $>$ 99 % dry DMF.

3.6.7 Solid-state Nuclear Magnetic Resonance Analysis of Activated MOF-5

Natural abundant non-solvated MOF-5 was analyzed using solid-state NMR under spinning and non-spinning conditions to characterize its structure and NMR properties at 21.1 T. Under MAS the chemical shift anisotropy (CSA) and dipolar coupling interactions are attenuated leaving only the residual second-order quadrupolar broadening of the central transition, which is the dominant interaction for ^{67}Zn, being solely responsible for the observed linewidth and shape. The spectrum represented within 3a was simulated (inset) with the following parameters: isotropic chemical shift (δ_{iso}) = 158 ppm, quadrupolar coupling constant (C_Q) = 1.65 MHz, and asymmetry parameter (η) = 0.

Under non-spinning condition all the anisotropic interactions are present. Figure 3-3b and 3c are the non-spinning spectra without and with ^1H decoupling, respectively. In Figure 3-3c, the "horns" of the spectrum are narrowed compared to Figure 3-3b, denoting the effect of the ^1H radio frequency field that decouples the ^1H dipolar interaction. The observed CSA is significant, leading to the characteristic shape with the span (Ω) = 87 ppm and skew (κ) = 1. The near tetrahedral symmetry of the Zn-MOF, combined with the reduction of the second-order quadrupolar broadening at ultrahigh magnetic fields, creates a unique circumstance whereby the breadth of the

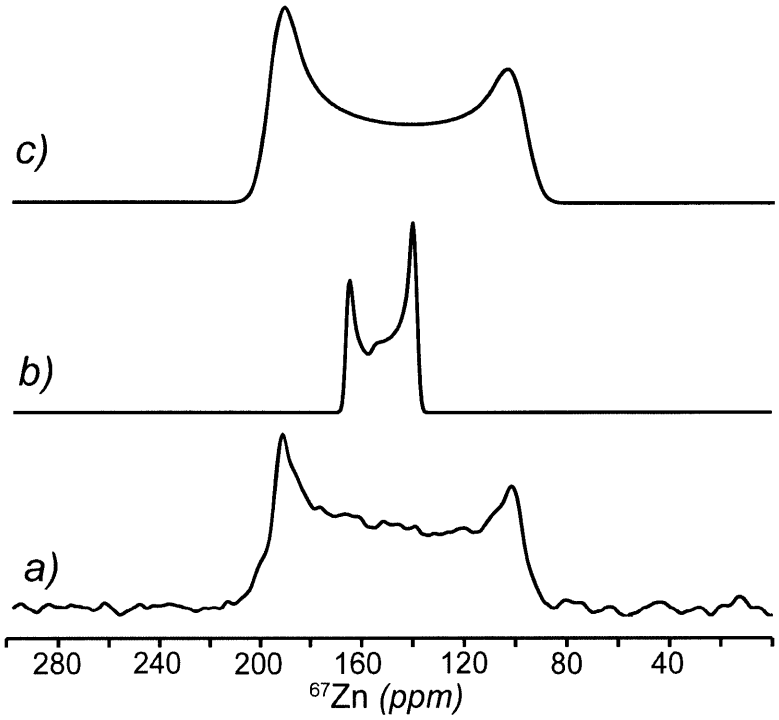

Figure 3-10: ^{67}Zn NMR spectrum of natural abundance desolvated Zn-MOF acquired at 21.1 T (900 MHz, ^{1}H), (a) the experimental spectrum under non-spinning conditions, (b) the corresponding quadrupolar simulation (C_Q = 1.65 MHz and η = 0, determined from MAS NMR) under non-spinning conditions (with no consideration of CSA), and (c) the complete simulation incorporating both the chemical shift anisotropy and quadrupolar coupling.

lineshape begins to be dominated by the CSA rather than by the quadrupolar interaction. This is more clearly shown in Figure 3-10 where the non-spinning experimental spectrum (Fig. 3-10a) cannot be simulated solely using the quadrupolar coupling parameters determined from the MAS experiment (Fig. 3-10b). A CSA interaction of considerable magnitude is required to provide excellent agreement between the simulation and experimental data (Fig. 3-10c).

3.6.8 Solid-state Nuclear Magnetic Resonance Analysis of DMF-Solvated ^{67}Zn Enriched MOF-5

The non-spinning spectrum of the evacuated MOF-5 spectra revealed that the powdered lineshape was affected by dipolar, chemical shift anisotropy (CSA), and quadrupo-

lar interactions. Magic-angle spinning (MAS) NMR was acquired to attenuate the first two interactions and partially reduce the second-order quadrupolar broadening of the central transition (Figure 3-4B). Surprisingly, the linewidth of the resulting spectrum was nearly identical to the spectrum under non-spinning conditions, while the "horns" attributed to the solvated site disappeared (Figure 3-4B). This result indicates that the linewidth of the unsolvated site is no longer dominated by quadrupolar broadening at ultrahigh magnetic fields, while the FWHM of the linewidth of the solvated site reduces from 21 kHz to an expected value of ~6 kHz, thereby obscuring it by the main resonance of the unsolvated site (~14 kHz). This contraction indicates the solvated site is still the dominated by quadrupolar broadening, although disorder could also impact its signal.

3.6.9 Other Physical Measurements

TGA was performed on a TA Instruments Q500 Thermogravimetric Analyzer at a heating rate of 0.5 °C/min under a nitrogen gas flow of 90 mL/min. Fourier-transform infrared spectroscopic measurements were performed in a N_2-filled glovebox using a Bruker Alfa spectrometer. The data was averaged over 32 scans at 4 cm^{-1} resolution between $8000 - 500$ cm^{-1}. Mass spectrometry was conducted in multi-ion detection mode using a Hiden Analytical HPR20 QIC benchtop gas analysis system. The exhaust gas from a TGA measurement of DMF-soaked natural abundance MOF-5 was sampled in situ using the N_2 flow as a carrier gas. The TGA was connected to the QIC capillary inlet using standard Swagelok fittings, with the capillary held at 160 °C and 3 mbar.

3.6.10 Sample Preparation for Calorimetry Studies

25 mg of fully evacuated MOF-5 was suspended in 5 mL of DMF and left for at least 12 h. The DMF was replaced by 20 mL of CH_2Cl_2, left for 8 h, then replaced two more times. These crystals were placed under reduced pressure at room temperature for several hours with no additional heating.

Chapter 4

Extending Co^{2+} Exchange in MOF-5 by Sidestepping Lattice Strain

4.1 Abstract

This chapter demonstrates that the extent of Co^{2+} exchange into MOF-5 is inherently limited, but can be extended by employing Co^{2+} species that makes the thermodynamics of the process more favorable. UV-Vis-NIR and ICP-AES analysis indicates that Co^{2+} inserts only once into each metal node of MOF-5, when starting from O_h species, but inserts multiple times when the species is T_d. Density functional theory (DFT) suggests the latter enhances the thermodynamics of replacing the four-coordinate Zn^{2+} sites of MOF-5, thus allowing Co^{2+} to substitute more than the six-coordinate site. These results explain why the exchange of other cations into MOF-5 does not go to completion. More generally, they demonstrate the importance of the intrinsic properties of the MOF and the identity of the inserting metal species in cation exchange, and that the process can be explained and manipulated.

4.2 Introduction

Little is understood about critical aspects of cation exchange, such as which metal sites undergo exchange, why certain ions replace others, and what dictates the extent

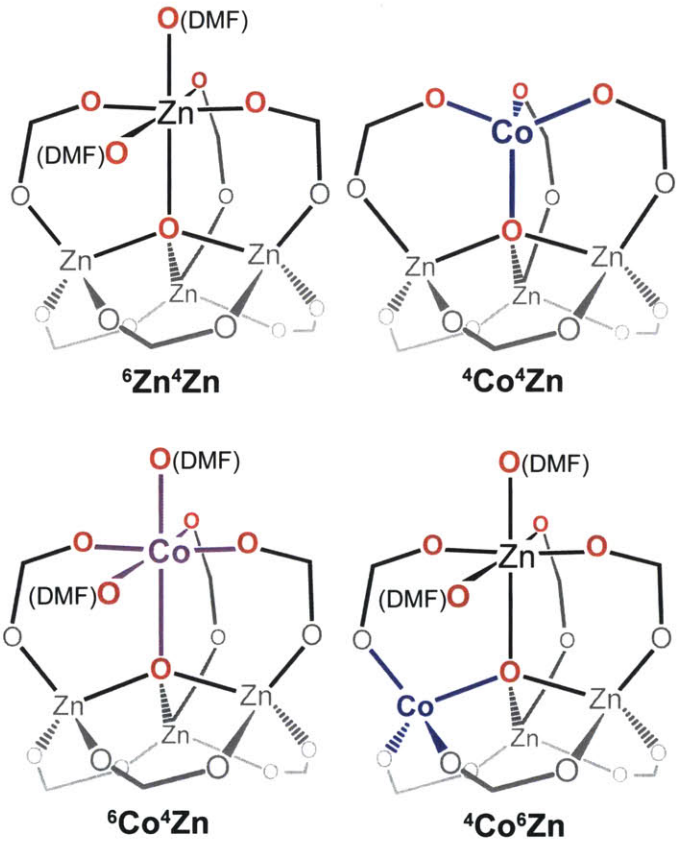

Figure 4-1: MOF-5 clusters relevant to Co^{2+}-exchange with the corresponding nomenclature.

of exchange. We sought to answer this third question, since cation exchange does not go to completion in many systems,[3,18,24,26,31,33,34,38,42] including what we describe in Chapters 2, 7, and 8, where only one Zn^{2+} per Zn_4O cluster is replaced by V^{2+}, Cr^{2+}, Mn^{2+}, Fe^{2+}, or Ni^{2+}.[17,99] We propose that this limit is related to our finding in the preceding chapter that MOF-5 accommodates up to one six-coordinate Zn^{2+} per cluster, to furnish clusters labeled $^6Zn^4Co$ in Figure 4-1. Perhaps metal species only insert once if the thermodynamics favor six-coordinate but not four-coordinate geometry. On the other hand, species that can adopt a pseudo-tetrahedral configuration might replace the remaining three Zn^{2+} sites. We report our ability to circumvent this barrier by employing anhydrous $CoCl_2$ since it is known to exist as both four-coordinate and six-coordinate in DMF. These results illustrate that MOFs can pose energetic barriers to cation exchange, which can be sidestepped by appropriate synthetic conditions.

4.3 Results and Discussion

We hypothesized that tetrahedral metal species would be more thermodynamically favored to exchange into both the six- and four-coordinate metal sites of MOF-5 since octahedral metal species were used to synthesize the previous variants of MOF-5 and never exchanged more than one cation per cluster. We suspended crystals of MOF-5 in 0.1 M solutions of anhydrous $CoCl_2$ in dry DMF at room temperature, knowing that anhydrous $CoCl_2$ exists in several equilibria, as shown in 4.1–4.3.[146,147] Although Co^{2+} was not known to exchange into MOF-5, previous reports of Co^{2+} analogues synthesized through solvothermal routes suggested it would be possible.[63] To monitor the Co^{2+} incorporation with time, we repeated this soak for 1 min, 30 min, 1 h, 1 day, 1 week, and 1 month under otherwise identical conditions. For comparison, we suspended MOF-5 crystals in 0.1 M DMF solutions of $Ni(NO_3)_2{\cdot}xH_2O$ or $Co(NO_3)_2{\cdot}xH_2O$ for similar time periods.

$$2CoCl_2 + DMF \rightleftharpoons [CoCl_4]^{2-} + [Co(DMF)_6]^{2+} \tag{4.1}$$

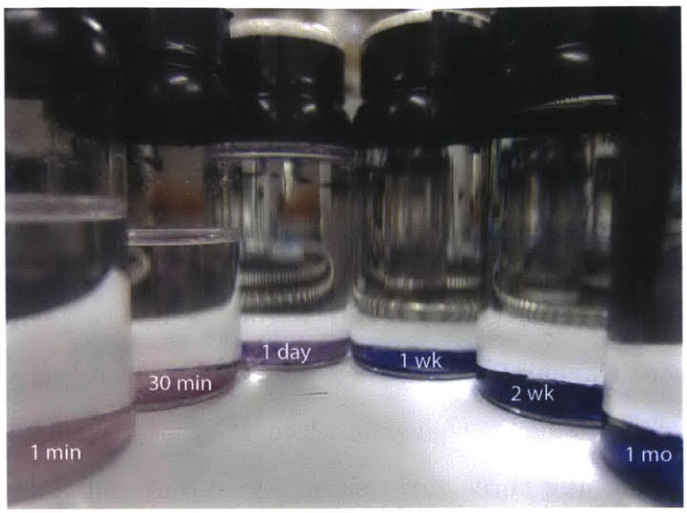

Figure 4-2: Optical photographs of Co-MOF-5 after different periods of cation exchange.

$$[CoCl_4]^{2-} + DMF \rightleftharpoons [CoCl_3(DMF)]^- + Cl^- \tag{4.2}$$

$$[Co(DMF)_6]^{2+} + Cl^- \rightleftharpoons [Co(DMF)_5(Cl)]^- + DMF \tag{4.3}$$

After isolating and washing the crystals, they displayed a striking color progression that suggested Co^{2+} inserted with octahedral geometry at first, but incorporated more tetrahedral Co^{2+} with time. As shown in Figure 4-2, MOF-5 soaked for 1 min and 30 min appear pink, but materials soaked for at least 1 day appear more blue. Diffuse reflectance UV-vis spectra of these materials support this observation, with the 1 min spectrum depicting a profile indicative of Co^{2+} in O_h symmetry (Figure 4-3). With increasing soaking times, the spectra are more characteristic of T_d Co^{2+}. These data are consistent with Co^{2+} first inserting into the available six-coordinate metal site of the MOF-5 SBU to furnish a cluster akin to $^6Co^4Zn$, in Figure 4-1, then exchanging further to give sites with pseudo-T_d symmetry.

Quantifying the Co^{2+} incorporation with inductively coupled plasma atomic emission spectroscopy (ICP-AES) indicates that, indeed, using anhydrous $CoCl_2$ breaks the previous barrier of one cation per cluster in MOF-5. As shown in Figure 4-4, one

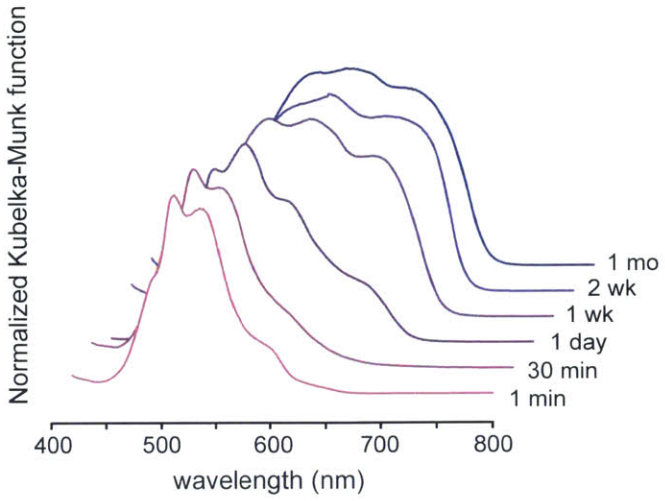

Figure 4-3: Diffuse reflectance visible spectra of MOF-5 after soaking in $CoCl_2$-DMF solutions for specified lengths of time, with normalized intensities.

Co^{2+} incorporates in each cluster after one day and nearly three after one month. From this plot, substituting the first metal appears to occur faster than substituting the subsequent sites. As expected, ICP-AES analysis of the materials soaked in $Ni(NO_3)_2{\cdot}xH_2O$ and $Co(NO_3)_2{\cdot}xH_2O$ confirms that these O_h metal species permit the substitution of up to just one Zn^{2+} per cluster, on average (Figures 4-5 and 4-6). Inspecting these ICP-AES results reveals that anhydrous $CoCl_2$ not only facilitates more Co^{2+} substitution, but inserting the first cation into each cluster occurs faster.

We investigated why anhydrous $CoCl_2$ improved the cation-exchange process by comparing calculated Gibbs free enthalpies of formation (ΔG_f) using density functional theory. Rather than consider the entire lattice, we employed truncated model compounds based on the clusters in Figure 4-1 with benzoates in place of 1,4-p-terephthalates. Since the solvated $Co(NO_3)_2$ and $CoCl_2$ are known to exist as several species in equilibrium, we simplified the calculations by modeling them as O_h $Co(DMF)_6{}^{2+}$ and T_d $Co(DMF)_4{}^{2+}$. Using the reaction equations shown below, we calculated ΔG_{rxn} of Co^{2+} exchanging into MOF-5 from either O_h or T_d species, assuming the MOF-5 clusters to begin as $^6Zn^4Co$.

As summarized in Table 4.1, these calculations conclude that cation exchange is thermodynamically favored for the T_d over O_h species for each of the possible

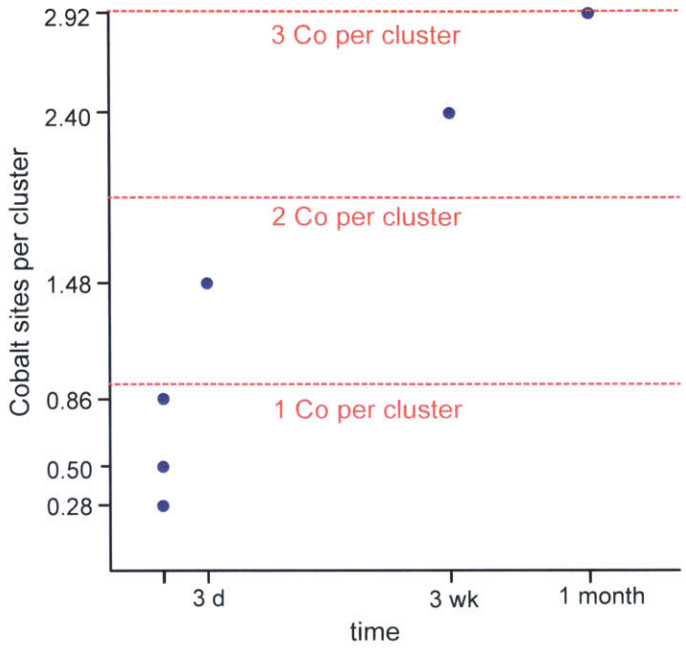

Figure 4-4: Amount of Co^{2+}-exchanged into each MOF-5 cluster as determined from ICP-AES analysis when using $CoCl_2$.

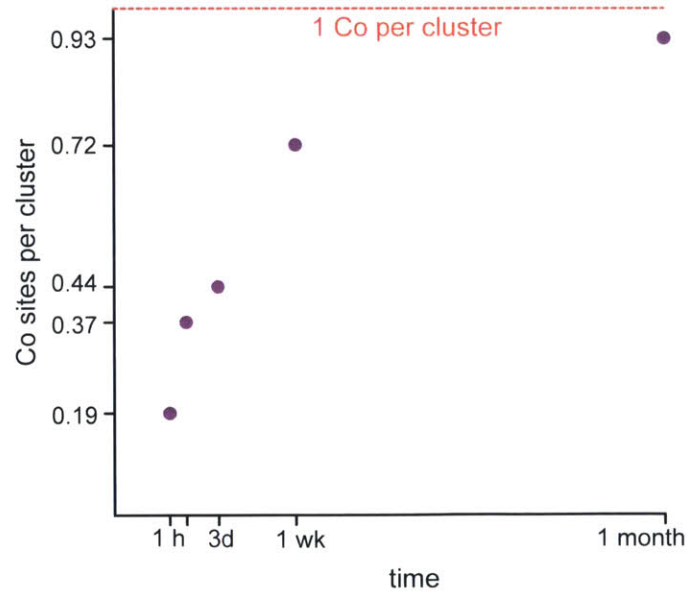

Figure 4-5: Amount of Co^{2+}-exchanged into each MOF-5 cluster as determined from ICP-AES analysis when using $Co(NO_3)_2 \cdot xH_2O$.

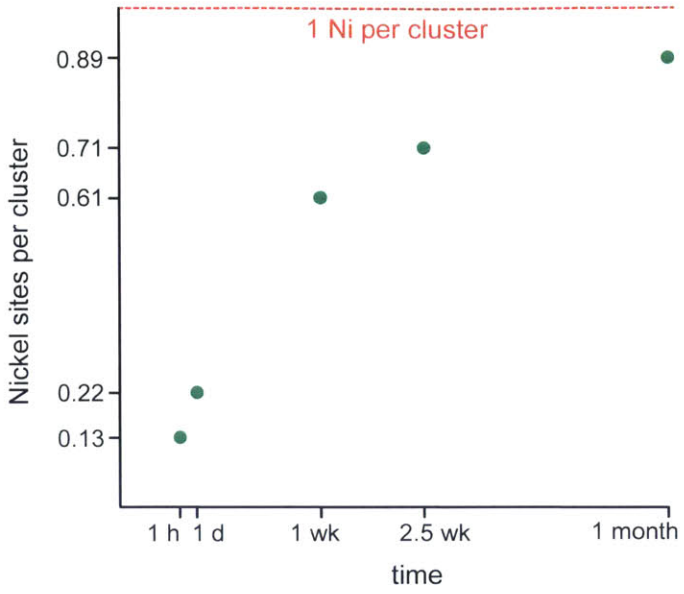

Figure 4-6: Amount of Ni^{2+}-exchanged into each MOF-5 cluster as determined from ICP-AES analysis when using $Ni(NO_3)_2 \cdot xH_2O$.

	$^6Co^4Zn$	$^4Co^4Zn$	$^6Zn^4Co$
$Co(DMF)_6{}^{2+}$	−1.369186445	56.46149631	−0.618554806
$Co(DMF)_4{}^{2+}$	−10.8810589	46.94962386	−10.13042726

Table 4.1: Simulated ΔG_{rxn}, in kcal/mol, of various Co-MOF-5 clusters (columns) starting from $Co(DMF)_6{}^{2+}$ (top row) or $Co(DMF)_4{}^{2+}$ (bottom row) and $^6Zn^4Zn$.

products, $^6Co^4Zn$, $^4Co^4Zn$, or $^4Co^6Zn$. When starting from O_h $Co(DMF)_6{}^{2+}$, ΔG_{run} is nearly thermoneutral in producing $^6Co^4Zn$ and $^4Co^6Zn$, yet K_{eq} for these species is $\sim 10^7$ when starting from T_d $Co(DMF)_4{}^{2+}$. In either case, $^6Co^4Zn$ is most favorable, which is consistent with our observation with Co^{2+} inserting first in the six-coordinate site. Synthesizing $^4Co^4Zn$, on the other hand, is highly disfavored, for both O_h or T_d species, with K_{eq} at $\sim 10^{-42}$ and $\sim 10^{-35}$. This result is also consistent with our observation that the SBUs always contain at least one metal site with coordinated DMF molecules.

More revealing is that the calculated formation enthalpy for $^4Co^6Zn$ is nearly the same as for $^6Co^4Zn$, yet our experimental evidence also detects a pseudo-O_h Co^{2+} in Co-MOF-5. To reconcile the evidence with these calculations, we propose that Co^{2+}

inserts first into the six-coordinate site of MOF-5, but the lattice imposes a kinetic barrier to additional six-coordinate sites in each cluster. The DMF molecules on Co might transfer to Zn, causing the O_h Co^{2+} to adopt T_d geometry, but that K_{eq} for this process is small when starting from O_h $Co(DMF)_6{}^{2+}$ and larger when starting from T_d $Co(DMF)_4{}^{2+}$. It is important to note that these calculations do not explore possible mechanisms and intermediate species. For example, the compounds in a $CoCl_2$-DMF solution might exchange directly into the four-coordinate sites of MOF-5, or might only replace Zn sites with pendant DMF molecules.

4.4 Conclusion

In conclusion, the extent of Co^{2+} exchange into MOF-5 is limited by lattice strain and depends on the identity of the inserting metal species. This barrier can be circumvented by choosing a species that enhances the thermodynamics of the process and can be rationalized by theory. Although the Co^{2+} analogue of MOF-5 is already known,[73] this technique could be employed to stabilize unprecedented variants. These results are specific to Co-MOF-5, but could be applied to cation exchange in other MOFs and, perhaps, other classes of materials. The identity of the inserting cation is typically overlooked as a critical aspect of the exchange process, yet thermodynamic calculations could screen for appropriate metal species that enable precise control over the composition of new materials.

4.5 Methods

All synthetic manipulations were performed under an inert atmosphere of a N_2 glove box, unless stated otherwise.

Materials. Dichloromethane (HPLC grade, Honeywell), *N*,*N*-dimethylformamide (DMF) (99.8%, VWR), $Co(NO_3)_2{\cdot}6H_2O$ (99.9%, Strem), $Ni(NO_3)_2{\cdot}6H_2O$ (99.9%, Strem), $CoCl_2{\cdot}6H_2O$ (98%, Strem) and $Zn(NO_3)_2{\cdot}6H_2O$ (99%, Alfa Aesar) were used as received. Dry, deaerated DMF was obtained by degassing with a flow of argon gas

for 30 min and by passing the solvent through two silica columns in a Glass Contour Solvent System. Anhydrous $CoCl_2$ was obtained by heating the hydrate salt at 100 °C under reduced pressure on a Schlenk line.

4.5.1 Physical Measurements

Powder X-ray diffraction (PXRD) patterns were recorded on a Bruker Advance II diffractometer equipped with $\theta/2\theta$ Bragg-Brentano geometry and Ni-filtered Cu-K_α radiation ($K_{\alpha 1}$ = 1.5406 Å). The tube voltage and current were 40 kV and 40 mA, respectively. Samples for PXRD were prepared by placing a thin layer of samples on a zero-background silicon crystal plate supported on a cup with dome that screwed-on with a rubber O-ring fitting. Diffuse reflectance UV-Vis spectra were collected between on a Varian Cary 5000 UV-Vis-NIR spectrometer equipped with a Praying Mantis diffuse reflectance accessory and an environmental chamber (Harrick Scientific Products) and referenced to $BaSO_4$. Cobalt, nickel, and zinc analyses were conducted at the MIT Center for Materials Science and Engineering Shared Experimental Facility (CSME-SEF) using a HORIBA Jobin ACTIVA inductively coupled plasma atomic emission spectrometer (ICP-AES). Standards were prepared from solutions purchased from ULTRA Scientific©, designated suitable for ICP analysis.

4.5.2 $Zn_{4-x}M_{4-x}O(C_8H_4O_4)_3$ (M = Ni or Co).

$M(NO_3)_2{\cdot}6H_2O$ where M = Co or Ni, (0.30 mmol) or $CoCl_2$ were dissolved in 10 mL of dry, deaerated DMF and added at room temperature to $Zn_4O_{13}C_{24}H_{12}$ (MOF-5) (50 mg, 6.5×10^{-2} mmol) that was washed once with 20 mL of DMF for 24 h. These suspensions were stirred gently for 1 week before replacing the solution with fresh DMF.[72]

4.5.3 Calculations

The ORCA 3.0.3 software package[148] was used for all computations. The all-electron Gaussian basis sets developed by the Ahlrichs group were employed in all calculations

with the basis sets TZV(p) (for H), TZV(2d) (for C, N, and O), and TZV(2pf) (for Zn and Fe).[93,94] Calculations were done using the resolution of the identity (RI) using the Becke-Perdew (BP) functional.[90,91] All structures containing Co were calculated with quartet spin multiplicity at the spin unrestricted level. Geometry optimizations of the truncated model compounds began from the crystallographically determined structure of MOF-5, where all atomic positions were optimized, with the 1 and 4 carbons atoms on each benzoate fixed in place. The optimized geometries were then used for calculating thermodynamic properties, which were performed using numerical differentiation of analytic gradients with an increment of 0.005 bohr. Because no negative frequencies were observed, the structures appeared to reside in potential energy minima.

The energies reported in Table 4.1 were calculated from balanced reactions using the Gibbs free enthalpies (ΔG_f) calculated for each species. For an example, the formation enthalpy of $^6Co^4Co$ from $Co(DMF)_4{}^{2+}$ was calculated as:

$$\begin{aligned}\Delta G_{rxn}(^6Co^4Zn) =& \left[\Delta G_f(^6Co^4Zn) + \Delta G_f(Zn(DMF)_6{}^{2+})\right] - \\ & \left[\Delta G_f(^6Zn^4Zn) + \Delta G_f(Co(DMF)_4{}^{2+}) + 2 \times \Delta G_f(DMF)\right] \\ & = -10.8810589 \text{ kcal/mol}\end{aligned}$$

Similarly, the remaining equations are as follows:

$$\begin{aligned}\Delta G_{rxn}(^6Co^4Zn) =& \left[\Delta G_f(^6Co^4Co) + \Delta G_f(Zn(DMF)_6{}^{2+})\right] - \\ & \left[\Delta G_f(^6Zn^4Zn) + \Delta G_f(Co(DMF)_6{}^{2+})\right] \\ & = -1.369186445 \text{ kcal/mol}\end{aligned}$$

$$\begin{aligned}\Delta G_{rxn}(^4\mathrm{Co}^4\mathrm{Zn}) =& \left[\Delta G_f(^4\mathrm{Co}^4\mathrm{Zn}) + \Delta G_f(\mathrm{Zn(DMF)_6}^{2+})\right] - \\ & \left[\Delta G_f(^6\mathrm{Zn}^4\mathrm{Zn}) + \Delta G_f(\mathrm{Co(DMF)_4}^{2+}) + 2 \times \Delta G_f(\mathrm{DMF})\right] \\ & = 46.94962386 \text{ kcal/mol}\end{aligned}$$

$$\begin{aligned}\Delta G_{rxn}(^4\mathrm{Co}^4\mathrm{Zn}) =& \left[\Delta G_f(^4\mathrm{Co}^4\mathrm{Zn}) + \Delta G_f(\mathrm{Zn(DMF)_6}^{2+})\right] - \\ & \left[\Delta G_f(^6\mathrm{Zn}^4\mathrm{Zn}) + \Delta G_f(\mathrm{Co(DMF)_4}^{2+})\right] \\ & = 56.46149631 \text{ kcal/mol}\end{aligned}$$

$$\begin{aligned}\Delta G_{rxn}(^6\mathrm{Zn}^4\mathrm{Co}) =& \left[\Delta G_f(^6\mathrm{Zn}^4\mathrm{Co}) + \Delta G_f(\mathrm{Zn(DMF)_6}^{2+})\right] - \\ & \left[\Delta G_f(^6\mathrm{Zn}^4\mathrm{Zn}) + \Delta G_f(\mathrm{Co(DMF)_4}^{2+}) + 2 \times \Delta G_f(\mathrm{DMF})\right] \\ & = -10.13042726 \text{ kcal/mol}\end{aligned}$$

$$\begin{aligned}\Delta G_{rxn}(^6\mathrm{Zn}^4\mathrm{Co}) =& \left[\Delta G_f(^6\mathrm{Zn}^4\mathrm{Co}) + \Delta G_f(\mathrm{Zn(DMF)_6}^{2+})\right] - \\ & \left[\Delta G_f(^6\mathrm{Zn}^4\mathrm{Zn}) + \Delta G_f(\mathrm{Co(DMF)_6}^{2+})\right] \\ & = -0.618554806 \text{ kcal/mol}\end{aligned}$$

atom	x	y	z	atom	x	y	z
Co	–0.006197	0.004241	–0.002610	O	–1.161521	1.318540	0.891745
O	–0.840895	–0.515908	–1.704418	O	1.760955	0.815068	–0.297029
O	0.225760	–1.604772	1.103021	C	–1.625909	0.158259	–2.446341
C	–0.460502	–2.677341	1.102122	C	2.899935	0.246022	–0.316933
C	–0.829641	2.284319	1.652039	H	–2.023725	1.130500	–2.116426
H	–1.241685	–2.850766	0.345804	H	3.008322	–0.815849	–0.046661
H	0.227917	2.553394	1.799069	N	–2.029348	–0.239299	–3.642717
N	–0.297373	–3.655732	1.978648	N	4.024278	0.861564	–0.647011
N	–1.698778	3.035010	2.310268	C	–2.956637	0.575245	–4.437568
C	–1.585472	–1.506099	–4.233951	C	0.694351	–3.579638	3.056591
C	–1.106019	–4.878894	1.905986	C	4.053050	2.273949	–1.041582
C	5.309278	0.151980	–0.625844	C	–3.145054	2.803760	2.231605
C	–1.249526	4.150348	3.152334	H	–3.211824	1.490857	–3.892513
H	–2.487205	0.841038	–5.394160	H	–3.873620	0.004242	–4.636119
H	–1.113016	–1.306004	–5.205029	H	–2.453553	–2.160848	–4.391634
H	–0.869629	–1.989870	–3.564429	H	1.194342	–2.608205	3.024023
H	0.188460	–3.707424	4.023031	H	1.431038	–4.385503	2.934193
H	–1.669441	–5.004753	2.840229	H	–0.449821	–5.748258	1.764737
H	–1.806953	–4.814705	1.066259	H	3.033669	2.667963	–1.060366
H	4.662079	2.842222	–0.325147	H	4.506305	2.361625	–2.038118
H	5.758743	0.172823	–1.627678	H	5.991257	0.642415	0.081760
H	5.156945	–0.888775	–0.318930	H	–3.340225	1.922031	1.615774
H	–3.633666	3.684126	1.791893	H	–3.541846	2.648298	3.243823
H	–1.679515	5.090580	2.781679	H	–1.581874	3.988966	4.186571
H	–0.156211	4.219262	3.130009				

Table 4.2: Optimized atomic coordinates for $Co(DMF)_4{}^{2+}$

atom	x	y	z	atom	x	y	z
Co	0.000021	0.000012	0.000078	O	–0.269182	1.800983	1.090095
O	1.709297	–0.522630	1.139954	O	–1.709281	0.522628	–1.139939
O	0.269171	–1.801002	–1.090089	O	1.290701	1.067966	–1.299366
O	–1.290645	–1.067916	1.299468	C	–2.479064	–0.352767	–1.614661
C	–0.909859	–2.100423	1.910196	C	1.351165	–2.064554	–1.676333
C	2.479166	0.352753	1.614565	C	0.909818	2.100325	–1.910283
C	–1.351191	2.064563	1.676303	H	–2.268266	–1.426475	–1.480622
H	0.123771	–2.470358	1.809714	H	2.190764	–1.350191	–1.666341
H	2.268518	1.426463	1.480318	H	–0.123921	2.470032	–1.810077
H	–2.190806	1.350220	1.666286	N	–3.589044	–0.087501	–2.309691
N	–1.683904	–2.829547	2.719357	N	1.590239	–3.192133	–2.352461
N	3.589072	0.087461	2.309701	N	1.683870	2.829525	–2.719371
N	–1.590253	3.192152	2.352415	C	–4.421938	–1.163941	–2.847089
C	–4.018699	1.283450	–2.583004	C	–3.082316	–2.481543	2.968591
C	–1.159728	–4.008329	3.409962	C	0.586424	–4.249392	–2.468248
C	2.871040	–3.416368	–3.023549	C	4.422108	1.163881	2.846919
C	4.018529	–1.283500	2.583278	C	3.082417	2.481822	–2.968256
C	1.159610	4.008179	–3.410130	C	–0.586408	4.249380	2.468233
C	–2.871075	3.416440	3.023445	H	–3.995197	–2.135139	–2.571182
H	–5.441173	–1.091488	–2.442052	H	–4.472823	–1.092680	–3.942872
H	–5.036889	1.436722	–2.198507	H	–4.023168	1.466416	–3.667124
H	–3.329632	1.977070	–2.093023	H	–3.346562	–1.611533	2.360908
H	–3.728599	–3.330296	2.704167	H	–3.227541	–2.250007	4.033560
H	–1.735694	–4.900368	3.125924	H	–1.233465	–3.873675	4.498456
H	–0.108526	–4.159454	3.138689	H	–0.296654	–3.967155	–1.888140
H	0.309767	–4.390635	–3.522921	H	0.996934	–5.194175	–2.085003
H	3.354379	–4.319278	–2.624390	H	2.714684	–3.549175	–4.103499
H	3.529991	–2.555684	–2.860831	H	3.329270	–1.977116	2.093564
H	5.036636	–1.437050	2.198668	H	4.023124	–1.466198	3.667441
H	4.472952	1.092813	3.942717	H	5.441344	1.091202	2.441925
H	3.995515	2.135088	2.570820	H	0.108318	4.159103	–3.139092
H	1.735335	4.900345	–3.126000	H	1.233611	3.873500	–4.498603
H	3.346525	1.611503	–2.360958	H	3.228051	2.250902	–4.033300
H	3.728530	3.330487	–2.703119	H	0.296741	3.967043	1.888283
H	–0.309902	4.390717	3.522933	H	–0.996816	5.194143	2.084829
H	–2.714753	3.549287	4.103394	H	–3.354383	4.319344	2.624233
H	–3.530037	2.555762	2.860739				

Table 4.3: Optimized atomic coordinates for $Co(DMF)_6^{2+}$

atom	x	y	z	atom	x	y	z
Zn	0.00000899382508	0.00001820994158	0.00004101923480	O	−0.27728646790571	1.81132166290315	1.10317401375079
O	1.72085245634923	−0.51612194899738	1.15808988704342	O	−1.72084420776910	0.51613845036422	−1.15808535611756
O	0.27727673737685	−1.81131151133895	−1.10315921110092	O	1.28968607648770	1.07682494820781	−1.32145542773737
O	−1.28966137318385	−1.07679670653934	1.32149045140856	C	−2.47340956849818	−0.35310484109406	−1.66844697482158
C	−0.90493818806567	−2.09161875408000	1.95750077529435	C	1.33875241763723	−2.06132767379057	−1.73017029608051
C	2.47345285948147	0.35311429075089	1.66841517434547	C	0.90492005643076	2.09156786945057	−1.95756568386166
C	−1.33875029839400	2.06134388198978	1.73020490867268	H	−2.24789455173835	−1.42850756582715	−1.57550579248288
H	0.13718410212251	−2.44575029137328	1.89047372726509	H	2.16091118140787	−1.32787159800199	−1.77517410068422
H	2.24800608603257	1.42852346853187	1.57538882063325	H	−0.13724293706266	2.44560195256023	−1.89065171111637
H	−2.16090583250106	1.32788631966263	1.77523615625398	N	−3.58540763411583	−0.08044920494666	−2.35734186962592
N	−1.68548237660866	−2.82368016608904	2.75769307431740	N	1.57763557602979	−3.19867462412839	−2.38964772426735
N	3.58541074836527	0.08044087467411	2.35736578463804	N	1.68545802611082	2.82364481684530	−2.75775100143808
N	−1.57761835493908	3.19869864972684	2.38967176621287	C	−4.40112042207848	−1.14957721453175	−2.93396088091055
C	−4.03767539873432	1.29256443927873	−2.57822373725826	C	−3.09655807324749	−2.49993807768455	2.96407839989843
C	−1.15840661500460	−3.98462287561896	3.47555652283795	C	0.59798385765357	−4.28353014503556	−2.43440527098688
C	2.83448559855536	−3.40830064719452	−3.10890502952109	C	4.40118161459050	1.14956194532954	2.93391608157918
C	4.03759267298386	−1.29258371444456	2.57835675153995	C	3.09658263939446	2.50002959441441	−2.96399675078348
C	1.15833995173805	3.98451306898285	−3.47570338773189	C	−0.59796916435313	4.28355854455485	2.43438732345785
C	−2.83445859141311	3.40833988037083	3.10894236604401	H	−3.95726263629948	−2.12316174984382	−2.69591918450946
H	−5.42058451106417	−1.11022677802885	−2.52493072434448	H	−4.45537532285980	−1.03771941115710	−4.02614117453652
H	−5.05861751183599	1.41393702347643	−2.18963215977464	H	−4.04421425521730	1.51728711277131	−3.65443932715003
H	−3.36090859911248	1.97797924315335	−2.06024585147637	H	−3.36026597330827	−1.64250959981200	2.33846451756353
H	−3.71908158057369	−3.36390283258052	2.69194159059466	H	−3.27576840991646	−2.25908545500934	4.02174688817480
H	−1.70986871489023	−4.89046159316567	3.18655396246801	H	−1.26355910912682	−3.83937528021435	4.56005898089298
H	−0.09769944380387	−4.11900708297066	3.23394018041482	H	−0.26536833397210	−4.00893158840811	−1.82176803699605
H	0.27861534099942	−4.45876412001559	−3.47174635588852	H	1.04991803519052	−5.20745753728225	−2.04694341904167
H	3.35849523399067	−4.28702111774895	−2.70711952804607	H	2.63636508646851	−3.57441666138237	−4.17728105406863
H	3.47622862861809	−2.52669219490370	−2.99723318039366	H	3.36074427480832	−1.97800101714169	2.06048949627613
H	5.05850206984248	−1.41407291933934	2.18971418703573	H	4.04418083778761	−1.51719441330054	3.65459476735206
H	4.45540930272505	1.03778406646189	4.02610585255395	H	5.42065046237775	1.11011471646508	2.52490710489669
H	3.95739037545611	2.12315619767634	2.69579098572042	H	0.09760543047678	4.11882417044935	−3.23416623996004
H	1.70970893172372	4.89040971855595	−3.18670377222557	H	1.26358059367398	3.83922459240270	−4.56019172986097
H	3.36023669965447	1.64245651140945	−2.33855896983200	H	3.27595646026704	2.25945654810912	−4.02169967055066
H	3.71903199093840	3.36395145222091	−2.69154722468933	H	0.26539983576916	4.00892294040506	1.82179078995688
H	−0.27863172211151	4.45885597834857	3.47172695702672	H	−1.04989250891207	5.20746197286390	2.04685502592860
H	−2.63632163746861	3.57448045192255	4.17731124254277	H	−3.35847450558333	4.28705100401270	2.70714437193843
H	−3.47620241167157	2.52672834377667	2.99729990410599				

Table 4.4: Optimized atomic coordinates for $Zn(DMF)_6^{2+}$

atom	x	y	z	atom	x	y	z	atom	x	y	z
Zn	1.305061	0.423128	1.943378	Zn	1.908443	0.644289	−1.155818	Zn	−0.567640	2.104212	0.059896
Zn	−0.648359	−1.166145	−0.248919	O	0.490766	0.478142	0.172528	O	3.290558	0.504131	1.867504
O	3.659652	1.059197	−0.309450	O	0.878627	−1.157761	3.015236	O	−0.379244	−2.294461	1.491723
O	0.803264	1.986672	3.068921	O	−0.177633	3.366594	1.547408	C	8.220289	1.381758	1.719973
C	7.734351	1.570089	0.422359	C	6.376876	1.396962	0.153553	C	5.494264	1.034774	1.182387
C	5.986595	0.846975	2.482490	C	7.344890	1.019760	2.748912	C	4.031993	0.850636	0.890745
C	−0.016595	−5.508573	5.315035	C	−0.330815	−5.681089	3.963591	C	−0.259164	−4.597182	3.088172
C	0.142743	−3.335726	3.551039	C	0.475571	−3.174079	4.903438	C	0.385798	−4.253930	5.783006
C	0.216691	−2.168899	2.597195	C	0.233060	6.272649	5.599008	C	−0.301632	6.478778	4.323450
C	−0.279850	5.449313	3.382861	C	0.278343	4.204755	3.711725	C	0.813701	4.003021	4.992622
C	0.790203	5.033828	5.932072	C	0.304112	3.097652	2.696663	N	−3.427782	−4.519871	−0.384210
O	−2.042962	−2.787380	−0.968083	C	−2.617010	−3.473921	−0.105753	C	−4.074143	−5.274481	0.678844
C	−3.680293	−4.928917	−1.759150	N	−2.481151	0.312851	−3.947551	O	−1.083124	−0.256446	−2.226015
C	−2.221559	−0.173500	−2.718259	C	−1.404069	0.787069	−4.810205	C	−3.844873	0.423054	−4.442140
O	−2.437957	−0.432266	0.592160	O	−2.512112	1.804633	0.174825	O	1.640657	2.183223	−2.386904
O	−0.230265	3.189128	−1.560145	O	2.234462	−0.939439	−2.263179	O	0.816148	−2.312530	−1.127819
C	−7.144889	0.832314	1.791344	C	−6.517221	1.988109	1.316755	C	−5.179083	1.945885	0.923486
C	−4.458998	0.743995	0.994653	C	−5.094492	−0.410589	1.474143	C	−6.430344	−0.366924	1.873409
C	−3.014837	0.690186	0.559393	C	0.923094	6.019526	−5.519198	C	1.873146	4.994726	−5.464635
C	1.812951	4.039870	−4.449401	C	0.799260	4.102602	−3.481425	C	−0.150386	5.133993	−3.539976
C	−0.088039	6.088295	−4.555553	C	0.733794	3.074021	−2.385131	C	3.266851	−5.463561	−4.147405
C	2.240796	−5.636715	−3.213123	C	1.742678	−4.538077	−2.512849	C	2.266992	−3.257067	−2.739578
C	3.297477	−3.089524	−3.675966	C	3.794146	−4.188958	−4.377480	C	1.719457	−2.078369	−1.975839
H	9.282894	1.517171	1.930058	H	8.416619	1.852406	−0.381228	H	5.979580	1.538940	−0.851086
H	5.289597	0.565209	3.271354	H	7.723523	0.872379	3.761746	H	−0.077292	−6.354154	6.002654
H	−0.626884	−6.664402	3.593353	H	−0.489315	−4.714445	2.029103	H	0.800645	−2.192966	5.249042
H	0.635963	−4.119133	6.836698	H	0.216319	7.078849	6.334767	H	−0.735742	7.445421	4.062500
H	−0.690481	5.591279	2.383588	H	1.245076	3.031692	5.233356	H	1.208476	4.872674	6.927036
H	−2.484916	−3.275515	0.972180	H	−3.772397	−4.867166	1.651568	H	−3.781553	−6.335201	0.633885
H	−5.170341	−5.211723	0.591085	H	−4.748404	−4.819743	−2.004317	H	−3.394401	−5.982410	−1.900410
H	−3.082408	−4.295262	−2.422490	H	−3.120656	−0.507206	−2.168585	H	−1.433389	0.253746	−5.772230
H	−0.448031	0.597242	−4.312240	H	−1.511639	1.865740	−4.998106	H	−4.541130	0.036560	−3.687602
H	−3.967285	−0.155359	−5.371112	H	−4.097341	1.474567	−4.648890	H	−8.190124	0.867759	2.103971
H	−7.072110	2.926087	1.259174	H	−4.670473	2.838768	0.560759	H	−4.517710	−1.333006	1.536344
H	−6.916774	−1.266745	2.254244	H	0.973084	6.768178	−6.312012	H	2.664992	4.943341	−6.213773
H	2.547538	3.237268	−4.387069	H	−0.926774	5.174683	−2.776262	H	−0.826054	6.891316	−4.594240
H	3.658608	−6.323130	−4.694612	H	1.832134	−6.632172	−3.029772	H	0.945274	−4.647930	−1.778247
H	3.699559	−2.089772	−3.838682	H	4.597544	−4.053614	−5.103732				

Table 4.5: Optimized atomic coordinates for $(DMF)_2Zn_4O(C_7H_5O_2)_6$

atom	x	y	z	atom	x	y	z	atom	x	y	z
Zn	1.300064	0.418425	1.948019	Zn	1.899740	0.635604	−1.156742	Zn	−0.574205	2.093802	0.059947
Co	−0.658968	−1.181301	−0.252604	O	0.481227	0.456757	0.175476	O	3.288703	0.511295	1.869030
O	3.656909	1.051872	−0.310289	O	0.884545	−1.161406	3.019639	O	−0.382993	−2.278276	1.491950
O	0.805076	1.987917	3.070423	O	−0.178640	3.361071	1.546025	C	8.220289	1.381758	1.719973
C	7.735699	1.562262	0.420641	C	6.378208	1.389166	0.151382	C	5.494121	1.034702	1.181594
C	5.985008	0.854534	2.483380	C	7.343232	1.027392	2.750179	C	4.031993	0.850636	0.890745
C	−0.016595	−5.508573	5.315035	C	−0.351760	−5.677732	3.967839	C	−0.281059	−4.595336	3.090086
C	0.140168	−3.337818	3.546393	C	0.492401	−3.179562	4.894742	C	0.404515	−4.257766	5.776239
C	0.216691	−2.168899	2.597195	C	0.233060	6.272649	5.599008	C	−0.304238	6.478446	4.324336
C	−0.282599	5.449617	3.382825	C	0.278151	4.205872	3.710107	C	0.816215	4.004484	4.990057
C	0.792886	5.034578	5.930208	C	0.304112	3.097652	2.696663	N	−3.472412	−4.453409	−0.340090
O	−2.066100	−2.748792	−0.951533	C	−2.654379	−3.411070	−0.077468	C	−4.132834	−5.180258	0.734153
C	−3.721682	−4.887810	−1.708179	N	−2.345838	0.309139	−3.968701	O	−1.012090	−0.284934	−2.205168
C	−2.133926	−0.183090	−2.732815	C	−1.234428	0.765662	−4.796828	C	−3.691436	0.444816	−4.504870
O	−2.416090	−0.419826	0.621964	O	−2.518966	1.804181	0.156617	O	1.639709	2.181643	−2.387089
O	−0.229804	3.185669	−1.558703	O	2.238790	−0.940691	−2.267562	O	0.818207	−2.294507	−1.120142
C	−7.144889	0.832314	1.791344	C	−6.529806	1.974637	1.270105	C	−5.192758	1.930131	0.873475
C	−4.459970	0.738669	0.986366	C	−5.083441	−0.402974	1.510719	C	−6.418168	−0.356434	1.913937
C	−3.014837	0.690186	0.559393	C	0.923094	6.019526	−5.519198	C	1.876429	4.997937	−5.460879
C	1.816353	4.043596	−4.445120	C	0.799611	4.103619	−3.480012	C	−0.152981	5.132136	−3.541751
C	−0.090795	6.085737	−4.558129	C	0.733794	3.074021	−2.385131	C	3.266851	−5.463561	−4.147405
C	2.239654	−5.638308	−3.213877	C	1.738666	−4.541616	−2.511851	C	2.261131	−3.259465	−2.736365
C	3.292701	−3.090410	−3.672196	C	3.791898	−4.187722	−4.374889	C	1.719457	−2.078369	−1.975839
H	9.282841	1.517247	1.930218	H	8.419101	1.838532	−0.384090	H	5.982136	1.525168	−0.854592
H	5.286804	0.578654	3.273241	H	7.720470	0.885986	3.764385	H	−0.076155	−6.353555	6.003438
H	−0.663206	−6.658068	3.602262	H	−0.527331	−4.711910	2.034445	H	0.831938	−2.201608	5.235022
H	0.670972	−4.124457	6.826134	H	0.216159	7.078481	6.335150	H	−0.740522	7.444479	4.064757
H	−0.695596	5.591580	2.384483	H	1.249443	3.033673	5.229412	H	1.213253	4.873345	6.924272
H	−2.525105	−3.187906	0.995370	H	−3.831094	−4.758217	1.700455	H	−3.851798	−6.244652	0.710213
H	−5.227593	−5.106506	0.638789	H	−4.787418	−4.773016	−1.960549	H	−3.445653	−5.946741	−1.825766
H	−3.114219	−4.274103	−2.381368	H	−3.053931	−0.505110	−2.212123	H	−1.246312	0.236797	−5.761696
H	−0.296907	0.555407	−4.272496	H	−1.315224	1.846968	−4.983015	H	−4.417561	0.068205	−3.773881
H	−3.794795	−0.128389	−5.439383	H	−3.918973	1.501249	−4.715478	H	−8.188731	0.869724	2.108195
H	−7.093184	2.904974	1.179863	H	−4.693626	2.814179	0.477596	H	−4.497707	−1.316761	1.608073
H	−6.893919	−1.245721	2.331316	H	0.972698	6.767628	−6.312527	H	2.670730	4.948549	−6.207541
H	2.553387	3.243461	−4.380048	H	−0.931671	5.171014	−2.780258	H	−0.831342	6.886282	−4.599462
H	3.660074	−6.322287	−4.694742	H	1.832165	−6.634500	−3.031825	H	0.941086	−4.655769	−1.777850
H	3.693837	−2.090034	−3.832725	H	4.595992	−4.049394	−5.099828				

Table 4.6: Optimized atomic coordinates for $(DMF)_2CoZn_3O(C_7H_5O_2)_6$

atom	x	y	z	atom	x	y	z	atom	x	y	z
C	19.378500	24.450500	19.378500	C	20.239677	25.134317	20.237847	C	18.516552	25.134298	18.519894
Zn	20.504391	31.173572	20.507683	Zn	20.504155	33.429494	18.254723	Zn	18.250115	31.174489	18.255181
Co	18.250839	33.423708	20.507228	O	19.371058	32.308360	19.388378	O	20.186604	31.491665	22.399530
O	22.404954	31.490012	20.183211	O	20.185793	29.275464	20.182487	O	20.184672	33.102709	16.356659
O	22.404616	33.104097	18.572789	O	20.187716	35.324407	18.570676	O	18.573763	31.491286	16.356601
O	16.356936	31.490907	18.570847	O	18.573192	29.275808	18.572891	O	18.572745	33.101023	22.396070
O	16.363069	33.100676	20.183675	O	18.575417	35.308890	20.181390	C	19.378500	32.297500	22.969980
C	22.969980	32.297500	19.378500	C	19.378500	28.706020	19.378500	C	19.378500	32.297500	15.787020
C	19.378500	35.888980	19.378500	C	15.787020	32.297500	19.378500	C	19.386657	32.289721	24.454965
C	24.471958	32.298667	19.379258	C	19.377575	27.218762	19.379370	C	19.378012	32.298138	14.299768
C	19.374246	37.374972	19.382137	C	19.378500	32.297500	11.531500	C	19.378500	40.144500	19.378500
C	14.304238	32.292409	19.372912	C	11.531500	32.297500	19.378500	C	20.247009	31.431380	25.156519
C	25.178874	31.440822	20.236092	C	20.240144	26.524976	20.239263	C	20.239652	33.158915	13.605935
C	25.178530	33.157617	18.523254	C	20.238966	33.157605	12.215270	C	20.238188	39.458325	18.519920
C	18.516396	31.437265	13.606006	C	13.605330	31.431614	18.511829	C	18.515133	26.524964	18.519370
C	18.517592	31.437902	12.215348	C	12.214403	31.434499	18.515019	C	18.527212	33.147909	25.147354
C	13.612359	33.150553	20.231408	C	18.513211	38.070962	20.241913	C	18.516638	39.461844	20.238777
C	12.223960	33.141880	20.222890	C	19.388011	32.289950	27.241600	C	20.247351	31.431782	26.550202
C	18.534110	33.141880	26.533040	C	27.272743	32.300728	19.380769	C	26.573492	31.442839	20.235814
C	26.573149	33.157613	18.524997	C	20.237003	38.067815	18.520787	H	19.378992	23.358506	19.378015
H	20.905357	24.580906	20.901153	H	17.851236	24.580853	17.856249	H	19.378784	32.297171	10.439507
H	19.379579	41.236452	19.377777	H	10.439818	32.301330	19.382607	H	20.906233	30.773221	24.592434
H	24.619507	30.778766	20.895965	H	20.897966	27.093106	20.895229	H	20.896861	33.815541	14.174013
H	24.618901	33.818901	17.862832	H	20.903889	33.821632	11.661814	H	20.904227	40.009522	17.855103
H	17.859173	30.780719	14.174165	H	14.170723	30.773719	17.853641	H	17.857192	27.093087	17.863510
H	17.852865	30.773624	11.661955	H	11.660912	30.770056	17.850494	H	17.867025	33.806575	24.585461
H	14.173994	33.809909	20.891003	H	17.854588	37.505407	20.899505	H	17.852305	40.016751	20.902219
H	11.675683	33.809182	20.890483	H	19.381428	32.297197	28.332584	H	20.915693	30.765019	27.096614
H	17.866296	33.808821	27.081314	H	28.363898	32.301533	19.381356	H	27.118020	30.774066	20.903803
H	27.117413	33.827253	17.857661	H	20.893698	37.498255	17.865126				

Table 4.7: Optimized atomic coordinates for $CoZn_3O(C_7H_5O_2)_6$

atom	x	y	z	atom	x	y	z	atom	x	y	z
Zn	1.305040	0.416370	1.946470	Co	1.959174	0.726945	−1.152976	Zn	−0.563750	2.112054	0.029315
Zn	−0.578556	−1.172652	−0.288548	O	0.536813	0.494792	0.144903	O	3.295695	0.487258	1.898698
O	3.689553	1.064559	−0.266090	O	0.811978	−1.129546	3.046166	O	−0.289663	−2.316613	1.448796
O	0.806006	1.987389	3.068556	O	−0.176715	3.360509	1.544704	C	8.242747	1.286086	1.813921
C	7.774301	1.500725	0.513536	C	6.417290	1.355075	0.226183	C	5.516390	0.993391	1.239639
C	5.991041	0.779411	2.542794	C	7.348870	0.925104	2.827148	C	4.056354	0.836419	0.934763
C	−0.018009	−5.508420	5.315182	C	−0.329693	−5.683291	3.963071	C	−0.260490	−4.600900	3.084870
C	0.133670	−3.336680	3.546290	C	0.460910	−3.171580	4.900000	C	0.376200	−4.250290	5.781010
C	0.216690	−2.168900	2.597200	C	0.233060	6.272650	5.599010	C	−0.301927	6.479028	4.323424
C	−0.281086	5.449772	3.382329	C	0.276508	4.204937	3.710823	C	0.811832	4.002758	4.991805
C	0.789278	5.033281	5.931579	C	0.304110	3.097650	2.696660	N	−3.361260	−4.483540	−0.323940
O	−1.964264	−2.772291	−0.909298	C	−2.570230	−3.425290	−0.041220	C	−4.055337	−5.207032	0.730993
C	−3.546093	−4.939240	−1.695084	N	−2.516389	0.390951	−3.898221	O	−1.082343	−0.219431	−2.221347
C	−2.230884	−0.127383	−2.688478	C	−1.458281	0.895731	−4.767151	C	−3.890319	0.513902	−4.360629
O	−2.417262	−0.421568	0.601308	O	−2.513627	1.806885	0.169571	O	1.683188	2.289264	−2.337529
O	−0.248493	3.227622	−1.585067	O	2.266484	−0.810446	−2.319434	O	0.860156	−2.282008	−1.307890
C	−7.145139	0.823459	1.794165	C	−6.519645	1.979179	1.315864	C	−5.182466	1.938521	0.918628
C	−4.458600	0.738420	0.989600	C	−5.092175	−0.416246	1.471609	C	−6.427465	−0.374392	1.874026
C	−3.014840	0.690190	0.559390	C	0.958752	6.099219	−5.511711	C	1.930546	5.096523	−5.427700
C	1.865152	4.141872	−4.412629	C	0.823454	4.181032	−3.472744	C	−0.148241	5.190233	−3.560240
C	−0.079606	6.144606	−4.575740	C	0.749376	3.154096	−2.380263	C	3.304716	−5.125790	−4.645121
C	2.295594	−5.396489	−3.715152	C	1.796446	−4.374261	−2.907300	C	2.303399	−3.071285	−3.020984
C	3.317302	−2.805583	−3.953681	C	3.814150	−3.828475	−4.762351	C	1.758547	−1.976695	−2.144362
H	9.304998	1.400235	2.037681	H	8.470335	1.782389	−0.278394	H	6.035438	1.518155	−0.781298
H	5.280301	0.498816	3.319634	H	7.712478	0.757126	3.842291	H	−0.075066	−6.353558	6.003530
H	−0.620580	−6.668284	3.593251	H	−0.483942	−4.722805	2.024819	H	0.778385	−2.187891	5.244989
H	0.624792	−4.111851	6.834605	H	0.217120	7.078877	6.334745	H	−0.735439	7.446001	4.062657
H	−0.691594	5.592192	2.383011	H	1.242747	3.031122	5.232066	H	1.207770	4.871450	6.926354
H	−2.487298	−3.184647	1.031656	H	−3.800618	−4.768664	1.703629	H	−3.758082	−6.267311	0.733192
H	−5.146296	−5.151587	0.589722	H	−4.601892	−4.844195	−1.993471	H	−3.250020	−5.995373	−1.786299
H	−2.920078	−4.324896	−2.350327	H	−3.117589	−0.479136	−2.129879	H	−1.512349	0.399770	−5.747812
H	−0.491443	0.684612	−4.299613	H	−1.566421	1.981139	−4.910525	H	−4.570389	0.103807	−3.603812
H	−4.031427	−0.036188	−5.303987	H	−4.147787	1.570869	−4.529830	H	−8.189258	0.857446	2.110373
H	−7.075279	2.916784	1.259019	H	−4.676415	2.832211	0.554298	H	−4.513770	−1.337660	1.534660
H	−6.910837	−1.275113	2.256711	H	1.012941	6.847564	−6.304426	H	2.743883	5.061924	−6.154462
H	2.616695	3.357039	−4.329483	H	−0.946540	5.213824	−2.818675	H	−0.835128	6.929895	−4.635712
H	3.696283	−5.926009	−5.275928	H	1.900037	−6.409378	−3.619066	H	1.012318	−4.562279	−2.174042
H	3.706813	−1.790562	−4.028930	H	4.604174	−3.615401	−5.484643				

Table 4.8: Optimized atomic coordinates for $(DMF)_2ZnCoZn_3O(C_7H_5O_2)_6$

Chapter 5

Quantifying and Locating Cation Exchange within MOFs through Multi-wavelength Anomalous Dispersion

5.1 Abstract

In this chapter, we employed multi-wavelength anomalous X-ray dispersion to determine the relative cation occupation at two crystallographically distinct metal sites in Fe^{2+}-, Cu^{2+}-, and Zn^{2+}-exchanged versions of the microporous MOF known as MnMnBTT (BTT = 1,3,5-benzenetristetrazolate). By exploiting the dispersive differences between Mn, Fe, Cu, and Zn, the extent and location of cation exchange was determined from single crystal X-ray diffraction datasets collected near the K edges of Mn^{2+} and of the substituting metal, and at a wavelength remote from either edge as a reference. Comparing the anomalous dispersion between these measurements indicated that the extent of Mn^{2+} replacement depends on the identity of the substituting metal. We contrasted two unique methods to analyze this data with a conventional approach and evaluated their limitations with emphasis on the general

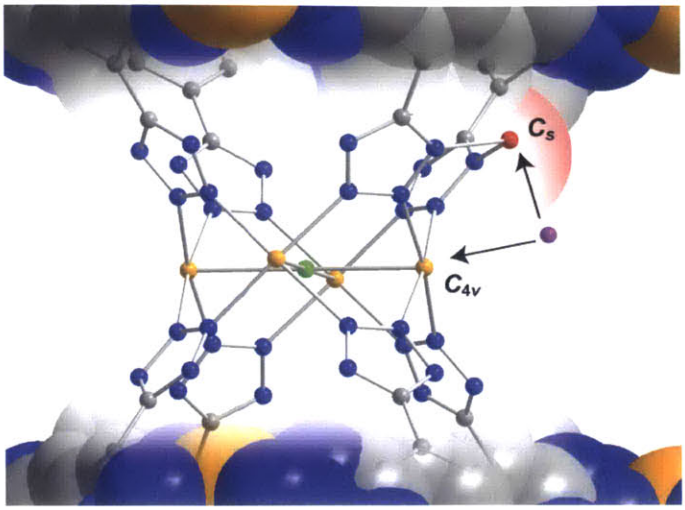

Figure 5-1: Exchangeable metal sites in M_1M_2BTT. Orange, red, green, blue and grey spheres represent the C_{4v} metal site, the partially occupied C_s metal site, Cl, N, and C atoms respectively. Pink sphere represents the substituting cation. H atoms have been removed for clarity.

application of this method to other heterometallic MOFs, where site-specific metal identification is fundamental to tuning catalytic and physical properties.[1]

5.2 Introduction

By inserting cations into well-defined environments, cation exchange enables the rational design of physical properties and chemical reactivity of materials that may otherwise be physically and chemically inactive. A clear structure–function understanding is needed to design these materials, though their enhanced structural complexity undermines atomic-level structural characterization. Therefore, developing analytical tools to determine the location and site-occupancy of both the substituting and parent cations in MOFs formed by cation exchange is paramount for establishing this technique as a reliable and rational synthetic method for MOFs.

This chapter demonstrates that multi-wavelength anomalous dispersion (MAD).[149–155] is a powerful method to quantify the extent and location of cation exchange in MOFs

[1]A portion of this work appeared previously in Brozek, C. K.; Cozzolino, A. F.; Teat, S. J.; Cheng, Y.-S.; Dincă, M. *Chem. Mater.* **2013**, *25*, 2998 and is reproduced here with permission from the American Chemical Society.

with multiple crystallographically independent metal sites, where the cation location is ambiguous. The material investigated here, $Mn_3[(Mn_4Cl)_3(BTT)_8]_2$ (MnMnBTT; BTT = 1,3,5-benzenetristetrazolate)[2] was chosen as a model system because its two crystallographically distinct Mn^{2+} ions can be exchanged for a variety of mono- and divalent metal ions,[3] and because the relatively low energy Mn K-edge provides a maximum resolution of 0.94 Å at $\theta = 85°$, the limit of our setup. By addressing these challenges, our analysis of MnMnBTT outlines key limitations of MAD, providing a guide for its use with other heterometallic MOFs. In its desolvated state, one metal site is coordinated equatorially to four nitrogen atoms from four tetrazole rings and an axially bound chloride anion, which together define an intraframework C_{4v} site, while the second is bound to two nitrogen atoms defining an extraframework C_s site (Figure 5-1).[2] Both Mn^{2+} cations exchange with other divalent or monovalent cations, but the location (i.e. C_{4v} versus C_s) and site occupation of the metal substitution could not be demonstrated experimentally.[3] Using variable wavelength synchrotron radiation, we took advantage of element-specific anomalous X-ray dispersion to locate the extent of Fe^{2+}, Cu^{2+}, and Zn^{2+} incorporation in the intraframework C_{4v} site of MnMnBTT, our benchmark system. We present three methods of analyzing these data to quantify the occupancy of either metal at each site and evaluate their limitations for use with future heterometallic materials.

5.3 Methods

5.3.1 Materials

N,*N*-dimethylformamide (DMF) (99.8%, Alfa Aesar), $MnCl_2$ (97% Strem), $FeCl_2$ (98% Strem), $CuCl_2$ (≥98% Strem), and $ZnCl_2$ (≥98% Sigma-Aldrich) were used as received. Dry, deaerated methanol (MeOH) and DMF were obtained by degassing with a flow of argon gas for 30 min and by passing the solvent through two silica columns in a Glass Contour Solvent System.

5.3.2 Preparation of MnMnBTT

Colorless MnMnBTT crystals were prepared by sonicating $MnCl_2 \cdot 4H_2O$ (2.8 g, 14 mmol) and $H_3BTT \cdot 2HCl \cdot H_2O \cdot MeOH$ (0.62 g, 1.5 mmol) in 140 mL of a 50/50 mixture of MeOH and DMF with 14 drops of concentrated HCl until all solids were completely dissolved. The solution was split equally between 12 scintillation vials and placed in a 70 °C oven until small cubic crystals began to appear. The vials were transferred to the glove box, and the solutions were decanted. The colorless cubic crystals were rinsed three times with DMF and three times with MeOH in 6 hour intervals to prepare them for exchange soaks. Three samples were treated, at 20 °C, with MeOH that was replaced 3 times over 3 days in order to obtain a sample of pristine MnMnBTT that could be activated as a control. The sample was activated by heating under dynamic vacuum for 12 h (4 mtorr, 150 °C) in a pre-scored ampoule which was flame sealed to preserve the integrity of the activated sample.

5.3.3 Metal exchange in MnMnBTT

Colorless MnMnBTT crystals were treated with concentrated solutions of either $FeCl_2$, $ZnCl_2$ or $CuCl_2$ in MeOH. The samples were soaked for 7 days total, replacing the solution every 2 days. Over the course of 7 days, the $FeCl_2$-soaked MnMnBTT (denoted FeMnBTT) became light yellow in color; the $ZnCl_2$ soaked MnMnBTT (denoted ZnMnBTT) remained colorless; and the $CuCl_2$ soaked MnMnBTT (denoted CuMnBTT) became dark green in color. The exchanged samples were treated, at RT (20 °C), with MeOH that was replaced 3 times over 3 days in order to remove any excess metal salts prior to activation. The samples were activated by heating under dynamic vacuum for 12 h (4 mtorr, 150 °C) in a pre-scored ampoule which was flame sealed to preserve the integrity of the activated sample.

5.3.4 Elemental analysis

Manganese, iron, nickel, copper, and zinc analyses were conducted at the MIT Center for Materials Science and Engineering Shared Experimental Facility (CMSE-SEF)

using a HORIBA Jobin ACTIVA inductively coupled plasma atomic emission spectrometer (ICP-AES). Standards were prepared from solutions purchased from ULTRA Scientific©, designated suitable for ICP analysis.

5.3.5 X-ray Absorption Spectroscopy

To determine the true K-edge values for the metals in each sample, X-ray absorption spectra were collected over a window spanning 100 eV above and below the reported values for the zero-valent metals. All spectra were collected at beamline 11.3.1 at the Advanced Light Source of Lawrence Berkeley National Laboratory using a Si(111) monochrometer and an International Radiation Detectors, Inc. AXUV100 photodiode detector. All data were taken in transmission mode at 1-eV intervals with powder samples that were appended to the detector with Kapton tape. The minimum in the real component of the scattering factor, f', was taken as the midpoint of the absorption edge. Data were collected 10 eV below this edge to minimize the changes in f', and the effects of beam instability at the edge where the slope of f' is steepest.

5.3.6 Multi-wavelength Anomalous Dispersion

A single crystal suitable for X-ray diffraction was chosen for each sample and mounted on a kapton loop. Data sets were collected at 100 (2) K at ChemMatCARS and at beamline 11.3.1 of the Advanced Light Source of Lawrence Berkeley National Laboratory using a double Si(111) monochromator with a Bruker AXS APEXII CCD and Bruker D8 diffractometer. The X-ray intensity was attenuated by physically blocking the beam path with filters of varying absorption strength until the CCD detector remained unsaturated. Optimal attenuation filters were chosen to maximize the intensity for each shell that was collected. Data sets were collected at wavelengths corresponding to 10 eV lower than the maximum f' values of the transition metals present in each sample as determined by the XAS experiments described above (see Figure 5-2). An additional data set was collected for each sample at 0.775 Å for overall structure determination.

5.3.7 Data Reduction

A preliminary unit cell was determined for each dataset by harvesting spots with I $> 10\sigma$ for a subset of the collected frames. The data were integrated by averaging the peak shape from each detector region and using a mask software[2] to remove the shadow of the beamstop. The unit cell was periodically updated using triclinic parameters. Integration was repeated after reading in the updated unit cell from the unmerged p4p file. The data were scaled using SADABS[87] following the default settings with the exception of choosing the m3m Laue group, increasing the restraint estimated standard deviations for equal consecutive scale factors to 0.02, and applying an angle of incidence correction. The crystals were not indexed, so a numerical absorption correction could not be applied. In the final reflection file the Bijvoet pairs were kept separate. The structure solution was deter-mined by either direct methods or by performing a Patterson heavy atom search. The structure of the framework was fully refined against the 0.775 Å dataset using SHELXL.[88] Residual density within the pores, aside from a partially occupied O atom of a bound methanol molecule, was not sufficiently localized to allow modeling. This residual density was not refined and does not represent a sizable contribution as the material was activated prior to collection.

5.3.8 Data Analysis

Three independent methods were used to quantify the composition at the C_{4v} metal site. The real and imaginary components (f' and f'') of the anomalous dispersion modify the atomic scattering factor $f(hkl, \lambda_{\mathrm{M}})$ according to equation 5.1. These factors cause an apparent decrease or increase in the electron density of an element if the incident wavelength corresponds to its absorption edge. We present two unique data analysis methods, which correlate site occupancy to differences in electron density. The third approach refines against the datasets taken at the three wavelengths

[2]Contact Yu-Sheng Chen, ChemMatCARS, The University of Chicago, yschen@cars.uchicago.edu

simultaneously while refining the occupancy of multiple metals at the same sites.[151]

$$f(000, \lambda_M) = f(000)_M + f'(\lambda_M)_M + if''(\lambda_M)_M \quad (5.1)$$

Refined Occupancy Difference (ROD) Method

The structure was solved and refined at a wavelength distant from a relevant absorption edge, while correcting for the anomalous dispersion of C, N, O, and Cl. Once this model was refined with the C_{4v} metal site fully occupied with Mn, this same model was refined against all the wavelengths with the appropriate dispersion corrections for C, N, O, and Cl while allowing the occupancy of the C_{4v} site to refine freely. The final occupancy was multiplied by the expected number of electrons for the element used during the refinement, giving the apparent electron density $\rho_{app}(M)$ at incident wavelengths near the K edges of M = Mn, Fe, Cu, or Zn.

Integrated Density Difference (IDD) Method

The structure was solved and fully refined against the remote wavelength data collected with radiation of 0.775 Å wavelength with the appropriate anomalous dispersion corrections for C, N, O, and Cl. This model was refined against the datasets collected at the K edges of Mn and the other metal to produce a structure factor file (SHELX type 6). A Fast Fourier Transform was applied to this file using the WinGX program suite with a grid spacing of 0.05 Å[156] to give the experimental relative electron densities. These values of arbitrary magnitude were scaled to the electron density of the nitrogen atoms because its anomalous dispersion coefficients are relatively invariant to the wavelengths used in this series of experiments. This scaling procedure provided apparent electron densities $\rho_{app}(\lambda_M)$.

For both ROD and IDD methods, the ratio of the two metals at the C_{4v} site in each material could be determined from equations 5.1-5.4, where α is the fraction of Mn or M at the site of interest, $|f(000, \lambda_{Mn})_M|$ is the magnitude of the atomic scattering factor at |hkl| = |000| for metal M near the K edge of Mn, $f'(\lambda_{Mn})_M$ is the real component of the anomalous dispersion coefficient for metal M near the

wavelength corresponding to the Mn absorption edge (and vice versa), $f''(\lambda_{Mn})_M$ is the imaginary component of the anomalous dispersion coefficient for metal M at a wavelength near the Mn absorption edge (and vice versa), and k is a scaling factor to recover the electron density at each edge due to the combination of metals in the site of interest.

$$\alpha_{Mn} + \alpha_{Mn} = 1 \tag{5.2}$$

(fractional occupancies of site)

$$\alpha_{Mn}|f(000, \lambda_{Mn})_{Mn}| + \alpha_{Mn}|f(000, \lambda_{Mn})_M| = k\rho_{app}(\lambda_{Mn}) \tag{5.3}$$

(anomalous dispersion at Mn edge)

$$\alpha_{Mn}|f(000, \lambda_M)_{Mn}| + \alpha_M|f(000, \lambda_M)_M| = k\rho_{app}(\lambda_M) \tag{5.4}$$

(anomalous dispersion at M edge)

Simultaneous Multi-wavelength Occupancy Refinement (SMOR) Method

We refined the model against all the datasets simultaneously with both possible metals at the C_{4v} site and allowed their occupancies to refine under the constraint that the total site occupation does not exceed unity. Anomalous dispersion coefficients were estimated from the theoretical dispersion curves given by the Kramers-Kronig relation[157] by selecting values that were 10 eV lower in energy from the f' minimum. This directly gave a metal ratio for the occupation of the C_{4v} site. The freely available software JANA was used for this refinement.[158]

5.4 Results and Discussion

Crystals of MnMnBTT were prepared according to a literature procedure[2] and soaked in methanol solutions of anhydrous $FeCl_2$, $CuCl_2$, or $ZnCl_2$ for seven days to afford

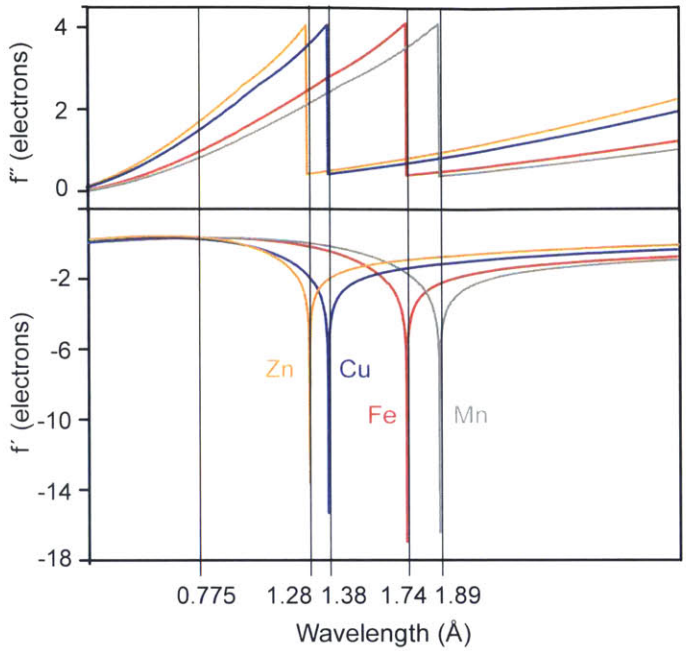

Figure 5-2: The f' and f'' curves derived from the Kramers–Kronig relation[157] shown in color with the incident wavelengths delineated by vertical lines.

FeMnBTT, CuMnBTT, or ZnMnBTT. To eliminate the possibility of extraneous metals residing within the pores as was previously observed,[53] we performed three successive three-day soaks in clean methanol, then desolvated the samples at 150 °C until a pressure of less than 4 mtorr could be maintained for 10 minutes under static vacuum. Each sample was protected with degassed Paratone-N oil and mounted under a 100 K N_2 stream. For each sample a full dataset was collected at 0.775 Å from which the structure was solved and refined.

Single-crystal X-ray diffraction datasets were collected for a MnMnBTT single crystal at wavelengths 10 eV lower than the K edges of Fe, Mn, Cu, and Zn, as determined by X-ray absorption spectroscopy of the substituted samples (1.898 Å, 1.744 Å, 1.381 Å, 1.284 Å for Mn, Fe, Cu, and Zn, respectively). These incident wavelengths are depicted in Figure 5-2 alongside the theoretical f' and f'' curves. A reference dataset was also collected at 0.775 Å, remote from the edges of these elements, where the anomalous scattering factors are indistinguishable.[159] For the exchanged materials, FeMnBTT, CuMnBTT, and ZnMnBTT, datasets were collected

MnMnBTT	λ = **Fe**	λ = **Cu**	λ = **Zn**
Unit cells (Å)	18.9153(5)	18.9153(5)	18.9153(5)
ICP-AES	0	0	0
IDD	10.1	2.3	0.3
ROD	13.2	2.1	0.3
SMOR	−14.9	−11.7	−9.6(3)

Table 5.1: Unit cell parameters and C_{4v} metal site occupancy data for MnMnBTT-7d collected at Fe, Cu and Zn edges shown as M%.

at the Mn K-edge, the substituting metal K edge, and at 0.775 Å.

To analyze the substituted materials, we established the behavior of the unsubstituted MnMnBTT with MAD since its metal occupancies were known. This control experiment allowed us to observe how $f(000, \lambda_{\mathrm{M}})$ deviates from the theoretical values at each wavelength in the absence of substituted cations, which is necessary for later contextualizing the apparent changes in $f(000, \lambda_{\mathrm{M}})$ of the substituted materials. To evaluate the IDD and ROD methods, we used the final apparent electron density, $\rho_{\mathrm{app}}(\lambda_{\mathrm{M}})$, at each K edge wavelength to calculate the ratio of Mn to the corresponding transition metal in the C_{4v} site (see equations 5.1-5.4). Using the SMOR method, the ratio of metals was available directly.

The relative metal occupancies from all three methods are provided in Table 5.1 for MnMnBTT and reveal that the methods each have intrinsic error as they all deviate from a substituting metal occupancy of 0%. In the IDD and ROD methods, the Fe, Cu or Zn occupancies, which are necessarily zero under the synthetic conditions, give positive non-zero values. The largest error occurs for the data evaluated at the Fe edge, which is likely due to the proximity of the Fe and Mn edges (see Figure 5-2). Both Cu and Zn have values that are closer to the expected 0%. The SMOR method tends to underestimate the occupancies such that Mn occupancies are greater than unity, which cannot be accounted for by the standard uncertainty in the refined value. Taken together, this control experiment provides a baseline uncertainty in ascribing deviations in $f(000, \lambda_{\mathrm{M}})$ to the occupancy of substituting cations with FeMnBTT, CuMnBTT, and ZnMnBTT.

MnMnBTT	M = Fe	M = Cu	M = Zn
Unit cells (Å)	19.0218(5)	18.4852(5)	18.8285(4)
ICP-AES	3.2	88.8	74.8
IDD	19.5 [9.4]	102.4 [100.1]	100.7 [100.4]
ROD	7.2 [-6.0]	106.9 [104.8]	100.8 [100.5]
SMOR	−7.8(5)[7.2]	88.3(3) [100.0]	66.2(4) [75.8]

Table 5.2: Unit cell parameters and C_{4v} metal site occupancy data for MMnBTT-7d (M = Fe, Cu and Zn) shown as M% [M% corrected for baseline from MnMnBTT].

As shown in Table 5.2, cation exchange for 7 days with MnMnBTT produced materials with significantly changed unit cell parameters, with the exception of FeMnBTT, whose unit cell edge was 19.0218(5) Å. This value is more consistent with that of the parent MnMnBTT structure, 19.009(1) Å,[2] than with the all iron analogue, FeFeBTT, which has a cell parameter of 18.824(1) Å[52]. The small difference between the unit cell dimensions of FeMnBTT and MnMnBTT suggests that Fe^{2+} exchanged minimally into the intraframework C_{4v} site after soaking for 7 days since the unit cell dimensions of MMnBTT are sensitive to changes in the metal–nitrogen bonds of the C_{4v} site, not changes in the C_s site. In contrast, CuMnBTT and ZnMnBTT prepared by week-long soaks showed unit cell parameters of 18.4852(5) Å and 18.8285(4) Å, respectively. The former value is closer to that of all-copper CuCuBTT, 18.595(7) Å,[53] which indicates the significant incorporation of Cu^{2+} at the C_{4v} sites, as had been previously proposed on the basis of elemental analysis.[3] See tables 3–5 for further crystallographic data.

MAD analysis of FeMnBTT, as shown in Table 5.2, corroborates the ICP-AES and unit cell analysis above that Fe^{2+} exchanges marginally in to the C_{4v} site. The metal content evaluated from each method reveals an Fe content at the C_{4v} site ranging from −7.8% to 19.5%. The results of each method report ICP-AES data, which give an Fe content of 3.2%, assuming that Fe^{2+} exchanges the charge-balancing C_s completely. These values can be improved by normalizing them to the occupancies derived from the control experiment (as shown in Table 5.1). This recalculation gives

[3]An independently synthesized all zinc analogue, ZnZnBTT, has not yet been reported and the unit cell of such a compound is therefore unknown.

values of 9.4%, −6.0%, and 7.2% for the IDD, ROD and SMOR methods, respectively. Despite the large variation between methods, they provide a consistent depiction of limited Fe^{2+} exchange at the C_{4v} metal site.

MAD analyses of the Cu^{2+} and Zn^{2+} exchanges indicate that they incorporate to a much greater extent into the C_{4v} site than Fe^{2+}, which agrees with the previously proposed formulas. Assuming that both metals exchange the C_s site completely, the ICP-AES values for the C_{4v} sites, as shown in Table 5.2, suggest Cu^{2+} occupies 88.8% of those sites, while Zn^{2+} occupies 74.8%. On the other hand, MAD analysis suggests that the occupancy of Cu^{2+} ranges from 88.3-106.9%. After normalizing to the occupancies derived from the MnMnBTT control, the values adjust to 100.1, 104.8 and 100.0% for the IDD, ROD and SMOR methods, respectively. The Zn^{2+} occupancy ranges from 66.2-100.8% between the three methods. The corrected values become 100.4%, 100.5% and 75.8% for the IDD, ROD and SMOR methods, which are more consistent with the ICP-AES data assuming a fully Zn^{2+}-occupied C_s site.

5.5 Conclusion

In conclusion, MAD is the only site-specific method for discerning site occupancy of metals with similar atomic numbers and electron density in MOFs. We presented two novel methods for analyzing the data, in addition to a previously reported method, and demonstrated their reliability so that meaningful conclusions could be drawn for more general examples. All three methods suffered from an inherent error as established by a control experiment, which could be minimized by performing the measurements on-edge to maximize f', as well as 10 eV above and below this value to maximize and minimize the f'' value. Because X-ray diffraction data collected near the Mn K-edge inherently limits the resolution, we expect that the errors obtained for materials with heavier atoms would be minimized. Therefore, the series of materials derived from MnMnBTT define a lower limit of precision for quantitative MAD analysis, though it still provided a practical account of the location and extent of cation exchange, especially when coupled with elemental analysis.

	FeMnBTT-7d
Formula	$C_{41}H_{12}Cl_{1.50}Fe_{1.11}Mn_{5.64}N_{48}O_5$
FW	1682.04
T, K	100(2)
group	$Pm\bar{3}m$
Z	4
a, Å	19.0218(5)
V, Å^3	6882.6(3)
d_{calc}, g/cm^3	1.672
μ, mm^{-1}	1.563
F(000)	3408
crystal size, mm	0.2 × 0.2 × 0.2
theta range	1.65 to 33.60
index ranges	$-27 \leq h \leq 27$
	$-23 \leq k \leq 27$
	$-25 \leq l \leq 27$
refl. collected	58863
data/restr./param.	2123/0/48
GOF on F^2	3.309
largest peak/hole, e/Å^3	3.835/−0.429
R_1 (wR_2), % [I>2sigma(I)]	13.84 (36.35)

Table 5.3: Crystallographic data for crystals of $C_{41}H_{12}Cl_{1.50}Fe_{1.11}Mn_{5.64}N_{48}O_5$.

	CuMnBTT-7d
Formula	$C_{41}H_{12}Cl_{1.38}Cu_{6.02}Mn_{0.67}N_{48}O_5$
FW	1727.22
T, K	100(2)
group	$Pm\bar{3}m$
Z	2
a, Å	18.4852(5)
V, Å^3	6316.4(3)
d_{calc}, g/cm^3	0.915
μ, mm^{-1}	0.905
F(000)	1710
crystal size, mm	0.2 × 0.2 × 0.2
theta range	1.56 to 27.48
index ranges	$-23 \leq h \leq 19$
	$-23 \leq k \leq 24$
	$-25 \leq l \leq 23$
refl. collected	45077
data/restr./param.	1489/0/54
GOF on F^2	1.883
largest peak/hole, e/Å^3	2.163/−0.452
R_1 (wR_2), % [I>2sigma(I)]	12.91 (35.87)

Table 5.4: Crystallographic data for crystals of $C_{41}H_{12}Cl_{1.38}Cu_{6.02}Mn_{0.67}N_{48}O_5$.

	FeMnBTT-7d
Formula	$C_{41}H_{12}Cl_{1.50}Zn_{4.85}Mn_{1.90}N_{48}O_5$
FW	1731.66
T, K	100(2)
group	$Pm\bar{3}m$
Z	2
a, Å	18.8285(4)
V, Å^3	6674.9(2)
d_{calc}, g/cm^3	1.734
μ, mm^{-1}	1.753
F(000)	3424
crystal size, mm	0.2 × 0.2 × 0.2
theta range	2.16 to 29.55
index ranges	$-25 \leq h \leq 21$
	$-26 \leq k \leq 26$
	$-26 \leq l \leq 25$
refl. collected	53913
data/restr./param.	1897/0/54
GOF on F^2	4.488
largest peak/hole, e/Å^3	6.296/−1.026
R_1 (wR_2), % [I>2sigma(I)]	19.91 (49.40)

Table 5.5: Crystallographic data for crystals of $C_{41}H_{12}Cl_{1.50}Zn_{4.85}Mn_{1.90}N_{48}O_5$.

Chapter 6

The Solvent Dependence of Cation Exchange in MOFs

6.1 Abstract

In this chapter, we investigated which factors govern the critical steps of cation exchange in MOFs by studying the effect of various solvents on the insertion of Ni^{2+} and Co^{2+} into MOF-5 and Co^{2+} into MFU-4*l*. After plotting the extent of cation insertion versus different solvent parameters, trends emerge that offer insight into the exchange processes for both systems. This approach establishes a method for understanding critical aspects of cation exchange in different MOFs and other materials.[1]

6.2 Introduction

Identifying the features underlying the cation-exchange mechanism in a given set of materials could enable the design of new compounds with precisely engineered functionality. These studies are rare, however, because the exchange processes are undoubtedly governed by numerous parameters corresponding to both the crystalline solids and their surrounding solutions. For instance, thermodynamic values, such

[1] A portion of this work appeared previously in Brozek, C. K.; Bellarosa, L.; Soejima, T.; Clark, T. V.; López, N.; and Dincă, M. *Chem.–Eur. J.* **2014**, *20*, 6871 and is reproduced here with permission from John Wiley and Sons.

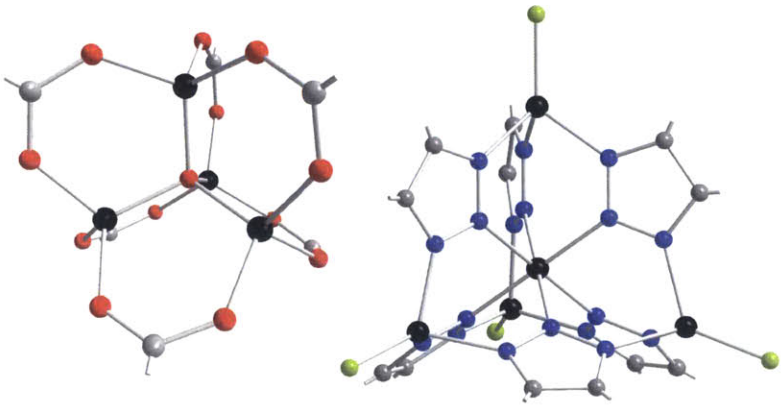

Figure 6-1: The SBUs of MOF-5 (left) and MFU-4*l* (right).

as cation solubility and lattice strain, are known to influence cation exchange in nanocrystals,[9] while ionic radius is significant for zeolites.[160,161] Despite the deep insight that could be gained by identifying the influence of solvent parameters on cation exchange, few if any studies have tackled this task. To endow cation exchange in MOFs with predictive power, we studied the solvent dependence for rates of exchange of native Zn^{2+} ions with Co^{2+} and Ni^{2+} in the materials known as MFU-4*l* (Zn_5Cl_4(bis(1*H*-1,2,3-triazolo-[4,5-*b*],[4′, 5′-*i*])dibenzo-[1,4]-dioxin)$_6$) and MOF-5. The secondary building units (SBUs) of these materials, the sites of cation exchange, are shown in Figure 6-1. Our findings demonstrate that by identifying the solvent parameters that best correlate with the cation exchange rate, we can determine critical aspects of the exchange process.

6.3 Results and Discussion

To examine the solvent dependence of Ni^{2+} exchanging into MOF-5, we repeated an exchange procedure previously reported for *N*,*N*-dimethylformamide (DMF) with a variety of other solvents under otherwise identical conditions. In addition to DMF, we used dimethyl sulfoxide (DMSO), *N*-methyl-2-pyrrolidone (NMP), *N*-methylformamide (NMF), tetrahydrofuran (THF), and acetonitrile (MeCN). MOF-5 was prepared and activated according to a literature procedure.[72] Soaking these crystals with gentle

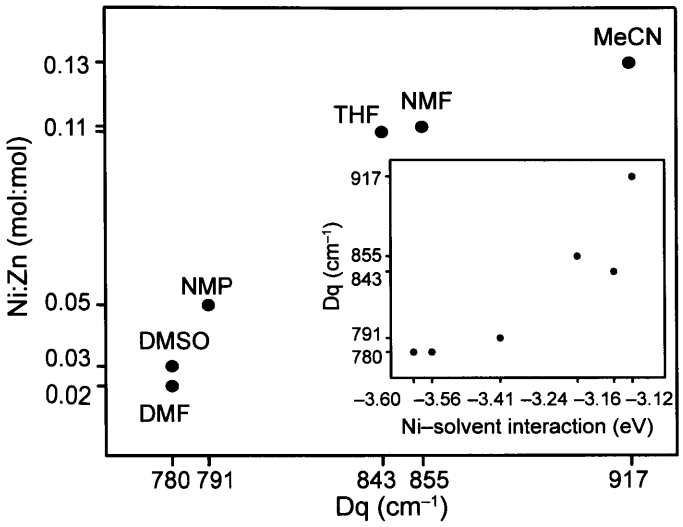

Figure 6-2: Ni:Zn molar ratio plotted against Dq. Inset: Dq determined from UV-Vis spectra of $[Ni(solvent)_6]^{2+}$ complexes versus calculated Ni–solvent bond strengths.

shaking for 1 week in 0.03 M solutions of $Ni(NO_3)_2{\cdot}xH_2O$ produced materials with a wide range of Ni:Zn molar ratios, as determined by inductively coupled atomic emission spectroscopy (ICP-AES).

The Ni:Zn ratios were plotted against several solvent parameters that we expected to impact the exchange process, including the ligand field parameter of the corresponding $[Ni(solvent)_x]^{2+}$ species (Dq), the solvent dielectric constant, the Snyder polarity index, the Hansen solubility parameter δ_H, and the Gutmann donor number. Among these, the closest trend was observed for the Dq parameters, which were derived by assigning d–d transitions to UV-Vis-NIR spectra of $Ni(NO_3)_2{\cdot}xH_2O$ solutions in the various solvents using theory derived elsewhere.[44] As shown in Figure 6-2, the Ni:Zn ratio increases monotonically with increasing values of Dq. To interpret this trend, we employed density functional theory to compute the metal–solvent bond strengths of $[Ni(solvent)_6]^{2+}$ and $[Zn(solvent)_6]^{2+}$ following equations 6.3-6.5. The results, plotted in the inset of Figure 6-2, indicate that high Dq values correlate with weak metal–solvent bonds. This inverse relationship reflects the solvents ranging on a spectrum from having π-donor character to being π acceptor ligands: the empty π^* orbitals of MeCN lead to large Dq, while the filled π-donating orbitals from $O^{\delta-}$ on DMSO lead to small Dq. Thus, the Ni:Zn ratio increases for solvents that form

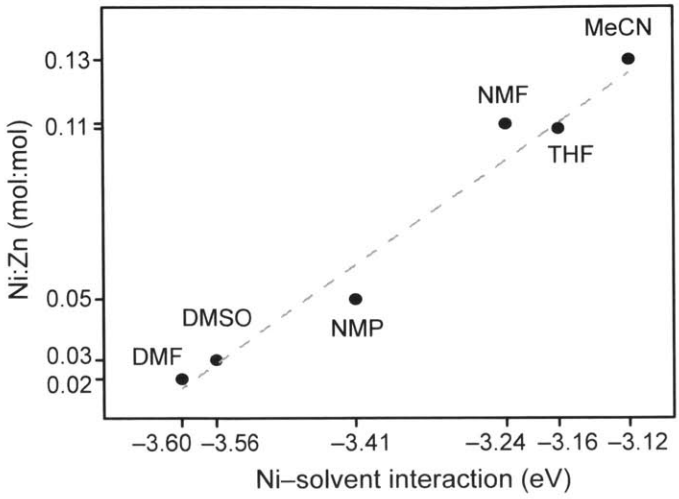

Figure 6-3: Ni:Zn ratio plotted against calculated Ni–Solvent interactions with a best fit line depicted by the dashed gray line, with $R^2 = 0.966$.

weaker metal–solvent bonds (as shown in Figures 6-3 and 6-4).

We also plotted the Ni:Zn ratio against the Gutmann donor numbers of the solvents. This number is the formation energy of complexes between solvents and $SbCl_5$ and has been used as a metric for the Lewis basicity of the respective solvents. We reasoned that an experimental measure of Lewis basicity should follow the same trend with bond strength.[162] Indeed, less basic solvents correlate with higher Ni^{2+} incorporation (Figure 6-5). Together, the correlations with Dq and the related Gutmann donor numbers suggest two possible scenarios: weak Ni^{2+}–solvent interactions (or large Dq values) lead to fast release of Ni^{2+}, or strong solvent association with the Zn^{2+} ions in MOF-5 lead to stable adducts in the framework, retarding the rate of exchange.

With evidence that the ligand strength of the solvents affects the exchange process, we turned our attention to parameters that measured electrostatic interactions. If the mechanism involved charge localization or neutralization, the rate of Ni^{2+} exchange should correlate to the polarity indices developed by Snyder.[163] Yet, a trend did not emerge from the resulting plot, displayed in Figure 6-5. We also investigated whether the rate of exchange correlated to the respective dielectric constants of the solvents, just as S_N1 reactions are known to proceed faster in solvents with high

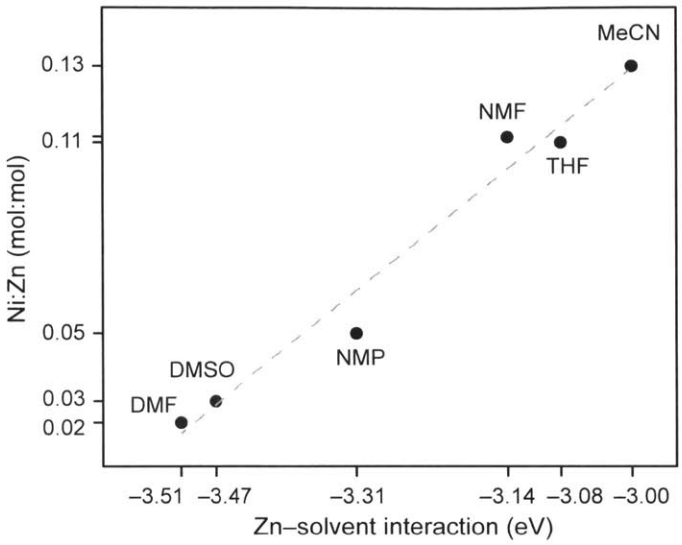

Figure 6-4: Ni:Zn ratio plotted against calculated Zn–Solvent interactions with a best fit line depicted by the dashed gray line, with $R^2 = 0.966$.

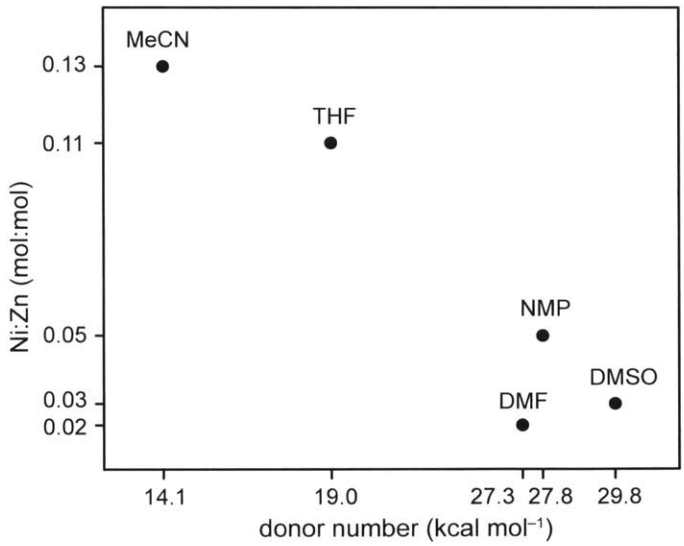

Figure 6-5: Ni:Zn molar ratio in Ni-MOF-5 plotted against Gutmann donor numbers of the various solvents.

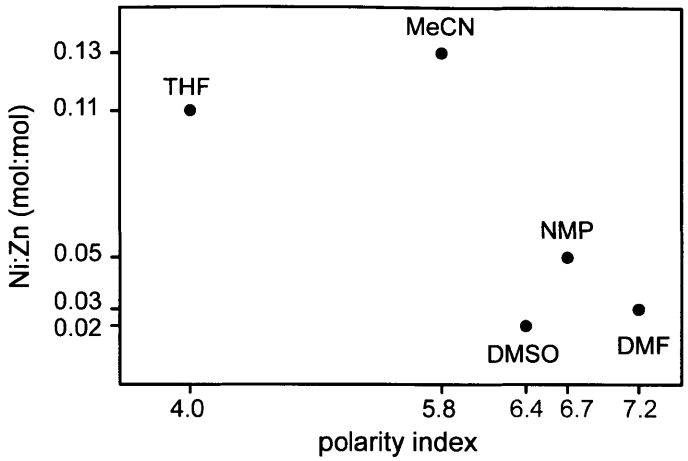

Figure 6-6: Ni:Zn molar ratio in Ni-MOF-5 plotted against the polarity index of each solvent.

dielectric constants by stabilizing charged intermediates. Again, plotting the Ni:Zn ratio versus the respective dielectric constants showed no correlation (Figure 6-7). Although electrostatics may still impact the cation-exchange mechanism, our analysis indicates that the cation–solvent interaction is dominant in the rate-determining step.

To investigate whether similar effects could be observed in other systems, we turned our attention to the study of Co^{2+} exchange into MFU-4*l*. This system had been explored extensively by Volkmer et al. to impart redox activity to the MOF.[19,164,165] We repeated the exchange procedure in a variety of solvents under otherwise identical conditions. In addition to DMF, we used DMSO, NMP, MeCN, dimethylacetamide (DMA), and methanol (MeOH). MFU-4*l* was prepared and activated according to a literature procedure and soaked in 0.1-M solutions of anhydrous $CoCl_2$.[19,164,165] To observe significant differences in the extent of cation exchange between the solvents, we prevented the process from going to completion by performing the exchange at a lower temperature than used previously. Whereas the original report of Co^{2+} exchange into MFU-4*l* required stirring for 20 h at a temperature of 140 °C, we soaked the all-Zn^{2+} parent material for exactly 1 week at room temperature with only gentle shaking to avoid breaking the crystals, which would otherwise affect the Co^{2+} diffusion. Studying the rate of exchange at first seems complicated because the SBU of MFU-4*l* contains two crystallographically distinct Zn^{2+} sites, as shown in

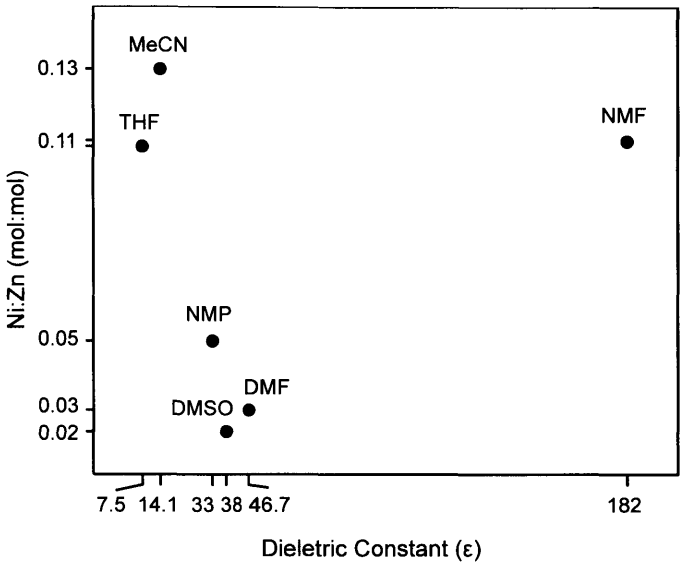

Figure 6-7: Ni:Zn molar ratio in Ni-MOF-5 plotted against the static dielectric constants of the various solvents.

Figure 6-1. The previous study showed, however, that only the peripheral tetracoordinated sites are replaceable by Co^{2+}, whereas the central octahedral atom remains unchanged even at 140 °C.

To investigate the dependence on ligand field strength, we calculated Dq for each solvent, knowing that in the UV-Vis spectra of the corresponding homoleptic metal complexes the transition $^4A_2 \rightarrow {}^4T_1(F)$ should occur at 18Dq.[44] To our surprise, plotting the extent of Co^{2+} exchange into MFU-4*l* versus Dq revealed a trend that is opposite to that found for Ni-MOF-5. Unlike in the latter, the extent of Co^{2+} incorporation into MFU-4*l* increases with lower values of Dq and displays a linear correlation with a R^2 of 0.922, shown in Figure 6-8. The reversal of Dq dependence trends between Co-MFU-4*l* and Ni-MOF-5 suggests that solvents participate in a different rate-limiting step in the two materials. To test whether this reversal was due to using Co^{2+} rather than Ni^{2+}, we soaked MOF-5 in cobalt nitrate solutions under otherwise identical conditions to what we used for Ni-MOF-5. Plotting the incorporation of Co^{2+} versus Dq that we measured for O_h Co^{2+} shows that the trend is maintained within MOF-5 and is independent of cation identity (Figure 6-9).

We anticipated that if Co-MFU-4*l* shows the opposite trend from Ni-MOF-5, then

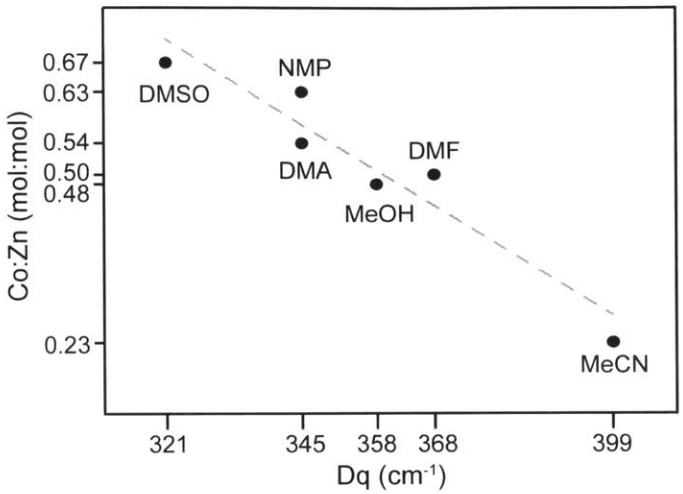

Figure 6-8: Co:Zn ratio of Co-MFU-4*l* plotted against ligand field parameter Dq. The dashed gray line depicts a best fit with R^2 of 0.922.

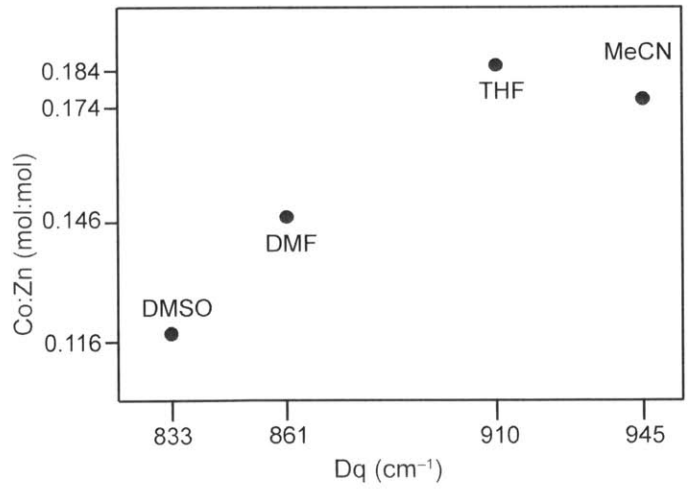

Figure 6-9: Co:Zn ratio of Co-MOF-5 plotted against ligand field parameter Dq.

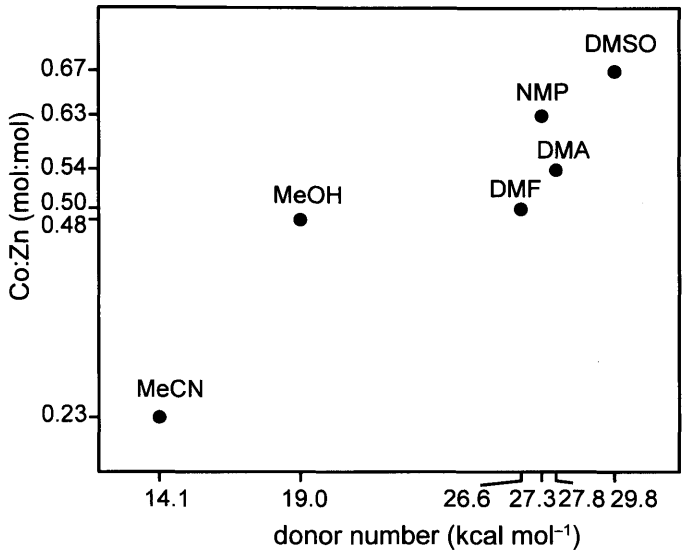

Figure 6-10: Co:Zn molar ratio of Co-MFU-4*l* plotted against Gutmann donor numbers of the various solvents.

the rate of exchange should increase for more Lewis basic solvents. Indeed, plotting the Co:Zn ratio against the Gutmann donor numbers revealed a convincing correlation, as shown in Figure 6-10. Unfortunately, because solvated $CoCl_2$ is known to exist in equilibrium between various four-coordinate and six-coordinate species,[146] extending our DFT analysis to this system is problematic and led to inferior correlations, as shown in Figures 6-11 and 6-12. Nevertheless, our experimental evidence indicates that solvents that solvate Zn^{2+} better enable faster exchange of Co^{2+} into the MFU-4*l* lattice.

Among the other solvent parameters we tested for the formation of Co-MFU-4*l*, the polarity indices reveal a strong correlation for the aprotic solvents. Figure 6-13 illustrates that Co^{2+} incorporates to a greater extent in solvents with higher indices, giving a linear fit with $R^2 = 0.905$ when MeOH, the only protic solvent, is excluded. Although this parameter provides a convincing trend, the presence of MeOH as an extreme outlier suggests that the metal–solvent interaction (i.e. Dq) exerts a more reliable influence on the cation-exchange mechanism because it demonstrates a strong correlation whether the solvent is protic or not. Nevertheless, the strong correlation between the Co:Zn ratio and the Snyder polarity indices suggests that the exchange

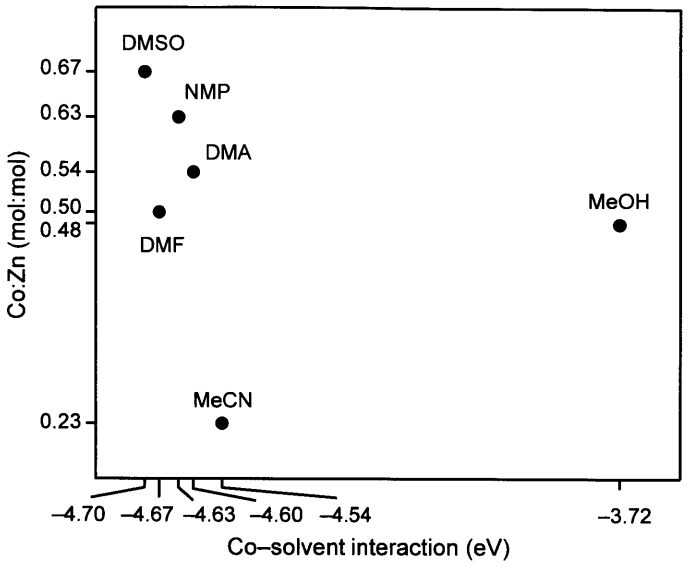

Figure 6-11: Co:Zn molar ratio of Co-MFU-4*l* plotted against the computed Co–solvent interaction of each solvent.

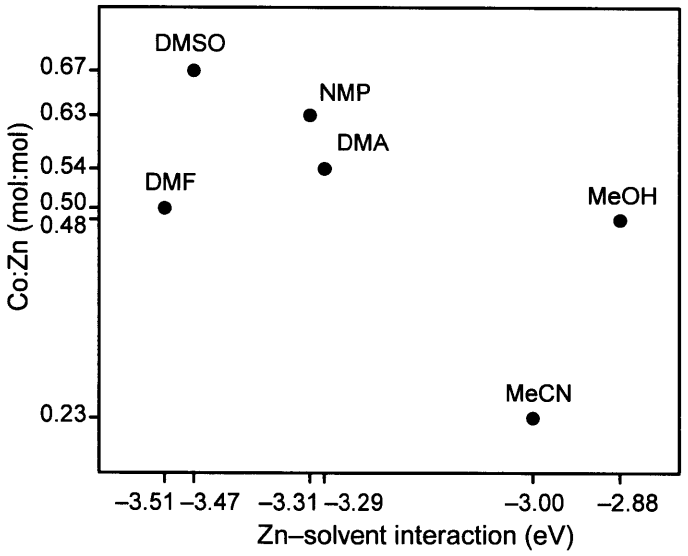

Figure 6-12: Co:Zn molar ratio of Co-MFU-4*l* plotted against the computed Zn–solvent interaction of each solvent.

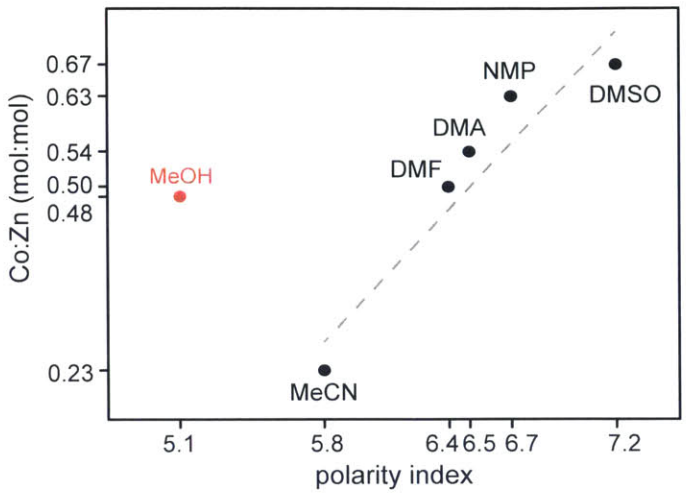

Figure 6-13: Co:Zn molar ratio of Co-MFU-4*l* plotted against Snyder polarity indices. The gray dashed line depicts a best fit with R^2 of 0.905.

process involves a highly polarized intermediate, and thus offers additional insight into the overall mechanism. Solvents with higher indices might better stabilize this polarized intermediate and enhance the rate of the exchange. This is not surprising since for MFU-4*l* the exchange process involves Cl^- transfer between Co^{2+} and Zn^{2+}. Indeed, we surmise that MeOH performs better than expected from the polarity trend because its protic groups enhance Cl^- solvation. Furthermore, it is possible that the Ni^{2+} exchange into MOF-5 does not correlate well to polarity indices because it lacks participating anions.

Whereas Dq and polarity values correlate well to the rate of Co^{2+} exchange into MFU-4*l*, other potentially relevant solvent parameters do not. Prompted by our hypothesis for why MeOH is the outlier in Figure 6-13, we plotted the Co:Zn ratio against the Hansen solubility parameter δ_H to determine the influence of hydrogen bonding.[166] As shown in Figure 6-14, no clear trend emerges. While hydrogen bonding may still influence the exchange process, our analysis suggests that it does not govern the rate through a clear relationship, and is likely not a significant factor prior to or during the rate-determining step.

Encouraged by the relevance of polarity indices on the Co^{2+} exchange in MFU-4*l*, we also investigated whether the rate of exchange correlates to the solvent dielectric

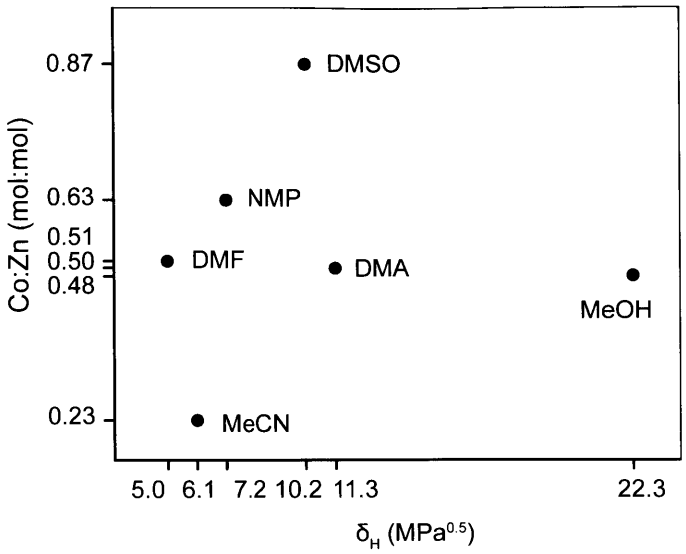

Figure 6-14: Co:Zn molar ratio of Co-MFU-4*l* plotted against the Hansen δ_{H} solubility parameter.

constants. We expected this parameter to correlate with the exchange rate at least as well as the polarity index, yet the resulting plot also did not display a convincing trend (Figure 6-15). This result reinforces that the solvent participates in the exchange process and cannot be treated as a homogeneous dielectric continuum.

In these preceding experiments, we terminated the the cation exchanges after 1 week, before the systems could reach dynamic equilibrium. Hence, our analysis examined how solvent parameters influenced the kinetics of cation exchange. To investigate whether they had a noticeable effect on the thermodynamics, we followed the thermochemical analysis applied to cation exchange in zeolites.[167–171] In a manner analogous to the work of Sherry et al.,[171] the free energy of the exchange, $\Delta G_{P,T}$, of $\mathrm{Zn}^{2+}_{\mathrm{MOF}} + \mathrm{Ni}^{2+}_{\mathrm{solution}} \rightarrow \mathrm{Zn}^{2+}_{\mathrm{solution}} + \mathrm{Ni}^{2+}_{\mathrm{MOF}}$ is given by the following relation:

$$\Delta G_{P,T} = -RT \ln K_{eq} + RT \ln \frac{f_{Zn}^2 Z_{Zn}^2 \gamma_{Ni}^2 m_{Ni}^2}{f_{Ni}^2 Z_{Ni}^2 \gamma_{Zn}^2 m_{Zn}^2} \tag{6.1}$$

Here, f_{Zn} and f_{Ni} and Z_{Zn} and Z_{Ni} represent the activity coefficients and molar fractions of Zn and Ni ions in MOF-5. Similarly, γ_{Ni} and γ_{Zn} and m_{Zn} and m_{Ni} represent the mean activity coefficients and molalities of the electrolytes in solution. All terms are squared as a consequence of both ions being divalent.

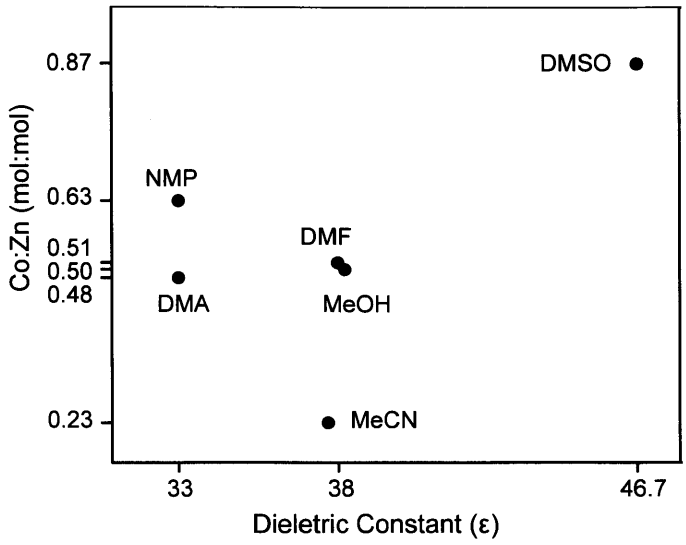

Figure 6-15: Co:Zn molar ratio of Co-MFU-4*l* plotted against the static dielectric constants of the various solvents.

To reach equilibrium conditions, we left MOF-5 suspended in nickel nitrate DMF solutions for 4 months at 238, 265, 296, and 313 K. Determining accurate values for K_{eq} requires knowing all of the terms mentioned above, so we instead employed an approximation. The moles of Ni^{2+} inserted into MOF-5 was calculated from relative Zn/Ni ratios determined by inductively coupled plasma atomic emission spectroscopy. Then, assuming each inserted Ni^{2+} displaces a Zn^{2+} from MOF-5 into solution, we employed the following relation in 6.2 to approximate K_{eq}. Here, Z_{Ni} and Z_{Zn} represent the molar fraction of Ni and Zn ions among all metal ions in MOF-5. Similarly, S_{Ni} and S_{Zn} represent the molar fraction of Ni and Zn ions among all metal ions in solution.

$$K_{eq} = \frac{Z_{Ni}^2 S_{Zn}^2}{Z_{Zn}^2 S_{Ni}^2} \tag{6.2}$$

Assuming the system reached equilibrium, and using $\Delta G^{\circ}_{P,T} = -RT \ln K_{eq} = \Delta H - T\Delta S$, a plot of $\ln K_{eq}$ vs. 1/T yields approximate thermodynamics parameters. The data in Figure 6-16 yield $\Delta G^{\circ}_{1\text{ atm, }238\text{ K}} = 12.9$ kcal/mol, $\Delta G^{\circ}_{1\text{ atm, }281\text{ K}} = 13.9$ kcal/mol, $\Delta G^{\circ}_{1\text{ atm, }296\text{ K}} = 11.3$ kcal/mol, and $\Delta G^{\circ}_{1\text{ atm, }313\text{ K}} = 10.7$ kcal/mol. The slope and y intercept of the resulting line implies $\Delta H = 19.2$ kcal/mol and $\Delta S =$

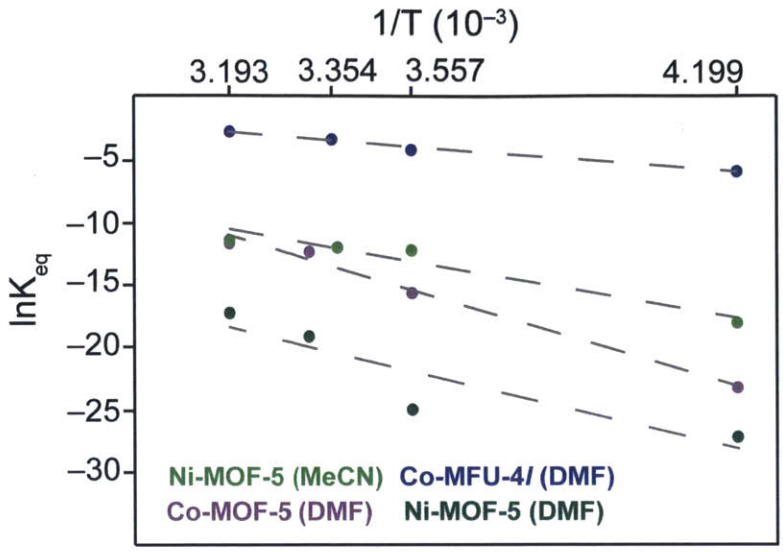

Figure 6-16: Approximate ln K_{eq} versus 1/T.

24.7 cal/mol·T. Hence, entropy increases in the replacement of Zn^{2+} by Ni^{2+}, but is endothermic to yield an overall endergonic process. Yet, the free energy values suggest it is essentially thermally neutral such that large excess of inserting Ni^{2+} can drive cation exchange in accordance with Le Chatelier's Principle.

We explored the possibility of solvent dependence by repeating this procedure using MeCN instead under otherwise identical conditions. The same analysis suggests the process is less endothermic with $\Delta H = 13.8$ kcal/mol, but less disordered with $\Delta S = 23.0$ cal/mol·T. Driven by these interesting results, we extended our method to other metals and MOF systems. Repeating these measurements in DMF, but with Co^{2+} yielded a ΔH similar to Ni^{2+} in DMF, at 23.8 kcal/mol, but with a significantly more positive ΔS, at 54.2 cal/mol·T. We repeated the Co^{2+} exchange into MFU-4*l* with DMF at these same temperatures for 4 months. Applying the same analysis suggested that the process, although quite different from MOF-5, is less endothermic, with $\Delta H = 6.28$ kcal/mol, but with a less positive ΔS, at 14.6 cal/mol·T.

6.4 Conclusion

In conclusion, this chapter illustrates that solvents influence the cation-exchange mechanism, as might be expected, but only a select group of relevant parameters correlate with the exchange rates. These studies also reveal that cation exchange in Co- and Ni-MOF-5 and Co-MFU-4*l* relies on different rate determining steps. The trends displayed by solvent polarity and ligand field strength suggest that the replacement of Zn^{2+} by Co^{2+} in MFU-4*l* involves a polarized intermediate and is limited by the ability of the solvent to solvate the dissociating Zn^{2+} ions. Similar analyses of MOF-5 suggest instead that the dissociation of solvent from Ni^{2+} or the stability of solvent-MOF (i.e. Zn^{2+}) adducts dictates the rate of exchange in MOF-5. An approximation for measuring K_{eq} suggests solvent impacts the thermodynamics as well. Mechanisms of cation exchange may differ from material to material, but systematic studies of solvent dependence are a first step towards understanding these mechanisms. In identifying the few parameters with the greatest influence on the exchange rate, future studies will glean not only mechanistic insight, but acquire a handle for manipulating the exchange process to control physical properties a priori.

6.5 Methods

Unless stated otherwise, all operations were performed under rigorously air-free conditions using standard Schlenk technique or performed in a N_2-filled glovebox.

6.5.1 Materials

Fuming HNO_3 (EMD), trifluoroacetic acid anhydride (99%, Alfa Aesar), dibenzo[1,4]dioxin (99.0%, TCI), acetic acid (Mallinckrodt), $NaNO_2$ (97%, Alfa), anhydrous $ZnCl_2$ (98%, Sigma), terephthalic acid (Sigma), $Ni(NO_3)_2{\cdot}xH_2O$ (99.9%, Strem), and $Zn(NO_3)_2{\cdot}xH_2O$ (99%, Alfa) were used as received. Anhydrous $CoCl_2$ was prepared by placing $CoCl_2{\cdot}xH_2O$ (99.9% Alfa) under high vacuum for 24 h. Dry, deaerated acetonitrile (MeCN, HPLC grade, Sigma), dichloromethane (DCM, HPLC grade, Honeywell), *N*,*N*-dimethylformamide

(DMF, 99.8%, VWR), dimethyl sulfoxide (DMSO, ACS grade, EMD), methanol (MeOH, 99.9%, VWR), and tetrahydrofuran (THF, ACS grade, BDH), were obtained by degassing with a flow of argon gas for 30 min and by passing the solvent through two silica columns in a Glass Contour Solvent System. Dimethylacetamide (DMA, 99.9%, Sigma) and *N*-methylformamide (NMF, 99%, Alfa) were dried over molecular sieves for two days, distilled, and degassed under vacuum while frozen. N-methyl-2-pyrrolidone (NMP, 99%, Acros) was dried by removing water as the benzene azeotrope and then fractionally distilled. MFU-4*l*[164] and MOF-5[72] were prepared according to literature procedure.

6.5.2 Synthetic Aspects of Co^{2+} Exchange in MFU-4*l*

Anhydrous $CoCl_2$ (0.080 g, 0.62 mmol) was dissolved in 5 mL of solvent and added to freshly activated MFU-4*l* (15 mg, 0.012 mmol) at room temperature and left for one week. The resulting powders were collected by gravity filtration and washed with fresh solvent repeatedly until UV-Vis spectra of the mother liquor no longer showed absorption bands characteristic of Co^{2+}.

6.5.3 Synthetic Aspects of Ni^{2+} Exchange in MOF-5

$Ni(NO_3)_2{\cdot}xH_2O$ (0.250 g) was dissolved in 20 mL of the solvent and added to $Zn_4O_{13}C_{24}H_{12}$ (MOF-5) (30 mg, 4.0×10^{-5} mmol) at room temperature and left for 1 week. Afterwards, the crystals were collected by gravity filtration and soaked in fresh solvent. The solvent was replaced until UV-Vis spectra of the mother liquor no longer displayed absorptions characteristic of Ni^{2+}.

6.5.4 Physical Measurements

Diffuse reflectance UV-Vis spectra were collected between 200 – 2000 nm on a Varian Cary 5000 UV-Vis-NIR spectrometer equipped with a Praying Mantis diffuse reflectance accessory and an environmental chamber (Harrick Scientific Products) and referenced to $BaSO_4$.

Cobalt, nickel and zinc analyses were conducted at the MIT Center for Materials Science and Engineering Shared Experimental Facility (CSME-SEF) using a HORIBA Jobin ACTIVA inductively coupled plasma atomic emission spectrometer (ICP-AES). Standards were prepared from solutions purchased from ULTRA Scientific©, designated suitable for ICP analysis.

6.5.5 Computational Details

Density functional theory (DFT) calculations were carried out to identify the minima of the $MS_x{}^{2+}$ complexes ($x = 4$ for Co^{2+}, and 6 for all the other metals) as well as the M^{2+} and S (solvent) basic geometry and electronic density. The geometry optimizations have been carried out with the program package Gaussian 09 using the B3LYP functional.[172–174] The basis set employed is the 6-311G(d) for the H, C, N, O, and S atoms,[175,176] and the SDD pseudopotential with associated basis set for the Co, Ni, and Zn center.[177,178] Different spin multiplicities were tested for each metal complex; in all cases, the most stable one is characterized by the highest multiplicity: 4 for $CoS_4{}^{2+}$ complexes, 3 for $NiS_6{}^{2+}$, and 1 for $ZnS_6{}^{2+}$.

$$M^{2+}(gas) + xS(gas) \rightarrow MS_x{}^{2+}(gas) \tag{6.3}$$

$$\Delta E = E[MS_x{}^{2+}] - E[M^{2+}] - xE[S] \tag{6.4}$$

$$E_I(\text{interaction energy}) = \frac{\Delta E}{x} \tag{6.5}$$

In the case of M = Ni and Zn, $x = 6$ (octahedral complexes).

In the case of M = Co, $x = 4$ (tetrahedral complexes).

Part II

Reactivity of MOF-5

Chapter 7

Dynamic Structural Flexibility of Fe^{2+} Centers in MOF-5

7.1 Abstract

Using the design principles of cation exchange discussed in the preceding chapters, we synthesized an Fe^{2+}-exchanged variant of MOF-5. As with Ni-MOF-5 and Co-MOF-5, elemental analysis suggests that at most one Zn in every Zn_4O cluster is replaceable by Fe. Magnetic susceptibility measurements confirm that the inserted Fe atoms are indeed magnetically isolated and that they exhibit a S = 2 ground spin state. This assignment is further corroborated by the values of the 4.2 K, zero-field Mössbauer parameters that are typical of high-spin ferrous ions. The temperature dependence of the zero-field Mössbauer spectra recorded for evacuated samples can be well understood by considering the presence of a thermally accessible, low-lying orbital state for these iron sites. In contrast, the spectra of N_2-containing, non-evacuated Fe-MOF-5 samples exhibit an unusual temperature-dependent behavior that is consistent with the thermal population of distinct sites which are characterized by dissimilar quadrupole splitting values. This difference suggests that the Fe^{2+} sites of Fe-MOF-5 not only exhibit increased conformational flexibility but also that they

interact readily with redox-inert moieties such as N_2.[1]

7.2 Introduction

In the prevailing view of MOFs, the metal-containing clusters are rigid and static. Because so many structures rely on cations with inaccessible redox couples, such as Zn^{2+}, Cd^{2+}, and Mg^{2+}, the clusters are also thought to be chemically inert. Many structures do contain redox active cations, such as Co^{2+} and Fe^{2+}, but few are reported to promote redox reactivity.[19,179–181] Only recently, studies have begun to understand the role of the metal clusters during these reactions and have concluded that they can withstand electron transfer without compromising the integrity of the framework.[180–182] In this and following chapters we describe our contributions to the groundwork for performing redox reactivity at the metal-containing clusters of MOFs.

In Chapter 1, we demonstrated that MOF clusters can support unusual metal species that could undergo geometrical transformations and that these species were identifiable by spectroscopy and other physical methods. Chapter 3 built on this evidence to suggest that MOF clusters are in general less rigid than thought previously, which might explain various phenomena in the MOF field that were previously misunderstood. Here, we synthesize an Fe^{2+}-containing variant of MOF-5, termed Fe-MOF-5. By investigating this iron-based MOF, we seek to answer the next logical question: can MOF clusters promote redox transformations of guest molecules? A prerequisite of performing such reactivity is having enough structural flexibility to bind substrates. Based on analysis of the Mössbauer spectra, we propose that the inserted Fe^{2+} centers, shown in Figure 7-1, interact dynamically with N_2, leading to rapid fluctuations in the coordination environment of the iron sites. Consequently, this behavior makes Fe-MOF-5 a promising candidate for redox reactivity with other substrates and heterogeneous catalysis.

[1] At the time of writing this thesis, the work presented in this chapter was unpublished. Mössbauer experiments and analyses were conducted in collaboration with Sebastian A. Stoian.

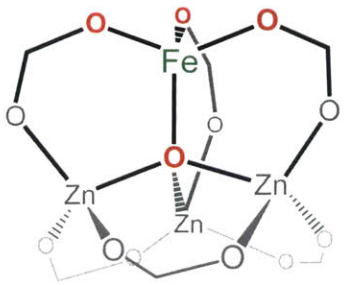

Figure 7-1: An illustration of the metal cluster of Fe^{2+}-MOF-5.

7.3 Results

Soaking crystals of MOF-5 in a DMF solution of $Fe(BF_4)_2 \cdot 6H_2O$ for one week at room temperature furnished cubic yellow crystals of Fe-MOF-5. Soaking with anhydrous halide salts, such as $FeCl_2$ and $FeBr_2$, proceeded rapidly and produced material that was inhomogeneous in appearance. We reasoned that bound aqua ligands slowed the cation-exchange process and the non-coordinating BF_4^- did not interfere, whereas halide anions might. Unlike with Ni-MOF-5 and Co-MOF-5, Fe-MOF-5 could not be synthesized through solvothermal methods. Powder X-ray diffraction of these crystals gave patterns expected of MOF-5 (Figure 7-2). Brunauer-Emmett-Teller (BET) analysis of a N_2 isotherm collected at 77 K and shown in Figure 7-3, produced an apparent surface area of 2472 m^2/g. Although this value is lower than the approximate 3300 m^2/g expected of MOF-5,[72] it is still high and its isotherm shape is consistent with microporosity. We noticed that for Fe-MOF-5, the exchange occurs faster than in Ni-MOF-5 and Co-MOF-5, which might compromise the pore structure and result in lower BET values.

Insertion of Fe^{2+} into the MOF-5 cluster leads to a species that has little precedent among materials and molecules. When viewed as chelating ligand, the MOF-5 cluster is both dianionic and tripodal with C_3 symmetry, as shown in Figure 7-1. Few ligands are known with this combination.[183–185] Also, Fe^{2+}-based MOFs are generally uncommon.[52,180,186,187] Furthermore, the weak-field carboxylates are expected to induce a high-spin ferrous center, poised well for reducing substrates. To establish

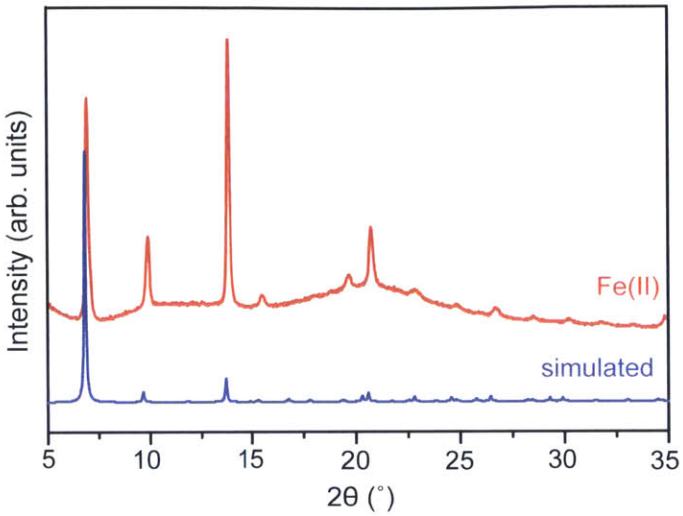

Figure 7-2: Powder X-ray diffraction pattern of Fe^{2+}-MOF-5.

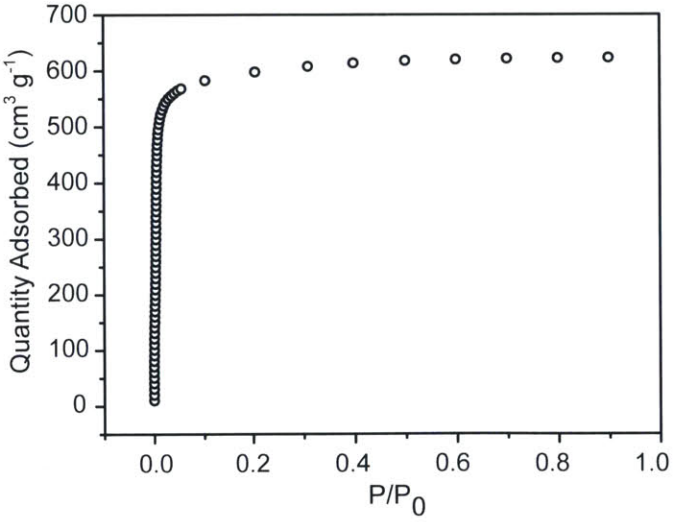

Figure 7-3: N_2 isotherm at 77 K of Fe^{2+}-MOF-5.

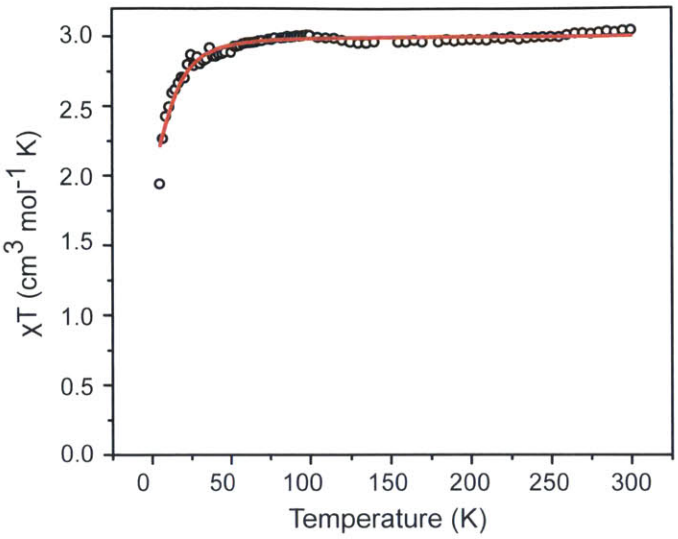

Figure 7-4: Temperature dependent magnetic susceptibility of Fe-MOF-5 under an applied field of 1000 G. Data are shown in open black circles, and the fit is overlaid in red.

the spin ground state of the iron sites, we measured the magnetic susceptibility of Fe-MOF-5 from 5-300 K, cooled under zero applied field. As shown in Figure 7-4, the material displays a χT of 3.04 cm^3 mol^{-1} K, which is close to the 3.00 cm^3 mol^{-1} K spin-only value expected for a S = 2 system. Our best fit to the data is shown as a red trace and was obtained using a standard spin-Hamilton model as implemented in julX.[2] This curve was obtained using $g_{iso} = 2$, an axial zero field splitting tensor ($E/D = 0$) and $|D| = 11$ cm^{-1}.

To probe the electronic structure of the MOF-incorporated iron sites, we used ^{57}Fe Mössbauer spectroscopy. Thus, we recorded a zero-field, 80-K spectrum using a standard 8 mCi ^{57}Co source. To our surprise, even after several weeks of data collection, the signal we observed was barely larger than twice the noise level of the baseline. Consequently, to improve the statistics of our spectra we switched to a 100 mCi source. Furthermore, we optimized the effective thickness of the absorber, that is, the amount of ^{57}Fe in the path of the γ rays, to maximize the signal strength while at the same time minimizing the non-resonant absorption of the 14.4-keV radiation.

[2]E. Bill, Max Planck Institute for Chemical Energy Conversion in Muelheim, Germany, 2013. Available from the author by e-mail to ebill@gwdg.de.

The relative strength of a Mössbauer spectrum is determined not only by the intensity of the ^{57}Co source and the amount of ^{57}Fe contained by the sample but also by the fraction of the incoming radiation that is non-resonantly absorbed. Thus, the signal-to-noise (STN) ratio is dependent on the sample thickness t', such that $\mathrm{SNT}(t') \propto t'e^{-t'\mu_e/2}$, where μ_e represents the total mass absorption coefficient of the sample. This coefficient is an additive quantity and can be easily calculated from the sum of the individual mass absorptions coefficients of the elements present in the sample weighted by their concentration. At 14.41 keV, the absorption coefficient for Zn is 92 $\mathrm{cm^2\ g^{-1}}$, whereas for Fe it is only 75 $\mathrm{cm^2\ g^{-1}}$.[188] With at least 3 Zn for every Fe in the material, most irradiated 14.41-keV light was not available for Fe to absorb.

After carefully optimizing the amount of sample needed to counterbalance the Zn and Fe content, we acquired zero-field Mössbauer spectra for a non-evacuated sample at temperatures between 4.2 K and 100 K, in Figure 7-5. Prior to recording these spectra, the neat Fe-MOF-5 sample was stored and mounted in the spectrometer at 77 K under liquid N_2, which we assumed penetrated the pores of Fe-MOF-5. Under these conditions, consequently, the MOF was able to soak in as much nitrogen it could absorb. At 4.2 K we observe a well-defined quadrupole doublet with an isomer shift, δ, of 1.156(3) mm/s, a quadrupole splitting, ΔE_Q, of 3.02(2) mm/s, and a full width at half maximum, Γ, of 0.26(1) mm/s. These values are typical of high-spin Fe^{2+} sites that have a tetrahedral coordination environment. Moreover, the rather narrow linewidths demonstrate that at 4.2 K the coordination environment of all iron sites is fairly homogeneuous. Interestingly, increasing the temperature leads to both an overall drop in the intensity of these spectra and also to a dramatic line broadening that is concomitant with a decrease in the apparent value of the quadrupole splitting. For example, inspection of the 70-K spectrum reveals that while its isomer shift value of 1.1(1) mm/s is essentially unchanged from that observed at 4.2 K, ΔE_Q contracts to 1.0(1) mm/s and Γ broadens to 0.80(6) mm/s. Close examination of these spectra reveals that above 4.2 K some of these resonances exhibit fine structure. This observation suggests that the increase in temperature induces a differentiation in the coordination environment of the iron ions. The solid gray lines

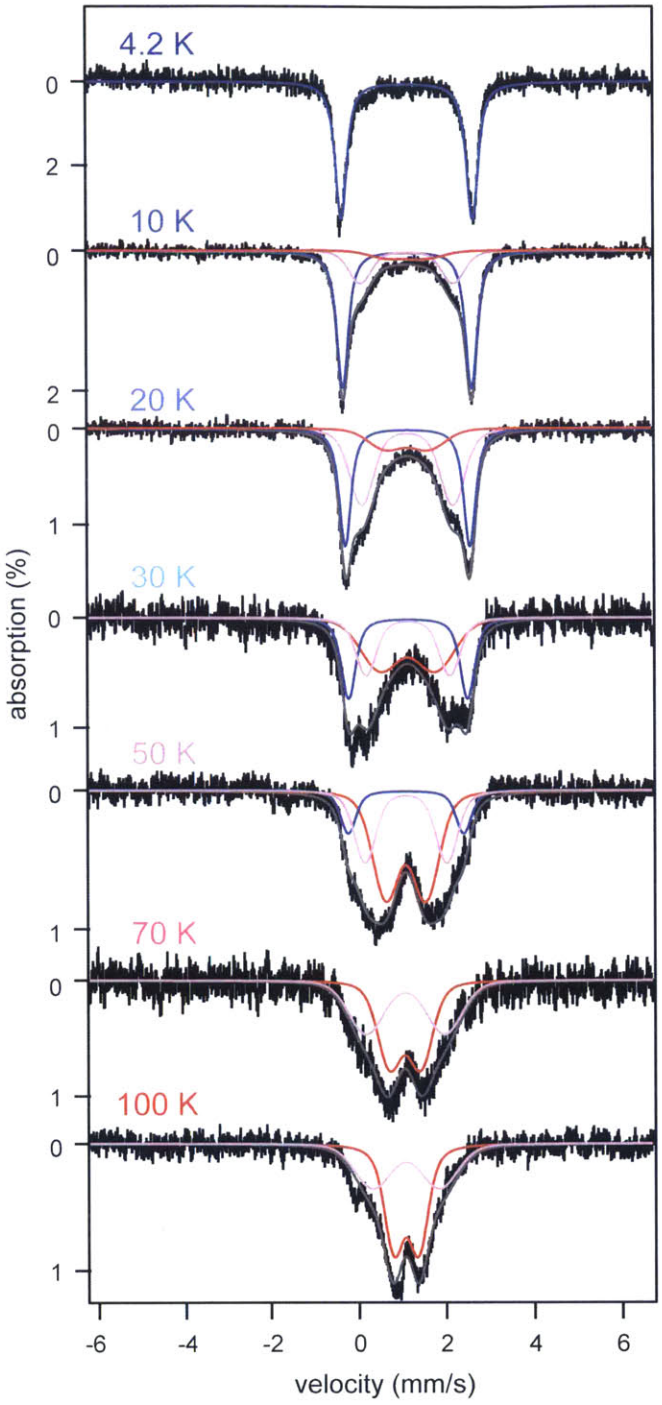

Figure 7-5: Temperature-dependence of the zero-field Mössbauer spectra recorded for a non-evacuated, N_2-soaked Fe-MOF-5 sample. The solid gray lines are simulations obtained considering a distribution in ΔE_Q values. The blue, pink and red traces illustrate the three Gaussian components of the ΔE_Q distribution.

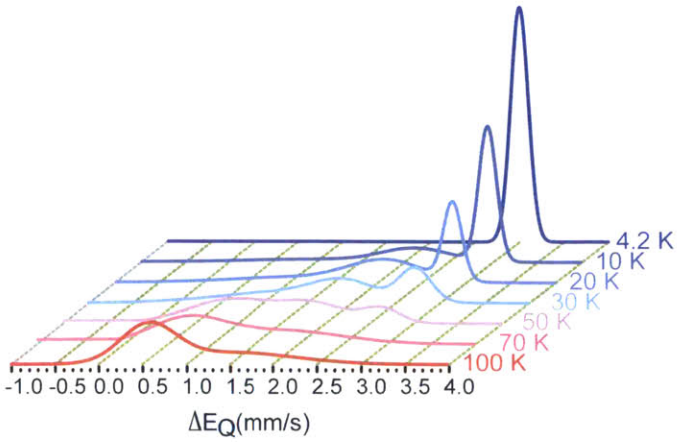

Figure 7-6: The temperature-dependence of the quadrupole splitting distribution observed for the zero-field Mossbauer spectra of a non-evacuated Fe-MOF-5 sample. The colors for each temperature match those shown in Figure 7-5.

overlaid over the experimental data are simulations which were obtained by using the model of multidimensional hyperfine parameter distributions developed by Rancourt et al.[189] For this model, the distribution of a hyperfine splitting parameter, in this instance ΔE_Q, is described using a sum of individual Gaussian components. Thus, the temperature-dependent spectra could be rationalized only by considering three distinct components centered at ΔE_Q = 2.8(2) mm/s, 1.9(1) mm/s, and 1.2(2) mm/s. The subspectra generated by each individual component are shown as blue, pink, and red traces overlaid over the experimental data of Figure 7-5, and the temperature dependence of the overall distribution in the ΔE_Q value is shown in Figure 7-6. Finally, analysis of the field-dependent spectra recorded at 4.2 K indicated the presence even at this temperature of two distinct spectral components (Figure 7-7), due to dissimilar ^{57}Fe hyperfine coupling constants.

To eliminate the possibility of O_2 contamination in the N_2 causing the observed Mössbauer behavior, we collected a Mössbauer spectrum of Fe-MOF-5 deliberately exposed to O_2. Freshly cleaned Fe-MOF-5 was heated to 180 °C at 10^{-5} torr for 24 h, then backfilled with 1 atm of O_2 and sealed for 6 h. After being placed under vacuum, it was prepared for Mössbauer spectroscopy in a manner identical to the previous Fe-MOF-5 sample. As shown in Figure 7-8, the resulting spectrum cannot account

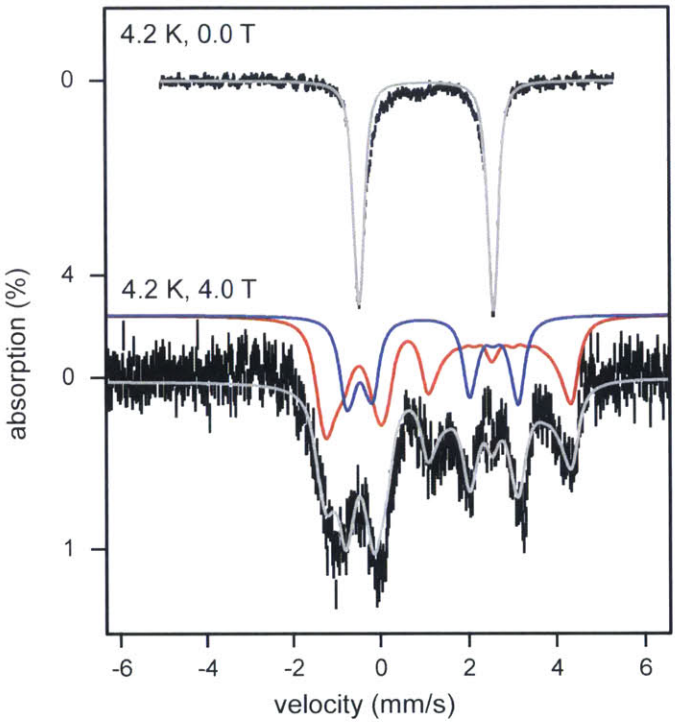

Figure 7-7: 4.2-K, field-dependent Mössbauer spectra recorded for a non-evacuated Fe-MOF-5 sample. The blue and red traces overlaid over the 4-T spectrum are spectral simulations obtained using a S = 2 spin-Hamiltonian. These two components are distinguished from one another by an hyperfine coupling tensor for which one of the principal components is larger (red) by $\Delta A_y/g_n\beta_n \sim 4.5$ T than for the other (blue).

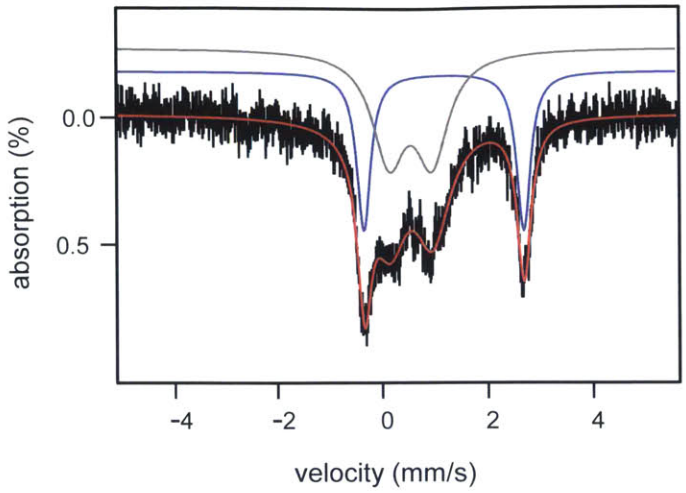

Figure 7-8: The 4.2-K, 0-T Mössbauer spectrum of Fe-MOF-5 after exposure to O_2. The simulated spectrum which is shown in red arises from the sum of two components. Thus, the component shown in blue accounts for the Fe^{2+} sites and the one shown in gray for the Fe^{3+} sites present in the sample.

for the anomalous temperature dependence. While the 4.2-K, 0-T spectrum of the previous sample exhibits a single, well-defined quadrupole doublet, we observe two nested quadrupole doublets for the O_2-exposed sample. Whereas the outer doublet is essentially identical to the starting material, the inner doublet is characterized by δ =0.55 mm/s and ΔE_Q =0.81 mm/s, consistent with high spin ferric.

To assess the effect of adsorbed guest molecules on the iron sites in Fe-MOF-5, we placed the sample that produced the anomalous temperature dependence under high vacuum for approximately 24 h, brought it into an Ar-filled glovebox, and then placed it under Paratone® N oil. The resulting spectra, shown in Figure 7-9, display a temperature dependence that is quite different from the sample under N_2. Although the ΔE_Q also decreases at higher temperature and the line width expands, the effect is much less severe and the spectra appear as a single species converting into another. The stark difference before and after evacuation of the MOF is best illustrated by Figure 7-10, which shows a side-by-side comparison of the spectra recorded at 4.2 K and 70 K. Table 7.1 shows that even at 4.2 K, the Mössbauer parameters are not the same.

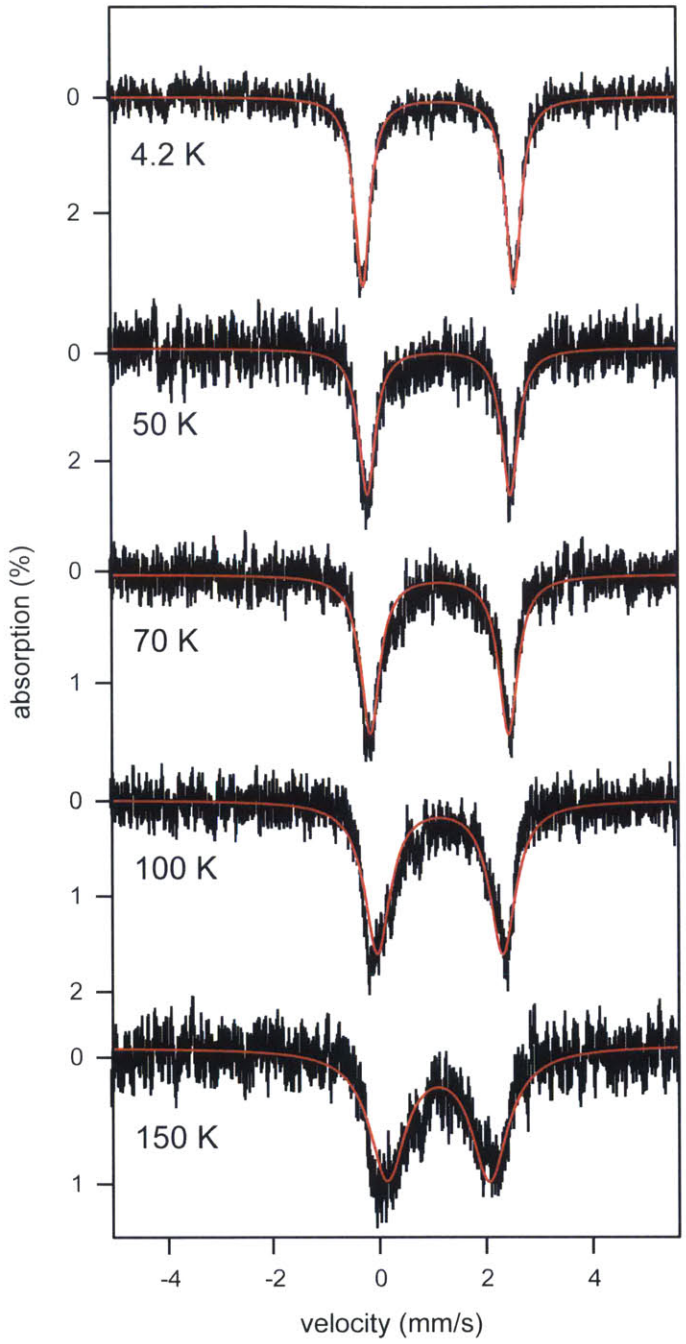

Figure 7-9: Temperature dependence of the zero-field Mössbauer spectra recorded for the evacuated Fe-MOF-5 sample. The solid red lines are simulations obtained using a single quadrupole doublet. The temperature dependence of the quadrupole splitting is shown in Figure 7-11

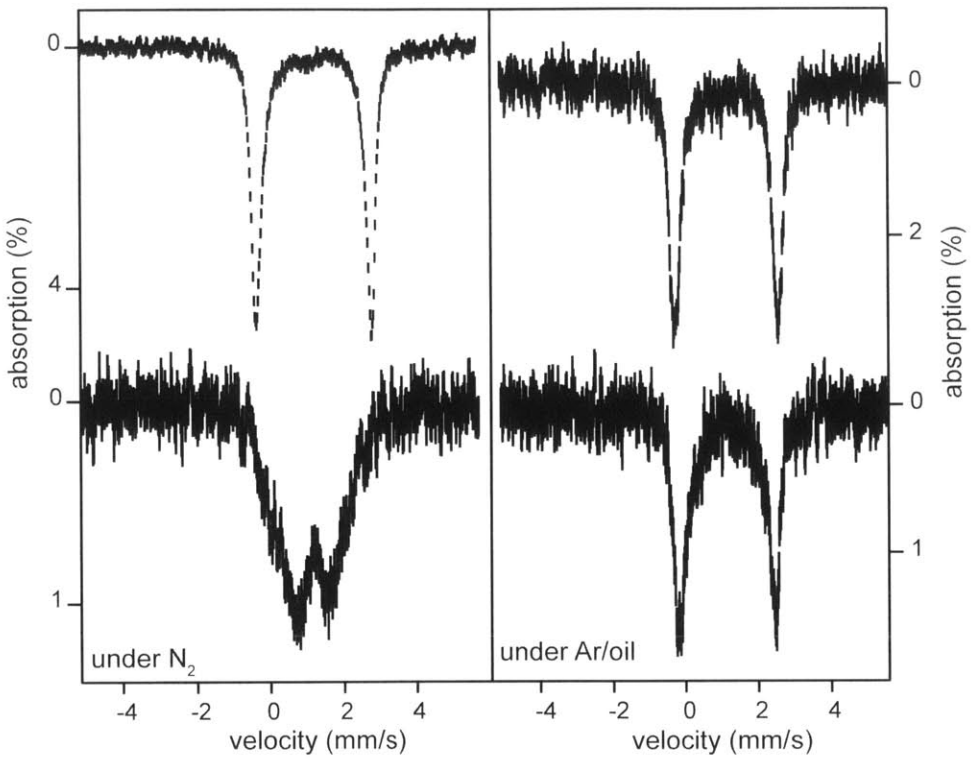

Figure 7-10: Comparison of the zero-field Mössbauer spectra recorded at 4.2 (top) and 70 K (bottom) of the evacuated (right) and non-evacuated (left) Fe-MOF-5 samples.

	δ	ΔE_Q	Γ
non-evacuated	1.156(3)	3.02(2)	0.26(1)
evacuated	1.15(1)	2.83(2)	0.33(1)

Table 7.1: Comparison of Mössbauer parameters determined at 4.3 K for the evacuated and non-evacuated Fe-MOF-5. Values are presented in mm/s.

7.4 Discussion

As a starting point for our analysis, we employed density functional theory (DFT) to explore the electronic and Mössbauer parameters predicted for the ground state of the iron sites of Fe-MOF-5. Rather than consider the entire lattice, we employed a truncated model compound with the molecular formula $FeZn_3O(O_2C\text{–}C_6H_5)_6$. Following the computational methodology developed by Neese,[190] to enhance the accuracy of the predicted quadrupole splitting and electron density ρ, we used an expanded triple ζ valence basis set and BP86 functional. Using the same initial structure and setting a +2 formal charge on the molecule, we obtained optimized geometries of the S = 0, 1, or 2 states. We found that not only is the S = 2 state the lowest in energy, but also that the δ and ΔE_Q values predicted for this state are the closest to the experimental values observed at 4.2 K, namely 0.88 and 3.143 mm/s, respectively. Although the isomer shift deviates by 24% from the experimental value, this error is sensitive to the quality of the calibration curve used in correlating calculated ρ to isomer shift. Furthermore, the quadrupole splitting, which is calculated directly, is within only 5% of the experimental value.

With further support that the Fe centers in Fe-MOF-5 are isolated and high-spin ferrous, we sought to explain the anomalous temperature-dependent Mössbauer spectra. Initially we considered the possibility that the data could be attributed to thermal population of different spin states, but this explanation was not reflected in the magnetic susceptibility, which showed temperature dependence as a consequence of negative zero-field splitting instead. Also, altering the spin state would lead to greater changes in the isomer shift.

For the sample under N_2 and the other under Paratone® N oil, the Mössbauer spectra are better explained as the consequence of a fluctuating electric field gradient at the Fe nucleus. Based on reports of Fe subject to various dynamic processes, Tjon and Blume put forth a theoretical model using a time-dependent Hamiltonian that reproduced the line shapes of experimental spectra.[191,192] It specifically accounted for Jahn-Teller distortions and vacancy hopping where the electric field gradient jumps at random in the x, y, and z directions. These spectra often displayed intense transmission at low temperature with well-defined doublets, then diminished and collapsed at higher temperature, akin to what we were observing.

This phenomenon seemed appropriate to understanding the observed Mössbauer spectra Fe-MOF-5, so we considered the possible dynamical processes and why the spectra were affected by the presence of N_2. In a report by Lindley et al., the Mössbauer spectra of Fe-doped AgCl displayed a doublet at 80 K that converged toward a single band at 458 K without much change in the peak width or absorption.[193] The authors attributed this behavior to the charge-balancing vacancy hopping at random across the crystal, therefore disrupting the ligand field around Fe and causing its electric field gradient to approach zero. Because this explanation invokes a level of geometric shuffling beyond what should be possible in Fe-MOF-5, we do not think it is relevant.

The spectra of Fe-MOF-5 collected under Ar are best fit to a model used to understand the temperature-dependent spectra of FeX_4^{2-}, where X = halides. Work by Edwards et al. has shown that in the solid state, these ferrous salts undergo a Jahn-Teller distortion so that the e orbital set expected of a T_d point group is split by some amount, Δ, that is near k_BT.[194] Lowering the symmetry of the ferrous sites forces the β-spin electron to localize in either $d_{x^2-y^2}$ or d_{z^2}, which contribute expectation values of either $+4/7$ or $-4/7\ e\langle r^{-3}\rangle$ to the zz component of the electric field gradient tensor, V, where e is the proton charge and $\langle r^{-3}\rangle = 5a_0^{-3}$. Because the splitting Δ is on the order of k_BT, however, the β-spin electron populates the next low-lying d orbital, which has an expectation value of V_{zz} that is equal and opposite in magnitude. As a result, the electric field gradient approaches zero at

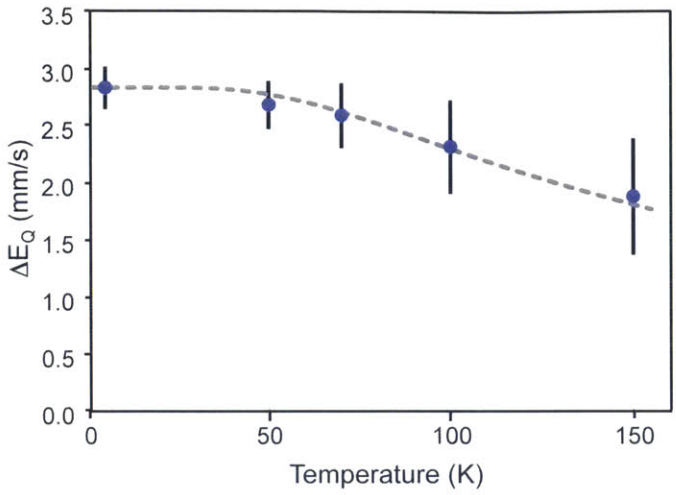

Figure 7-11: The temperature-dependence of the ΔE_Q determined for the evacuated Fe-MOF-5 sample. Data is shown in blue circles with error bars, and the fit is shown as a dashed gray line.

higher temperature. This model also provides a relation to extract Δ. As shown in Figure 7-11, plotting ΔE_Q for Fe-MOF-5 prepared under Ar versus temperature, t, fits well to the relation $\Delta E_Q(t) = \Delta E_Q(4.2\text{ K})\tanh(\Delta/2k_BT)$. Solving for Δ gives an energy splitting of 160 cm^{-1}, which is lower than the 200 cm^{-1} of room temperature.

Because Fe in the Ar-prepared sample is therefore well-described as an isolated ion, the magnetic Mössbauer spectra can be fit to a single species and interpreted further. We could assess the fine structure of the quintet ground state by recording a series of field-dependent spectra and analyze them using a standard S = 2 spin-Hamiltonian. Thus our analysis revealed that $\Delta E_Q < 0$, $\eta = 0.4(2)$ and that $D = 9(1)$ cm^{-1}, $E/D = 0.15(5)$, $g_{x,y} = 2.1(1)$, g_z =2.0, $A_x/g_n\beta_n$ = –14 T, $A_y/g_n\beta_n$ = –10 T, $A_z/g_n\beta_n$ = –24 T. Furthermore, the 2.0 T spectrum in Figure 7-12 shows the appearance of the doublet from the $|\pm 1/2\rangle \rightarrow |\pm 1/2\rangle$ transitions sits on the negative side, so that we can infer that $V_{zz} < 0$ and β-spin resides in d_{z^2} in the ground state.

Clearly, a different dynamic process is needed to describe Fe-MOF-5 under N_2. A Jahn-Teller distortion alone cannot account for the extreme temperature dependence of the quadrupole splitting. A more appropriate model may be similar to that invoked to described the spectra of $[Fe(\eta^6\text{-}C_6H_6)(\eta^5\text{-}C_5H_5)][AsF_6]$ and related com-

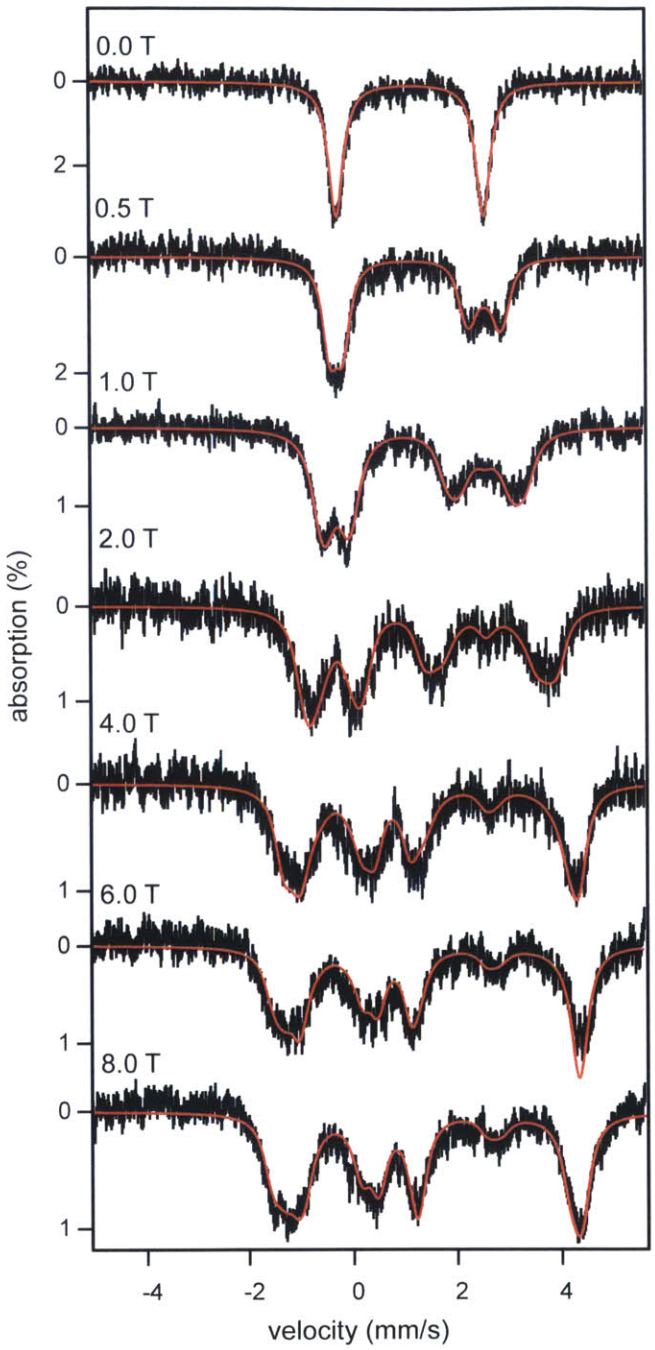

Figure 7-12: The field-dependent Mössbauer spectra recorded at 4.2 K for the evacuated Fe-MOF-5 under Ar and Paratone® N oil. The red traces overlaid over the experimental data are simulations obtained using S = 2 spin-Hamiltonian and the parameters listed in the text.

pounds.[195,196] In the solid state, the AsF_6 ions encapsulate the ferrous ion in anionic cubic cage. At low temperature the cation orients along a specific axis within the cage, thereby preserving a non-zero electric field gradient. As the sample warms, however, the sandwich molecules fluctuate randomly along different axes, causing the electric field gradient to average to zero. In this example, the dynamic process involves the Fe nucleus moving at random along x, y, and z at smaller distances than in Fe-doped AgCl.

If nuclear displacement explains the Mössbauer spectra of Fe-MOF-5 under N_2, then we might infer that the Fe^{2+} sites interact with N_2. Because the isomer shift remains nearly constant, this interaction cannot involve electron transfer or significant changes to the spin state and coordination number around Fe. Nevertheless, the effect is reproducible. The presence of multiple species fit to the spectra in Figure 7-5 also suggests the interaction is uneven across all Fe sites in the MOF.

7.5 Conclusion

Through characterization of Fe^{2+}-exchanged MOF-5, we provide evidence that the inserted ferrous sites posses both the flexibility and reactivity to interact with N_2 and that such subtle phenomena can be documented with precision. These results lay the groundwork of the following chapters, where MOF-5 is shown to host other redox-active cations in unusual environments and support electron transfer reactions at the metal nodes and at small molecule substrates.

7.6 Methods

Unless otherwise stated, all materials were treated as air sensitive and were manipulated using common Schlenk and inert atmosphere glovebox technique.

7.6.1 Materials

Dry, deaerated dichloromethane (DCM, HPLC grade, Honeywell) and DMF (99.8%, VWR) were obtained by degassing with a flow of argon gas for 30 min and by passing the solvent through two silica columns in a Glass Contour Solvent System. 70% HNO_3 (ICP-AES grade, EMD), $Fe(BF_4)_2 \cdot 6H_2O$ (97% Sigma-Aldrich), and $Zn(NO_3)_2 \cdot 6H_2O$ (99%, Alfa Aesar), and terephthalic acid (Sigma-Aldrich) were used without further modification. MOF-5 was prepared according to literature.[72]

7.6.2 Physical Measurements

Powder X-ray diffraction (PXRD) patterns were recorded on a Bruker Advance II diffractometer equipped with $\theta/2\theta$ Bragg-Brentano geometry and Ni-filtered Cu-K_α radiation ($K_{\alpha 1}$ = 1.5406 Å). The tube voltage and current were 40 kV and 40 mA, respectively. Samples for PXRD were prepared by placing a thin layer of samples on a zero-background silicon crystal plate supported on a cup with dome that screwed-on with a rubber O-ring fitting.

A Micromeritics ASAP 2020 Surface Area and Porosity Analyzer was used to measure nitrogen adsorption isotherms. Oven-dried sample tubes equipped with TranSeals™(Micrometrics) were evacuated and tared. Samples were transferred to the sample tubes, heated to 200 °C for 12 h, and held at that temperature until the outgas rate was less than 2 mtorr/minute. The evacuated sample tubes were weighed again and the sample mass was determined by subtracting the mass of the previously tared tube. N_2 isotherms were measured using liquid nitrogen baths (77 K). UHP grade (99.999% purity) N_2 and He, oil-free valves and gas regulators were used for all free space corrections and measurements.

Iron and zinc analyses were conducted at the MIT Center for Materials Science and Engineering Shared Experimental Facility (CSME-SEF) using a HORIBA Jobin ACTIVA inductively coupled plasma atomic emission spectrometer (ICP-AES). Standards were prepared from solutions purchased from ULTRA Scientific©, designated suitable for ICP analysis. Elemental analysis was performed by Complete Analysis

Laboratories, Parsippany, NJ.

Magnetic Susceptibility

Magnetic data were collected using a Quantum Design MPMS-XL SQUID magnetometer. A gelatin capsule was filled with evacuated crystals of $Fe_{0.67}Zn_{3.33}O$(1,4-benzene dicarboxylate)$_3$ to obtain susceptibility data. DC susceptibility measurements were obtained under a DC field of 1000 Oe between 5 K and 300 K. All data were corrected for diamagnetic contributions from the capsule, and the sample using Pascal's constants.[89]

Mössbauer Susceptibility

The samples investigated here consisted of unenriched, natural abundance iron containing 30–40 mg Fe-MOF-5 powder contained in a custom-made Delrin® cups. The samples were prepared in Cambridge, MA and shipped to Tallahassee, FL under N_2 in a standard, air-free, round bottom flask that was sealed using a ground glass joint and stopper. The shipping glass vial was cooled at 77 K by using liquid nitrogen and was opened while cold. Subsequently, the samples were stored and handled under liquid nitrogen. The variable-field, variable-temperature spectra were recorded using a constant acceleration spectrometer. The spectrometer was fitted with a flow-type Janis 8DT cryostat that was cooled with liquid helium and was equipped with an 8 T superconducting magnet. Thus the temperature could be varied from 4.2 to 250 K. The magnetic field was applied parallel to the 14.4-keV radiation. The source consisted of 100 mCi ^{57}Co dispersed in a rhodium foil. The 4.2-K spectra were recorded by flooding the sample space with liquid helium. At higher temperatures the spectra were recorded in a flow of helium gas that was controlled using a needle-type valve. The sample temperature was measured using a Cernox® sensor and was maintained using a 50-Ω heater powered by a Cryocon 32B temperature controller. The isomer shifts are reported against the centroid of a α-iron metal foil spectrum recorded at room temperature. The spectra were analyzed in the framework of a standard S = 2 spin-Hamiltonian and using the Voigt-based model of assessing a distribution in

hyperfine splitting parameters developed by Rancourt et al. as implemented in by the WMOSS spectral analysis software (See Co., formerly Web Research Co., Edina, MN).

7.6.3 $Zn_{4-x}Fe_xO_{13}C_{24}H_{12}$ (Fe-MOF-5)

Evacuated MOF-5 crystals (490 mg, 0.636 mmol) were suspended in 40 mL of DMF and allowed to sit for one minute. A solution of 990 mg (2.93 mmol) of $Fe(BF_4)_2 \cdot 6H_2O$ in 20 mL of DMF was added to this suspension in a 100 mL jar. This material were stirred gently for a week and subsequently washed and activated in a manner typical for MOF-5 to give cubic yellow crystals.

7.6.4 Partial Oxidation of Fe-MOF-5 by O_2

A dry 10 mL Schlenk flask was charged with 100 mg of yellow Fe-MOF-5 and heated to 120 °C at 10^{-5} torr for 18 h. While maintaining heat, the flask was then backfilled with 1 atm of dry O_2 and sealed for 6 h, at which point the material appeared bright orange. The flask was returned to vacuum, then brought into an Ar-filled glovebox to prepare as a sample for Mössbauer spectroscopy.

7.6.5 Calculations

The ORCA 2.9.1 software package was used for all computations.[197] Calculations were done using the resolution of the identity (RI) at the spin-unrestricted level using the pure DFT Becke-Perdew functional (BP86) and all-electron Gaussian basis sets developed by the Ahlrichs group, with TZV(p) (for H), TZV(2d) (for C, N, and O), and TZV(2pf) (for Zn).[93,94] During geometry optimizations, TZV(2pf) was used for Fe, as well, but in simulating Mössbauer parameters, the Fe basis set was expanded as described previously.[190] To model Fe-MOF-5, we considered a compound with the formula $FeZn_3O(O_2C\text{–}C_6H_5)_6$, whose starting geometry was taken from the crystallographically-determined structure of MOF-5. All atomic positions were optimized, with the 1 and 4 carbons atoms on each benzoate fixed in place. While the

quadrupole splitting could be computed directly, calculating the isomer shift required a calibration curve. The geometries of $FeCl_4^-$, $FeCl_4^{2-}$, $Fe(H_2O)_6^{2+}$, $Fe(H_2O)_6^{3+}$, and FeO_4^{2-} were optimized, using their reported crystal structures as starting points. The electron densities at the Fe nuclei were then plotted against their reported isomer shifts. The linear fit of this plot provided a relation to compute the isomer shift of Fe-MOF-5 from its calculated electron density.

Chapter 8

Redox-active Cations within MOF-5

8.1 Abstract

Few reports have explored the ability of metal nodes in MOFs to mediate electron transfer. With weak and unusual ligand fields, these clusters are well poised for redox reactivity, but typical synthetic conditions are often incapable of preserving low oxidation states at the metal. In this chapter, we demonstrate that $MZn_3O(O_2C–)_6$ clusters in Zn_4O(1,4-benzenedicarboxylate)$_3$ (MOF-5) can support the first examples of V^{2+} and Ti^{3+} in a MOF, by employing cation exchange in a manner similar to what was shown with Co^{2+}, Fe^{2+}, and Ni^{2+} in previous chapters. We also report other variants of MOF-5 with Cr^{2+}, Cr^{3+}, and Mn^{2+} at the metal nodes. The inserted metal ions are coordinated within an unusual all-oxygen trigonal ligand field and are accessible to both inner- and outer-sphere oxidants: Cr^{2+}- converts into Cr^{3+}-substituted MOF-5, while Fe^{2+}-MOF-5 activates nitric oxide (NO) to produce an unusual Fe-nitrosyl complex.[1]

[1]A portion of this work appeared previously in Brozek, C. K. and Dincă, M. *J. Am. Chem. Soc.* **2013**, *135*, 12886 and is reproduced here with permission from the American Chemical Society.

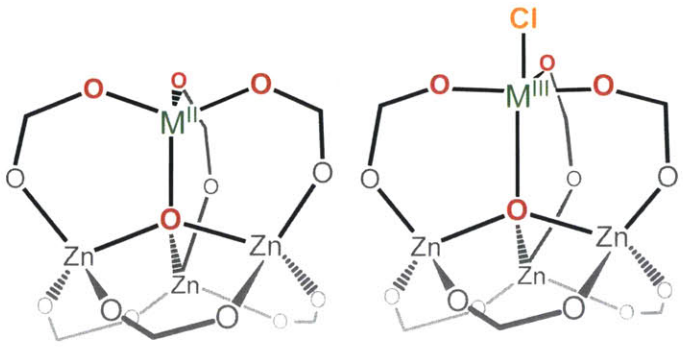

Figure 8-1: The MOF-5 cluster acts as a unique tripodal chelating ligand for pseudo-tetrahedral V^{2+}, Cr^{2+}, Mn^{2+}, Fe^{2+}, Co^{2+}, and Ni^{2+} and pseudo-trigonal bipyramidal Ti^{3+}, V^{3+}, and Cr^{3+} with terminal chloride moieties.

8.2 Introduction

Reactivity and catalysis studies of SBUs in MOFs have centered on their Lewis-acid properties,[198] while studies of their redox reactivity remain an area for exploration.[17,180–182,199] The dearth of SBU redox reactivity studies is partly due to the general incompatibility of reduced metal cations such as Ti^{3+}, V^{2+}, and Cr^{2+} with the typical conditions required for MOF synthesis. Among the thousands of reported MOFs, none are known to contain Ti^{3+}[2] or V^{2+},[200,201] while those made from Cr^{2+} or Fe^{2+} are rare.[52,180,186,187,202,203] Employing reactive cations to access SBUs without molecular precedent would enable novel coordination chemistry and redox catalysis.[16] Herein, we report that Ti^{3+}, V^{2+}, V^{3+}, Cr^{2+}, Cr^{3+}, and Mn^{2+}, in addition to Fe^{2+} as discussed in the preceding chapter, incorporate into the SBUs of MOF-5 using mild synthetic methods. The $MZn_3O(O_2C–)_6$ clusters in MOF-5 act as structurally flexible dianionic pseudo-tetrahedral or trigonal bipyramidal all-oxygen coordination spheres. We demonstrate that MOF-5,[55] when viewed as a ligand, enables reactions at the inserted metal ions with both inner- and outer-sphere oxidants—requisites of small-molecule activation. Thus, we provide the first evidence of redox activity in MOF-5 analogues with the stoichiometric single-electron oxidation of Cr^{2+}-MOF-

[2]The existence of Ti^{3+} has been observed during photoreduction studies with Ti^{4+}-containing MOFs.

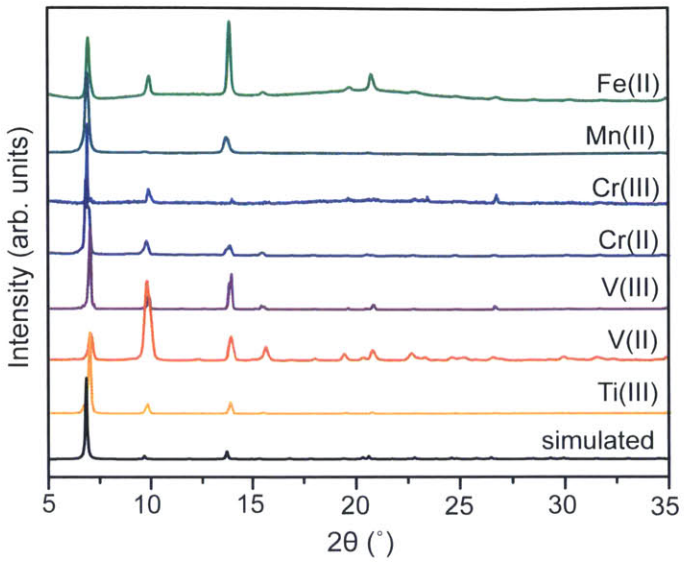

Figure 8-2: Powder X-ray diffraction patterns of MOF-5 exchanged with Ti^{3+}, V^{3+}, V^{2+}, Cr^{3+}, Cr^{2+}, Mn^{2+}, and Fe^{2+} juxtaposed the calculated pattern of MOF-5.

5, and demonstrate that Fe-MOF-5 activates NO via electron transfer from the Fe center.

8.3 Results and Discussion

The redox-active MOF-5 analogues, denoted M-MOF-5 and ClM-MOF-5 for divalent and trivalent inserted metal ions, respectively, were accessed using cation exchange,[99] at room temperature under conditions mirroring those we reported for the isola-

ClM-MOF-5	**Molecular Formula**
ClTi-MOF-5	$Zn_{3.91}Ti_{0.09}Cl_{0.09}O_{13}C_{24}H_{12}\cdot(CH_2Cl_2)$
V-MOF-5	$Zn_{3.83}V_{0.17}O_{13}C_{24}H_{12}$
ClV-MOF-5	$Zn_{3.80}V_{0.20}Cl_{0.20}O_{13}C_{24}H_{12}$
Cr-MOF-5	$Zn_{3.06}Cr_{0.94}O_{13}C_{24}H_{12}$
ClCr-MOF-5	$Zn_{2.59}Cr_{1.41}Cl_{1.41}O_{13}C_{24}H_{12}\cdot(DMF)_{0.4}$
Mn-MOF-5	$Zn_{3.58}Mn_{0.42}O_{13}C_{24}H_{12}$
Fe-MOF-5	$Zn_{3.04}Fe_{0.96}O_{13}C_{24}H_{12}$

Table 8.1: Molecular formulas of (Cl)M-MOF-5 based on ICP-AES results and C, H, N, Cl elemental analysis

tion of Ni-MOF-5.[16] Although Ni-MOF-5 could be obtained by direct solvothermal synthesis from $Ni(NO_3)_2 \cdot xH_2O$ and $Zn(NO_3)_2 \cdot xH_2O$, attempts to synthesize (Cl)M-MOF-5 analogues directly by the reaction of terephthalic acid with $Zn(NO_3)_2 \cdot xH_2O$ and Ti^{3+}, $V^{2+/3+}$, Cr^{2+}, Mn^{2+}, or Fe^{2+} salts were unsuccessful. Instead, soaking crystals of MOF-5 in concentrated DMF solutions of $VCl_2(pyridine)_4$, $CrCl_2$, $MnCl_2$, and $Fe(BF_4)_2 \cdot 6H_2O$ for one week furnished M-MOF-5 (M = V^{2+}, Cr^{2+}, Mn^{2+}, or Fe^{2+}), while identical procedures involving $TiCl_3 \cdot 3THF$, $VCl_3 \cdot 3THF$, or $CrCl_3 \cdot 3THF$ produced ClM-MOF-5 (M = Ti^{3+}, V^{3+}, or Cr^{3+}) (Figure 8-1). Powder X-ray diffraction patterns of the (Cl)M-MOF-5 materials, shown in Figure 8-2, confirmed that the materials retained the MOF-5 morphology.

We determined the degree of cation substitution and the formula of each new MOF-5 analogue by inductively coupled atomic emission spectroscopy (ICP-AES) and elemental microanalysis (EA). As shown in Table 8.1, the degree of exchange after one week under otherwise identical conditions varied drastically. Because the rate of solvent and ligand exchange depends on the nature of each cation, these data suggest that the ion metathesis reactions do not reach equilibrium after one week. Instead, the degree of exchange is kinetically controlled by the stability constants of each substituting cation.[49] The agreement between ICP-AES analysis of the metals and the C, H and N analysis by EA confirms that the cations exchanged into the Zn_4O clusters and did not simply reside in the pores. Furthermore, we confirmed the absence of halides or other anions that would be necessary for charge balance if metal addition, rather than substitution occurred. These results are consistent with the structural assignment in Ni-MOF-5 and Co-MOF-5 where definitive substitution into the SBUs had been demonstrated previously.[16,63,204] Energy-dispersive X-ray (EDX) spectra and optical microscope images of these samples depict the inserted metal ions distributed throughout the crystals, not solely at the surface (see Figures 8-3 through 8-9), confirming that homogeneous substitution occurs throughout the entire crystal.[3] Because the shape of the crystals and the total crystalline mass did not

[3]Definitive EDX spectra could not be obtained for Cr-MOF-5, ClV-MOF-5 and V-MOF-5 since the L edge of V and Cr nearly overlaps with the K edge of O. Detecting for Cr and V at the K edge by radiating at high energy destroyed the samples, making data collection impossible, yet sufficient

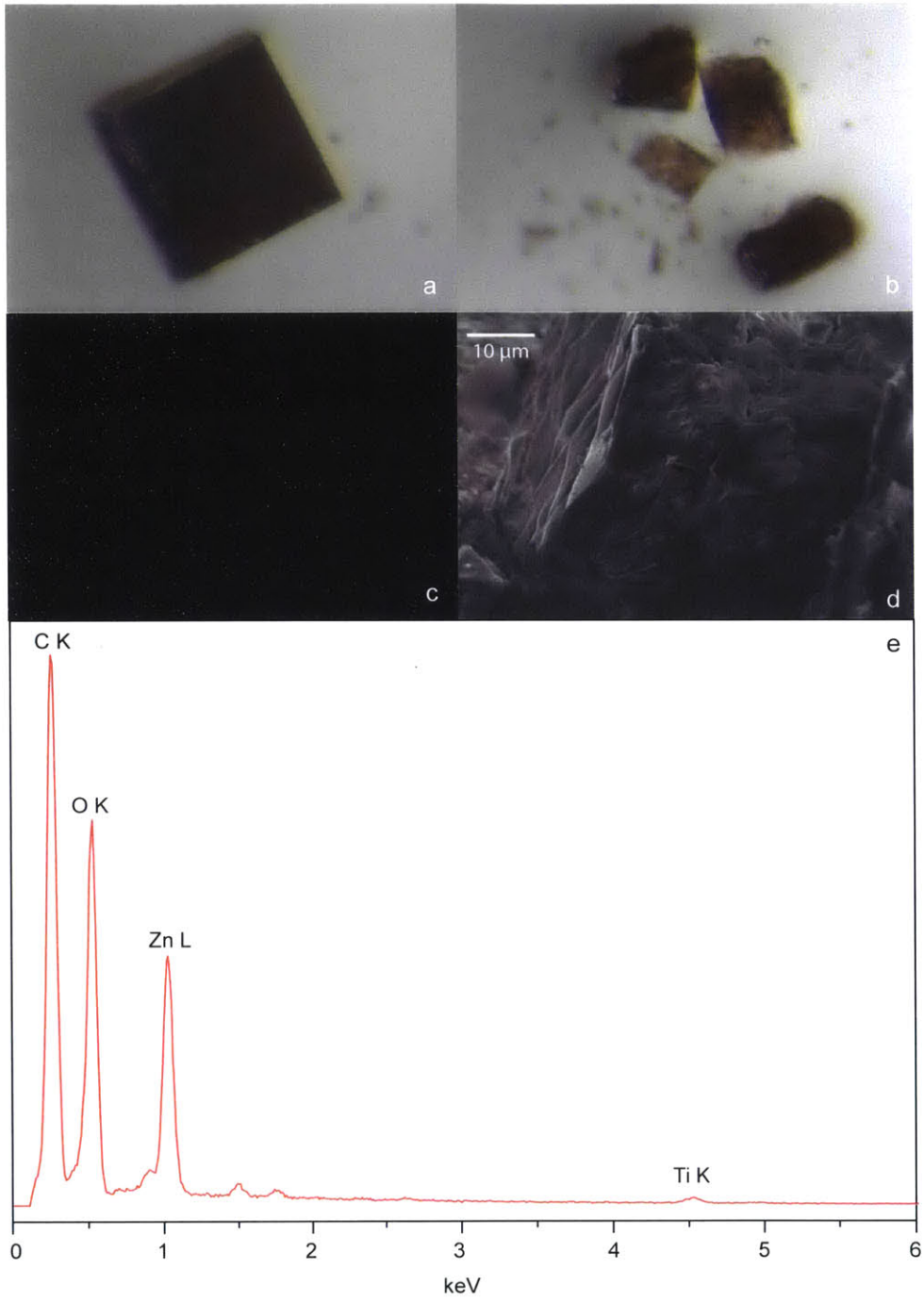

Figure 8-3: Optical microscope photographs of a single crystal of ClTi-MOF-5 before (a) and after (b) crushing to expose the interior portion. A two-dimensional EDX map (c) where white points denote the location of Ti on the exposed interior of a ClTi-MOF-5 crystal shown in SEM image (d). The corresponding EDX spectrum is shown in (e) with the elemental absorption edges denoted.

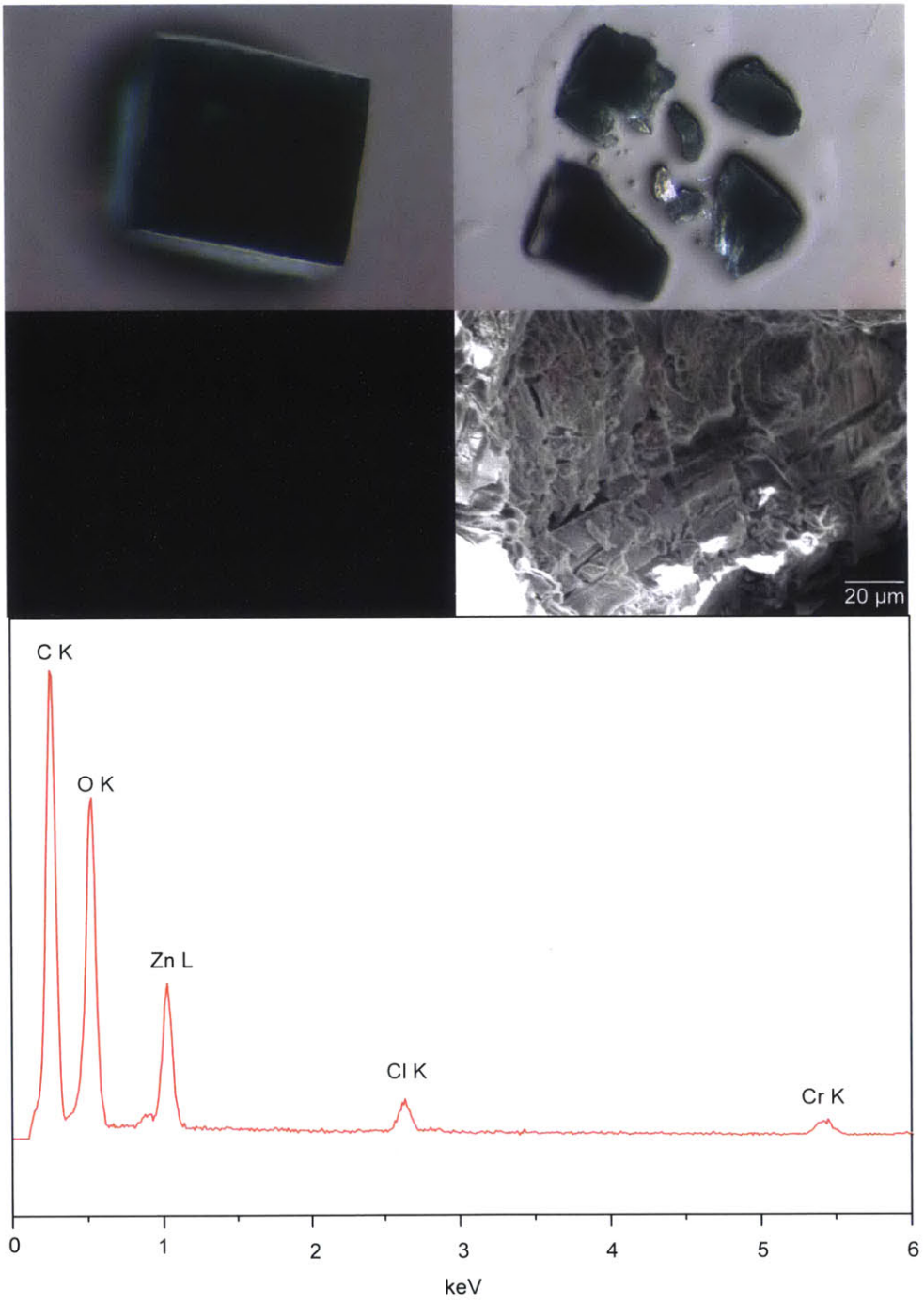

Figure 8-4: Optical microscope photographs of a single crystal of ClCr-MOF-5 before (a) and after (b) crushing to expose the interior portion. A two-dimensional EDX map (c) where white points denote the location of Cr on the exposed interior of a ClCr-MOF-5 crystal shown in SEM image (d). The corresponding EDX spectrum is shown in (e) with the elemental absorption edges denoted.

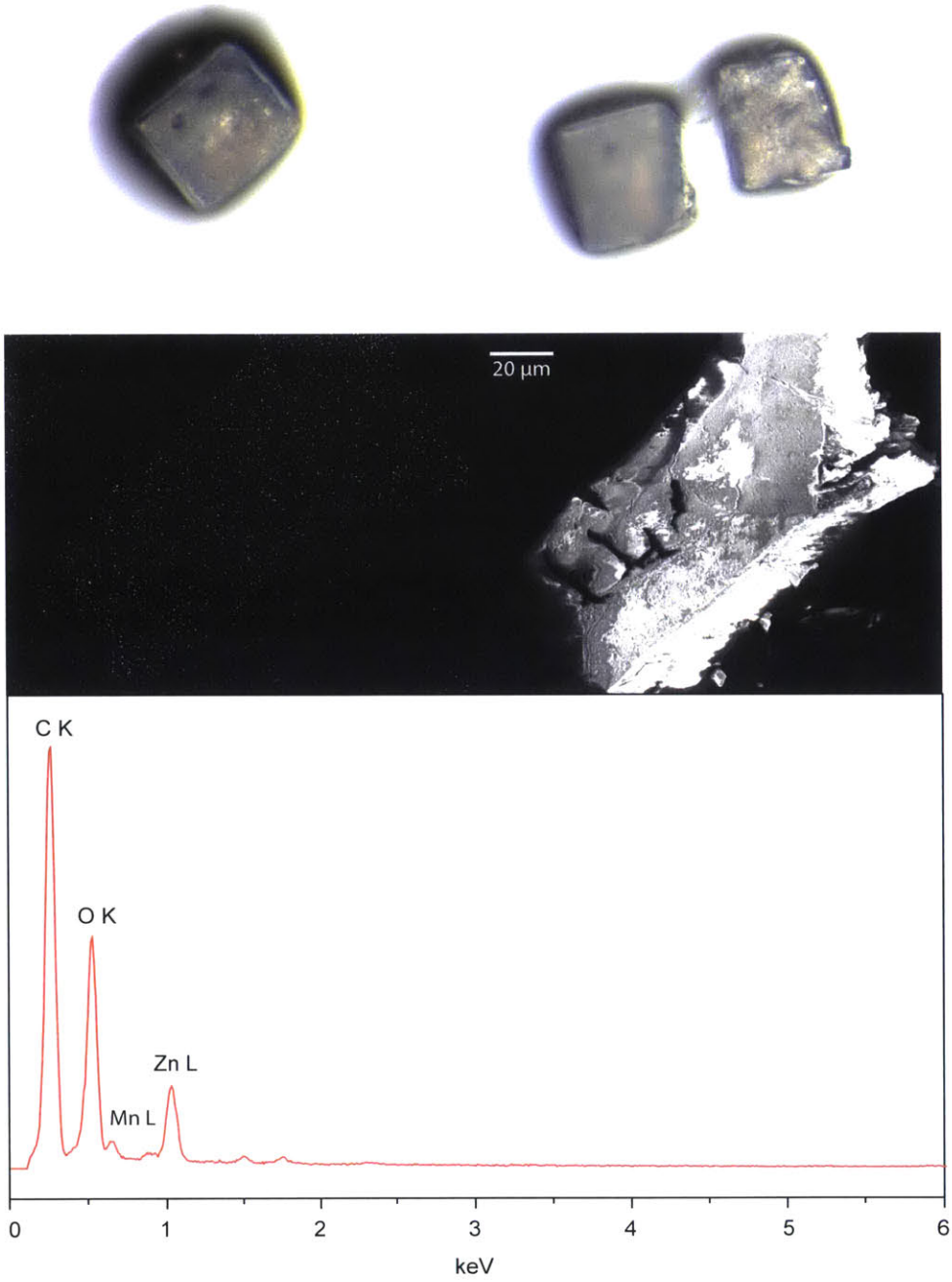

Figure 8-5: Optical microscope photographs of a single crystal of Mn-MOF-5 before (a) and after (b) crushing to expose the interior portion. A two-dimensional EDX map (c) where white points denote the location of Mn on the exposed interior of a Mn-MOF-5 crystal shown in SEM image (d). The corresponding EDX spectrum is shown in (e) with the elemental absorption edges denoted.

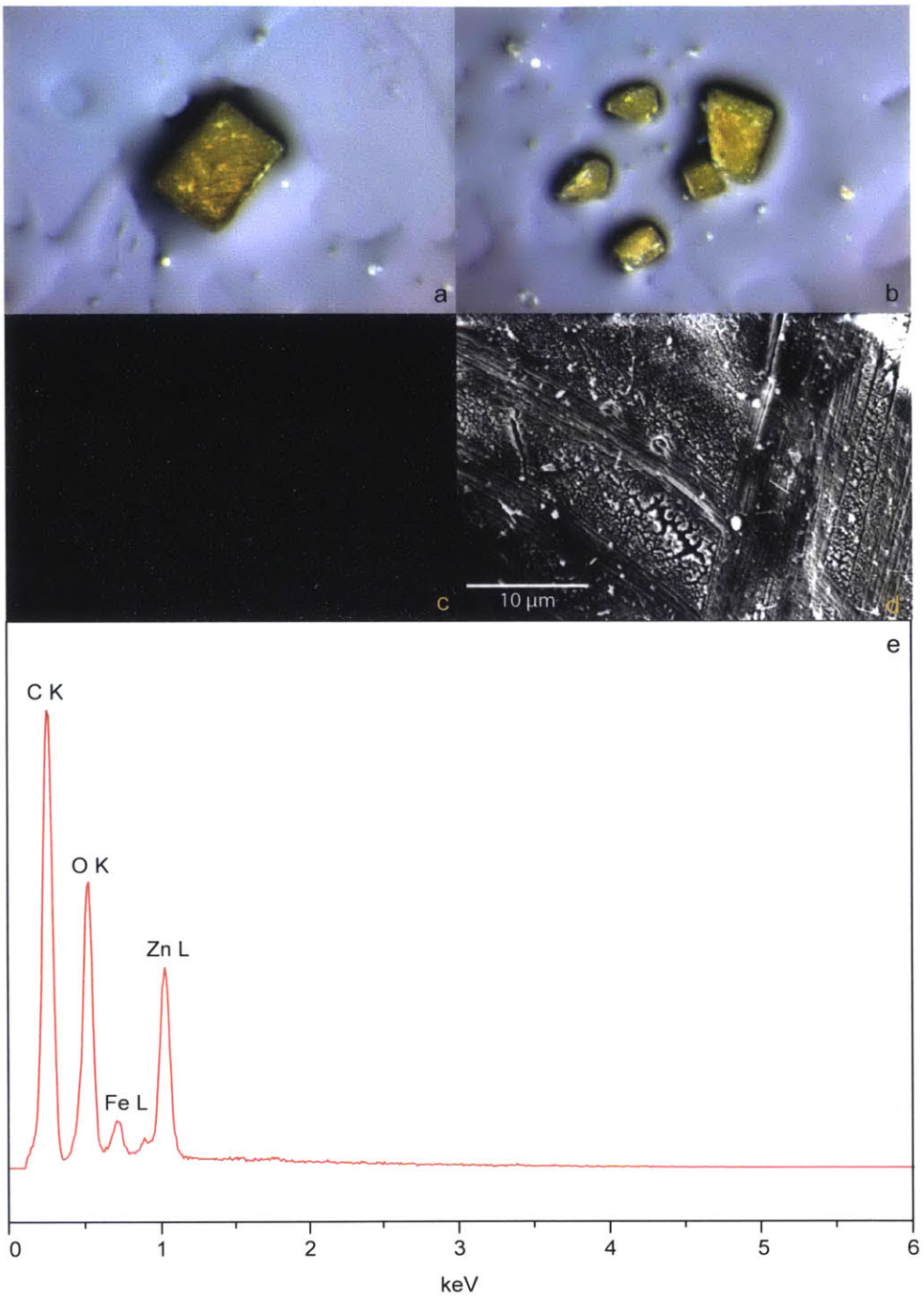

Figure 8-6: Optical microscope photographs of a single crystal of Fe-MOF-5 before (a) and after (b) crushing to expose the interior portion. A two-dimensional EDX map (c) where white points denote the location of Mn on the exposed interior of a Mn-MOF-5 crystal shown in SEM image (d). The corresponding EDX spectrum is shown in (e) with the elemental absorption edges denoted.

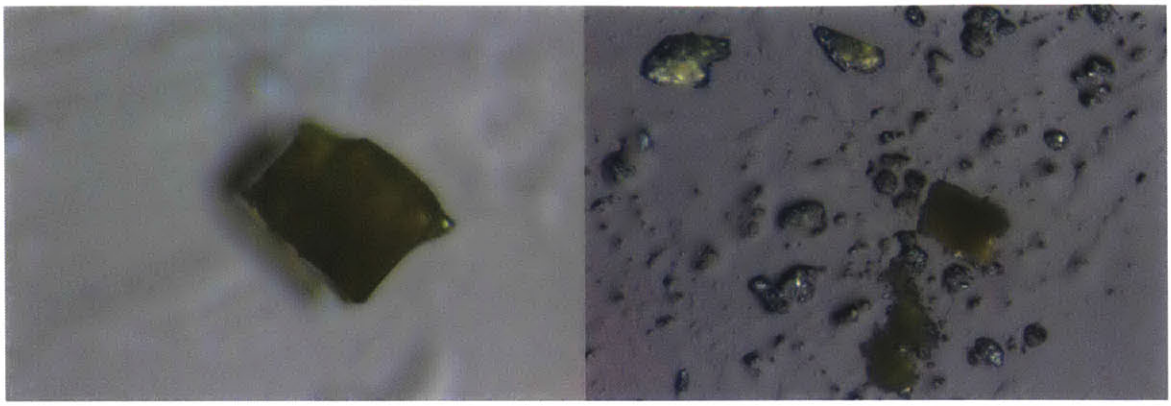

Figure 8-7: Optical microscope photographs of a single crystal of V-MOF-5 before (left) and after (right) being crushed to expose the interior portion.

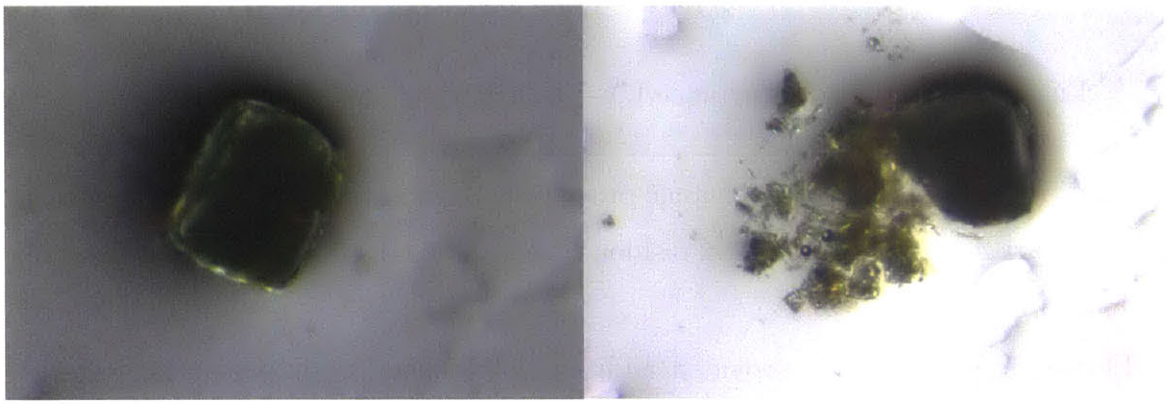

Figure 8-8: Optical microscope photographs of a single crystal of ClV-MOF-5 before (left) and after (right) being crushed to expose the interior portion.

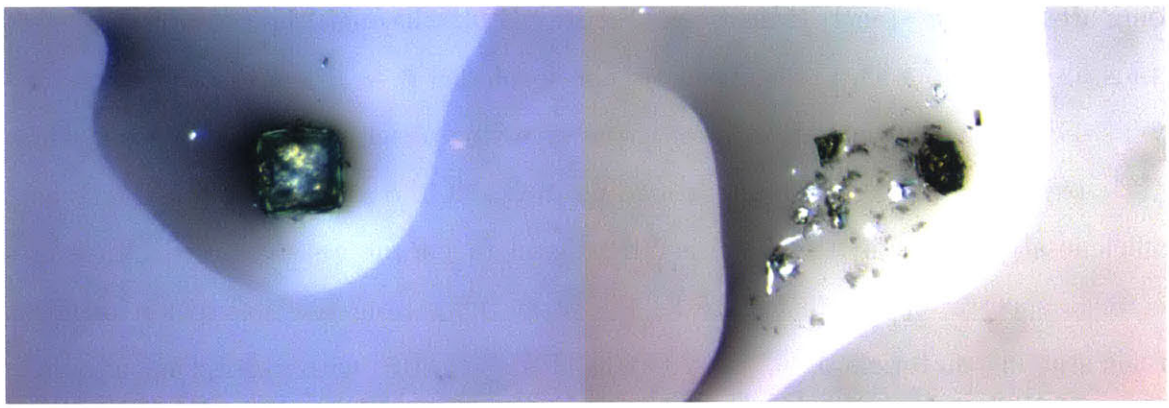

Figure 8-9: Optical microscope photographs of a single crystal of Cr-MOF-5 before (left) and after (right) being crushed to expose the interior portion.

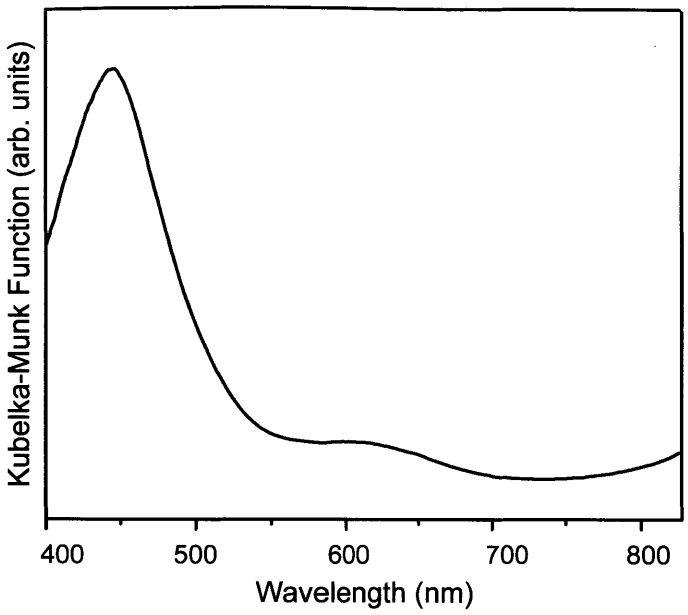

Figure 8-10: Diffuse reflectance UV-Vis-NIR spectrum of ClTi-MOF-5.

change throughout the cation exchange procedure, these data suggest that the substitution occurs in a crystal-to-crystal fashion rather than a dissolution-recrystallization mechanism.

Electronic spectroscopy provided additional evidence for the formation of site-isolated $(Cl)_xM_xZn_{4-x}O(O_2C–)_6$ clusters. A diffuse reflectance UV-Vis-NIR spectrum of activated ClTi-MOF-5 showed absorption bands in the visible region at 450 nm and 625 nm, which our time-dependent DFT (TD-DFT) analysis suggests are predominately d $\rightarrow \pi^*$ (aryl) transitions (Figure 8-10). Although these charge transfer bands also overlap with lower intensity spin-forbidden d $\rightarrow$ d transitions, predicted by TD-DFT in the same region, transitions involving d electrons are consistent with a Ti^{3+} oxidation state. The high Cr loading in Cr-MOF-5 and ClCr-MOF-5 enabled sufficient absorbance in the UV-Vis-NIR region to permit well-resolved diffuse reflectance spectra, shown in Figure 8-11. These differ from the absorption profiles of the starting materials, $CrCl_2$ and $CrCl_3 \cdot 3THF$ in DMF, with absorption maxima that are shifted to higher energy, as expected for the stronger ligand field provided by MOF-5.[16] The spectra of these materials would show additional overlapping ab-

data could be collected at the Cr K edge for ClCr-MOF-5 before compromising the crystal integrity.

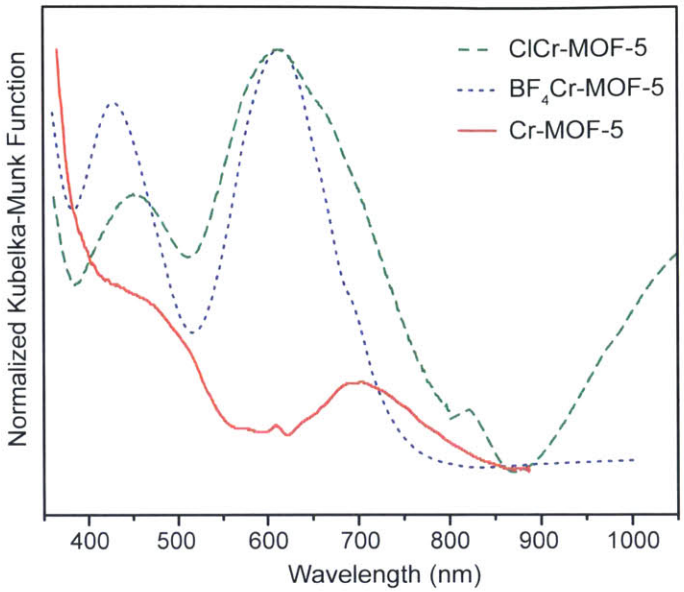

Figure 8-11: Diffuse reflectance UV-Vis-NIR spectra of ClCr-MOF-5, Cr-MOF-5, and Cr-MOF-5 after treatment with $NOBF_4$ to afford BF_4Cr-MOF-5.

sorption bands if other metal complexes resided in the pores, but they do not.

Electron paramagnetic resonance (EPR) spectroscopy provided further confirmation of the oxidation state, coordination environment, and the associated electronic structures of the inserted metal ions. Materials with half-integer spin cations, expected to display degenerate ground m_s states, produced spectra that differed from the parent solutions. ClTi-MOF-5 displayed a well-resolved, sharp axial signal consistent with an S = $\frac{1}{2}$ system with $g_{x,y} = 1.93$ and $g_z = 2.09$ (Figure 8-12), while Mn-MOF-5 and ClCr-MOF-5 produced broad axial signals (see Figures 8-13 and 8-14). As expected for an S = $\frac{5}{2}$ (L = 0) ion, the broad signal of Mn-MOF-5 fits to $g_{iso} = 2.00$, while the spectrum of ClCr-MOF-5 illustrates the strong axial symmetry imparted by the terminal chloride on the S = $\frac{3}{2}$ ion, giving $g_z = 4.27$ and $g_{x,y} = 1.93$. We assign the difference in resolution between the Ti^{3+}- and Cr^{3+}/Mn^{2+}-MOF-5 to the higher Cr and Mn content relative to Ti. Because the inserted metal ions incorporate homogeneously throughout the lattice, as discussed above, higher loadings bring the paramagnetic ions in close proximity, leading to short spin-spin relaxation times and loss of signal and hyperfine resolution in the Cr and Mn materials.[205] The

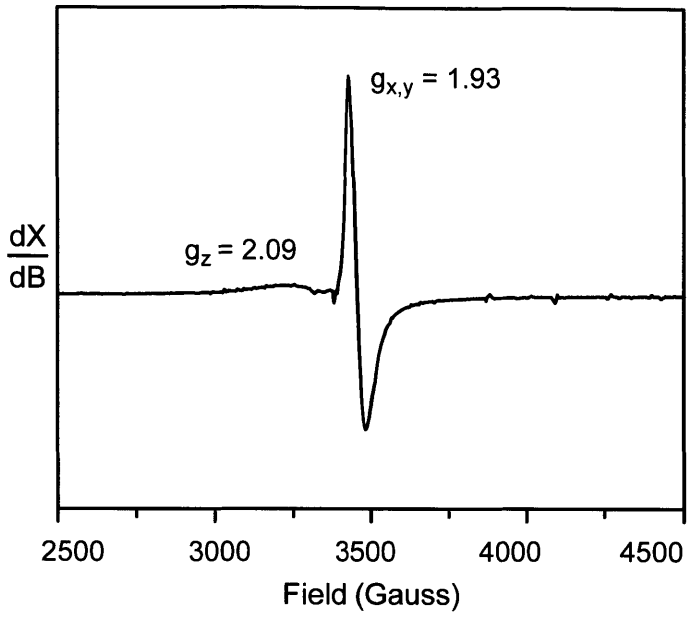

Figure 8-12: Continuous wave X-band EPR spectrum of ClTi-MOF-5 collected at 77 K.

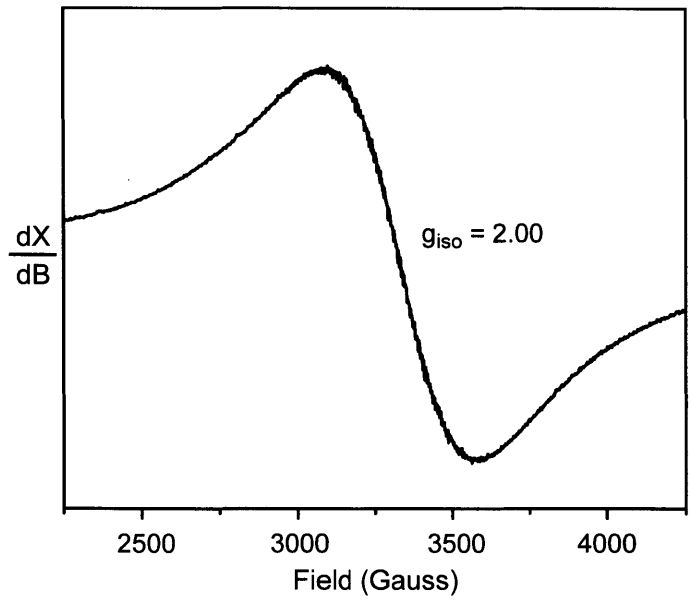

Figure 8-13: Continuous-wave X-band EPR spectrum of Mn-MOF-5 collected at 77 K.

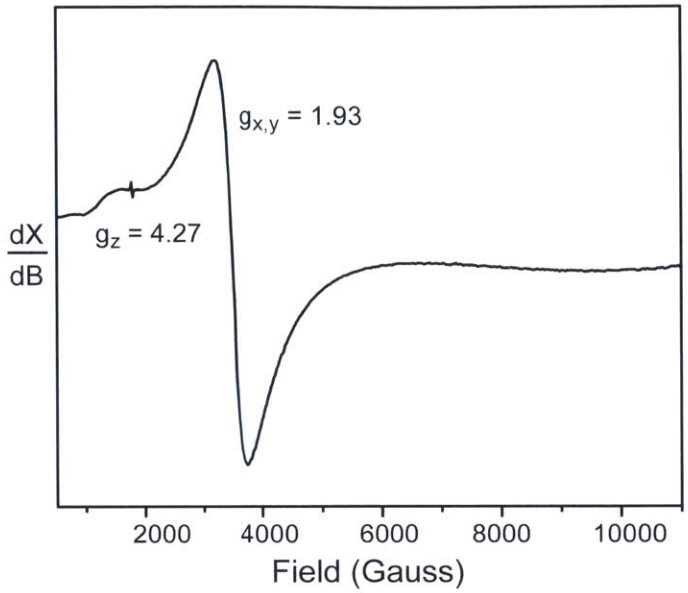

Figure 8-14: Continuous-wave X-band EPR spectrum of ClCr-MOF-5 collected at 77 K.

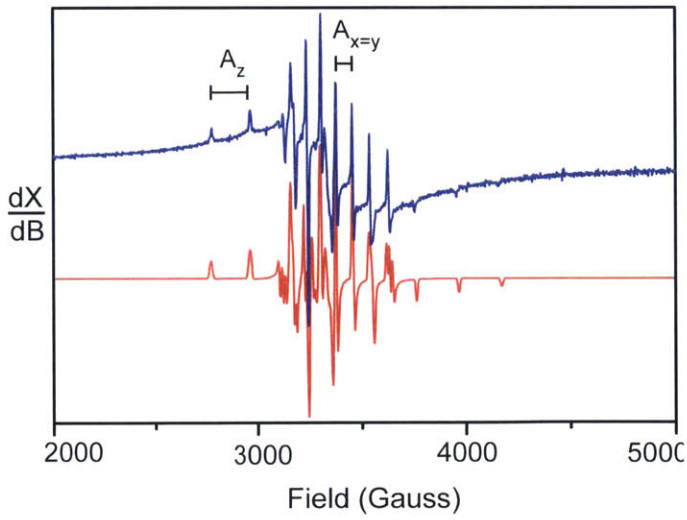

Figure 8-15: Continuous-wave X-band EPR spectrum of V-MOF-5 at 77 K (blue) and a simulated trace (red).

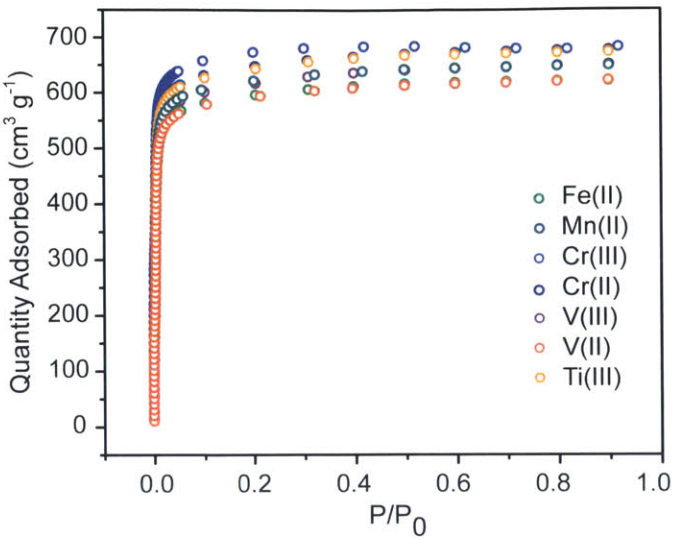

Figure 8-16: The N_2 uptake at 77 K of Ti^{3+}, V^{3+}, V^{2+}, Cr^{3+}, Cr^{2+}, Mn^{2+}, and Fe^{2+}-exchanged MOF-5.

signals for these two MOFs are nevertheless consistent with Mn^{2+} and Cr^{3+} trapped in solid lattices.[206,207] Our explanation for the resolution differences in the EPR spectra is corroborated by the spectrum collected for V-MOF-5, shown in Figure 8-15, where the low loading of the I = $\frac{7}{2}$ ^{51}V nucleus (see Table 8.1) enabled the resolution of fine structure and permitted a quantitative analysis of the axial symmetry and metal-ligand interaction. Here, the curvature of the baseline is likely a broad signal resulting from V^{2+} (S = $\frac{3}{2}$) ions that are in near proximity, making the overall signal a superposition of short and fast T_2 values. A good fit to the spectrum of V-MOF-5 was obtained using $g_{x,y} = 1.97$, $g_z = 1.93$, $A_{x,y} = -200.66$ MHz, $A_z = -539.72$ MHz, and S = $\frac{3}{2}$. The strong axial signal is consistent with the expected C_{3v} symmetry about V^{2+}, while the large difference in the hyperfine coupling constants reveals the dissimilarity between the metal-μ_4-oxo bond and that with the carboxylate oxygen atoms. Fe-MOF-5, Cr-MOF-5, and ClV-MOF-5, all expected to be of integer spin, were indeed EPR silent under these experimental conditions.

To examine the porosity of the MOF-5 analogues, the materials were activated under conditions reported for synthesizing conventional MOF-5.[72] N_2 adsorption isotherms collected at 77 K (see Figure 8-16) confirmed that all the materials were

highly porous, with apparent BET surface areas ranging from 2393 m^2/g for V-MOF-5 to 2700 m^2/g for ClCr-MOF-5. These values are lower than the highest value reported for MOF-5, 3300 m^2/g,[72] and that reported for Ni-MOF-5.[16] We note, however, that the exchange of Ni^{2+} is much slower than those observed with the cations we report here. The rapid exchange of these metals might partially disrupt the MOF lattice and introduce defects that lead to reduced surface areas. Our motivation for incorporating metal ions with reduced oxidation states in MOF-5 was to enable redox reactivity at the SBUs. To demonstrate the viability of this strategy, we monitored the response of representative examples of these to both inner- and outer-sphere oxidants. Combining green crystals of Cr^{2+}-MOF-5 with $NOBF_4$ in acetonitrile caused the rapid formation of blue $(BF_4)Cr^{3+}$-MOF-5. The transformation from Cr^{2+} to Cr^{3+} within MOF-5 was examined by electronic spectroscopy of activated samples, shown in Figure 8-11. Similar to ClTi-MOF-5, the λ_{max} at 700 nm of the Cr^{2+} material arises from a d $\rightarrow \pi^*$ (aryl) transition, while both Cr^{3+} materials exhibit λ_{max} at 620 nm, assignable to d $\rightarrow$ d transitions. The small blue-shift of the higher energy peak in (BF_4)Cr-MOF-5 versus ClCr-MOF-5 can be attributed to the different geometries of the pseudo-tetrahedral Cr^{3+} center in the former versus that of the Cr^{3+} ion in the latter. TD-DFT calculations of geometry-optimized truncated models of the $Cr^{3+}Zn_3O(O_2C–)_6$ SBUs with and without coordinated chloride anions agree well with the experimental traces for the Cr^{3+}-substituted MOF-5 analogues and therefore substantiate a single-electron oxidation of Cr^{2+} to Cr^{3+} (see Figures 8-17-8-20).

PXRD and N_2 isotherms of (BF_4)Cr-MOF-5 confirm that the lattice remains crystalline and porous after the oxidation reaction (see Figures 8-21 and 8-22). Though the overall N_2 uptake decreases to give a surface area of 1010 $m^2\ g^{-1}$, the initial uptake of (BF_4)Cr-MOF-5 at low pressures mirrors what is normally observed for MOF-5, while the second expected uptake does not occur at higher pressures (as shown in the inset of Figure 8-22). Following a report by Snurr et al.,[108] this initial uptake corresponds to N_2 covering the pore exterior, while the absence of the second suggests the pore interiors may be blocked by solvated BF_4^- ions.

We demonstrated the ability of the inserted metal ions to undergo inner-sphere

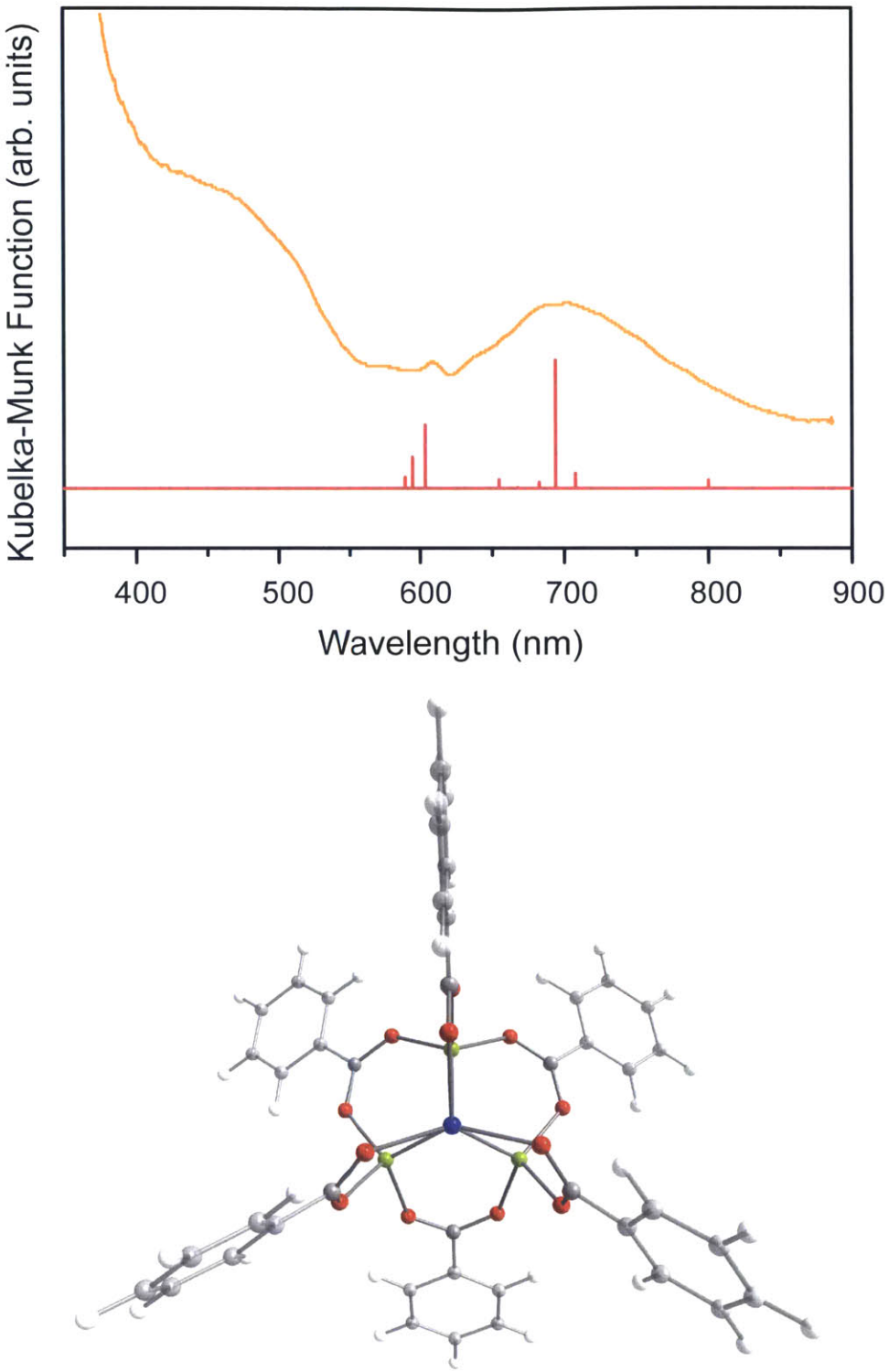

Figure 8-17: Diffuse reflectance UV-Vis-NIR spectrum of Cr-MOF-5 shown in orange with TD-DFT-predicted transitions shown in red, based on a model compound depicted below. Blue, green, red, grey, and white atoms represent Cr, Zn, O, C, and H respectively.

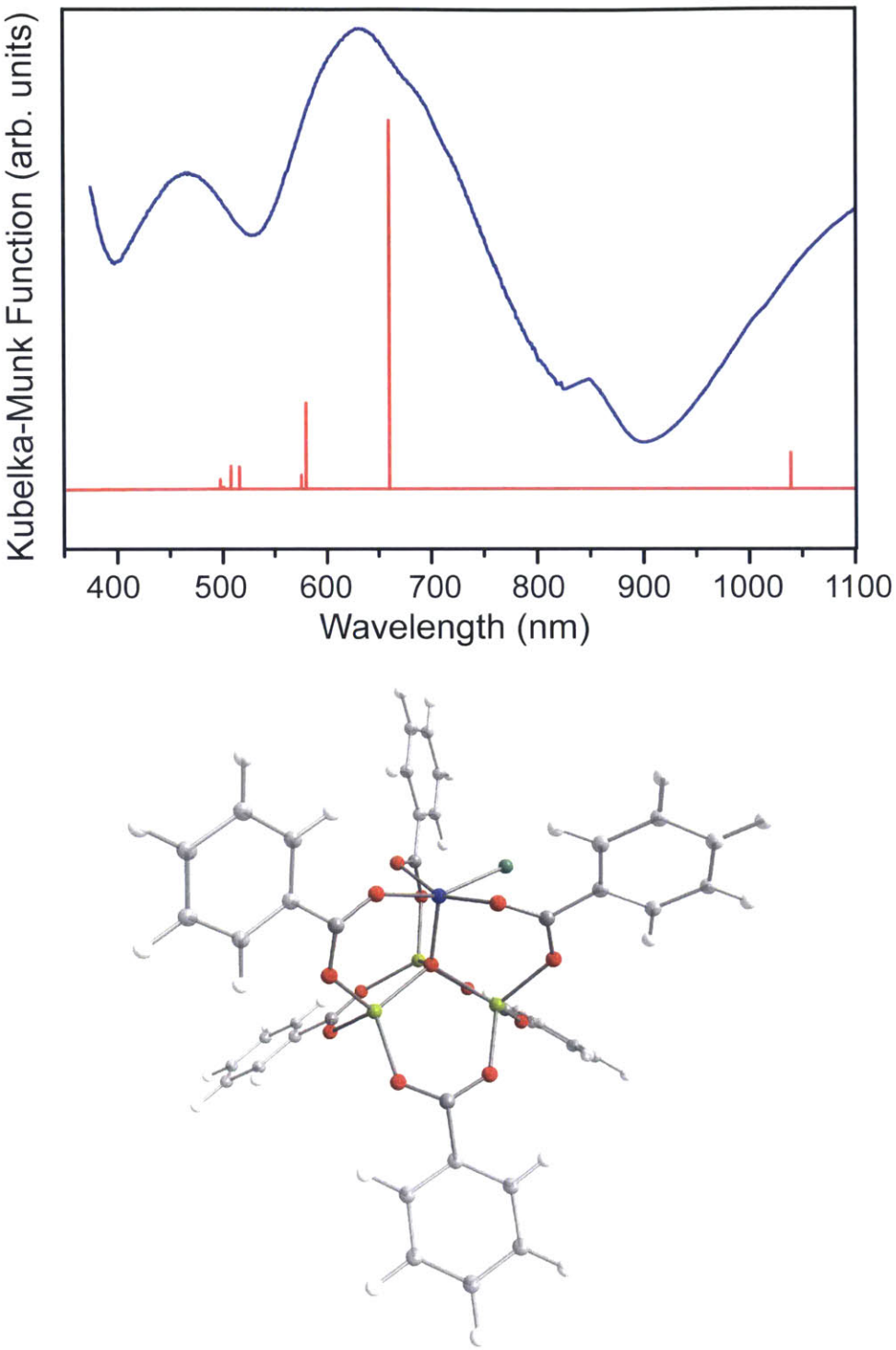

Figure 8-18: Diffuse reflectance UV-Vis-NIR spectrum of ClCr-MOF-5 shown in purple with TD-DFT transitions, shown in red, predicted from a $ClCrZn_3O(O_2C_7H_5)_6$ model compound depicted below. Blue, green, dark green, red, grey, and white atoms represent Cr, Zn, Cl, O, C, and H respectively.

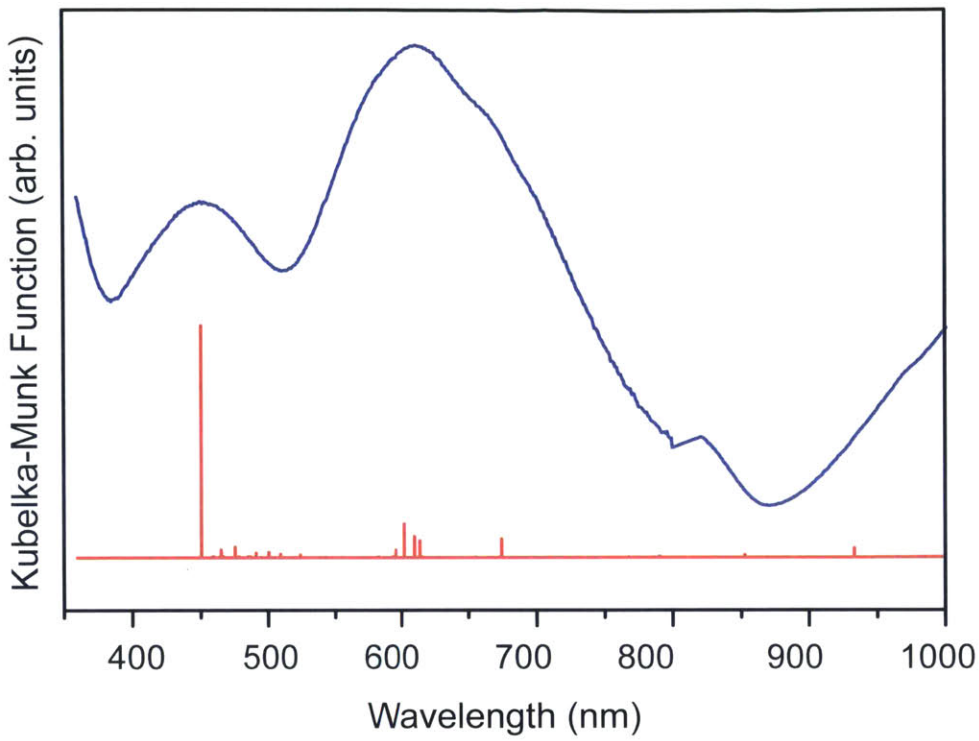

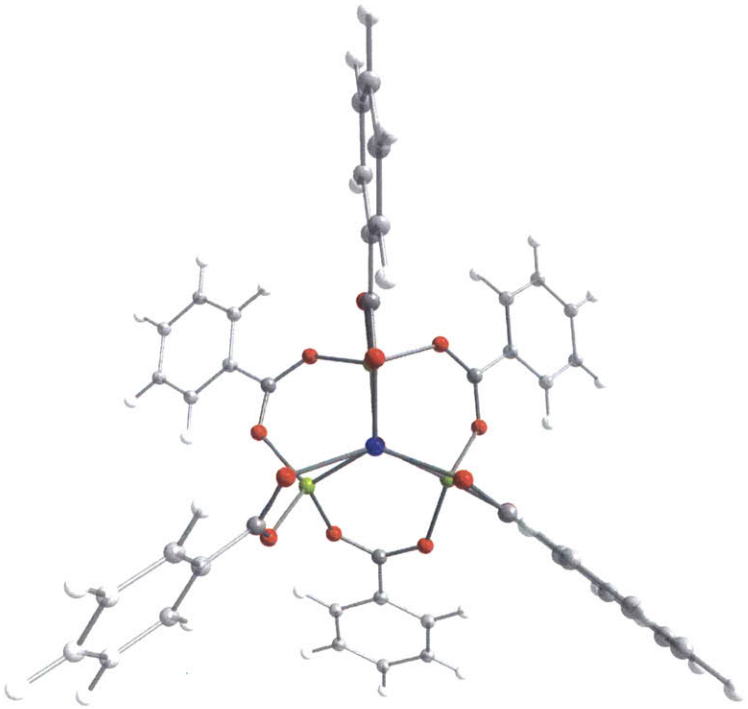

Figure 8-19: Diffuse reflectance UV-Vis-NIR spectrum of ClCr-MOF-5 shown in purple with TD-DFT transitions, shown in red, predicted from a $[CrZn_3O(O_2C_7H_5)_6]^+$ model compound depicted below. Blue, green, red, grey, and white atoms represent Cr, Zn, O, C, and H respectively.

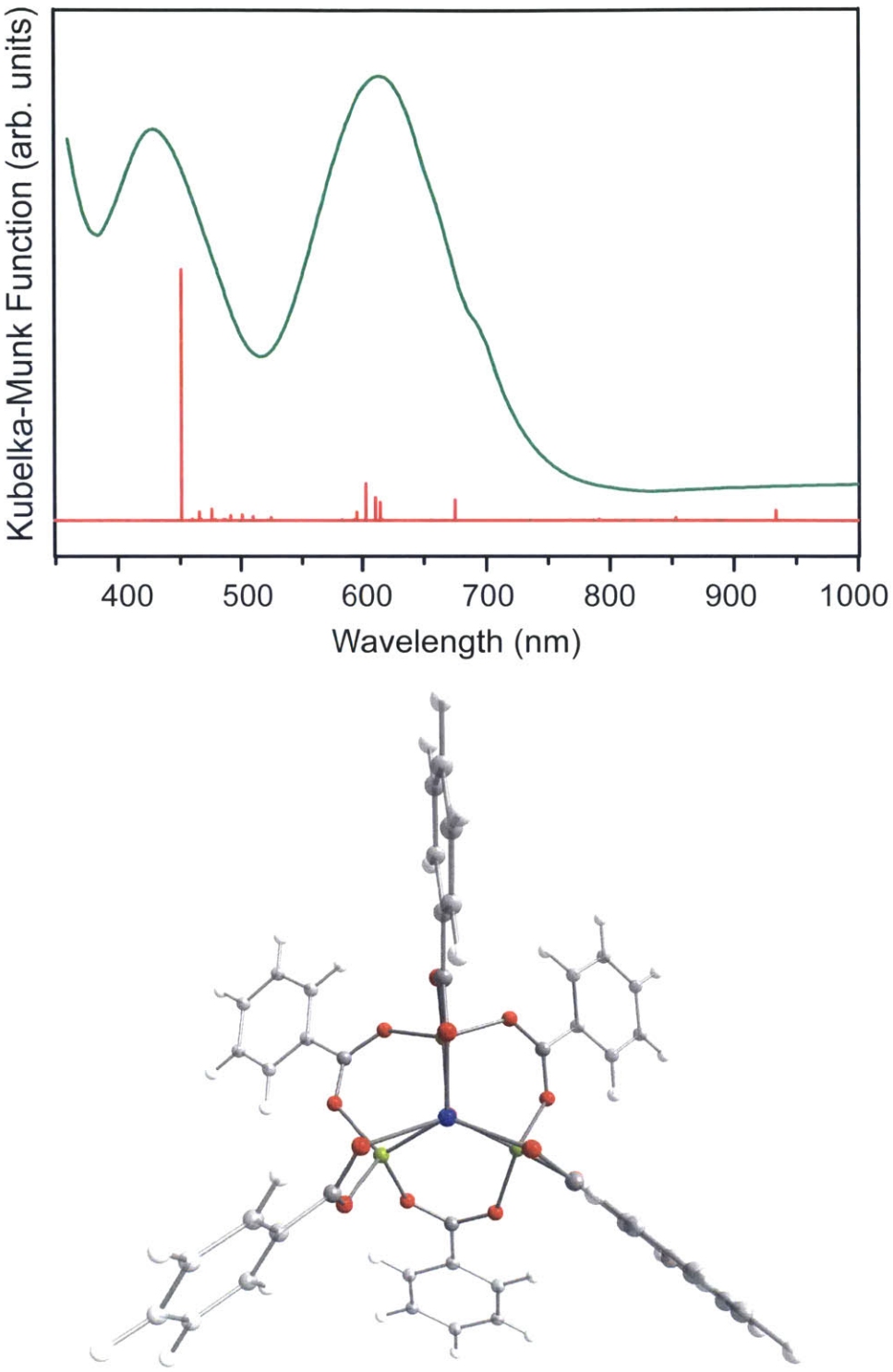

Figure 8-20: Diffuse reflectance UV-Vis-NIR spectrum of BF_4Cr-MOF-5 shown in green with TD-DFT transitions predicted from a $[CrZn_3O(O_2C_7H_5)_6]^+$ model compound shown in red. Blue, green, red, grey, and white atoms represent Cr, Zn, O, C, and H respectively.

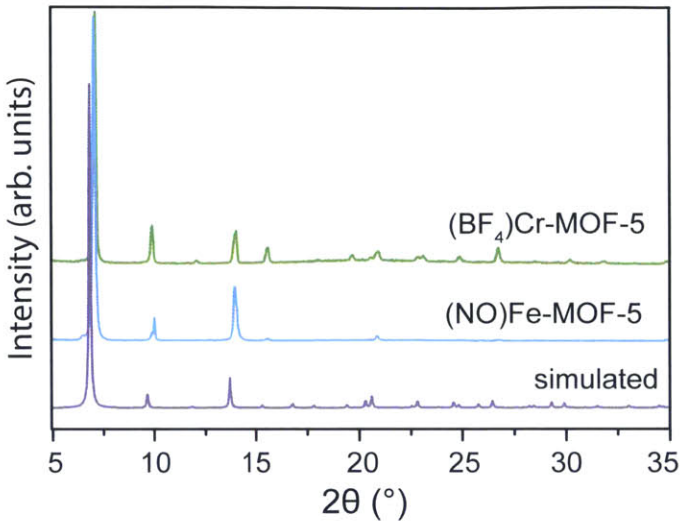

Figure 8-21: PXRD patterns of (BF_4)Cr-MOF-5 and (NO)Fe-MOF-5 compared to that simulated for MOF-5.

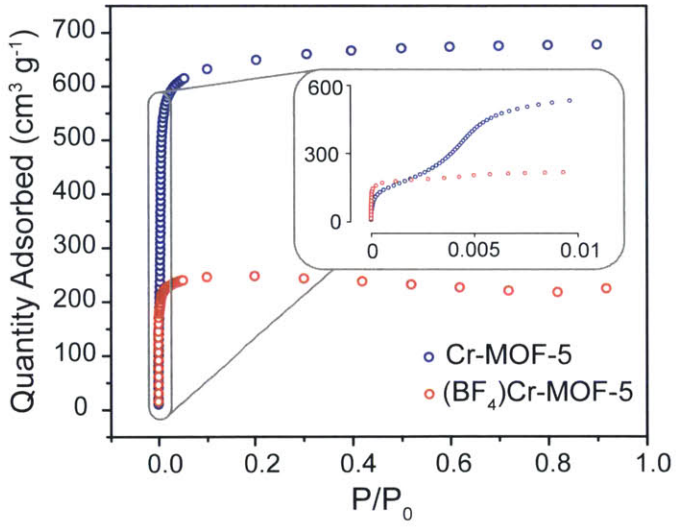

Figure 8-22: N_2 isotherms of Cr-MOF-5 and (BF_4)Cr-MOF-5. Inset: expansion of the low-pressure regime.

oxidation with the reaction between NO and Fe-MOF-5. Iron-nitrosyl complexes are widely studied due to their relevance to biology. From a more fundamental viewpoint, reactions involving nitric oxide are useful because the vibrational frequency of the N–O stretch offers insight into the electronic properties of the iron center. The reaction of NO gas with Fe-MOF-5 was monitored in situ by diffuse reflectance infrared Fourier transform spectroscopy (DRIFTS), as depicted in Figure 8-23. Upon exposure of activated Fe-MOF-5 to NO, a new resonance appears, centered at 1788 cm^{-1}. This value is lower than the stretch (ν_{N-O}) of free NO (1876 cm^{-1}) and the ν_{N-O} we observed for pristine (all-zinc) MOF-5 after exposure to NO (1815 cm^{-1}) (see Figure 8-24), indicating that NO is bound and activated at the iron center. PXRD of the resulting crystals confirms that they retain the MOF-5 crystalline lattice (see Figure 8-24). The value of ν_{N-O} in Fe-MOF-5 is in fact lower than those observed in all other MOFs thus far (see Table 8.2),[203,208–213] and is better compared to molecular species supported by similar ligand environments. Using the Enemark and Feltham notation,[214] the MOF-5 ligand, abbreviated $\boldsymbol{O}(O)_3^{3-}$ where $\boldsymbol{O}$ is the μ_4-oxo and O are the trigonally-symmetric carboxylate arms of the $Zn_3O(O_2C–)_6^{2-}$ SBU, produces an {Fe–NO}^{7} complex that fits into a series of {Fe–NO}^{7} compounds based on trigonal tetradentate ligands denoted similarly as $\boldsymbol{N}(O)_3^{3-}$,[215] $\boldsymbol{N}(N)_3^{3-}$,[216] and $\boldsymbol{N}(S)_3^{3-}$.[217] The greater electron density of $\boldsymbol{N}(S)_3^{3-}$ in $[Me_4N][Fe(NS_3)(NO)]$ and $\boldsymbol{N}(N)_3^{3-}$ in $[Fe(1^{iPr})(NO)]$ enhances the iron-to-NO backbonding, leading to lower values of ν_{N-O} (see Table 8.2). The $\boldsymbol{N}(O)_3^{3-}$ scaffold in [Fe(nta)(NO)] would be expected to impart greater density on iron than MOF-5, though its ν_{N-O} is higher than that in (NO)FeMOF-5. This observation is in line with the assignment of O in MOF-5 as a strong Lewis base on the basis of EPR experiments discussed above. Comparisons with other structurally unrelated ligand fields of biological {Fe–NO}^{7} species offer another basis for evaluating (NO)Fe-MOF-5. For instance, although both support penta-coordinate nitrosyl species, the biomolecule HemeA activates NO to a far greater degree than MOF-5 due to the strong ligand field of the porphyrin ring.[218] Conversely, the amino-acid ligand field of superoxide reductase generates only a slightly more activated nitrosyl species than MOF-5.[219] The zeolite Fe-ZSM-5, which is known to catalyze

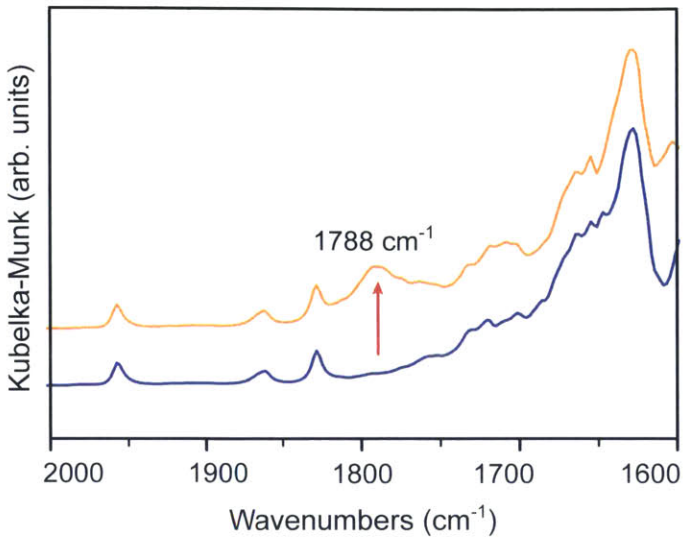

Figure 8-23: DRIFTS spectra of Fe-MOF-5 before (blue) and after (yellow) exposure to NO at room temperature and ambient pressure.

the reduction of NO by ammonia by first binding NO, provides a relevant comparison with our material, but shows only weak NO activation with $\nu_{\text{N-O}}$ at 1880 cm^{-1}.[220]

(NO)Fe-MOF-5 also displays two new bands in the visible region of its electronic absorption spectrum, shown in Figure 8-25. The bands at 395 nm and 476 nm are characteristic of ligand-to-metal NO(π^*) $\rightarrow$ d charge transfer and are similar to transitions observed for the complexes in Table 8.2. EPR spectroscopic analysis of (NO)Fe-MOF-5, shown in Figure 8-26, displays two signals at $g_{x,y} = 4.5$ and $g_z = 2.00$. Based on assignments of similar $\{\text{Fe–NO}\}^7$ complexes,[221] these reflect the axial symmetry of the ligand field and an overall $S = \frac{3}{2}$ arising from strong antiferromagnetic coupling between the $S = \frac{5}{2}$ iron and $S = \frac{1}{2}$ NO fragment. The corresponding transitions most likely result from $|\pm\frac{1}{2}\rangle$ states, whereas the splitting of $|\pm\frac{3}{2}\rangle$ is too large to observe under the experimental conditions. Hence, due to its heterogeneous nature, a $\{\text{Fe–NO}\}^7$ fragment in the solid-state lattice of MOF-5 offers a distinct reactivity landscape from the solution-phase chemistry of metal nitrosyls and is the first such species in an all-oxygen ligand field. Unlike previous examples of NO activation by MOFs, the value of $\nu_{\text{N–O}}$ in (NO)Fe-MOF-5 is consistent with electron transfer by the metal center.

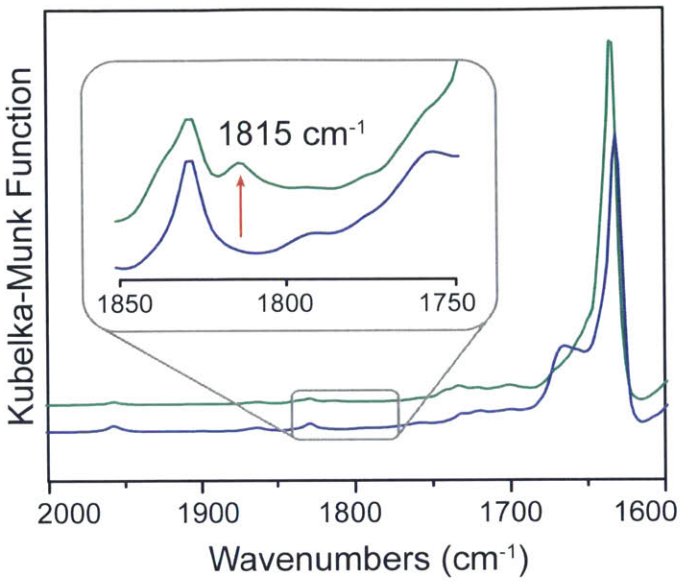

Figure 8-24: DRIFTS spectra of fully activated MOF-5 before (blue) and after (green) being exposed to NO gas. Inset: a new resonance emerges at 1815 cm^{-1}.

	ν_{N-O}	λ_{max} (nm)	**System**
HKUST-1	1887	–	MOF
Fe-ZSM-5	1880	–	zeolite
CPO-27-Ni	1843	–	MOF
MIL-100(V)	1841	–	MOF
MIL-100(Fe)	1825	–	MOF
MOF-5	1815	–	MOF
[Fe(nta)(NO)]	1793	342, 439	molecule
(NO)FeMOF-5	1788	395, 476	MOF
[Fe(1^{iPr})(NO)]	1739	350, 500	molecule
superoxide reductase	1721	475	enzyme
HemeA(NO)	1668	–	molecule
$[Me_4N][Fe(NS_3)(NO)]$	1630	–	molecule

Table 8.2: Comparison of ν_{N-O} and λ_{max} values for the nitrosyl-to-iron charge transfer band in (NO)Fe-MOF-5 with relevant $\{Fe\text{-}NO\}^7$ complexes and other MOFs.

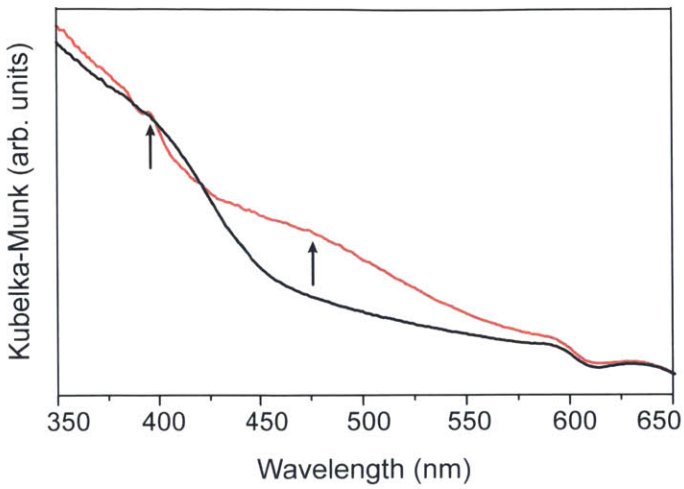

Figure 8-25: Diffuse reflectance UV-Vis-NIR of FeMOF-5 before (black) and after (red) treatment with NO gas at room temperature.

Reduction of the inserted cations is also possible. To demonstrate this capability, we chose Cl-V-MOF-5 because 1 e^- transfer to generate V^{2+} ions would be easily identified by X-band EPR spectroscopy. Adding a THF solution containing a stoichiometric quantity of $[(THF)_3Na^+(TEMPO^-)]_4$ (TEMPO = 2,2,6,6-tetramethyl-1-piperidinyloxy) to a THF suspension of ClV-MOF-5 resulted in the crystalline MOF turning from forest green to light green/gray in several minutes. After repeated washing in fresh THF, the otherwise untreated crystals were examined by X-band EPR at 77 K. As shown in Figure 8-27, the formerly EPR-silent material gave rise to a pattern indicative of V^{2+} with near isotropic symmetry. Unlike the axial signal displayed in Figure 8-15, the V centers most likely feature two pendant THF molecules to furnish pseudo-octahedral geometry.

8.4 Conclusion

We have shown that redox-active di- and trivalent first-row transition metals can be substituted into MOF-5 to give materials that are inaccessible by typical synthetic pathways. In particular, we have reported the first examples of Ti^{3+}- and V^{2+}-containing MOFs, along with five other previously unknown analogues of MOF-5

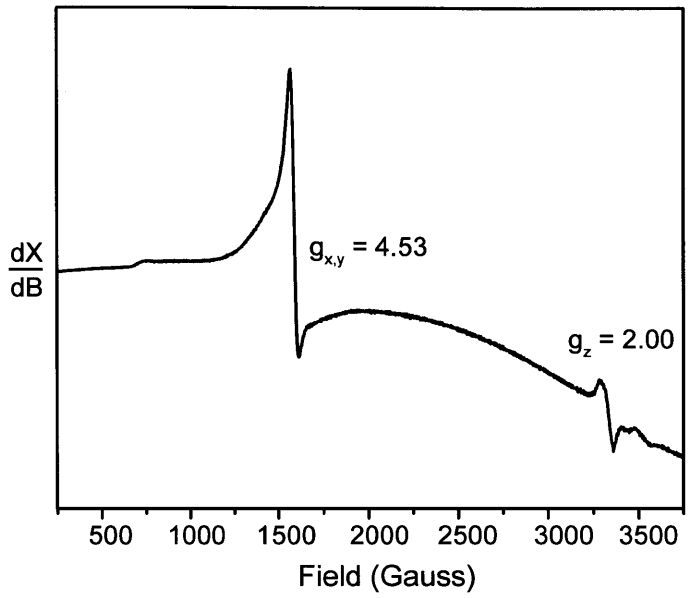

Figure 8-26: Continuous-wave X-band EPR spectrum of (NO)Fe-MOF-5 collected at 77 K.

itself. The inserted metal ions resemble the molecular species of coordination chemistry and catalysis, yet the solid-state lattice provides a unique platform for future reactivity studies. As a proof of this concept, we demonstrated that outer-sphere electron transfer can be achieved in Cr-MOF-5 and that Fe-MOF-5 activates NO more than any other MOF. These experiments illustrate rare examples of stoichiometric redox reactivity at MOF SBUs and emphasize the unique coordination environment and ligand field character of the metal nodes when regarded as ligands. The following chapter will build on these results to demonstrate that these SBU are also capable of small-molecule activation.

8.5 Methods

All synthetic manipulations were performed under an inert atmosphere of a N_2 glove box, unless stated otherwise.

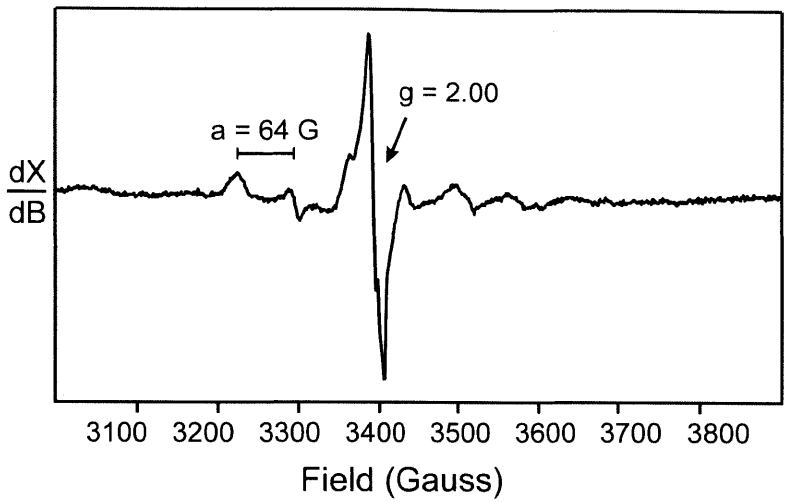

Figure 8-27: Continuous-wave X-band EPR spectrum of ClV-MOF-5 after treatment with $[(THF)_3Na^+(TEMPO^-)]_4$ collected at 77 K.

8.5.1 Materials

Dichloromethane (HPLC grade, Honeywell), *N*,*N*-dimethylformamide (DMF) (99.8%, VWR), NO/N_2 (5% Airgas), $TiCl_3{\cdot}3THF$ (97% Strem), $CrCl_2$ (99.9%, Strem), $MnCl_2$ (97% Strem), $Fe(BF_4)_2{\cdot}6H_2O$ (97% Sigma-Aldrich), and $Zn(NO_3)_2{\cdot}6H_2O$ (99%, Alfa Aesar) were used as received. Dry, deaerated tetrahydrofuran (THF) and DMF were obtained by degassing with a flow of argon gas for 30 min and by passing the solvent through two silica columns in a Glass Contour Solvent System. VCl_2(pyridine)4,[222,223] $VCl_3{\cdot}3THF$,[224] $CrCl_3{\cdot}3THF$,[225] $[(THF)_3Na^+(TEMPO^-)]_4$,[226] and MOF-5[72] were prepared according to literature procedure.

8.5.2 Physical Measurements

Powder X-ray diffraction (PXRD) patterns were recorded on a Bruker Advance II diffractometer equipped with $\theta/2\theta$ Bragg-Brentano geometry and Ni-filtered Cu-K_α radiation ($K_{\alpha 1}$ = 1.5406 Å). The tube voltage and current were 40 kV and 40 mA, respectively. Samples for PXRD were prepared by placing a thin layer of samples on a zero-background silicon crystal plate supported on a cup with dome that screwed-on with a rubber O-ring fitting. Diffuse reflectance UV-Vis spectra of ClCr-MOF-5 were

collected between 1.0 and 3.5 eV on a Varian Cary 5000 UV-Vis-NIR spectrometer equipped with a Praying Mantis diffuse reflectance accessory and an environmental chamber (Harrick Scientific Products) and referenced to $BaSO_4$. An adequate spectrum of Cr-MOF-5 was not achieved using this setup. Instead, an Ocean Optics Jaz spectrometer was used, but interpretable only between 1.5 and 3.0 eV.

A Micromeritics ASAP 2020 Surface Area and Porosity Analyzer was used to measure nitrogen adsorption isotherms. Oven-dried sample tubes equipped with TranSeals™(Micrometrics) were evacuated and tared. Samples were transferred to the sample tubes, heated to 200 °C for 12 h, and held at that temperature until the outgas rate was less than 2 mtorr/minute. The evacuated sample tubes were weighed again and the sample mass was determined by subtracting the mass of the previously tared tube. N_2 isotherms were measured using liquid nitrogen baths (77 K). UHP grade (99.999% purity) N_2 and He, oil-free valves and gas regulators were used for all free space corrections and measurements.

Titanium, vanadium, chromium, manganese, iron, and zinc analyses were conducted at the MIT Center for Materials Science and Engineering Shared Experimental Facility (CSME-SEF) using a HORIBA Jobin ACTIVA inductively coupled plasma atomic emission spectrometer (ICP-AES). Standards were prepared from solutions purchased from ULTRA Scientific©, designated suitable for ICP analysis. Elemental analysis was performed by Complete Analysis Laboratories, Parsippany, NJ.

Continuous wave X-band EPR spectra were recorded using a Bruker EMX spectrometer with a Gunn diode and an ER 4199HS cavity. The microwave frequency of 9.351 GHz was set to 2.021 mW and a modulation frequency of 100.00 kHz was used with an amplitude of 10.00 G. The signals resulted from averaging 10 scans. All spectra were recorded near 77 K by setting the sample tube in a cold-finger dewar containing liquid N_2.

Diffuse reflectance infrared Fourier transform spectroscopy (DRIFTS) was performed on a Bruker Tensor 37 with a mercury cadmium telluride detector. Data were collected in the "MIR_DRIFTS" mode with a 6-mm aperture setting and a KBr beam splitter. The data was averaged over 32 scans between 7000 and 600 cm^{-1}.

Field emission scanning electron microscopy (FESEM) was performed with a Zeiss Supra55VP on crushed crystalline sample dispersed on double-sided copper tape and mounted on an aluminum stub. The FESEM was operated at a beam voltage from 8–11 kV at a working distance of 10–15 mm with a 30-μm aperture and used with a Everhart-Thornley (SE2) detector. Elemental composition was determined by an energy dispersive X-ray spectrometer (EDX) connected to the FESEM. A dwell time of 200 μs and 8 frames were used to collect 512 $\times$ 400 px EDX maps from 0–10 keV for a total of about 650 s run time. Optical microscope photographs were captured with a Zeiss Discovery V8 Stereomicroscope configured with transmitted light polarization optics using a Plan-Achromat S1.0$\times$ Objective, Zoom setting of 8$\times$, and axiocamERc 5s Color CCd with Axiovision software (Carl Zeiss Miroscopy, Thornwood, NY).

8.5.3 $Zn_{4-x}M_xCl_xO_{13}C_{24}H_{12}$ (ClM-MOF-5, M = Ti, V, Cr)

MCl_3·3THF, where M = Ti, V, or Cr, (0.30 mmol) was dissolved in 10 mL of dry, deaerated DMF and added at room temperature to $Zn_4O_{13}C_{24}H_{12}$ (MOF-5) (50 mg, 6.5 $\times$ 10^{-2} mmol) that was washed once with 20 mL of DMF for 24 h. These suspensions were stirred gently for 1 week before replacing the solution with fresh DMF. The crystals were washed with DMF and CH_2Cl_2 and activated according to standard procedure for MOF-5.[72] Our failed efforts to synthesize these materials directly followed the typical preparation of MOF-5, but with using deaerated DMF and heating at 100 °C under air-free conditions. Elemental analysis for $Zn_{3.91}Ti_{0.09}Cl_{0.09}O_{13}C_{24}H_{12}$·($CH_2Cl_2$) : Calculated: C% 35.06, H% 1.66, N% 0.0, Cl% 0.37, Found: C% 35.29, H% 1.38, N% 0.00, Cl% 0.27; $Zn_{3.80}V_{0.20}Cl_{0.20}O_{13}C_{24}H_{12}$: Calculated: C% 37.77, H% 1.59, N% 0.00, Cl% 0.10, Found: C% 37.12, H% 1.46, N% 0.00, Cl% 0.34; $Zn_{2.59}Cr_{1.41}Cl_{1.41}O_{13}C_{24}H_{12}$·(DMF)0.4: Calculated: C% 36.45, H% 1.80, N% 0.67, Cl% 6.02, Found: C% 36.04, H% 2.27, N% 0.75, Cl% 5.39.

8.5.4 $Zn_{4-x}M_xO_{13}C_{24}H_{12}$ (M-MOF-5, M = V, Cr, Mn, Fe)

In a manner similar to above, DMF-washed MOF-5 crystals (50 mg, 6.5×10^{-2} mmol) were combined with saturated 10 mL DMF solutions of $VCl_2(pyridine)_4$, $CrCl_2$, $MnCl_2$, or $Fe(BF_4)_2 \cdot 6H_2O$. These were stirred gently for a week and subsequently washed and activated. Elemental analysis for $Zn_{3.83}V_{0.17}O_{13}C_{24}H_{12}$: Calculated: C% 37.56, H% 1.46, N% 0.00, Found: C% 37.48, H% 1.46, N% 0.00; $Zn_{3.06}Cr_{0.94}O_{13}C_{24}H_{12}$: Calculated: C% 38.06, H% 1.60, N% 0.00, Found: C% 37.79, H% 1.49, N% 0.34; $Zn_{3.58}Mn_{0.42}O_{13}C_{24}H_{12}$: Calculated: C% 38.20, H% 1.61, N% 0.00, Found: C% 37.59, H% 1.42, N% 0.00. $Zn_{3.04}Fe_{0.96}O_{13}C_{24}H_{12}$: Calculated: C% 37.89, H% 1.59, N% 0.00, Found: C% 37.02, H% 1.80, N% 0.00.

8.5.5 In Situ DRIFTS of NO + Fe-MOF-5

Fully activated Fe-MOF-5 was loaded into the Harrick low temperature environmental chamber and attached to the Harrick Praying Mantis accessory to perform DRIFTS measurements with the Bruker Tensor 37 infrared spectrometer. A measurement was taken of the sample under dynamic vacuum at room temperature, then 1 atm of NO/N_2 was added from a 100 mL Schlenk flask through a Swagelok valve. A spectrum was collected immediately afterwards. An identical procedure was used to monitor the interaction of MOF-5 and NO, as a control experiment.

8.5.6 Reduction of ClV-MOF-5 by $[(THF)_3Na^+(TEMPO^-)]_4$

0.0325 mmol of ClV-MOF-5 was suspended in 3 mL of THF. At room temperature, a 3-mL THF solution containing 0.0325 mmol of $[(THF)_3Na^+(TEMPO^-)]_4$ was added to these crystals. The contents were left at room temperature for 18 h with gentle stirring. The resulting material was washed 3 × with 20 mL of fresh THF.

8.5.7 Calculations

All time-dependent density functional theory (TD-DFT) calculations and geometry optimizations were performed at the spin-unrestricted level using the Becke-Perdew (BP) functional[90,91] with the ORCA 2.8.0 software package.[92] For the TD-DFT calculations of Cr-MOF-5 and ClCr-MOF-5, 50 and 10 excited states, respectively, were included using one-electron transitions. All geometry optimizations began from crystallographically determined structures. To simulate the lattice-imposed strain, the carbon atoms in the 1 and 4 positions of the benzoate rings were fixed, while the rest of the molecule was allowed to optimize. The all-electron Gaussian basis sets developed by the Ahlrichs group were employed in all calculations.[93,94] The standard basis sets TZV(p) (for H), TZV(2d) (for C, N, and O), and TZV(2pf) (for Zn and Cr) were used. The resolution of the identity (RI) approach was taken for geometry optimizations, though not for TD-DFT calculations. The zeroth-order regular approximation (ZORA)[95–97] method was implemented for all calculations involving Cr. The model compounds for ClTi-MOF-5, ClCr-MOF-5, Cr^{3+}-MOF-5, and Cr-MOF-5 were calculated with doublet, quartet, quartet, and quintet spin multiplicities, respectively.

8.5.8 EPR Simulation

EasySpin 4.0.0 was run as a toolbox within MATLAB. The continuous-wave solid-state EPR spectrum of V-MOF-5 was modeled with the "pepper" function and fitted using "esfit". Axial symmetry was assumed from the experimental data and hyperfine values were measured from the splitting between peaks to derive starting points for fitting A_z and $A_{x,y}$. The experimental microwave frequency and temperature were incorporated into the simulation and fitting was based on a ^{51}V nucleus with $S = \pm\frac{3}{2}$. The "genetic" method was used to fit the experimental data as is, rather than its integral or derivative. The fitting was run with g_z, $g_{x,y}$, A_z, and $A_{x,y}$ as parameters until a satisfactory simulation was achieved.

atom	x	y	z	atom	x	y	z	atom	x	y	z
C	-0.027226	-7.819769	-0.027228	C	0.168838	-7.133367	1.175259	C	-0.145323	-7.125890	-1.233867
Ti	1.293128	-1.314023	1.160894	Zn	1.215601	1.112953	-1.134445	Zn	-1.100049	-1.179218	-1.144808
Zn	-1.095788	1.097200	1.070025	O	0.157655	-0.148917	0.063533	O	0.762016	-0.781144	2.940598
O	2.855883	-0.005533	1.048155	O	0.005295	-2.911460	1.080745	O	0.780011	0.824069	-3.034712
O	3.085195	0.438194	-1.139147	O	0.869741	3.023765	-0.728757	O	-0.878061	-0.729301	-3.042502
O	-3.017355	-0.856911	-0.741523	O	-0.293689	-2.994069	-1.143794	O	-0.822773	0.842284	2.979916
O	-3.031011	0.889034	0.705131	O	-0.903081	3.026779	0.685191	C	-0.027226	0.027231	3.564252
C	3.564254	0.027231	-0.027228	C	-0.027226	-3.564249	-0.027228	C	-0.027226	0.027231	-3.618708
C	-0.027226	3.618711	-0.027228	C	-3.618706	0.027231	-0.027228	C	-0.012396	0.007471	5.037841
C	5.007515	-0.313027	0.036144	C	0.069414	-5.040174	-0.025649	C	-0.010706	0.012272	-5.103878
C	-0.032304	5.101263	-0.039091	C	-0.027226	0.027231	-7.874228	C	-0.027226	7.874231	-0.027228
C	-5.099340	0.025162	-0.046440	C	-7.874226	0.027231	-0.027228	C	0.834726	-0.861314	5.748315
C	5.598085	-0.653251	1.263372	C	0.220491	-5.741446	1.179137	C	0.877848	0.844534	-5.798661
C	5.791163	-0.274980	-1.128843	C	0.868350	0.850741	-7.189641	C	0.919884	7.188790	-0.790911
C	-0.901721	-0.818420	-5.797872	C	-5.800249	-0.838853	-0.902360	C	-0.101013	-5.735929	-1.234063
C	-0.909152	-0.809642	-7.188608	C	-7.191569	-0.833443	-0.894698	C	-0.866942	0.875717	5.738522
C	-5.791527	0.884994	0.813175	C	-0.983130	5.795100	0.723505	C	-0.979355	7.186175	0.727629
C	-7.181766	0.871611	0.817162	C	-0.028455	0.006968	7.835140	C	0.824456	-0.859027	7.141337
C	-0.871616	0.871611	7.127312	C	7.735322	-0.912189	0.161022	C	6.958645	-0.947607	1.323920
C	7.149795	-0.577809	-1.064818	C	0.918741	5.797533	-0.798655	H	-0.076438	-8.910477	-0.023138
H	0.273271	-7.686963	2.109392	H	-0.284207	-7.670656	-2.168734	H	-0.035575	0.035680	-8.966329
H	-0.023780	8.966221	-0.021195	H	-8.966112	0.026415	-0.019449	H	1.493260	-1.531236	5.196048
H	4.975873	-0.685506	2.156520	H	0.359371	-5.180970	2.102927	H	1.559400	1.477494	-5.231839
H	5.318796	-0.010505	-2.074426	H	1.552772	1.495361	-7.742778	H	1.656306	7.741491	-1.375737
H	-1.579094	-1.454751	-5.229992	H	-5.238621	-1.501048	-1.560137	H	-0.213696	-5.167362	-2.156102
H	-1.599547	-1.448888	-7.740567	H	-7.746818	-1.497695	-1.558214	H	-1.517409	1.542999	5.174950
H	-5.227307	1.546124	1.469286	H	-1.709325	5.227205	1.303700	H	-1.713140	7.736692	1.317831
H	-7.726646	1.535986	1.490375	H	-0.036265	0.008146	8.926318	H	1.482802	-1.534266	7.690068
H	-1.536083	1.546383	7.669795	H	8.799990	-1.147608	0.209693	H	7.415669	-1.211290	2.278735
H	7.755886	-0.553488	-1.971658	H	1.645197	5.232319	-1.381052	Cl	2.917221	-2.951937	0.730864

Table 8.3: Optimized atomic coordinates for $ClTiZn_3O(C_8H_4O_4)_6$

atom	x	y	z	atom	x	y	z	atom	x	y	z
C	-0.027226	-7.819769	-0.027228	C	0.369316	-7.137810	1.126696	C	-0.332159	-7.123923	-1.198843
Cr	1.286610	-1.277821	1.010490	Zn	1.204236	1.122952	-1.140036	Zn	-1.108491	-1.146177	-1.144918
Zn	-1.099692	1.102525	1.097598	O	0.116632	-0.093452	0.049610	O	0.753596	-0.762614	2.913888
O	2.877116	-0.146381	1.063834	O	0.238197	-2.926292	1.069864	O	0.786693	0.818836	-3.037176
O	3.118002	0.656447	-1.036626	O	0.834879	3.031217	-0.769469	O	-0.876158	-0.730901	-3.044167
O	-3.024851	-0.820233	-0.781416	O	-0.583295	-3.030440	-1.038942	O	-0.839732	0.847030	3.019876
O	-3.032747	0.857693	0.745016	O	-0.872155	3.029044	0.726069	C	-0.027226	0.027231	3.564252
C	3.564254	0.027231	-0.027228	C	-0.027226	-3.564249	-0.027228	C	-0.027226	0.027231	-3.618708
C	-0.027226	3.618711	-0.027228	C	-3.618706	0.027231	-0.027228	C	-0.002518	0.000843	5.048255
C	5.001187	-0.359440	-0.015649	C	0.086045	-5.041768	-0.038905	C	-0.014190	0.015672	-5.104189
C	-0.034480	5.102235	-0.036395	C	-0.027226	0.027231	-7.874228	C	-0.027226	7.874231	-0.027228
C	-5.099920	0.027091	-0.044554	C	-7.874226	0.027231	-0.027228	C	0.848461	-0.859647	5.755439
C	5.579742	-0.912809	1.136884	C	0.432023	-5.745894	1.122405	C	0.879346	0.842549	-5.798814
C	5.787764	-0.159265	-1.161271	C	0.871696	0.847058	-7.189787	C	0.891110	7.188296	-0.824380
C	-0.909540	-0.810295	-5.798013	C	-5.799928	-0.834303	-0.904038	C	-0.281485	-5.734800	-1.204031
C	-0.915290	-0.803138	-7.188775	C	-7.191173	-0.831448	-0.896033	C	-0.862812	0.867014	5.739451
C	-5.792048	0.884246	0.816444	C	-0.956281	5.796723	0.759936	C	-0.951615	7.187821	0.762609
C	-7.181766	0.871611	0.817162	C	-0.022755	0.013266	7.836834	C	0.836250	-0.851153	7.150340
C	-0.871616	0.871611	7.127312	C	7.709007	-1.062840	-0.001326	C	6.929957	-1.259474	1.143469
C	7.135476	-0.513870	-1.153209	C	0.888597	5.797219	-0.830768	H	-0.084570	-8.910065	-0.014728
H	0.618019	-7.693986	2.031638	H	-0.623685	-7.666071	-2.099460	H	-0.033676	0.033665	-8.966400
H	-0.023319	8.966287	-0.022319	H	-8.966130	0.026355	-0.019352	H	1.509635	-1.525632	5.201521
H	4.959892	-1.062249	2.020146	H	0.717073	-5.190447	2.015421	H	1.564358	1.471533	-5.231808
H	5.324776	0.267861	-2.050181	H	1.560625	1.486790	-7.743054	H	1.605807	7.740420	-1.436130
H	-1.590399	-1.442784	-5.230036	H	-5.237010	-1.493308	-1.563856	H	-0.541594	-5.163647	-2.093767
H	-1.608467	-1.439238	-7.740936	H	-7.745675	-1.495393	-1.560535	H	-1.514832	1.526518	5.169248
H	-5.228561	1.543883	1.474638	H	-1.661304	5.229550	1.366353	H	-1.663138	7.739801	1.378230
H	-7.727675	1.535798	1.489907	H	-0.031181	0.018527	8.928163	H	1.497090	-1.519266	7.704529
H	-1.539964	1.544396	7.666983	H	8.764837	-1.339252	0.003367	H	7.376958	-1.687280	2.042085
H	7.742382	-0.362947	-2.047225	H	1.592530	5.230595	-1.438839	Cl	2.439397	-2.399195	-0.687175

Table 8.4: Optimized atomic coordinates for $ClCrZn_3O(C_8H_4O_4)_6$

atom	x	y	z	atom	x	y	z	atom	x	y	z
C	19.378500	24.450500	19.378500	C	19.796514	25.135277	20.524387	C	18.998017	25.149324	18.228908
Cr	20.511984	31.088627	20.570201	Zn	20.540773	33.446544	18.223242	Zn	18.238180	31.148132	18.220922
Zn	18.245291	33.433732	20.470195	O	19.508732	32.179806	19.461453	O	20.210695	31.486160	22.366201
O	22.294278	31.674111	20.302896	O	19.742351	29.334592	20.462965	O	20.357793	32.868540	16.378691
O	22.450204	33.110135	18.562467	O	20.015899	35.293254	18.437848	O	18.394694	31.731532	16.381836
O	16.386918	31.343024	18.767016	O	18.944772	29.307250	18.346098	O	18.538871	33.022255	22.372730
O	16.377317	33.242996	20.008756	O	18.749213	35.297247	20.320068	C	19.378500	32.297500	22.969980
C	22.969980	32.297500	19.378500	C	19.378500	28.706020	19.378500	C	19.378500	32.297500	15.787020
C	19.378500	35.888980	19.378500	C	15.787020	32.297500	19.378500	C	19.436740	32.315830	24.445459
C	24.424939	32.038610	19.320860	C	19.429569	27.234165	19.380672	C	19.378805	32.293900	14.308188
C	19.378226	37.367267	19.374807	C	19.378500	32.297500	11.531500	C	19.378500	40.144500	19.378500
C	14.310758	32.291789	19.368575	C	11.531500	32.297500	19.378500	C	20.375374	31.543605	25.152137
C	25.044192	31.190681	20.256817	C	19.825271	26.526850	20.529322	C	20.412667	32.939763	13.610949
C	25.195345	32.654582	18.317446	C	20.410565	32.939481	12.220174	C	20.081075	39.457064	18.385468
C	18.344686	31.649788	13.609992	C	13.608613	31.416287	18.521765	C	19.019745	26.539570	18.227484
C	18.346727	31.653540	12.219052	C	12.217713	31.427724	18.521469	C	18.516553	33.118931	25.143081
C	13.614311	33.160299	20.218829	C	18.672111	38.064260	20.368957	C	18.674619	39.455007	20.368880
C	12.223960	33.141880	20.222890	C	19.470047	32.373582	27.235158	C	20.390163	31.577439	26.544393
C	18.534110	33.141880	26.533040	C	27.177980	31.577580	19.187339	C	26.416506	30.963835	20.187777
C	26.566422	32.421999	18.253786	C	20.083161	38.066108	18.381407	H	19.352498	23.359632	19.381575
H	20.092906	24.579988	21.414719	H	18.678188	24.606979	17.338754	H	19.377627	32.299641	10.439968
H	19.378722	41.236001	19.379731	H	10.440114	32.300307	19.380481	H	21.085530	30.924194	24.605823
H	24.444719	30.720590	21.035433	H	20.134443	27.075114	21.418581	H	21.203872	33.434803	14.172249
H	24.705823	33.310136	17.598194	H	21.208385	33.438893	11.669543	H	20.624753	40.008691	17.617891
H	17.550938	31.157174	14.169925	H	14.165480	30.744531	17.869768	H	18.715093	27.103917	17.347226
H	17.547324	31.157815	11.667400	H	11.664781	30.761343	17.858732	H	17.795233	33.711947	24.582713
H	14.169841	33.833333	20.870118	H	18.130321	37.503066	21.128979	H	18.129532	40.004842	21.136774
H	11.678937	33.810752	20.890952	H	19.482262	32.395380	28.325789	H	21.118571	30.981453	27.094997
H	17.818625	33.760822	27.075321	H	28.252774	31.397964	19.135462	H	26.896676	30.308666	20.915264
H	27.162845	32.899630	17.475866	H	20.622817	37.507185	17.618137				

Table 8.5: Optimized atomic coordinates for $Cr^{3+}Zn_3O(C_8H_4O_4)_6$

atom	x	y	z	atom	x	y	z	atom	x	y	z
C	19.378500	24.450500	19.378500	C	20.524709	25.133685	19.793194	C	18.219944	25.142185	19.020877
Cr	20.512907	31.073551	20.553004	Zn	20.437734	33.379985	18.292912	Zn	18.242113	31.122209	18.257527
Zn	18.238423	33.414132	20.540514	O	19.343207	32.218440	19.453809	O	20.381390	31.798222	22.349106
O	22.498796	31.470097	20.212529	O	20.458382	29.320122	19.700074	O	20.057770	33.200490	16.371049
O	22.324070	33.052251	18.574090	O	20.125275	35.305473	18.530285	O	18.704992	31.372690	16.364488
O	16.357544	31.544370	18.523642	O	18.328769	29.271629	18.920156	O	18.384402	32.874748	22.419090
O	16.346108	33.099308	20.192914	O	18.636191	35.313606	20.248613	C	19.378500	32.297500	22.969980
C	22.969980	32.297500	19.378500	C	19.378500	28.706020	19.378500	C	19.378500	32.297500	15.787020
C	19.378500	35.888980	19.378500	C	15.787020	32.297500	19.378500	C	19.413916	32.286846	24.453609
C	24.469518	32.413369	19.311508	C	19.368257	27.226511	19.450918	C	19.370957	32.301598	14.301920
C	19.371972	37.374386	19.373435	C	19.378500	32.297500	11.531500	C	19.378500	40.144500	19.378500
C	14.302023	32.268215	19.388850	C	11.531500	32.297500	19.378500	C	20.406677	31.588115	25.157277
C	25.273225	31.627359	20.151717	C	20.521701	26.524937	19.832499	C	20.107457	33.272152	13.608316
C	25.077513	33.303763	18.412933	C	20.109669	33.268978	12.217316	C	20.177667	39.459110	18.461857
C	18.636225	31.330766	13.606840	C	13.602276	31.405057	18.532127	C	18.214082	26.532279	19.053464
C	18.641397	31.329764	12.215920	C	12.211370	31.418570	18.528936	C	18.470540	33.057017	25.149198
C	13.612251	33.135046	20.240495	C	18.569542	38.069150	20.289342	C	18.573994	39.460013	20.290812
C	12.223960	33.141880	20.222890	C	19.519486	32.441554	27.238486	C	20.451868	31.659546	26.549060
C	18.534110	33.141880	26.533040	C	27.263033	32.619193	19.196095	C	26.662965	31.730367	20.093909
C	26.467775	33.405103	18.356284	C	20.175782	38.068099	18.458099	H	19.387880	23.359170	19.341036
H	21.420497	24.578510	20.075136	H	17.329388	24.595660	18.707207	H	19.382654	32.295256	10.439283
H	19.382262	41.236731	19.381124	H	10.439473	32.312718	19.372469	H	21.139892	31.003642	24.601840
H	24.790427	30.939738	20.845750	H	21.407553	27.084128	20.132512	H	20.668401	34.013291	14.176336
H	24.445544	33.910081	17.764734	H	20.679153	34.017948	11.665243	H	20.799267	40.011514	17.755799
H	18.073822	30.589854	14.173447	H	14.165692	30.741262	17.877565	H	17.333420	27.102339	18.760891
H	18.075276	30.578872	11.663005	H	11.655305	30.753345	17.866802	H	17.710058	33.594604	24.584964
H	14.177037	33.795671	20.896291	H	17.955720	37.502135	20.987905	H	17.955298	40.012780	20.999133
H	11.677024	33.820387	20.880632	H	19.562397	32.508584	28.326970	H	21.220945	31.113473	27.097509
H	17.809796	33.752663	27.074772	H	28.350698	32.699393	19.151087	H	27.281283	31.116100	20.750698
H	26.933520	34.099480	17.654888	H	20.788311	37.500236	17.758861				

Table 8.6: Optimized atomic coordinates for $Cr^{2+}Zn_3O(C_8H_4O_4)_6$

Chapter 9

Nitric Oxide Disproportionation Promoted by Fe-MOF-5

9.1 Abstract

The weak-field ligand environments at the metal nodes of metal-organic frameworks resemble the electronic environment of metalloenzyme active sites, but few reports have studied the reactivity of MOF nodes towards small molecules of biological relevance. In this final chapter, we report that the ferrous ions in Fe^{2+}-exchanged MOF-5 disproportionate nitric oxide to produce nitrous oxide and a ferric nitrito complex. Although mechanistic studies of N–N bond forming transformations often invoke a hyponitrite species, as in nitric oxide reductase and nitrogen reduction catalysis, little is known about this intermediate in its monoanionic oxidation state. Together, with the first report of N–N coupling between NO molecules in a MOF, we present evidence for a species that is consistent with a ferric hyponitrite, whose isolation is enabled by the spatial constraints of the MOF matrix.[1]

[1] At the time of writing this thesis, the work presented in this chapter was unpublished. Mössbauer experiments and analyses were conducted in collaboration with Sebastian A. Stoian. X-ray absorption spectroscopy was conducted by and analyzed in collaboration with Jeffrey T. Miller.

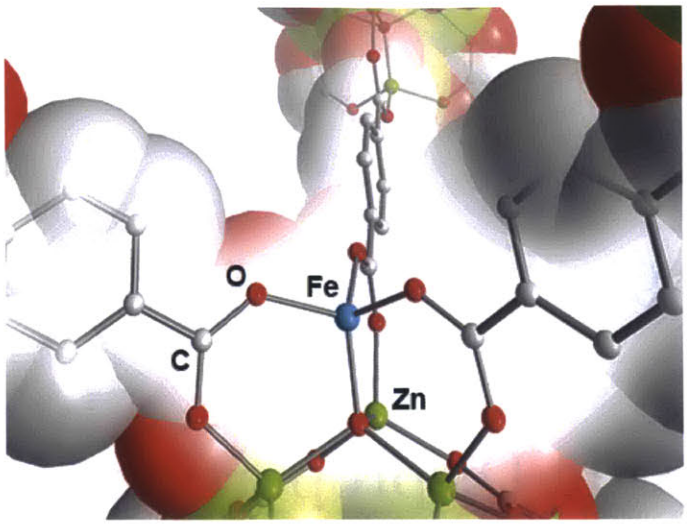

Figure 9-1: Single crystal X-ray structure of MOF-5, depicting the metal node where Fe^{2+} inserts to furnish Fe^{2+}-MOF-5.

9.2 Introduction

The chemical transformation of nitric oxide mediated by transition metal ions underlies crucial processes in both Nature and in environmental protection. NO is a chief component of N_xO_y species that contaminate the atmosphere[227] and is targeted in N_xO_y reduction catalysis.[228,229] Immune response, blood pressure control, and neurotransmission require the generation and decay of nitric oxide[230] by metal-containing molecules such as the heme enzyme known as soluble guanylyl cyclase (sGC).[231] Although NO transformations in these biological examples occur under homogeneous conditions, they are mediated by active sites and clusters supported by weak-field ligands such as carboxylates and imidazolates. These functionalities are identical to those found in most MOFs, making the latter prime candidates for biomimetic studies.

With mounting recent evidence from us and others that MOF nodes can undergo redox transformations,[17,180–182,199] we have begun exploring the chemistry of biologically relevant small molecules by conceiving of the metal nodes as electronically isolated molecules. Here, we show that Fe^{2+}-substituted $Zn_4O(BDC)_3$ (Fe^{2+}-MOF-5) facilitates the disproportionation of NO with formation of N_2O, a reaction that is rem-

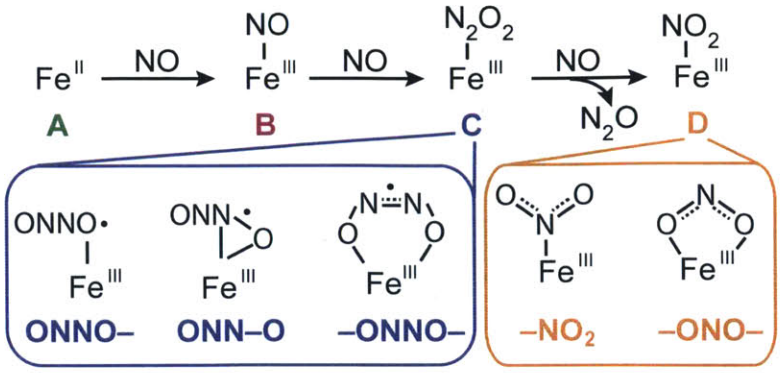

Scheme 9.1

iniscent of the reductive N–N coupling in nitric oxide reductase (NOR) to evolve N_2O. In contrast to NOR and the majority of its small molecule mimics, which promote N–N bond formation at bimetallic centers,[232–235] a single Fe atom is involved in NO disproportionation in Fe^{2+}-MOF-5. Additional investigations into the mechanism of this reaction allow us to isolate a species that is most consistent with a ferric hyponitrite. To our knowledge, these results are the first to provide experimental evidence of a mono-anionic hyponitrite radical intermediate implicated in the formation of a N–N bond, and constitute the first example of a MOF promoting NO reactivity of any kind. The disproportionation of three equivalents of NO in Fe^{2+}-MOF-5 is, of course, a different reaction from what occurs in NOR and deNO$_x$ catalysts, but it provides a useful medium for studying the general features that underlie transformations of N_xO_y molecules. We hope to gain new insight into these specific systems by simplifying the mechanism to a single metal site and isolating uncommon intermediates in biologically relevant ligand fields that are otherwise difficult to achieve.

9.3 Results

In Chapter 8, we introduced a series of first-row transition metal ions in the the all oxygen dianionic tripodal environment of the MOF-5 clusters (Figure 9-1). As discussed in Chapter 7, magnetic susceptibility measurements confirm that the material we termed Fe-MOF-5 features isolated S = 2 ferrous ions (Figure 7-4). To demon-

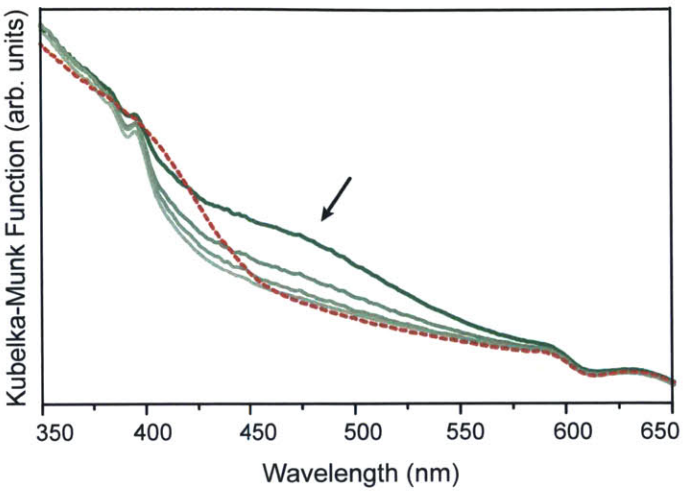

Figure 9-2: Diffuse reflectance UV-visible spectrum of Fe-MOF-5 as it performs NO disproportionation. The starting ferrous material is shown in red, while the $\{FeNO\}^7$ nitrosyl (species **B**) is shown in darkest green. Progressively lighter green spectra correspond to the decay of this species.

strate the promise of these high-spin centers towards redox chemistry, we reported the characterization of a $\{FeNO\}^7$ fragment.[16,17] Our initial evidence that Fe^{2+}-MOF-5 promotes nitric oxide disproportionation was in observing the spectral features of the $\{FeNO\}^7$ species decay over the course of several minutes. Backfilling an evacuated sample of yellow Fe^{2+}-MOF-5 with NO/N_2 at room temperature induced a color change to black, corresponding to the formation of iron nitrosyl $\{FeNO\}^7$ (**B**, in Scheme 9.1). Continued exposure to NO caused the black crystals to gradually turn bright orange. The decay of the black $\{FeNO\}^7$ adduct and the formation of the new orange product were followed by in situ diffuse reflectance UV-Vis-NIR spectroscopy, which evidenced the decay of the broad ligand-to-metal $NO(\pi^*)\rightarrow d$ charge transfer band at 476 nm present in B (Figure 9-2).

In situ diffuse reflectance infrared Fourier transform spectroscopy (DRIFTS) provided further evidence for the decomposition of **B**. The strong band centered at 1793 cm^{-1}, attributed to the N–O stretch (ν_{NO}) of the nitrosyl group in **B**, decreased in intensity over 10 minutes (Figure 9-3), with concomitant emergence of new peaks at 1178 and 868 cm^{-1} arising from what we label as species **C**. Surprisingly, the new peaks from **C** reached their maximum intensity after 30 min and then receded over

	natural abundance NO	^{15}NO
B	1796 (s)	1760 (s)
C	1178 (m), 868 (w)	1155 (m), 863 (w)
D	1220 (m), 1000 (m), 797 (w)	1193 (m), 1000 (s), 776 (w)

Table 9.1: Measured DRIFTS bands for species **B**–**D** in cm^{-1} that appear after treating Fe-MOF-5 with NO. Intensities are indicated in parentheses.

the course of another 30 min, leaving a new set of resonant features appeared at 1220, 1000, and 797 cm^{-1}, evidencing the formation of yet a new species, **D**. Representative spectra from the time evolution DRIFTS analysis of the last two steps, **B**→**C** and **C**→**D**, are shown in Figure 9-3. For completeness, the full set of spectra is displayed in Figure 9-4. These new bands are summarized in Table 9.1. Although species **C** was observed only transiently under a NO atmosphere, we were able to isolate it by evacuating our in situ DRIFTS cell immediately before the spectral features from species **D** began to emerge. Species **C** is stable indefinitely under vacuum or N_2, but produces species **D** in less than a minute after exposure to NO. Analysis of the final material confirms that the lattice is retained. Powder X-ray diffraction of the final material matches the simulated pattern of MOF-5 (Figure 9-5) and Brunauer-Emmett-Teller (BET) analysis based on an N_2 isotherm of these crystals gives a value of 3218 m^2/g, which is expected of fully activated MOF-5 (Figure 9-6).

To investigate whether any gases are evolved during the **B**→**C**→**D** reaction sequence, we sampled the headspace of the batch reactor used for in situ DRIFTS by real-time gas analysis and quadrupole mass spectrometry (RGA-MS). Because signal spikes can be artifacts of monitoring MS in flow, we altered the setup to detect N_2O with greater certainty: once the full **B**→**D** sequence was completed after about 1 h, as indicated by DRIFTS, we cooled the reactor to –150 °C and applied vacuum so that frozen N_2O would remain in the chamber, but excess NO and N_2, expected to remain in the gaseous phase at this temperature, would not. The reactor was warmed to room temperature and attached in line to the mass spectrometer with a flow of He/Ar. After establishing a stable baseline for signals at 30 and 44 amu, corresponding to NO and N_2O, respectively, the reactor was opened to the flow setup

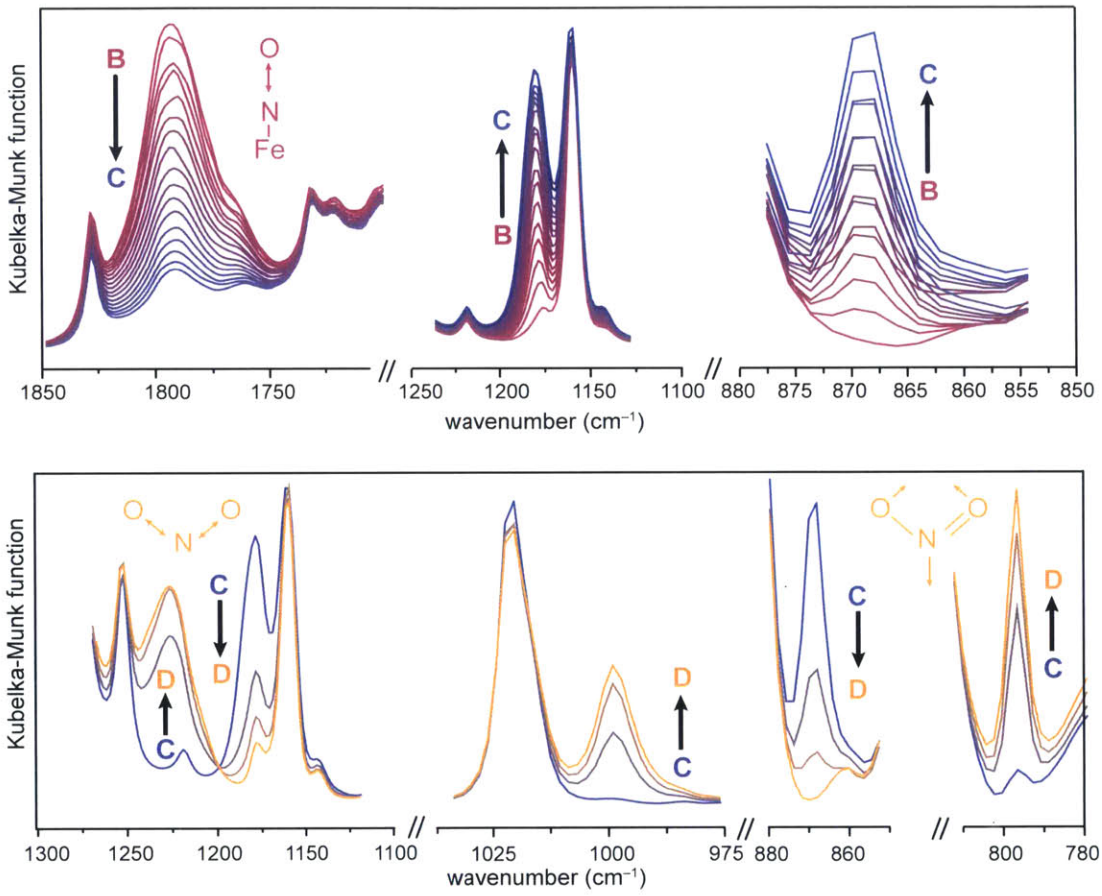

Figure 9-3: Selected In situ DRIFTS collected on Fe-MOF-5 during NO disproportionation. Species **B** is shown in pink, species **C** in blue, and species **D** in gold. IR-active modes are depicted in the same color as the corresponding spectral feature.

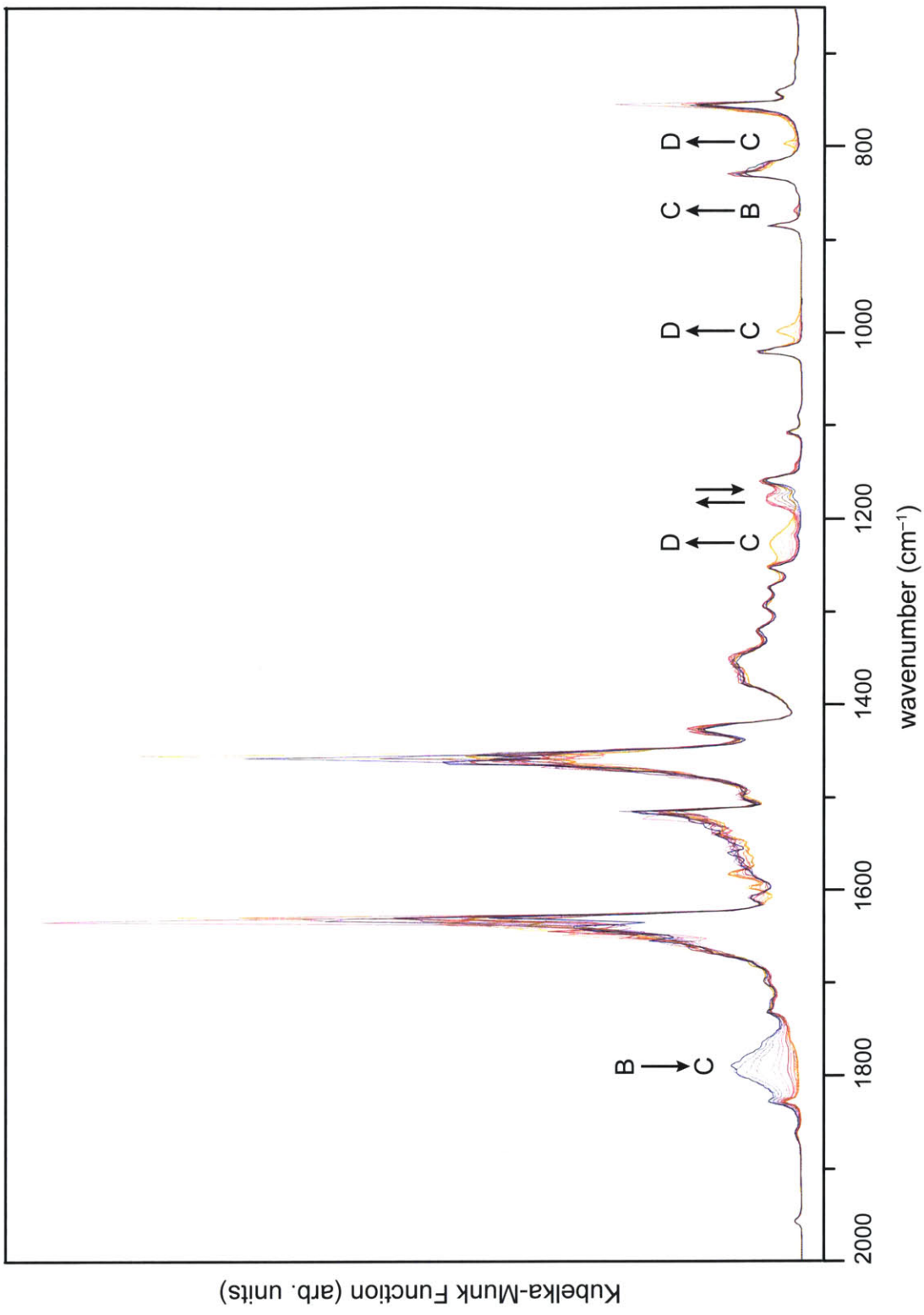

Figure 9-4: Complete in situ DRIFTS collected on Fe-MOF-5 during NO disproportionation starting from species **B** is shown in pink, species **C** in blue, and species **D** in gold.

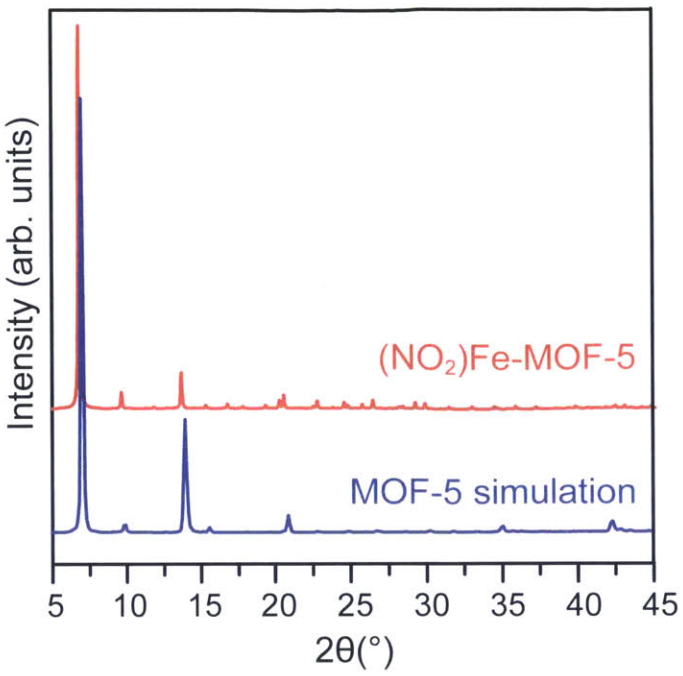

Figure 9-5: Powder X-ray diffraction pattern of species **D** and the simulated pattern of MOF-5.

for detection. As shown in Figure 9-7, a signal appeared for N_2O and took 132 s to reach baseline levels, whereas the detection of NO remained unperturbed.

With evidence that N_2O is evolved as part of the sequential **B**→**C**→**D** transformation, we employed X-ray absorption spectroscopy (XAS) to probe the oxidation states and coordination environments of the iron sites in **C** and **D**, since they were expected to change during these transformations. Comparing the K-edge spectra of pristine Fe^{2+}-MOF-5 to that of species **C** and **D** revealed a shift to higher energy in both the pre-edge (1s→3d) and rising edge (1s→2p) features (Figure 9-8), suggesting that the iron sites undergo one e^- oxidation to Fe^{3+} relative to species **A** (Fe^{2+}-MOF-5), a ferrous compound. By analyzing the difference spectrum from the XAS data, the extended X-ray absorption fine structure (EXAFS) regions indicate that both **C** and **D** contain additional ligands (Figure 9-8). These new scattering pairs were fit to a coordination number of 0.9 at a distance of 1.98(2) Å for **C** and 1.2 at a distance of 2.08(2) Å for **D**.

A zero-field Mössbauer spectrum was also collected at 70 K on species **D** and

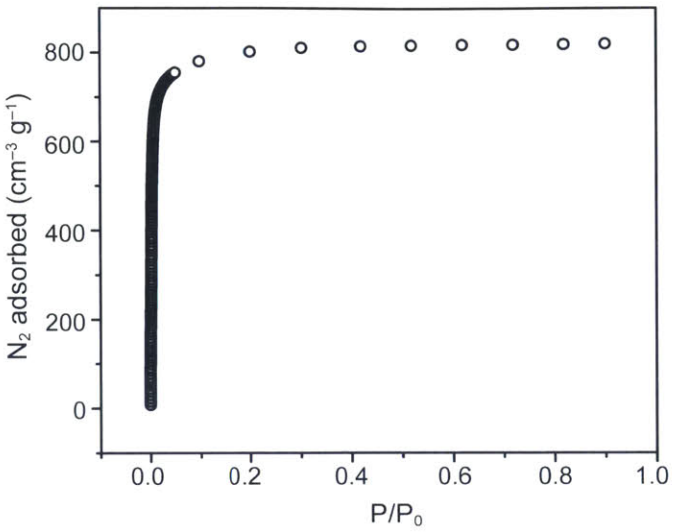

Figure 9-6: N_2 isotherm of NO_2Fe-MOF-5.

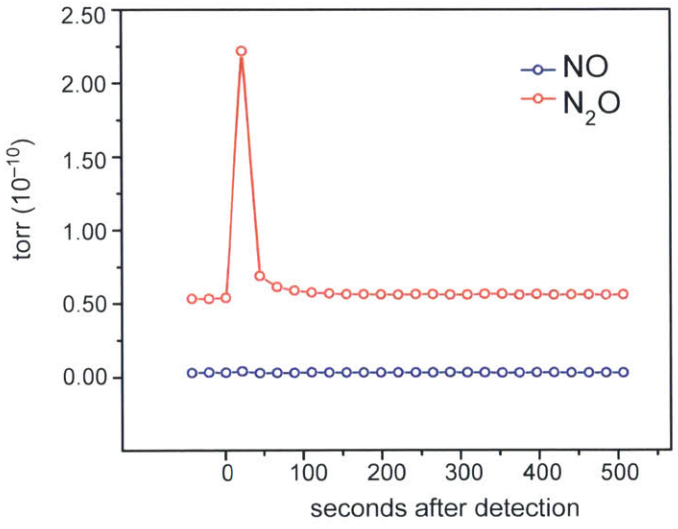

Figure 9-7: Real time analysis mass spectrometry of the head space sampled from a batch NO disproportionation promoted by Fe-MOF-5.

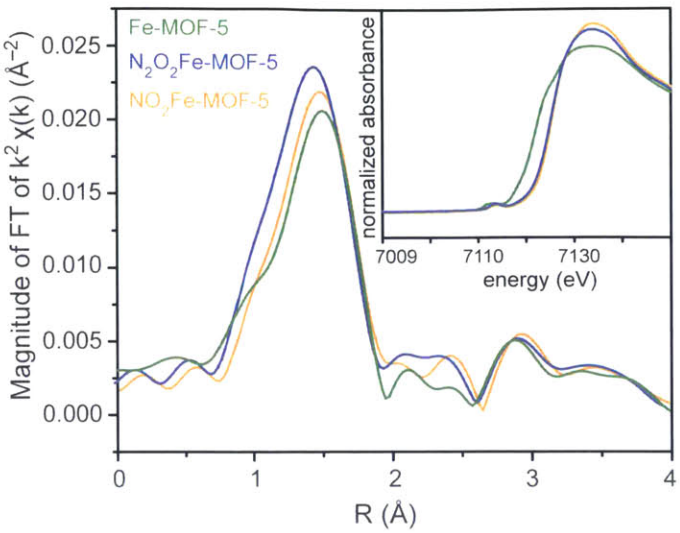

Figure 9-8: X-ray absorption spectra of Fe-MOF-5 (green), species C (blue), and species D (gold). Comparative R-space EXAFS are shown in large format with comparative XANES shown as an inset.

confirmed it is ferric. As shown in Figure 9-9, the doublet of the ferrous starting material **A** with $\delta = 1.05(2)$ mm/s and $\Delta E_Q = 3.03(1)$ mm/s shifted to $\delta = 0.5(1)$ mm/s and $\Delta E_Q = 0.75(4)$ mm/s after the completion of the sequence. These values and the relaxation-induced broadening that is typically observed for Kramers systems, i.e. half-integer spins, are consistent with a high spin Fe^{3+} center.[188] These data also suggest the reaction consumes all Fe^{2+} sites because the signal could not be fit to the original ferrous doublet. Furthermore, X-band electron paramagnetic resonance analysis of both species **C** and **D** showed broad signals at $g_{iso} = 4.2$ common for high-spin ferric species (Figures 9-10 and 9-11).[236]

To verify our mass spectrometry assignment of N_2O evolution as well as the vibrational spectral features of our DRIFTS data, we repeated these experiments using ^{15}NO. As shown in Figure 9-12, most of the peaks that evolve during the **B**→**C**→**D** sequence are sensitive to isotopic substitution, indicating that they involve the transformation of N_xO_y species. The ν_{NO} of **B** shifts from 1793 to 1760 cm^{-1}, which is close to the difference of 32 cm^{-1} expected from the harmonic oscillator approximation. With the emergence of species **C** by using ^{15}NO, peaks grow in at 1155 and 863 cm^{-1}. These are shifted by 25 and 5 cm^{-1} relative to those observed with natural

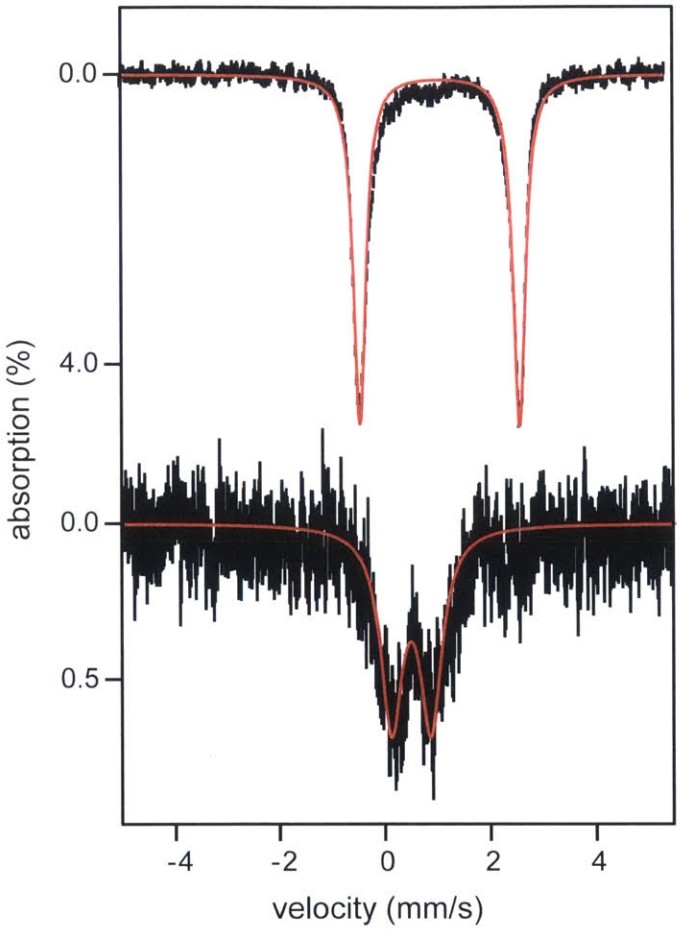

Figure 9-9: Zero-field ^{57}Fe Mössbauer spectra recorded at 4.2 K for Fe-MOF-5 (top) and at 70 K for NO treated Fe-MOF-5 (bottom). While the simulation of the starting Fe-MOF-5 sample used δ = 1.05(2) mm/s, ΔE_Q = 3.03(1) mm/s, and Γ = 0.28(1) mm/s, that of the NO treated Fe-MOF-5 was obtained using ΔE_Q = 0.5(1) mm/s, ΔE_Q = 0.75(4) mm/s, and linewidth Γ = 0.7(1) mm/s.

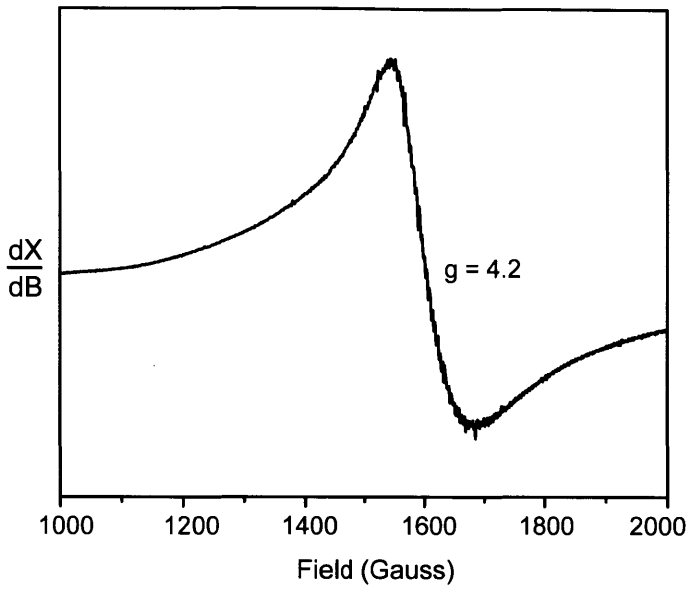

Figure 9-10: X-band EPR spectrum collected at 77 K for the ferric hyponitrite-containing MOF-5 (species **C**)

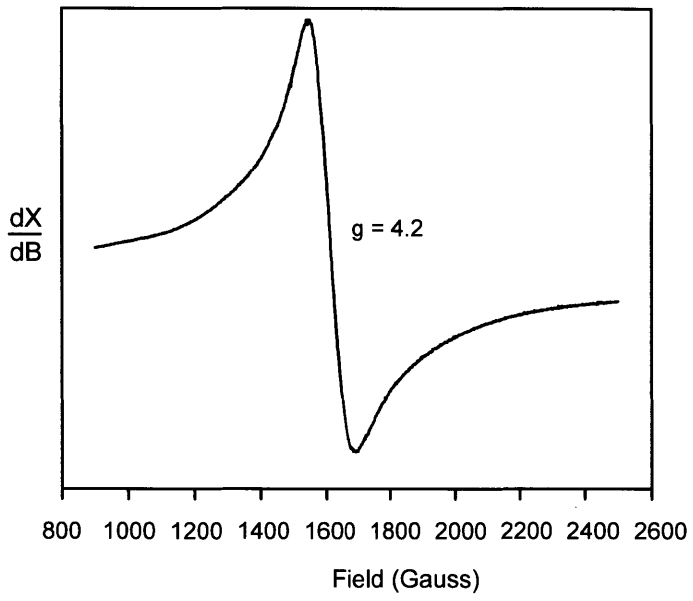

Figure 9-11: X-band EPR spectrum collected at 77 K for the ferric nitrite-containing MOF-5 (species **D**)

abundance NO, but deviate from the shifts of 21 and 15.5 cm^{-1} predicted by the harmonic oscillator approximation. The larger deviation of the latter mode is consistent with bands observed near this energy being ascribed to bending, not linear stretching modes. As species **D** is formed from ^{15}NO, features appear at 1193 and 776 cm^{-1}that are shifted by 33 and 20 cm^{-1}, respectively, and do not match the harmonic oscillator predictions of 22 and 14 cm^{-1} for pure N–O stretches. The transient DRIFTS spectra under ^{15}NO are shown in Figure 9-13. See Table 9.1 for a summary of observed DRFITS features. Interestingly, the mode at 1000 cm^{-1} is not sensitive to isotopic substitution. Finally, sampling the headspace by using the same procedure as before revealed a prominent mass fragment at 46 amu, as expected for doubly ^{15}N-labeled $(^{15}N)_2O$, confirming that both expected products from NO disproportionation are present at the end of the reaction sequence (Figure 9-14).

9.4 Discussion

Taken together, the observations described above are consistent with the reaction sequence shown in Scheme 9.1. Because the transformation occurs over the span of an hour, by assuming pseudo-first-order dependence on Fe^{2+} sites, we estimate that k ≤ 0.01 s^{-1} for the rate-limiting step. The energies of the isotopically sensitive normal modes are consistent with the N–O IR-active modes of various N_xO_y species, such as NO_2^- or $N_2O_2^{m-}$, where $m = 1$ or 2, which are expected to result as products or intermediates from nitric oxide disproportionation.[237] The vibrational feature that emerges with **D** at 1000 cm^{-1} is most likely a new lattice mode since it is not isotopically sensitive—perhaps caused instead by a lattice vibration induced by geometrical distortions at the iron sites. Of the three possible binding modes of NO_2^- to the ferric centers, the EXAFS data of **D** are best fitted to a model where the NO_2^- is bound to Fe^{3+} in an η^1 fashion. The distance of 2.08(2) Å is suggestive of either a nitrito[238–240] or N-bound (i.e. nitro)[241–243]. Although η^2 nitrito species show distances above 2.10 Å.[239,244,245] EXAFS analysis identified only one scatterer near the Fe atom, not two. The DRIFTS feature at 797 cm^{-1} observed for species **D** is similar to reported values

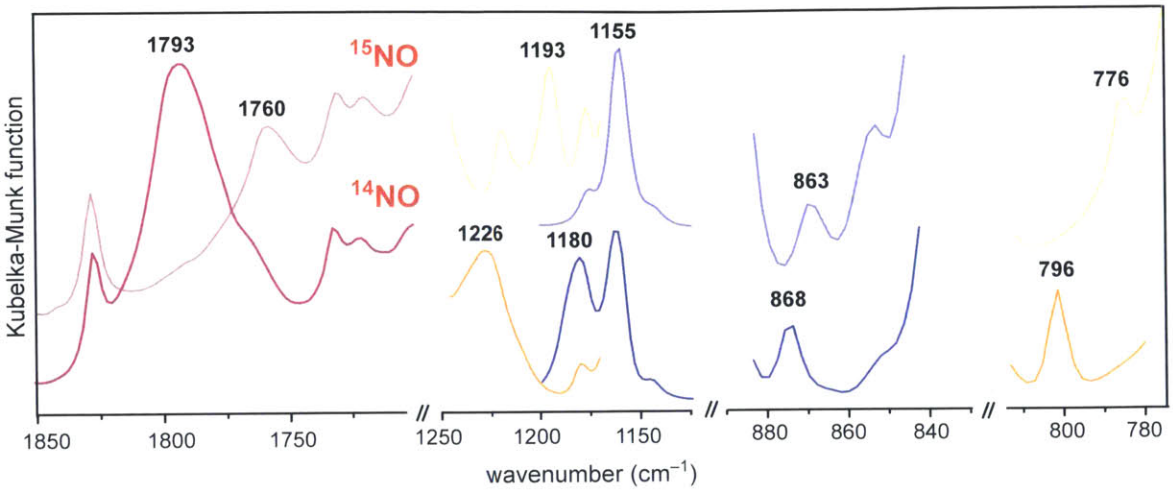

Figure 9-12: Comparative DRIFTS features for species **B** (pink), species **C** (blue), and species **D** (gold) shofwn when using natural abundance NO (dark) and ^{15}NO (light).

for δ_{ONO}, while 1220 cm^{-1} is reasonable for ν_{NO} for N–O species with bond orders between one and two, as found in nitrite.[246]

We could infer the identity of **C** in attempting its isolation. Initially, the conversion from **C** to **D** seemed to be an isomerization between coordination modes of NO_2^-, such as between N-bound and chelating. However, the observation that **C** is isolable by applying vacuum and forms **D** only upon addition of NO necessarily implies that **C** be an intermediate formed by the reaction of Fe^{2+}-MOF-5 with only two equivalents of NO. The EXAFS fitting for **C** suggests that the N_xO_y species bound to Fe is η^1 at a distance of 1.98 Å, while the near-edge data confirms that **C** is most likely a ferric species, as corroborated by EPR (Figure 9-10). Finally, the IR stretch observed in C at 1178 cm^{-1} is in the region of N–O bond orders between one and two, while the feature at 868 cm^{-1} is consistent with N_xO_y bending modes.[246–248] Together, these data point to **C** as a ferric η^1 hyponitrite species.

We performed density functional theory calculations on truncated model compounds to identify **C** and **D** and to assign their DRIFTS spectra. Rather than consider the entire lattice, calculations were based on $FeZn_3O(O_2C–C_6H_5)_6$ molecules where carbon atoms in the 1 and 4 positions of the benzoate were fixed to sim-

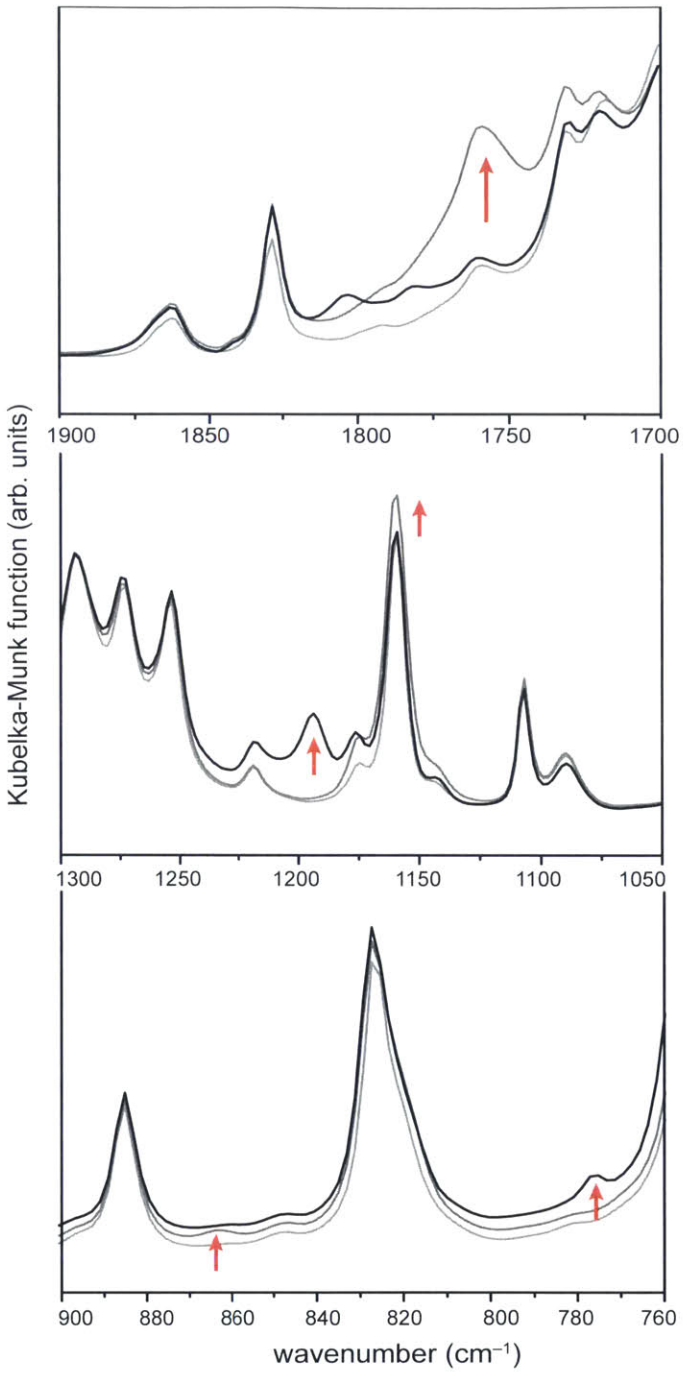

Figure 9-13: Diffuse reflectance infrared Fourier transform spectra of Fe-MOF-5 in the presence of ^{15}NO. Spectra begin in light grey and evolve towards black. N_xO_y-related bands are indicated in red arrows.

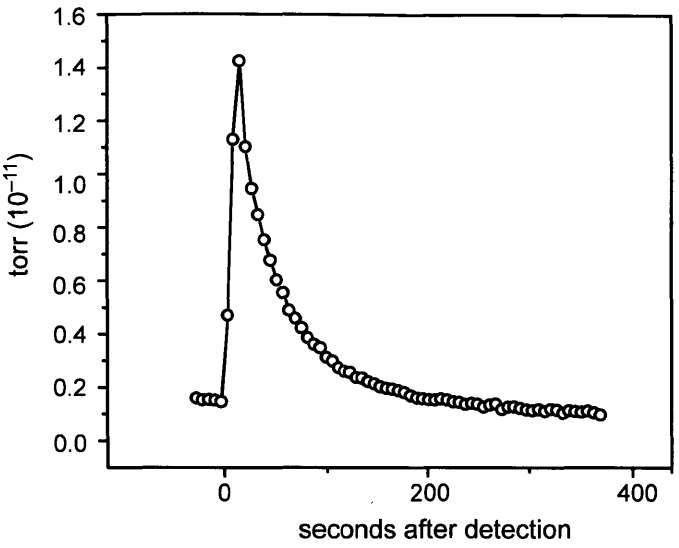

Figure 9-14: Real time analysis mass spectrometry of the head space sampled from a batch NO disproportionation reaction promoted by Fe-MOF-5 using ^{15}NO, detecting for the 46 amu mass fragment.

ulate geometrical constraints imposed by the MOF. To interrogate **C**, we studied three model compounds with the formula $N_2O_2FeZn_3O(O_2C–C_6H_5)_3$ where N_2O_2 is bound either η^1 through a terminal O (ONNO–), η^2 through a side-bound NO group (ONN–O), or η^1 with chelated O atoms (–ONNO–). These coordination modes are shown in Scheme 9.1. For **D**, we studied two model compounds with the formula $NO_2FeZn_3O(O_2C–C_6H_5)_3$ where NO_2 is either bound η^1 through the N atom (–NO_2) or η^2 through chelating O atoms (–ONO–), also shown in Scheme 9.1. We also attempted to calculate the isomer where NO_2 is bound η^2 through an O atom, but it converged into chelating coordination. See Figures 9-15, 9-16, 9-17, 9-18, and 9-19 for images of these structures. After geometry optimizations, frequency calculations were performed on all compounds to simulate IR spectra and Gibbs free enthalpies at 298.15 K (ΔG_f). Among the N_2O_2 isomers, –ONNO– is most stable, being 3.59 and 7.08 kcal/mol lower in energy than ONNO– and ONN–O, respectively. Yet, these energetic differences are quite small considering the limitations of these models. Comparing the calculated parameters with measured observables is more informative. For example, its Fe–ligand bonds are quite different from the 1.98 Å measured by XAS,

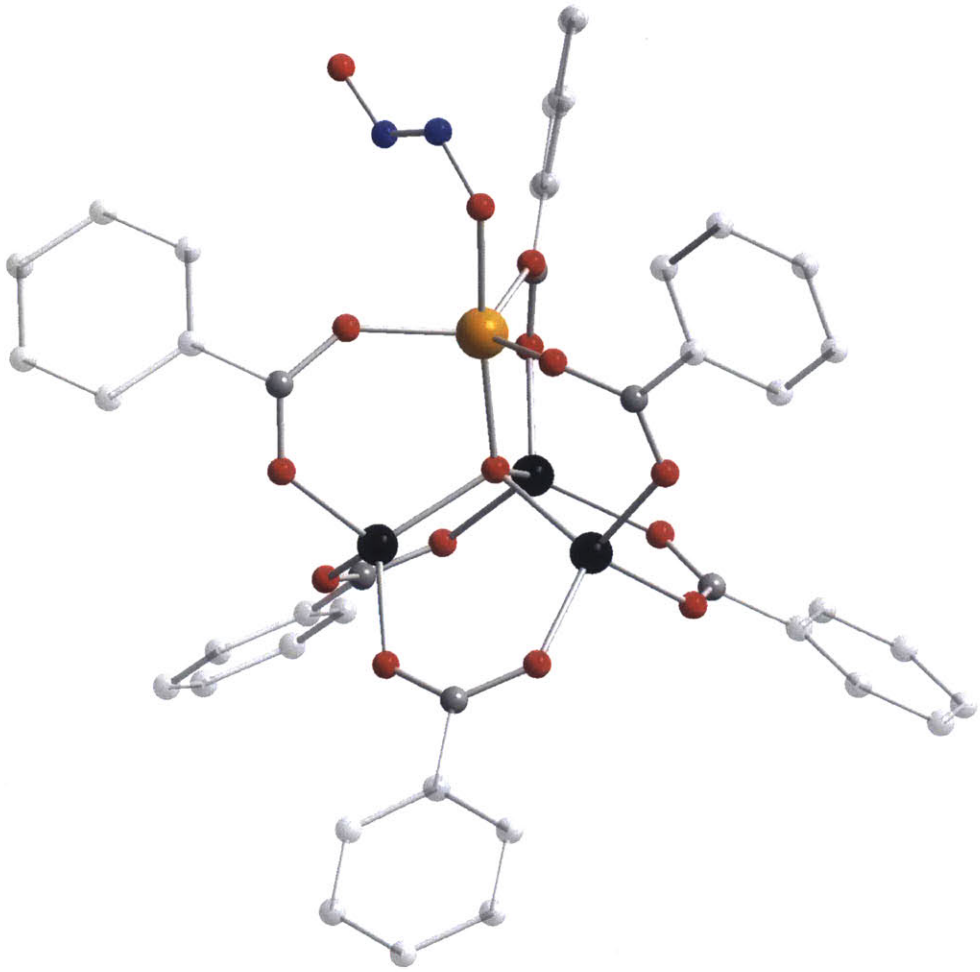

Figure 9-15: Geometry-optimized structure of ONNO–. Fe, Zn, O, N, and C atoms are shown in orange, black, red, blue, and gray. H atoms are omitted for clarity.

at 1.88 and 1.89 Å, in contrast with the more accurate 2.02 Å for ONNO– and 2.07 Å for ONN–O. Between the NO_2 isomers, –ONO– is more stable by 3.63 kcal/mol, yet its Fe–O_2N bonds of 2.19 and 2.25 Å are slightly longer than the 2.18 Å of –NO_2 and the experimental value of 2.08 Å. Despite the chelating isomers being predicted to be more thermodynamically stable, the final geometries resemble end-on coordination modes.

Comparing the calculated frequencies of these model compounds to the observed values aids our identification of **C** and **D**. Among the isomers of N_2O_2, the structurally similar ONNO– and ONN–O agree better than the chelating –ONNO– (see Table 9.2). Their bands at 1164 and 1158 cm^{-1} resemble the observed value of 1178 cm^{-1}, whereas

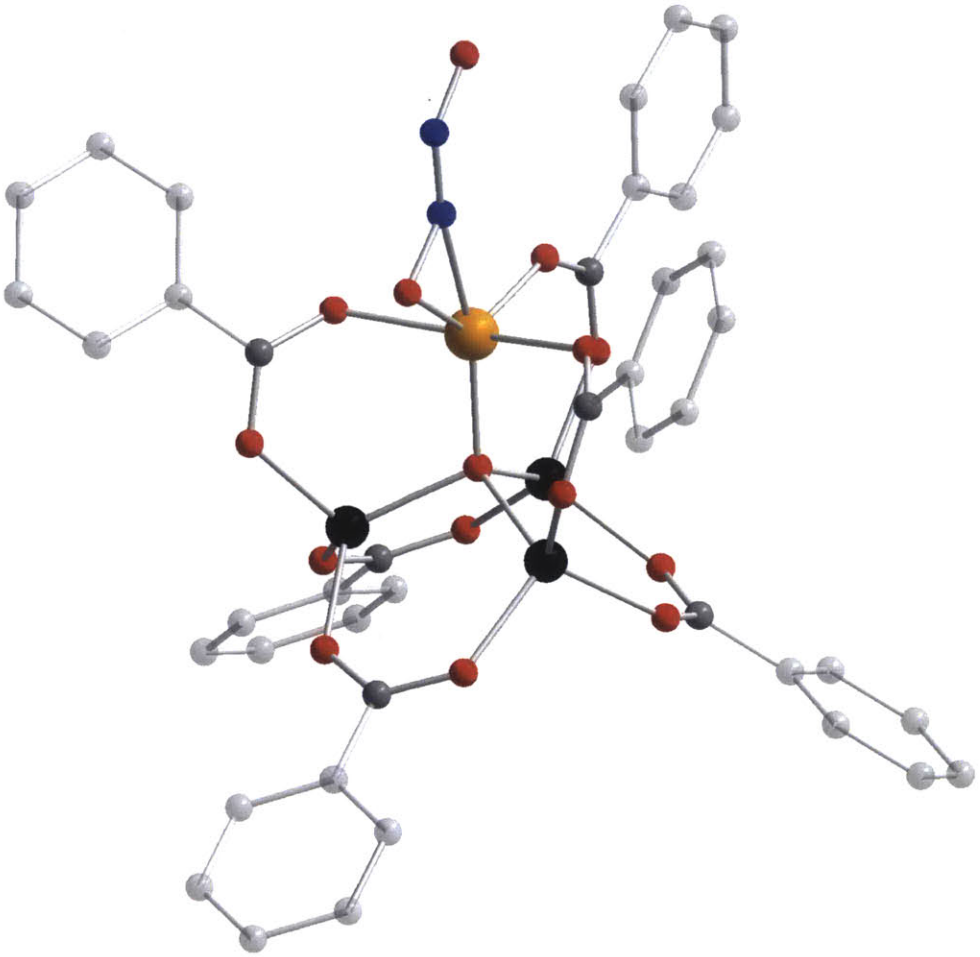

Figure 9-16: Geometry-optimized structure of ONN–O. Fe, Zn, O, N, and C atoms are shown in orange, black, red, blue, and gray. H atoms are omitted for clarity.

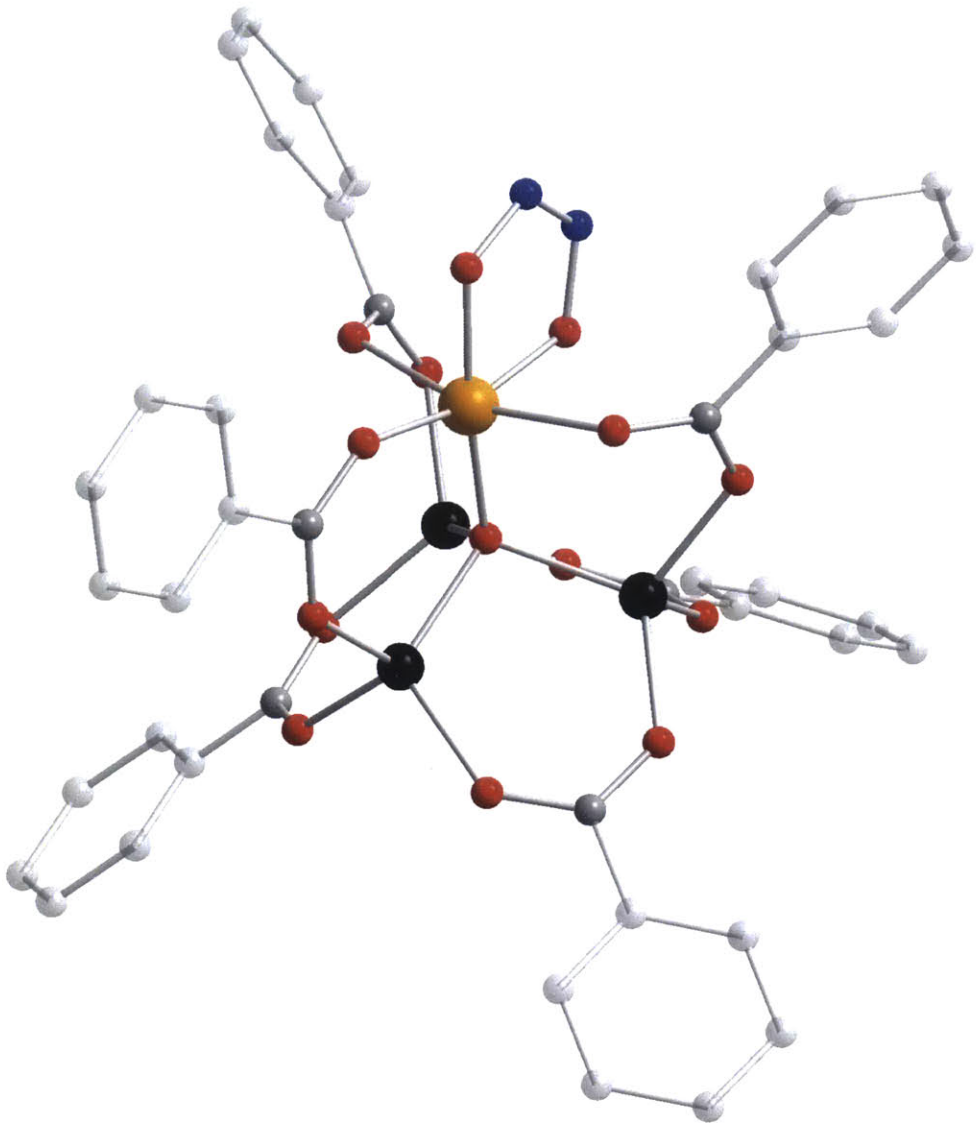

Figure 9-17: Geometry-optimized structure of –ONNO–. Fe, Zn, O, N, and C atoms are shown in orange, black, red, blue, and gray. H atoms are omitted for clarity.

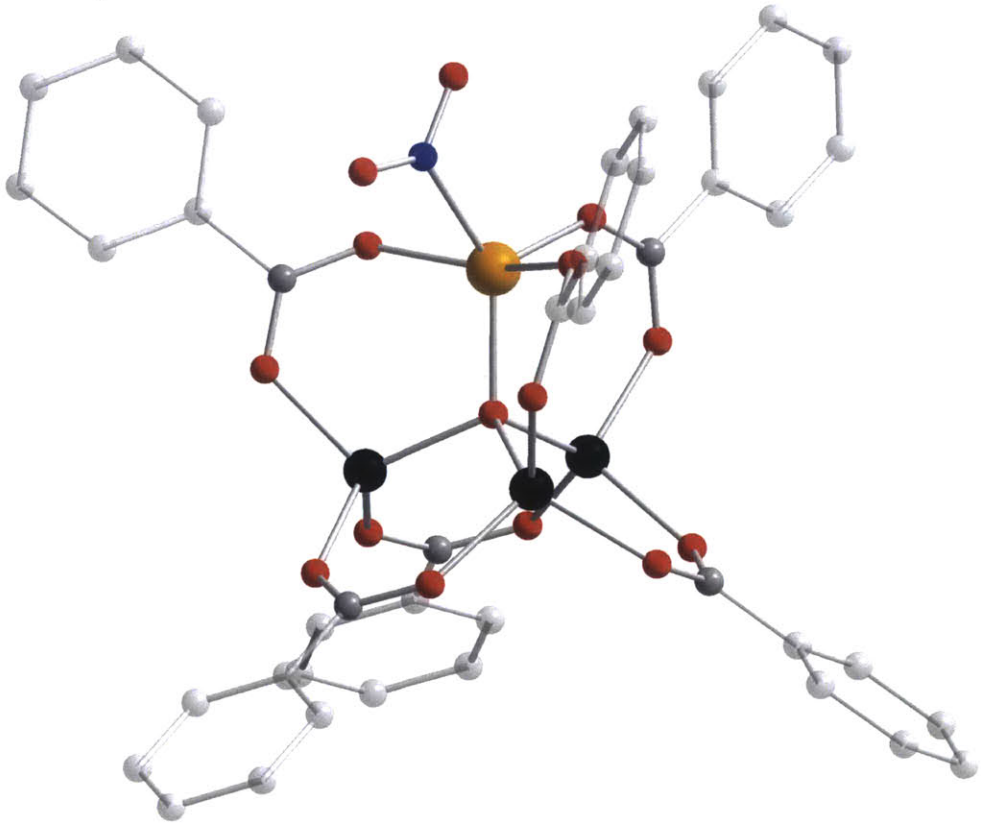

Figure 9-18: Geometry-optimized structure of –NO2. Fe, Zn, O, N, and C atoms are shown in orange, black, red, blue, and gray. H atoms are omitted for clarity.

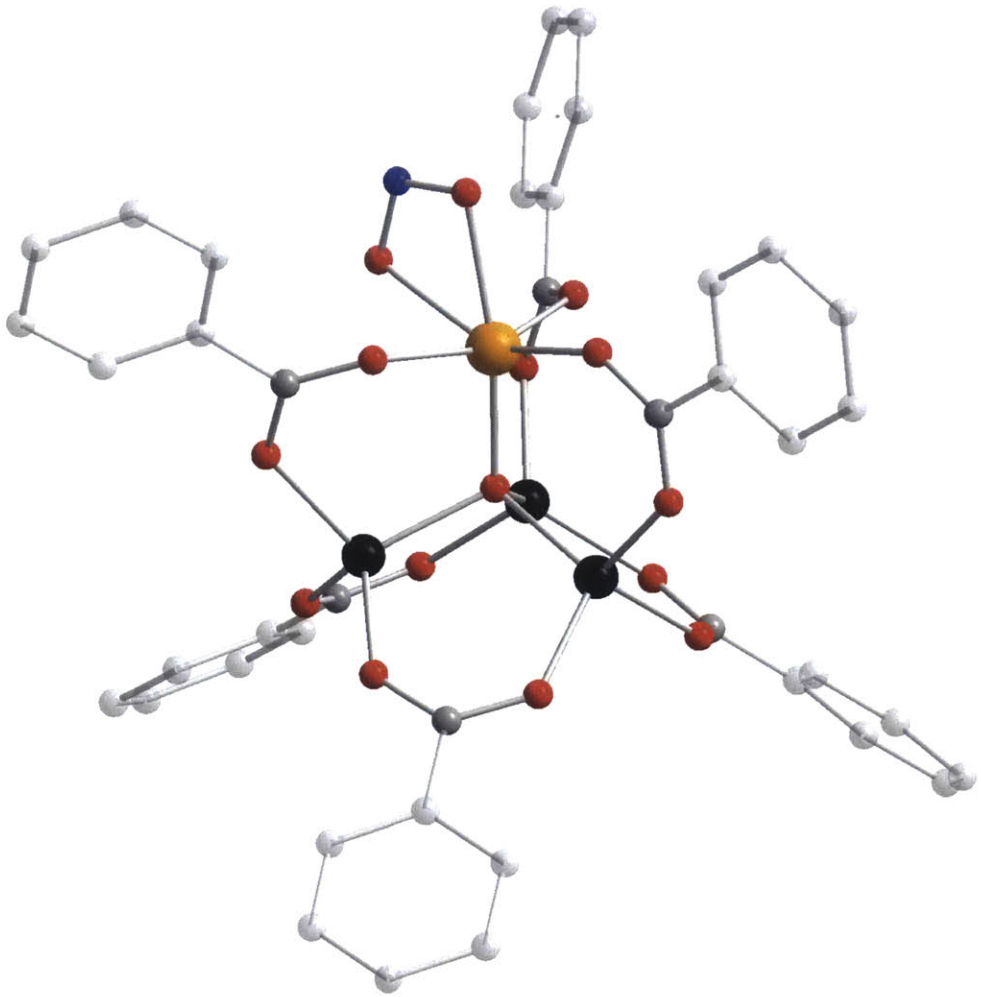

Figure 9-19: Geometry-optimized structure of –ONO—. Fe, Zn, O, N, and C atoms are shown in orange, black, red, blue, and gray. H atoms are omitted for clarity.

–ONNO– lacks any band in that region. It is important to note that **C** and **D** should exhibit bands between 1400 and 1500 cm^{-1}, but, as shown in Figure 9-4, that region is dominated by strong MOF-based transitions. For **D**, the –NO_2 isomer shows the best agreement with the experiments. Most tellingly, the alternative –ONO– isomer lacks a band around 700-800 cm^{-1} corresponding to NO_2-based dipole changes. Because this region is devoid of any other bands, the absence of the expected bands for the –ONO– isomer strongly point to ĐNO_2 (i.e. nitro) as the correct assignment for **D**.

By assigning **C**, we provide the first experimental evidence for an η^1monoanionic hyponitrite transition metal complex. In addition to NO disproportionation,[249–251] transition metal hyponitrite species are invoked as intermediates in NO reduction catalysis for environmental safety[252,253] and in the naturally occurring NO reductase.[254] In the few cases where hyponitrite can be isolated, it features as a closed-shell dianion, and only in select cases it is reported to react further with NO to release N_2O or with acid to produce H_2O.[255,256] In more active catalytic systems, such as NOR, hyponitrite intermediates are invoked, but have not been observed as monoanionic radicals. So far $N_2O_2^-$ has only been observed transiently by UV-Vis spectroscopy or studied in frozen gas matrices.[257–264]

9.5 Conclusion

We have shown through site-specific spectroscopy and a host of complimentary evidence that Fe^{2+}-MOF-5 promotes nitric oxide disproportionation to release N_2O, while also producing a ferric nitrito product. This report is a rare example of unusual redox transformations occurring at the metal nodes of a MOF with well-characterized changes to their coordination environment and oxidation state. Among the systems known to facilitate nitric oxide disproportionation, Fe^{2+}-MOF-5 is one of the only examples where the mechanism must involve a single iron atom, whereas this mechanistic aspect of previous homogeneous systems has been contentious, since bimolecular species can rarely be fully discounted. By elucidating how this reaction occurs at the site-isolated metal sites in a MOF, we hope to learn about mechanistically similar

–ONNO–		ONNO–		ONN–O		$–NO_2$		–ONO–	
1430, *1429* (m)	$\nu_{N–N}$	1442, *1429* (s)	$\nu_{N–O}$	1429, *1407* (m)	$\nu_{N–O}$	1417, *1394* (s)	$\nu_{N–O}$ (ant)	1237, *1216* (w)	$\nu_{N–O}$ (sym)
1426, *1381* (m)	$\nu_{N–N}$	1164, *1140* (m)	$\nu_{N–O}$	1158, *1131* (m)	$\nu_{N–O}$	1267, *1250* (s)	$\nu_{N–O}$ (sym)	1168, *1136* (w)	$\nu_{N–O}$ (ant)
749, *734* (m)	$\nu_{O–NN–O}$	772, *749* (w)	$\nu_{N–N}$	982, *956* (w)	$\nu_{N–N}$	752, *745* (w)	δ_{ONO}		

Table 9.2: Selected frequencies of model compounds with assignments. Intensities are indicated in parentheses and ^{15}N isotope shifts in italics

reactions, such as the N–N coupling of two equivalents of NO in nitric oxide reductase to produce N_2O, and to optimize these materials as unique platforms for N_xO_y reduction catalysis. More generally, the metal nodes of cation-exchanged MOF-5 offer a platform for studying reactions of both industrial and biological relevance. As artificial constructs, they enable the isolation of unusual species that are otherwise difficult or impossible to achieve with molecules and other materials.

9.6 Methods

Unless otherwise stated, all materials were treated as air sensitive and were manipulated using common Schlenk and inert atmosphere glovebox technique.

9.6.1 Materials

Dry, deaerated dichloromethane (DCM, HPLC grade, Honeywell) and DMF (99.8%, VWR) were obtained by degassing with a flow of argon gas for 30 min and by passing the solvent through two silica columns in a Glass Contour Solvent System. 70% HNO_3 (ICP-AES grade, EMD), H_2SO_4 (ACS grade, EMD), $FeSO_4 \cdot 7H_2O$ ($\geq$99%, Strem), NO/N_2 (5%), Airgas), $Fe(BF_4)_2 \cdot 6H_2O$ (97% Sigma-Aldrich), and $Zn(NO_3)_2 \cdot 6H_2O$ (99%, Alfa Aesar), sodium nitrite ($\geq$97%, Sigma-Aldrich), $Na^{15}NO_2$ (95%, Sigma-Aldirch), and terephthalic acid (Sigma-Aldrich) were used without further modification. MOF-5 was prepared according to literature.[72]

9.6.2 Physical Measurements

In situ DRIFTS

Diffuse reflectance UV-Vis spectra were collected between 2000 nm and 200 nm on a Varian Cary 5000 UV-Vis-NIR spectrometer equipped with a Praying Mantis diffuse reflectance accessory and an environmental chamber (Harrick Scientific Products) and referenced to $BaSO_4$. Iron and zinc analyses were conducted at the MIT Center for Materials Science and Engineering Shared Experimental Facility (CMSE-SEF) using

a HORIBA Jobin ACTIVA inductively coupled plasma atomic emission spectrometer (ICP-AES). Standards were prepared from solutions purchased from ULTRA Scientific©, designated suitable for ICP analysis. Measurements were performed on a Bruker Tensor 37 with a mercury cadmium telluride detector cooled to 77 K. Data were collected in the 'MIR_DRIFTS' mode with a 6-mm aperture setting and a KBr beam splitter. The data were averaged over 14 scans between 5000 and 650 cm^{-1} every 15 s. Fully activated Fe-MOF-5 was loaded into a Harrick low temperature environmental chamber and attached to a Harrick Praying Mantis accessory to perform DRIFTS measurements. A measurement was taken of the sample under dynamic vacuum at room temperature, then NO/N_2 was added from a 100-mL Schlenk flask through a Swagelok valve. A spectrum was collected immediately afterwards and at regular intervals thereafter.

XAS

Experiments were conducted in the bending magnet beam line of the Materials Research Collaborative Access Team (MRCAT) at the Advanced Photon Source (APS), Argonne National Laboratory. XAS data were acquired at the Fe K edge (7.112 keV) in transmission step scan mode with photon energies selected using a water-cooled, double-crystal Si(111) monochromator. The monochromator was detuned by approximately 50%, reducing harmonic reflections. The ionization chambers were optimized for the maximum current with linear response (~1010 photons detected/sec) with 10% absorption (30% N_2 and 70% He) in the incident ion chamber and 70% absorption (90% N_2 and 10% Ar) in the transmission detector.

Each solid standard sample was mixed with boron nitride to a weight ratio of about 4% Fe and the MOF samples were loaded in a glove box as neat powders. The samples were ground with a mortar and pestle to a uniform size and composition, and then approximately 5–10 mg of the mixture was pressed into a cylindrical sample holder consisting of six wells with a radius of 2.0 mm, forming a self-supporting wafer. An Fe foil spectrum was acquired simultaneously with each measurement for energy calibration. The sample holder was placed in a quartz tube (1 in. OD, 10 in. length)

sealed with Kapton windows by two Ultra-Torr fittings and then used for transmission mode measurement.

The edge energy of the X-ray absorption near edge structure (XANES) spectrum was determined from the inflection point in the edge, i.e., the maximum in the first derivative of the XANES spectrum. The pre-edge energy was determined from the maximum of the pre-edge peak. Experimental phase shift and back scattering amplitude were used to fit the EXAFS data. Fe–O phase shift and back scattering amplitude were obtained from reference compounds: $Fe(acac)_3$ (6 Fe–O at 1.91 Å). Background removal and normalization procedures were carried out using the Athena software package using standard methods. Standard procedures based on WinXAS 3.2 software were used to extract the extended X-ray absorption fine structure (EXAFS) data. The coordination parameters were obtained by a least square fit in R-space of the nearest neighbor, k^2-weighted Fourier transform data.

Continuous-wave X-band EPR

Spectra were recorded using a Bruker EMX spectrometer with a Gunn diode and an ER 4199HS cavity. The microwave frequency of 9.46 GHz was set to 2.021 mW and a modulation frequency of 100.00 kHz was used with an amplitude of 10.00 G. All spectra were recorded near 77 K by setting the sample tube in a cold-finger dewar containing liquid N_2.

Zero-field Mössbauer

Spectra were recorded at 4.2 K and 80 K using a spectrometer equipped with a liquid helium cooled Janis 8DT Supervaritemp cryostat. The spectrometer was used in transmission mode, operated in a constant acceleration mode and used a 100 mCi $^{57}Co(Rh)$ source. Isomer shifts are reported relative to the centroid of the iron metal spectrum recorded at room temperature. The spectral simulations were realized using the WMOSS software (See Co., formerly WEB Research Co., Edina, MN). The absorbers used here consisted of approximately 30 mg finely ground powder loaded under an inert atmosphere in custom made Delrin containers. Although the samples

were shipped from Boston to Tallahassee at room-temperature in standard, air-free sealed glass flasks, once removed from these containers they were handled and stored at 77 K under liquid nitrogen.

Mass Spectrometry

Data were conducted in multi-ion detection mode using a Hiden Analytical HPR20 QIC benchtop gas analysis system.

9.6.3 Calculations

The ORCA 3.0.3 software package[148] was used for all computations. The all-electron Gaussian basis sets developed by the Ahlrichs group were employed in all calculations with the basis sets TZV(p) (for H), TZV(2d) (for C, N, and O), and TZV(2pf) (for Zn and Fe).[93,94] Calculations were done using the resolution of the identity (RI) at the spin-unrestricted level using the meta-GGA functional Tao-Perdew-Staroverov-Scuseria (TPSS).[265] Geometry optimizations began from crystallographically determined structures, where all atomic positions were optimized, with the 1 and 4 carbons atoms on each benzoate fixed in place. The optimized geometries were then used for calculating energies and vibrational frequencies, which were performed using numerical differentiation of analytic gradients with an increment of 0.005 bohr. Because no negative frequencies were observed, the structures appeared to reside in potential energy minima. The isomers bearing hyponitrite species were calculated with quintet spin multiplicity, while those with nitrite species were given sextet spin multiplicity.

9.6.4 $Zn_{4-x}Fe_xO_{13}C_{24}H_{12}$ (Fe-MOF-5)

Evacuated MOF-5 crystals (490 mg, 0.636 mmol) were suspended in 40 mL of DMF and allowed to sit for one minute. A solution of 990 mg (2.93 mmol) of $Fe(BF_4)_2 \cdot 6H_2O$ in 20 mL of DMF was added to this suspension in a 100 mL jar. This material were stirred gently for a week and subsequently washed and activated in a manner typical for MOF-5 to give cubic yellow crystals.

9.6.5 Synthesis of ^{15}NO

The setup shown in Figure 9-20 was used for the following procedure. The drying tubes in this apparatus were filled with 1:1 drierite:KOH. 0.1 mL of sulfuric acid (1.6 mmol) and 0.270 g of $FeSO_4 \cdot 7H_2O$ (0.96 mmol) were added to 100 mL of deionized water. This solution was sparged with N_2 for 15 min. After adding this solution to a three-neck RB flask, it was frozen and put under dynamic vacuum with the rest of the apparatus for approximately 15 min. The solution was allowed to warm to room temperature and vacuum was briefly applied. This solution was sealed from the rest of the apparatus. With vigorous stirring at room temperature, a 2-mL deionized water solution of $NaNO_2$ (0.066 g, 0.96 mmol) was syringed into the three-neck flask. The solution turned green/yellow and effervescence was observed immediately but gradually waned, as the atmosphere and solution of the closed three-neck flask became saturated with ^{15}NO. At the same time, the central collection tube was submerged in a liquid N_2 dewar. Upon opening the three-neck flask, NO rapidly transferred to the collection tube driven by the temperature (and pressure) gradient. After the dissolved NO also effervesced into the collection tube, the $NaNO_2$ solution turned back from greenish-yellow to yellow, and the valve between the three-neck flask and the collection tube was once again closed. The procedure was repeated two more times to collect a total of 0.96 mmol of ^{15}NO. The ^{15}NO was transferred to a dry Schlenk flask by submerging it in a liquid N_2 dewar and heating the collection flask with a heat gun.

Figure 9-20: Apparatus for the synthesis of ^{15}NO.

atom	x	y	z	atom	x	y	z
C	-0.79703000456655	-7.95723999056300	-0.81457998887546	C	0.22576407885818	-7.44520423274926	-0.01052338190659
C	-1.66259018138579	-7.07860449237411	-1.47260564918752	Zn	1.23459939519060	-1.40734546214335	0.76966144708688
Zn	1.07765578256822	1.05953453709907	-1.15312274754673	Zn	-1.33929092455936	-0.95003589515209	-0.94703810234791
Fe	-0.88912351216112	1.22490123571220	1.71357165351636	O	-0.01557498340708	0.04574381316246	0.17720114168703
O	1.54219287465789	-1.13310084741385	2.72924827120299	O	3.09469048123561	-1.33679034862195	0.02314830231640
O	0.62156673714020	-3.28264127684367	0.38964076389274	O	0.49163830153239	0.88289718382822	-3.05650254284106
O	3.03072275470472	0.58940415633336	-1.16218809223547	O	0.82496846735185	3.00622927630797	-0.80234162563525
O	-1.37396227738760	-0.38660495670671	-2.86972046520955	O	-3.16001170857914	-0.64642392353408	-0.19779663417065
O	-1.13542206937613	-2.94677047227339	-0.99625570351444	O	-0.35754308837015	0.01165560781524	3.12539062135256
O	-2.76706272627993	1.10809319533953	1.17614382226625	O	-0.00996646749013	2.93612226605997	1.29790554194326
C	0.73111988389812	-0.54338991652570	3.51166996420891	C	3.64933999762722	-0.42694995594340	-0.68417995091831
C	-0.32217995691577	-3.70683001134923	-0.36694010206642	C	-0.54531008972485	0.31791997534599	-3.54467002389730
C	0.43353028401066	3.56318009299183	0.27328000694064	C	-3.54172015765012	0.27807982940304	0.58979010829115
C	1.03067991221588	-0.53492940214453	4.97302465433907	C	5.10470548742948	-0.55468943179170	-0.97331238591976
C	-0.48427258960429	-5.18499492951314	-0.52269583531663	C	-0.80288497446974	0.48576855390000	-5.00859567218254
C	0.54464931929678	5.05030652277326	0.36412570091390	C	-1.27580999496262	0.79867000143610	-7.75502000343454
C	0.79118997577265	7.83863995774090	0.52207999139683	C	-5.01006499920824	0.43355743222958	0.82473926740904
C	-7.76688994592651	0.76514997200913	1.20621998021511	C	2.15765703338870	-1.21816555832920	5.45445619546459
C	5.82833842433080	-1.64187116308421	-0.46473674382704	C	0.38339475680538	-6.06788617058000	0.13600312898484
C	0.06898165839415	1.25352430274411	-5.79399143533878	C	5.75374221371048	0.41151503406869	-1.75400811575478
C	-0.16781027195075	1.40751525621500	-7.15873939576766	C	1.06329977378381	7.17593392769864	-0.67892963749645
C	-1.91389446512510	-0.12362347694831	-5.60869893566356	C	-5.92392359109862	-0.29552915150692	0.04936732091663
C	-1.50931640899288	-5.70067790353312	-1.32897237219404	C	-2.14695299005287	0.03355858310911	-6.97394383540961
C	-7.29373961774408	-0.12451554066469	0.23719846340698	C	0.19174290982966	0.14521544284430	5.87074473877965
C	-5.48668563026111	1.32114607670635	1.80107424143904	C	0.27006681762018	5.71761927586675	1.56661939105056
C	0.39633787990734	7.10343569684759	1.64285215480692	C	-6.85774000399824	1.47910004590188	1.99516000105344
C	1.59925509207526	-0.54793985494191	7.70898935107042	C	2.43811638691446	-1.22265881558199	6.81739345420329
C	0.47724000440719	0.13648999539437	7.23731000240382	C	7.83313605026299	-0.79488091014767	-1.51392972595045
C	7.18888380450149	-1.75963021184940	-0.73603072814693	C	7.11453524719034	0.28990694322459	-2.02203437902242
C	0.94575902874959	5.79052583774730	-0.75883839718709	H	-0.91799508992885	-9.03098761768026	-0.92716437467553
H	0.90268385184308	-8.12150150958818	0.50407243793322	H	-2.45982387911601	-7.46853260518967	-2.09932464953159
H	-1.45923917411415	0.91955805845679	-8.81899996661735	H	0.88507132612843	8.91926392019529	0.58275515717060
H	-8.83557743152986	0.89727741825491	1.35042705815971	H	2.79824946943454	-1.73835601674264	4.75013053298839
H	5.31075205180135	-2.38111546454954	0.13728540200021	H	1.17415843183282	-5.66125792691594	0.75763915118374
H	0.92620791139959	1.72130606961303	-5.32141447849436	H	5.17913668880443	1.24655299112445	-2.14034993788941
H	0.51336213392728	2.00386340116970	-7.75941720575052	H	1.36899759654035	7.74162022137073	-1.55465429359884
H	-2.58345059991525	-0.71614935463304	-4.99412295790265	H	-5.54650091407952	-0.98213294450263	-0.70106508344937
H	-2.17622289097307	-5.01053378615910	-1.83484332018575	H	-3.01033763443476	-0.44222326972315	-7.43071760373053
H	-7.99507436111860	-0.68442100152262	-0.37517519541185	H	-0.67185063941195	0.67697870333060	5.48367887637976
H	-4.77678976348518	1.88059810405084	2.39983290424800	H	-0.03627033291299	5.14273581672894	2.43333953810896
H	0.18201370727487	7.61084446056986	2.57903198786327	H	-7.21780474596270	2.16804684624656	2.75368828297196
H	1.82224161235133	-0.55573043025217	8.77261235496372	H	3.31071166032285	-1.75278133181853	7.18838171815078
H	-0.17333434333008	0.66414545612541	7.92843413965095	H	8.89518135901501	-0.88846772988540	-1.72432072355868
H	7.74872672476808	-2.60300905383089	-0.34169220821139	H	7.61656215646677	1.03962877527793	-2.62702421372912
H	1.15883707162927	5.26653388939581	-1.68453938799174	N	-2.29788925462335	3.31797679714031	3.35151860462005
O	-1.59855227909953	2.23970137254187	3.31590102647234	N	-2.66349725263552	3.86988226068653	2.19762626955311
O	-3.34052142246777	4.88523300681584	2.11792046157414				

Table 9.3: Optimized atomic coordinates for the ONNO– isomer

atom	x	y	z	atom	x	y	z
C	-0.79703000797458	-7.95724000799079	-0.81457999124231	C	0.25082529098744	-7.44448214685487	-0.04377489416213
C	-1.68384341077953	-7.07870196825614	-1.44404838350288	Zn	1.25257368556880	-1.41722338037385	0.81685493202006
Zn	1.12631230781916	1.12309901378376	-1.13085047552811	Zn	-1.33203471489717	-0.95125705899340	-0.96381537349782
Fe	-0.77107866110107	1.18733387457810	1.63064751469007	O	0.01222962849604	0.04395076909073	0.16064904064567
O	1.62166804891381	-1.03786637255510	2.73802324842101	O	3.10635408385726	-1.28927677614011	0.08627535372951
O	0.64394713991841	-3.27884859823502	0.35985806855485	O	0.37111872857549	1.03465040272664	-3.00287860068045
O	3.02207533342027	0.51878853855248	-1.27386004582536	O	1.38451123500407	2.93715582071348	-0.31528439730518
O	-1.27261683908834	-0.52124968281143	-2.91256125803017	O	-3.16843472341650	-0.49717697934964	-0.34920395502789
O	-1.16843277543640	-2.94804875799216	-0.95323311337234	O	-0.43820391241862	-0.21870594873412	3.08506814932295
O	-2.74955196598945	0.92274579149854	1.37209649757665	O	-0.65816333612086	2.98209461663131	0.61520161544643
C	0.73111999920611	-0.54338996635590	3.51166993499370	C	3.64933998434109	-0.42695010727667	-0.68417996793642
C	-0.32217989378019	-3.70683000062337	-0.36694005325899	C	-0.54531002627823	0.31791999437626	-3.54467003199485
C	0.43352997612561	3.56318008549472	0.27328003145718	C	-3.54172005009909	0.27808005903354	0.58979007868230
C	1.07261881813358	-0.41335649482013	4.95397335296059	C	5.11633626372768	-0.54035620663068	-0.92694927586830
C	-0.47904707665493	-5.18451259090226	-0.52840425050481	C	-0.78940446424573	0.48180348489245	-5.01077399182338
C	0.57171443413403	5.04078016440286	0.42585425224658	C	-1.27580999862056	0.79866999799269	-7.75501998163603
C	0.79118999940421	7.83863996714503	0.52207999532457	C	-5.00973459540534	0.45359863545324	0.80830536493841
C	-7.76689004211356	0.76515002733146	1.20622004621467	C	2.36639928936027	-0.75245860834407	5.38136477573566
C	5.85222005333150	-1.56355658834984	-0.31435775247579	C	0.41115835412440	-6.06713808303513	0.10002138240005
C	-0.02874085464274	1.38767419444203	-5.76352089033900	C	5.76316255483087	0.37656805757380	-1.76636827061428
C	-0.27257034638359	1.54325540071336	-7.12728401105602	C	1.82668480051523	7.07006995117365	-0.01830145084692
C	-1.79354204793234	-0.26582120780650	-5.64316613378812	C	-5.92401059487886	-0.25666314460138	0.01585535316185
C	-1.52800476550749	-5.70084859679507	-1.30317033010226	C	-2.03343753842473	-0.10691502334030	-7.00677501586923
C	-7.29368641070165	-0.10169615442212	0.21692617629662	C	0.12875255540223	0.03318494141211	5.88987574459274
C	-5.48572054491804	1.32322732436812	1.80130728873454	C	-0.45783796500529	5.81111830995512	0.98536379765731
C	-0.34570991101886	7.20096841139188	1.03061768777297	C	-6.85773994468374	1.47909993230390	1.99515991782589
C	1.76631087675181	-0.19817696216819	7.65424682011837	C	2.71045636769259	-0.64129915603764	6.72436762674908
C	0.47723999644409	0.13649000382750	7.23731002805524	C	7.86374281320417	-0.75236778248683	-1.37894950442075
C	7.22201802670342	-1.66765280107148	-0.54139526793980	C	7.13319036863404	0.26896522537738	-1.99043083075091
C	1.71855254218608	5.68231010496731	-0.06923569656452	H	-0.92058363401932	-9.03097751552746	-0.92412688188620
H	0.94470486191988	-8.12054945693390	0.44798280326661	H	-2.50020671492990	-7.46889398356377	-2.04545177101287
H	-1.46453864968074	0.92276653274099	-8.81767416930829	H	0.87081500884855	8.92153411842552	0.55383929760910
H	-8.83545446294515	0.88566490349029	1.36112867474748	H	3.08668736397018	-1.09642003974493	4.64713582933212
H	5.33679383965010	-2.26488650504023	0.33314864025317	H	1.22013670018157	-5.66036009507608	0.69765175424275
H	0.74634567474821	1.96229463387744	-5.26739012628063	H	5.17955169950813	1.16335309608019	-2.23218116825698
H	0.32097727418902	2.24835082836176	-7.70252633598814	H	2.71742702352779	7.55457269567784	-0.40885196589618
H	-2.37722343129747	-0.96438481228146	-5.05308748323838	H	-5.54614635811455	-0.92573141746649	-0.74993932712964
H	-2.21231689189480	-5.01114803388420	-1.78585986729538	H	-2.81424707764770	-0.68984762916122	-7.48729825653702
H	-7.99469089011429	-0.65788021696050	-0.39920267348158	H	-0.87004622871752	0.29039850017547	5.55230710530171
H	-4.77326666788932	1.86884298765070	2.41138694315750	H	-1.34363456376541	5.31355415178054	1.36658163349808
H	-1.15164201238983	7.78935435760822	1.45965000676340	H	-7.21840197308925	2.15530152805238	2.76493819368131
H	2.03603863672805	-0.11338144759168	8.70355490058957	H	3.71422340404957	-0.89998707671036	7.04906211642949
H	-0.25728872494966	0.48159459375484	7.95888203323249	H	8.93297139216377	-0.83478850308818	-1.55488064294284
H	7.79099981182523	-2.46160665194285	-0.06596859867410	H	7.63324490477219	0.98073823204919	-2.64130253237260
H	2.50970257686999	5.07869943834014	-0.50114678321197	N	-1.39797608365461	3.26060710877193	4.26570429515563
N	-0.99927459249527	2.50473382732193	3.31521100911361	O	0.26691555858466	2.34357575902321	3.00435517242874
O	-2.55182771095686	3.47973432230462	4.62805548119871				

Table 9.4: Optimized atomic coordinates for the ONN–O isomer

atom	x	y	z	atom	x	y	z
C	-0.79702999475500	-7.95723996949545	-0.81458000241372	C	0.24938768197867	-7.44421098886773	-0.04156737659899
C	-1.68188741732486	-7.07835056383086	-1.44630533637928	Zn	1.25993946807113	-1.40464219451009	0.85631018790168
Zn	1.12923443065898	1.15224381790417	-1.10108113093225	Zn	-1.33518727466807	-0.95683579032721	-0.97007494568689
Fe	-0.79808279693220	1.15528224787155	1.63024337223627	O	-0.03341543284226	0.07171010611476	0.20714937018984
O	1.64813104932432	-1.01457333483250	2.74630490347741	O	3.09937515000434	-1.29549741045422	0.07587181119027
O	0.64223086114478	-3.26872814024681	0.35367320191792	O	0.37502455454315	1.01858261573135	-2.99239230081094
O	3.01737594235387	0.51883985436762	-1.26995318485303	O	1.39163745899068	2.94841245279071	-0.32367089598566
O	-1.28316587081417	-0.51718672709672	-2.91194208898226	O	-3.17473117543051	-0.48752565647140	-0.35428937308873
O	-1.17435218754526	-2.94811772463247	-0.95183716633001	O	-0.46806424411301	-0.35334802961666	3.10779188616780
O	-2.72362883432229	0.90450404190182	1.37402392359425	O	-0.68437439737767	3.01308567274244	0.54577919227665
C	0.73112003031043	-0.54339013442267	3.51167003691231	C	3.64933999930931	-0.42694990779478	-0.68418012857640
C	-0.32217991607409	-3.70683011480884	-0.36693987476364	C	-0.54531004250734	0.31791986097757	-3.54466995912106
C	0.43352993494804	3.56317993913550	0.27328017022139	C	-3.54172000202022	0.27808032635989	0.58978978154994
C	1.09413006924539	-0.34120485492508	4.94372367186426	C	5.11613771045306	-0.53601938581231	-0.92162486521263
C	-0.47820691559881	-5.18403950787467	-0.52837182390015	C	-0.78865729498615	0.48313874113846	-5.01000118910680
C	0.59144852586167	5.03995051077645	0.45599757067593	C	-1.27581000628622	0.79867000645467	-7.75502000904053
C	0.79119000037716	7.83864001845048	0.52207998489684	C	-5.00402034801691	0.46186261705912	0.81692641470160
C	-7.76689001544093	0.76515000926297	1.20622000791533	C	2.42600826915180	-0.52124011011155	5.34768383654156
C	5.85168218004826	-1.56101549839628	-0.31158418165845	C	0.41041351605464	-6.06670479505276	0.10226583538232
C	-0.02654376332184	1.38722193329730	-5.76342385004553	C	5.76375811628318	0.38761674428624	-1.75302913063024
C	-0.27110985946196	1.54204279415236	-7.12745137612872	C	1.84417704745764	7.07063724048576	0.01692706466817
C	-1.79450964356523	-0.26311817237843	-5.64195404873263	C	-5.91625971853355	-0.25015009003388	0.02119036863095
C	-1.52574152548825	-5.70045207648484	-1.30539805612398	C	-2.03460727905704	-0.10500675443350	-7.00565780102022
C	-7.28694801960090	-0.09984910267476	0.21779550197446	C	0.12087703086905	-0.00597463881654	5.89558064870876
C	-5.48376234734572	1.32941957428090	1.80865520314681	C	-0.45168555946821	5.81003765370587	0.98900975360293
C	-0.34981563218774	7.20070650827292	1.01980356911116	C	-6.85773997847684	1.47909994138106	1.99516000989832
C	1.80447627770101	-0.03907815150727	7.63147118936755	C	2.77867401283102	-0.36375618564855	6.68417362303394
C	0.47724000375394	0.13649000975798	7.23730999429794	C	7.86523412351546	-0.73910513094673	-1.36383366152807
C	7.22253779409634	-1.66057324243145	-0.53387953380682	C	7.13482397242595	0.28426837984608	-1.97223867178845
C	1.74555308232861	5.68124471404465	-0.01944853822076	H	-0.92060432382184	-9.03094311705315	-0.92386813543269
H	0.94187923826937	-8.12012473535654	0.45217669035406	H	-2.49698092569041	-7.46804114424805	-2.04965920833277
H	-1.46426821196747	0.92250273359925	-8.81768495432159	H	0.86205330584460	8.92262993427240	0.53821171386662
H	-8.83547872582285	0.88419408606031	1.35985629266813	H	3.16863986030965	-0.78035913736132	4.60104438262564
H	5.33546220976936	-2.26642913610206	0.33077048314484	H	1.21817479749291	-5.66033182545828	0.70184430577700
H	0.74974349495433	1.96103342948459	-5.26812929123315	H	5.18022072960892	1.17643753402325	-2.21551650832525
H	0.32340972405860	2.24588824393776	-7.70309574680600	H	2.73929269792862	7.55666271320076	-0.36138771385831
H	-2.37915962738741	-0.96052352406488	-5.05161530689470	H	-5.53538962900237	-0.91777015018034	-0.74408374615426
H	-2.20871716253736	-5.01100468612665	-1.79017273531425	H	-2.81639736298840	-0.68734115172271	-7.48522453681335
H	-7.98260380299186	-0.65863793751694	-0.40175345399279	H	-0.90575332924340	0.13360794913867	5.57199319405896
H	-4.77550865983607	1.87769174919045	2.42135817297670	H	-1.34138863809667	5.30838491243266	1.35594860896705
H	-1.16776913984665	7.79008923384028	1.42482892633117	H	-7.22191939992392	2.15463104441217	2.76397748697936
H	2.08025856491385	0.07812227397826	8.67609634078260	H	3.81254502669404	-0.49662250080063	6.99030716573984
H	-0.28061219697141	0.39115487932947	7.97268914113135	H	8.93538562185347	-0.81793848519501	-1.53569272173825
H	7.79161413550081	-2.45549775301932	-0.06013359152475	H	7.63577480186234	1.00135389948566	-2.61645611054409
H	2.54697079995752	5.07758236125699	-0.43161585009919	N	0.87708567070874	2.64677936560358	3.25046836325274
O	0.88667976930904	1.74130896214907	2.22271964386873	N	-0.25129398617536	2.91163741780475	3.68032768592198
O	-1.26801056368511	2.27857403955735	3.07004685411669				

Table 9.5: Optimized atomic coordinates for the –ONNO– isomer

atom	x	y	z	atom	x	y	z
C	-0.79703000015440	-7.95723997439530	-0.81457998966115	C	0.24709784242367	-7.44432869603275	-0.03899906003188
C	-1.68113859832189	-7.07909591481164	-1.44828928858030	Zn	1.25670890276588	-1.42102524399450	0.80455719884811
Zn	1.13259327036756	1.10971097346680	-1.14453347517623	Zn	-1.31517738777661	-0.95473861497297	-0.96859332592009
Fe	-0.83643310184228	1.16379390961168	1.59498205676362	O	0.02912068877285	0.03658585359642	0.14727100686809
O	1.58417548610759	-1.09412918712429	2.73779648676332	O	3.10530095432914	-1.29390801835113	0.07975212013871
O	0.64527660159080	-3.28145617291817	0.35749699302051	O	0.38083173373135	1.02428620675350	-3.01019571096655
O	3.02637017436464	0.52005261194503	-1.27506954109031	O	1.33399824205608	2.94757396463733	-0.39449028918392
O	-1.27943303734748	-0.51426541263541	-2.91042654304402	O	-3.15292040351102	-0.49384159890568	-0.34115205899112
O	-1.16921398181620	-2.94815118616262	-0.95307063114014	O	-0.40099104830258	-0.09882311325246	3.09286585457031
O	-2.76514211797713	0.93192341254293	1.37965311341257	O	-0.61328195660483	2.98013582871430	0.73158929283152
C	0.73112010542184	-0.54338990034007	3.51166989042658	C	3.64934004122727	-0.42695000908826	-0.68417980984448
C	-0.32218001419691	-3.70683010180812	-0.36694004779009	C	-0.54531016168166	0.31792011912746	-3.54467007665980
C	0.43353005491709	3.56317989110606	0.27327996013063	C	-3.54172004944004	0.27807995636315	0.58978999095361
C	1.04875052162959	-0.48187421328366	4.96423411867510	C	5.11828666817838	-0.53716002239335	-0.91802683609757
C	-0.48074761577778	-5.18452613461924	-0.52784510234437	C	-0.79266791775041	0.48286432445049	-5.01037274708652
C	0.57071672322845	5.04196236272653	0.41324879631188	C	-1.27580998102570	0.79866998674905	-7.75501995932818
C	0.79118999821827	7.83864002727794	0.52208000074539	C	-5.01086429800943	0.45074521910316	0.80457314830515
C	-7.76688998117933	0.76514999501665	1.20621998975631	C	2.26170942790020	-1.02002408872290	5.42300733733979
C	5.85320601171218	-1.55813250399376	-0.30044331357205	C	0.40666687758566	-6.06693132417106	0.10481583484098
C	-0.02480381494350	1.38140115818526	-5.76464539847538	C	5.76791652418597	0.38107360705167	-1.75391202642693
C	-0.26699784485825	1.53664474320266	-7.12865689435518	C	1.74335443011117	7.08504507757657	-0.17084574495717
C	-1.80290809333630	-0.25757734152926	-5.64131495760457	C	-5.92577123134156	-0.25887559847081	0.01291288497615
C	-1.52625040535860	-5.70112687752268	-1.30700730190538	C	-2.04115998666055	-0.09915158227972	-7.00532747794635
C	-7.29512056457467	-0.10205710811419	0.21620639850759	C	0.15727469825843	0.09879151857148	5.87918121118646
C	-5.48604708501779	1.32130214061758	1.79849031705203	C	-0.37515896645355	5.79706573144484	1.12156202611654
C	-0.26149974485169	7.18661945756744	1.17339819612968	C	-6.85774000596068	1.47910000322935	1.99516000677898
C	1.68445216015708	-0.40113095366950	7.68564234142963	C	2.57610236061793	-0.97793781988121	6.77698300293534
C	0.47723998582541	0.13648999731223	7.23731004039364	C	7.86896531771043	-0.74230243215903	-1.35315700630079
C	7.22462087356022	-1.65873115854924	-0.51895217158384	C	7.13949711230829	0.27683059434492	-1.96968688821201
C	1.63539458186017	5.69769970676072	-0.22609702508930	H	-0.91987911871873	-9.03101870499669	-0.92455839439709
H	0.93893023135769	-8.11986609311649	0.45630726843405	H	-2.49456434753138	-7.46928678107978	-2.05363788851938
H	-1.46311876179995	0.92194431437120	-8.81802807311365	H	0.87089592488381	8.92132366626247	0.56116570779901
H	-8.83546290047522	0.88548155242283	1.36122098353238	H	2.94351331898191	-1.46272406191802	4.70499337965247
H	5.33585373908083	-2.26023546398616	0.34463253409349	H	1.21328669591317	-5.66019343073930	0.70562773386211
H	0.75520225318491	1.95035649597605	-5.26972688224171	H	5.18528957582647	1.16657566583129	-2.22317990988564
H	0.33247534094056	2.23587132671327	-7.70488807785777	H	2.56919163316214	7.58042813734128	-0.67377853824300
H	-2.39221842257825	-0.95085849753853	-5.05057338063384	H	-5.55025321641881	-0.92869838519751	-0.75357088178477
H	-2.20857592957519	-5.01202601513775	-1.79335753630611	H	-2.82643728451415	-0.67685933889399	-7.48487597870459
H	-7.99754272635853	-0.65737625349687	-0.39898146753698	H	-0.77556858742754	0.51882164305204	5.51788852745261
H	-4.77140866900402	1.86584379062306	2.40691589332382	H	-1.19408408422955	5.28931132689741	1.62083464551718
H	-1.00041649469493	7.76344065164051	1.72239647708045	H	-7.21695527563282	2.15557156378530	2.76522950675680
H	1.93310500409585	-0.36923799851613	8.74308489268418	H	3.51692150334432	-1.39297503813187	7.12729258026186
H	-0.21458286164188	0.58997988076630	7.94095052123729	H	8.93951834311636	-0.82192659335632	-1.52222044292935
H	7.79297561370070	-2.45058843200018	-0.03917997524443	H	7.64168597509263	0.98971992968514	-2.61763275354585
H	2.36374130192546	5.10530263281136	-0.76923830264842	O	-1.36133379158891	2.87146641997510	3.82901551481453
N	-0.33391391122137	2.49962809118399	3.24314922494364	O	0.81204159196192	2.83273160338347	3.54482505420983

Table 9.6: Optimized atomic coordinates for the $-NO_2$ isomer

atom	x	y	z	atom	x	y	z
C	-0.79702999980650	-7.95724000952113	-0.81457998917929	C	0.25361067558836	-7.44429326173507	-0.04772144308970
C	-1.68718845966643	-7.07921095523766	-1.43997995632301	Zn	1.24998522190360	-1.41371809736501	0.80903002101136
Zn	1.12859974792907	1.11082548161201	-1.13503174690246	Zn	-1.32719921714464	-0.95091475958540	-0.96338525873444
Fe	-0.79214468588607	1.19218068582562	1.63495083490931	O	0.01052770195781	0.04767764512818	0.16246180529969
O	1.59364277164879	-1.07853126934187	2.73831896886512	O	3.10271533635770	-1.29039210321100	0.08208188188015
O	0.64387859667391	-3.27967913758407	0.35878250182082	O	0.37951093476323	1.02427313497720	-3.00686336984650
O	3.02476793754843	0.51900268312197	-1.27636640253680	O	1.34036047942609	2.94590351218694	-0.38312800781560
O	-1.27983112045141	-0.51370916970205	-2.90956372356565	O	-3.16775195488365	-0.49822286862794	-0.34626338077984
O	-1.16894910478596	-2.94788879084894	-0.95355395870031	O	-0.42058662039648	-0.14677524572653	3.09498745997290
O	-2.74076842589051	0.92147590686300	1.36351855608823	O	-0.63104825378679	2.98669573889051	0.69948297653203
C	0.73111997896830	-0.54338985383604	3.51167008934310	C	3.64934003535398	-0.42695003522072	-0.68417988929607
C	-0.32218007050147	-3.70682994681227	-0.36694015371597	C	-0.54530996362362	0.31792009219014	-3.54467018289555
C	0.43353003078730	3.56317993108789	0.27327986923635	C	-3.54172004017880	0.27807983198520	0.58979027250997
C	1.05937259758704	-0.45936120058584	4.96103441665235	C	5.11731870809205	-0.53961181566282	-0.91976826551171
C	-0.48003976698092	-5.18476569193894	-0.52838781673455	C	-0.79132986442225	0.48229458520428	-5.01054612602783
C	0.57549337665630	5.04142312550508	0.41950296960855	C	-1.27580999400419	0.79866999315174	-7.75501993861829
C	0.79119000645526	7.83864002574793	0.52208001107938	C	-5.00880034250179	0.45374583043443	0.81000571902342
C	-7.76689002888974	0.76515001067658	1.20622001828239	C	2.30071670628564	-0.93630120700304	5.41093190756097
C	5.85085842077416	-1.56311454830513	-0.30486373134241	C	0.41332164905324	-6.06687767887557	0.09613215916746
C	-0.02307506444819	1.38023402609389	-5.76506040900926	C	5.76786965317539	0.37888236102405	-1.75463003688111
C	-0.26595244195632	1.53567639091307	-7.12896417634411	C	1.76910709096923	7.08145275013366	-0.13020099745867
C	-1.80239952443214	-0.25748328171515	-5.64108009731859	C	-5.92284083148550	-0.25736682621385	0.01787129848769
C	-1.53173405876664	-5.70126011061067	-1.29922623849486	C	-2.04129998537743	-0.09879751209900	-7.00491693948227
C	-7.29269960920542	-0.10238816558086	0.21785580179121	C	0.14848611070929	0.08014071640323	5.88171707770426
C	-5.48530360583888	1.32397971883304	1.80210467942794	C	-0.39500861538255	5.79976757184590	1.08995663307645
C	-0.28428379208852	7.18970352480955	1.13836169354167	C	-6.85773995427375	1.47909998519825	1.99515994080949
C	1.71334633286046	-0.33931014246597	7.67683991995479	C	2.62465146691154	-0.87397158176782	6.76198140012568
C	0.47723999697618	0.13648997648612	7.23730995892945	C	7.86719995671745	-0.74950391822990	-1.35829230903365
C	7.22181262280144	-1.66621045269577	-0.52518704198328	C	7.13902807873789	0.27231959915191	-1.97194600331043
C	1.66316875723530	5.69379402930749	-0.18313390799931	H	-0.92017993717908	-9.03101881699549	-0.92427310718346
H	0.94992671659344	-8.12032692945709	0.44057748878079	H	-2.50556374396198	-7.47003869097205	-2.03821434514065
H	-1.46362538686333	0.92235309318500	-8.81787957309668	H	0.86888470316063	8.92161118266790	0.55718246052980
H	-8.83542868542426	0.88596621356250	1.36057855205459	H	2.99709148501621	-1.34778989967368	4.68837615148903
H	5.33305485883277	-2.26538227220924	0.33969845967673	H	1.22429373997886	-5.65959439588793	0.69071259559877
H	0.75737051401179	1.94852726005773	-5.27002238266702	H	5.18656413856590	1.16648140239751	-2.22201306062541
H	0.33347884675540	2.23439200588612	-7.70587993540290	H	2.61272735089433	7.57517793941849	-0.60450605465084
H	-2.39173377064044	-0.95015241323782	-5.04964859674978	H	-5.54466261145875	-0.92697986715189	-0.74728418605177
H	-2.21815702545365	-5.01174901123388	-1.77917227151023	H	-2.82719571712515	-0.67565452635782	-7.48450205439291
H	-7.99307783488104	-0.65900200569473	-0.39848759284172	H	-0.80615120787627	0.45193925820023	5.52447962001086
H	-4.77229442776994	1.87048484838748	2.41086515464712	H	-1.23120439708879	5.29179092853411	1.55947762948831
H	-1.04339092124347	7.77001102622804	1.65533976159921	H	-7.21958327934014	2.15575487676528	2.76401323708896
H	1.96863532814750	-0.29238754426257	8.73214547548866	H	3.58780569253996	-1.24113163080597	7.10501576948035
H	-0.22997658571006	0.55601947574986	7.94683138448796	H	8.93739743017727	-0.83100570264918	-1.52870841886887
H	7.78887444797984	-2.46031528846562	-0.04759851019787	H	7.64177640353596	0.98563376151489	-2.61899986119046
H	2.40970205154986	5.09866334492880	-0.69793943871649	O	-1.17703044178765	2.50937437784596	3.34453585971924
N	0.03191567876506	2.79401914406618	3.59808720994810	O	0.83828179452225	2.21908347081329	2.79955047550248

Table 9.7: Optimized atomic coordinates for the –ONO– isomer

Abbreviations

ΔE_Q quadrupole splitting. 154, 214

ΔG_f Gibbs free enthalpy of formation. 101, 106

ΔG_{rxn} Gibbs free enthalpy of reaction. 21, 101, 103

ΔH_f formation enthalpy. 76

ΔH_s solution enthalpy. 76

Γ Full width at half-maximum of a Mössbauer signal. 154

Ω span. 94

$\chi_{\mathbf{m}}$ molar magnetic susceptibility. 54

δ isomer shift. 154, 214

$\delta_{\mathbf{H}}$ Hansen solubility parameter. 133

$\delta_{\mathbf{iso}}$ isotropic chemical shift. 78

η asymmetry parameter. 163

η asymmetry parameter. 78

η hapticity. 85

κ skew. 94

$\mu_{\mathbf{B}}$ Bohr magneton. 56

$\mu_{\mathbf{eff}}$ effective magnetic moment. 56

BDC 1,4-bezenedicarboxylate. 30, 33, 47–49

BDCPPI N,N′-bis(3,5-dicarboxyphenyl)pyromellitic diimide. 32, 48

BET Brunauer-Emmett-Teller. 53, 75

BIM 4′-[4-methyl-6-(1-methyl-1H-benzimidazolyl-2-group)-2-n-propyl-1H-benzimidazolyl methyl]. 36, 47

BODPDI N-phenyl-N'-phenyl bicyclo[2,2,2]oct-7-ene-2,3,5,6-tetracarboxdiimide tetracarboxylate. 30, 48

BOMD Born-Oppenheimer molecular dynamics. 82

BP 4,4′-bipyridine. 34, 47, 48

BPT biphenyl-3,4′,5-tricarboxylate. 33, 47

BTB 1,3,5-benzenetribenzoate. 32, 47, 48

BTC 1,3,5-benzenetricarboxylate. 30, 48

BTDD bis(1H-1,2,3-triazolo-[4,5-b],[4′,5′-i])dibenzo-[1,4]-dioxin. 30, 48

BTT 1,3,5-tris(2H-tetrazol-5-yl)benzene. 26, 30, 47, 48, 117

BTTN benzene-1,3,5-triyltriiso-nicotinate. 34, 47, 48

BTX 1,4-bis(triazol-1-ylmethyl)benzene. 34, 47

CBAI 5-(4-carboxybenzoylamino)-isophthalate. 30, 48

Cl_2Im dichloroimidazolate. 30

CP cross polarization. 79

CQ quadrupole coupling. 78

CSA chemical shift anisotropy. 94

DC direct current. 167

DCPP 4,5-bis(4′-carboxylphenyl)-phthalate. 30, 47, 48

DFT density functional theory. 97

DMA dimethylacetamide. 136

DMF *N*,*N*-dimethylformamide. 30, 50, 75, 151, 166

DMSO dimethyl sulfoxide. 32

DP direct polarization. 79

Dq ligand field parameter. 54, 133

EA elemental analysis. 174

EGME 2-methoxyethanol. 30, 48

ETTB 4′,4‴,4⁗,4⁗′,4⁗″-ethene-1,1,2,2-tetrayltetrakis([1,1′-biphenyl]-3,5-dicarboxylate. 30, 48

FBML Francis Bitter Magnet Laboratory. 91

Fc ferrocenyl. 32, 48

FcphSO$_3$ *m*-ferrocenyl benzenesulfonate. 34

FT-IR Fourier transform infrared. 53

FWHM full width half maximum. 78

HETT 5,5′,10,10′,15,15′-hexaethyltruxene-2,7,12-tricarboxylate. 32, 47, 48

HMBM 2-hydroxymethyl-4,6-bi(2′- methoxyl-4′-(2″-1″-carboxyl)-ethyene)-1,3,5-mesitylene. 33, 47

HMTT 5,5′,10,10′,15,15′-hexamethyltruxene-2,7,12-tricarboxylate. 32, 47, 48

ICP-AES inductively coupled plasma atomic emission spectroscopy. 64, 97, 100

INEPT insensitive nuclei enhanced by polarization transfer. 82

MAD multi-wavelength anomalous dispersion. 116

MAS magic-angle spinning. 77

MeCN acetonitrile. 56

MeIm methylimidazolate. 30

MeOH methanol. 136

MesCNO mesityl nitrile oxide. 57

MOF metal-organic framework. 26, 27, 73, 131, 206

MS mass spectrometry. 88

NMA *N*-methylacetamide. 77

NMF *N*-methylformamide. 132

NMP *N*-methyl-2-pyrrolidone. 132

NMR nuclear magnetic resonance. 77

Oe Oersted, the cgs unit of magnetic H-field strength. 167

PMe_3 trimethyl phosphine. 56

PXRD powder X-ray diffraction. 61

RGA-MS real-time gas analysis and quadrupole mass spectrometry. 209

RI resolution of the identity. 64

SBU secondary building unit. 26, 74, 132, 136, 172

SQUID superconducting quantum interference device. 62

STN signal-to-noise. 154

TATPT 2,4,6-tris(2,5-dicarboxylphenyl-amino)-1,3,5-triazine. 33, 47

TD-DFT time-dependent density functional theory. 62

TDCPEB 1,3,5-tris(3,5-dicarboxylphenylethynyl)benzene. 30

TDP 5,5′-(1*H*-1,2,3-triazole-1,4-diyl)-diisophthalate. 32, 48

TGA thermogravimetric analysis. 61, 75

THF tetrahydrofuran. 56

TIAPy 1,3,6,8-tetrakis(3,5-isophthalate)pyrene. 30, 48

TMPyP *meso*-tetrakis(*N*-methyl-4-pyridul)porphine tratosylate. 44

TZV triple zeta valence. 64

UV-Vis-NIR ultraviolet-visible-near infrared. 50, 97, 180

Bibliography

[1] Crabtree, R. H. *Chem. Rev.* **2015**, *115*, 127.

[2] Dincă, M.; Dailly, A.; Liu, Y.; Brown, C. M.; Neumann, D. A.; Long, J. R. *J. Am. Chem. Soc.* **2006**, *128*, 16876.

[3] Dincă, M.; Long, J. R. *J. Am. Chem. Soc.* **2007**, *129*, 11172.

[4] Misra, K. A. *Introduction to Geochemistry: Principles and Applications*; Wiley: West Sussex, 2012; pp 31–37.

[5] Jaffe, H. *Crystal Chemistry and Refractivity*; Dover, 1988.

[6] Putnis, A. *Mineral. Mag.* **2002**, *66*, 689.

[7] Goldschmidt, V. *J. Chem. Soc.* **1937**, 655.

[8] Ringwood, A. The principles governing trace element distribution during magmatic crystallization Part I: The influence of electronegativity. 1955; `http://linkinghub.elsevier.com/retrieve/pii/0016703755900296`.

[9] Rivest, J. B.; Jain, P. K. *Chem. Soc. Rev.* **2013**, *42*, 89.

[10] Luther, J. M.; Jain, P. K.; Ewers, T.; Alivisatos, A. P. *Nat. Mater.* **2011**, *10*, 361.

[11] Pietryga, J. M.; Werder, D. J.; Williams, D. J.; Casson, J. L.; Schaller, R. D.; Klimov, V. I.; Hollingsworth, J. A. *J. Am. Chem. Soc.* **2008**, *130*, 4879.

[12] EIGEN MANFRED,; WILKINS RALPH G., In *Mech. Inorg. React.*; Kleinberg, J., Murmann, R. K., Fraser, R. T. M., Bauman, J., Eds.; Advances in Chemistry; AMERICAN CHEMICAL SOCIETY: WASHINGTON, D.C., 1965; Vol. 49; pp 55–80.

[13] Hagen, K. S.; Stephan, D. W.; Holm, R. H. *Inorg. Chem.* **1982**, *21*, 3928.

[14] Autissier, V.; Henderson, R. A. *Inorg. Chem.* **2008**, *47*, 6393.

[15] Li, H.; Otvos, J. D. *Biochemistry* **1996**, *35*, 13929.

[16] Brozek, C. K.; Dincă, M. *Chem. Sci.* **2012**, *3*, 2110.

[17] Brozek, C. K.; Dincă, M. *J. Am. Chem. Soc.* **2013**, *135*, 12886.

[18] Fei, H.; Cahill, J. F.; Prather, K. a.; Cohen, S. M. *Inorg. Chem.* **2013**, *52*, 4011.

[19] Denysenko, D.; Werner, T.; Grzywa, M.; Puls, A.; Hagen, V.; Eickerling, G.; Jelic, J.; Reuter, K.; Volkmer, D. *Chem. Commun.* **2012**, *48*, 1236.

[20] Zhao, N.; Sun, F.; He, H.; Jia, J.; Zhu, G. *Cryst. Growth Des.* **2014**, *14*, 1738.

[21] Meng, W.; Li, H.; Xu, Z.; Du, S.; Li, Y.; Zhu, Y.; Han, Y.; Hou, H.; Fan, Y.; Tang, M. *Chem.—Eur. J.* **2014**, *20*, 2945.

[22] Niu, Y.-F.; Zhao, W.; Han, J.; Zhao, X.-L. *CrystEngComm* **2014**, *16*, 2344.

[23] Liao, J.-H.; Chen, W.-T.; Tsai, C.-S.; Wang, C.-C. *CrystEngComm* **2013**, *15*, 3377.

[24] Song, X.; Jeong, S.; Kim, D.; Lah, M. S. *CrystEngComm* **2012**, *14*, 5753.

[25] Wei, Z.; Lu, W.; Jiang, H.-L.; Zhou, H.-C. *Inorg. Chem.* **2013**, *52*, 1164.

[26] Zhang, Z.-J.; Shi, W.; Niu, Z.; Li, H.-H.; Zhao, B.; Cheng, P.; Liao, D.-Z.; Yan, S.-P. *Chem. Commun.* **2011**, *47*, 6425.

[27] Das, S.; Kim, H.; Kim, K. *J. Am. Chem. Soc.* **2009**, *131*, 3814.

[28] Kim, Y.; Das, S.; Bhattacharya, S.; Hong, S.; Kim, M. G.; Yoon, M.; Natarajan, S.; Kim, K. *Chem.—Eur. J.* **2012**, *18*, 16642.

[29] Szilágyi, P. A.; Serra-Crespo, P.; Dugulan, I.; Gascon, J.; Geerlings, H.; Dam, B. *Crystengcomm* **2013**, *15*, 10175.

[30] Tao, J.; Li, J.; Huang, P.; Wu, X.; Huang, R.-B.; Zheng, L. *Chem. Sci.* **2013**, 3232.

[31] Wang, X. X.-J.; Li, P.-Z.; Liu, L.; Zhang, Q.; Borah, P.; Wong, J. D.; Chan, X. X.; Rakesh, G.; Li, Y.; Zhao, Y. *Chem. Commun.* **2012**, *48*, 10286.

[32] Prasad, T. K.; Hong, D. H.; Suh, M. P. *Chem.—Eur. J.* **2010**, *16*, 14043.

[33] Li, J.; Li, L.; Hou, H.; Fan, Y. *Cryst. Growth Des.* **2009**, *9*, 4504.

[34] Zhang, Z.; Zhang, L.; Wojtas, L.; Nugent, P.; Eddaoudi, M.; Zaworotko, M. J. *J. Am. Chem. Soc.* **2012**, *134*, 924.

[35] Sun, C.-Y.; Wang, X.-L.; Zhang, X.; Qin, C.; Li, P.; Su, Z.-M.; Zhu, D.-X.; Shan, G.-G.; Shao, K.-Z.; Wu, H.; Li, J. *Nat. Commun.* **2013**, *4*, 2717.

[36] Kim, M.; Cahill, J. F.; Fei, H.; Prather, K. A.; Cohen, S. M. *J. Am. Chem. Soc.* **2012**, *134*, 18082.

[37] Zhang, H.-M.; Yang, J.; He, Y.-C.; Ma, J.-F. *Chem. Asian J.* **2013**, *8*, 2787.

[38] Yao, Q.; Sun, J.; Li, K.; Su, J.; Peskov, M. V.; Zou, X. *Dalton Trans.* **2012**, *41*, 3953.

[39] Song, X.; Kim, T. K.; Kim, H.; Kim, D.; Jeong, S.; Moon, H. R.; Lah, M. S. *Chem. Mater.* **2012**, *24*, 3065.

[40] Huang, S.; Li, X.; Shi, X.; Hou, H.; Fan, Y. *J. Mater. Chem.* **2010**, *20*, 5695.

[41] Mi, L.; Hou, H.; Song, Z.; Han, H.; Fan, Y. *Chem.—Eur. J.* **2008**, *14*, 1814.

[42] Mi, L.; Hou, H.; Song, Z.; Han, H.; Xu, H.; Fan, Y.; Ng, S. W. *Cryst. Growth Des.* **2007**, *7*, 2553.

[43] Mukherjee, G.; Biradha, K. *Chem. Commun.* **2012**, *48*, 4293.

[44] Lever, A. B. P. *J. Chem. Educ.* **1968**, *45*, 711.

[45] Zhang, Z.; Wojtas, L.; Eddaoudi, M.; Zaworotko, M. J. *J. Am. Chem. Soc.* **2013**, *135*, 5982.

[46] Zhao, J.; Mi, L.; Hu, J.; Hou, H.; Fan, Y. *J. Am. Chem. Soc.* **2008**, *130*, 15222.

[47] Brozek, C. K.; Cozzolino, A. F.; Teat, S. J.; Chen, Y. S.; Dincă, M. *Chem. Mater.* **2013**, *25*, 2998.

[48] Li, K.; Xue, D. *J. Phys. Chem. A* **2006**, *110*, 11332.

[49] Irving, B. H.; Williams, R. J. P. *J. Chem. Soc.* **1953**, 3192.

[50] Wang, X.-S.; Chrzanowski, M.; Wojtas, L.; Chen, Y.-S.; Ma, S. *Chem.—Eur. J.* **2013**, *19*, 3297.

[51] Brozek, C. K.; Bellarosa, L.; Soejima, T.; Clark, T. V.; López, N.; Dincă, M., Mircea *Chem.—Eur. J.* **2014**, *20*, 6871.

[52] Sumida, K.; Horike, S.; Kaye, S. S.; Herm, Z. R.; Queen, W. L.; Brown, C. M.; Grandjean, F.; Long, G. J.; Dailly, A.; Long, J. R. *Chem. Sci.* **2010**, *1*, 184.

[53] Dincă, M.; Han, W. S.; Liu, Y.; Dailly, A.; Brown, C. M.; Long, J. R. *Angew. Chem. Int. Ed.* **2007**, *46*, 1419.

[54] Sumida, K. et al. *J. Am. Chem. Soc.* **2013**, *135*, 1083–1091.

[55] Li, H.; Eddaoudi, M.; O'Keeffe, M.; Yaghi, O. M. *Nature* **1999**, *402*, 276.

[56] Weakliem, H. A. *J. Chem. Phys.* **1962**, *36*, 2117.

[57] Schwartz, D. A.; Norberg, N. S.; Nguyen, Q. P.; Parker, J. M.; Gamelin, D. R. *J. Am. Chem. Soc.* **2003**, *125*, 13205.

[58] Cui, X. B.; Zheng, S. T.; Yang, G. Y. *Zeitschrift fur Anorg. und Allg. Chemie* **2005**, *631*, 642.

[59] Zhao, J. W.; Jia, H. P.; Zhang, J.; Zheng, S. T.; Yang, G. Y. *Chem.—Eur. J.* **2007**, *13*, 10030.

[60] Gao, G.-G.; Xu, L.; Wang, W.-J.; Qu, X.-S.; Liu, H.; Yang, Y.-Y. *Inorg. Chem.* **2008**, *47*, 2325.

[61] Zheng, B.; Miranda, M. O.; DiPasquale, A. G.; Golen, J. A.; Rheingold, A. L.; Doerrer, L. H. *Inorg. Chem.* **2009**, *48*, 4274.

[62] Ma, P. T.; Bi, D. Q.; Wang, J. P.; Wang, W.; Niu, J. Y. *Inorg. Chem. Commun.* **2009**, *12*, 1182.

[63] Botas, J. A.; Calleja, G.; Sánchez-Sánchez, M.; Orcajo, M. G. *Langmuir* **2010**, *26*, 5300.

[64] Chae, H. K.; Eddaoudi, M.; Kim, J.; Hauck, S. I.; Hartwig, J. F.; O'Keeffe, M.; Yaghi, O. M. **2001**, *123*, 11482.

[65] Kesanli, B.; Cui, Y.; Smith, M. R.; Bittner, E. W.; Bockrath, B. C.; Lin, W. *Angew. Chem. Int. Ed.* **2004**, *44*, 72.

[66] Gedrich, K.; Senkovska, I.; Baburin, I. A.; Mueller, U.; Trapp, O.; Kaskel, S. *Inorg. Chem.* **2010**, *49*, 4440.

[67] Yao, Q.; Su, J.; Cheung, O.; Liu, Q.; Hedin, N.; Zou, X. *J. Mater. Chem.* **2012**, *22*, 10345.

[68] Burrows, A. D.; Hunter, S. O.; Mahon, M. F.; Richardson, C. *Chem. Commun.* **2013**, *49*, 990.

[69] Burrows, A. D.; Frost, C. G.; Mahon, M. F.; Richardson, C. *Angew. Chem. Int. Ed.* **2008**, *47*, 8482.

[70] Burrows, A. D.; Frost, C. G.; Mahon, M. F.; Richardson, C. *Chem. Commun.* **2009**, 4218.

[71] Burrows, A. D.; Fisher, L. C.; Hodgson, D.; Mahon, M. F.; Cessford, N. F.; Duren, T.; Richardson, C.; Rigby, S. P. *CrystEngComm* **2012**, *14*, 188.

[72] Kaye, S. S.; Dailly, A.; Yaghi, O. M.; Long, J. R. *J. Am. Chem. Soc.* **2007**, *129*, 14176.

[73] Hausdorf, S.; Baitalow, F.; Böhle, T.; Rafaja, D.; Mertens, F. O. R. L. *J. Am. Chem. Soc.* **2010**, *132*, 10978.

[74] Gordon, R. M.; Silver, H. B. *Can. J. Chem.* **1983**, *61*, 1218.

[75] Sundheim, B. R.; Harrington, G. *J. Chem. Phys.* **1959**, *3*, 1957.

[76] Gruen, D. *J. Phys. Chem.* **1959**, *63*, 393.

[77] Gill, N. S.; Nyholm, R. S. *J. Chem. Soc.* **1959**, 3997.

[78] Liehr, A. D.; Ballhausen, C. *Ann. Phys.* **1959**, *6*, 134.

[79] Furlani, C.; Morpurgo, G. *Zeitschrift für Physikalische Chemie* **1961**, *28*, 93.

[80] Cotton, M. G. M. G. F. *Amer. Chem. Soc.* **1961**, *83*, 4161.

[81] Ballhausen, C. J. *Introduction to Ligand Field Theory*; McGraw-Hill: New York, New York, 1962.

[82] Lever, A. B. P. *Inorganic Electronic Spectroscopy*; Elsevier: New York, New York, 1984; p 864.

[83] Figgis, B. N.; Lewis, J.; Mabbs, F. E.; Webb, G. A. *J. Chem. Soc. A Inorganic, Phys. Theor.* **1966**, 1411.

[84] Figgis, B. N. *Nature* **1958**, *182*, 1568.

[85] Figgis, B. N.; Lewis, J.; Mabbs, F.; Webb, G. A. *Nature* **1964**, *203*, 1138.

[86] Barybin, M. V.; Diaconescu, P. L.; Cummins, C. C. *Inorg. Chem.* **2001**, *40*, 2892.

[87] Sheldrick, G. M. SADABS: Programm for Empirical Absorption Correction of Area Detectors. 1996.

[88] Sheldrick, G. M. SHELX97 [Includes SHELXS97, SHELXL97, CIFTAB] - Programs for Crystal Structure Analysis, release 97-2. 1998.

[89] Bain, G. A.; Berry, J. F. *J. Chem. Educ.* **2008**, *85*, 532.

[90] Becke, a. D. *J. Chem. Phys.* **1986**, *84*, 4524.

[91] Perdew, J. P. *Phys. Rev. B* **1986**, *33*, 8822.

[92] Neese, F. *Orca*, version 2.8.0. 2010.

[93] Schaefer, A.; Horn, H.; Ahlrichs, R. *J. Chem. Phys.* **1992**, *97*, 2571.

[94] Schäfer, A.; Huber, C.; Ahlrichs, R. *J. Chem. Phys.* **1994**, *100*, 5829.

[95] van Wüllen, C. *J. Chem. Phys.* **1998**, *109*, 392.

[96] van Lenthe, E. J., E.and Baerends; Snijders, J. G. *J. Chem. Phys.* **1994**, *101*, 9783.

[97] van Lenthe, E.; Baerends, E. J.; Snijders, J. G. *J. Chem. Phys.* **1993**, *99*, 4597.

[98] Deria, P.; Mondloch, J. E.; Karagiaridi, O.; Bury, W.; Hupp, J. T.; Farha, O. K. *Chem. Soc. Rev.* **2014**, 41.

[99] Brozek, C. K.; Dincă, M. *Chem. Soc. Rev.* **2014**, *43*, 5456.

[100] Beier, M. J.; Kleist, W.; Wharmby, M. T.; Kissner, R.; Kimmerle, B.; Wright, P. a.; Grunwaldt, J. D.; Baiker, A. *Chem.—Eur. J.* **2012**, *18*, 887.

[101] Leus, K.; Muylaert, I.; Vandichel, M.; Marin, G. B.; Waroquier, M.; Van Speybroeck, V.; Van der Voort, P. *Chem. Commun.* **2010**, *46*, 5085.

[102] Liu, Y.-Y.; Leus, K.; Grzywa, M.; Weinberger, D.; Strubbe, K.; Vrielinck, H.; Van Deun, R.; Volkmer, D.; Van Speybroeck, V.; Van Der Voort, P. *Eur. J. Inorg. Chem.* **2012**, *2012*, 2819.

[103] Ravon, U.; Domine, M. E.; Gaudillère, C.; Desmartin-Chomel, A.; Farrusseng, D. *New J. Chem.* **2008**, *32*, 937.

[104] Sen, R.; Saha, D.; Mal, D.; Brandão, P.; Lin, Z. *Eur. J. Inorg. Chem.* **2013**, *2013*, 5103.

[105] Rosi, N. L.; Eckert, J.; Eddaoudi, M.; Vodak, D. T.; Kim, J.; O'Keeffe, M.; Yaghi, O. M. *Science* **2003**, *300*, 1127.

[106] Eddaoudi, M.; Kim, J.; Rosi, N.; Vodak, D.; Wachter, J.; O'Keeffe, M.; Yaghi, O. M. *Science* **2002**, *295*, 469.

[107] Rowsell, J. L. C.; Spencer, E. C.; Eckert, J.; Howard, J. A. K.; Yaghi, O. M. *Science* **2005**, *309*, 1350.

[108] Walton, K. S.; Snurr, R. Q. *J. Am. Chem. Soc.* **2007**, *129*, 8552.

[109] Hafizovic, J.; Bjørgen, M.; Olsbye, U.; Dietzel, P. D. C.; Bordiga, S.; Prestipino, C.; Lamberti, C.; Lillerud, K. P. *J. Am. Chem. Soc.* **2007**, *129*, 3612.

[110] Liu, Y.; Ng, Z.; Khan, E. A.; Jeong, H. K.; bun Ching, C.; Lai, Z. *Microporous Mesoporous Mater.* **2009**, *118*, 296.

[111] Hughes, J. T.; Navrotsky, A. *J. Am. Chem. Soc.* **2011**, *133*, 9184.

[112] Luo, Y.-R. *Comprehensive Handbook of Chemical Bond Energies*; CRC Press: Boca Raton, 2007.

[113] Larsen, F. H.; Jakobsen, H. J.; Ellis, P. D.; Nielsen, N. C. *J. Phys. Chem. A* **1997**, *101*, 8597.

[114] Lipton, A. S.; Heck, R. W.; Ellis, P. D. *J. Am. Chem. Soc.* **2004**, *126*, 4735.

[115] Hibble, S. J.; Chippindale, A. M.; Marelli, E.; Kroeker, S.; Michaelis, V. K.; Greer, B. J.; Aguiar, P. M.; Bilbé, E. J.; Barney, E. R.; Hannon, A. C. *J. Am. Chem. Soc.* **2013**, *135*, 16478.

[116] Sutrisno, A.; Terskikh, V. V.; Shi, Q.; Song, Z.; Dong, J.; Ding, S. Y.; Wang, W.; Provost, B. R.; Daff, T. D.; Woo, T. K.; Huang, Y. *Chem.—Eur. J.* **2012**, *18*, 12251.

[117] Bellarosa, L.; Castillo, J. M.; Vlugt, T.; Calero, S.; López, N. *Chem.—Eur. J.* **2012**, *18*, 12260.

[118] Han, S. S.; Choi, S.-H.; van Duin, A. C. T. *Chem. Commun.* **2010**, *46*, 5713.

[119] Greathouse, J. A.; Allendorf, M. D. *J. Am. Chem. Soc.* **2006**, *128*, 10678.

[120] Bury, W.; Justyniak, I.; Prochowicz, D.; Wróbel, Z.; Lewiński, J. *Chem. Commun.* **2012**, *48*, 7362.

[121] Perry IV, J. J.; Feng, P. L.; Meek, S. T.; Leong, K.; Doty, F. P.; Allendorf, M. D. *J. Mater. Chem.* **2012**, *22*, 10235.

[122] Zhou, X. P.; Xu, Z.; Zeller, M.; Hunter, A. D.; Chui, S. S. Y.; Che, C. M. *Inorg. Chem.* **2008**, *47*, 7459.

[123] Zhu, C.; Xuan, W.; Cui, Y. *Dalton Trans.* **2012**, *41*, 3928.

[124] Han, S.; Ma, Z.; Wei, Y.; Kravtsov, V. C.; Luisi, B. S.; Kulaots, I.; Moulton, B. *CrystEngComm* **2011**, *13*, 4838.

[125] Gole, B.; Bar, A. K.; Mukherjee, P. S. *Chem. Commun.* **2011**, *47*, 12137.

[126] Yang, G.-S.; Lang, Z.-L.; Zang, H.-Y.; Lan, Y.-Q.; He, W.-W.; Zhao, X.-L.; Yan, L.-K.; Wang, X.-L.; Su, Z.-M. *Chem. Commun.* **2013**, *49*, 1088.

[127] Barman, S.; Furukawa, H.; Blacque, O.; Venkatesan, K.; Yaghi, O. M.; Berke, H. *Chem. Commun.* **2010**, *46*, 7981.

[128] Davis, J.; Jeffrey, K.; Bloom, M.; Valic, M.; Higgs, T. *Chem. Phys. Lett.* **1976**, *42*, 390.

[129] Harris, R. K.; Becker, E. D.; Menezes, S. M. C. D. E. *Pure Appl. Chem.* **2001**, *73*, 1795.

[130] Bloch, F.; Hansen, W. W.; Packard, M. *Phys. Rev.* **1946**, *70*, 474.

[131] Eichele, K. WSOLIDS NMR Simulation Package. 2013.

[132] Pines, A. *J. Chem. Phys.* **1972**, *56*, 1776.

[133] Burum, D.; Ernst, R. *J. Magn. Reson.* **1980**, *39*, 163.

[134] Bennett, A. E.; Rienstra, C. M.; Auger, M.; Lakshmi, K. V.; Griffin, R. G. *J. Chem. Phys.* **1995**, *103*, 6951.

[135] Mulder, F. M.; Dingemans, T. J.; Wagemaker, M.; Kearley, G. J. *Chem. Phys.* **2005**, *317*, 113.

[136] Solomon, I. *Phys. Rev.* **1958**, *110*, 61.

[137] Mananga, E. S.; Rumala, Y. S.; Boutis, G. S. *J. Magn. Reson.* **2006**, *181*, 296.

[138] Kresse, G. *Phys. Rev. B* **1996**, *54*, 11169.

[139] Kresse, G.; Hafner, J. *Phys. Rev. B* **1993**, *47*, 558.

[140] Perdew, J.; Burke, K.; Ernzerhof, M. *Phys. Rev. Lett.* **1996**, *77*, 3865.

[141] Zhang, Y.; Pan, W.; Yang, W. *J. Chem. Phys.* **1997**, *107*, 7921.

[142] Patton, D.; Pederson, M. *Phys. Rev. A* **1997**, *56*, R2495.

[143] Grimme, S. *J. Comput. Chem.* **2006**, *27*, 1787.

[144] Kresse, G. *Phys. Rev. B* **1999**, *59*, 1758.

[145] Blöchl, P. E. *Phys. Rev. B* **1994**, *50*, 17953.

[146] Grzybkowski, W.; Pilarczyk, M. *J. Chem. Soc. Faraday Trans. 1* **1986**, *82*, 1703.

[147] Katzin, L. I. *J. Chem. Phys.* **1962**, *36*, 3034.

[148] Neese, F. ORCA, version 3.0.3. 2014.

[149] Wu, G.; Zhang, Y.; Ribaud, L.; Coppens, P.; Wilson, C.; Iversen, B. B.; Larsen, F. K. *Inorg. Chem.* **1998**, *37*, 6078.

[150] Helliwell, M. *J. Synchrotron Radiat.* **2000**, *7*, 139.

[151] Helliwell, M.; Helliwell, J. R.; Kaucic, V.; Zabukovec Logar, N.; Teat, S. J.; Warren, J. E.; Dodson, E. J. *Acta Crystallogr. Sect. B* **2010**, *66*, 345.

[152] Helliwell, M.; Helliwell, J. R.; Kaucic, V.; Zabukovec Logar, N.; Barba, L.; Busetto, E.; Lausi, A. **1999**, *55*, 327.

[153] Einsle, O.; Andrade, S. L. A.; Dobbek, H.; Meyer, J.; Rees, D. C. *J. Am. Chem. Soc.* **2007**, *129*, 2210.

[154] Wilkinson, A. P.; Cheetham, A. K.; Tang, S. C.; Reppart, W. J. *J. Chem. Soc. Chem. Commun.* **1992**, 1485.

[155] Freedman, D. E.; Han, T. H.; Prodi, A.; Müller, P.; Huang, Q.-Z.; Chen, Y.-S.; Webb, S. M.; Lee, Y. S.; McQueen, T. M.; Nocera, D. G. *J. Am. Chem. Soc.* **2010**, *132*, 16185.

[156] Farrugia, L. J. *J. Appl. Crystallogr.* **1999**, *32*, 837.

[157] Kissel, L.; Pratt, R. H. *Acta Crystallogr. Sect. A Found. Crystallogr.* **1990**, *46*, 170.

[158] Petricek, V.; Dusek, M.; Palatinus, L. JANA2006. 2006.

[159] Chantler, C.; Olsen, K.; Dragoset, R.; Chang, J.; Kishore, A.; Kotochigova, S.; Zucker, D. X-Ray Form Factor, Attenutaion, and Scattering Tables. 2013; `http://www.nist.gov/pml/data/ffast/index.cfm`.

[160] Kuhl, G. H. In *Catal. Zeolites Fundam. Appl.*; Weitkamp, J., Puppe, L., Eds.; 1999; Chapter 3, pp 81–197.

[161] Townsend, R. P.; Coker, E. N. In *Introd. to Zeolite Sci. Pract.*, 2nd ed.; van Bekkum, H., Flanigen, E. M., Jacobs, P. A., Jansen, J. C., Eds.; 2001; Chapter 11, pp 467–524.

[162] Viktor, G. *Coord. Chem. Rev.* **1976**, *18*, 225.

[163] Snyder, L. *J. Chromatogr. A* **1974**, *92*, 223.

[164] Denysenko, D.; Grzywa, M.; Tonigold, M.; Streppel, B.; Krkljus, I.; Hirscher, M.; Mugnaioli, E.; Kolb, U.; Hanss, J.; Volkmer, D. *Chem.—Eur. J.* **2011**, *17*, 1837.

[165] Jelic, J.; Denysenko, D.; Volkmer, D.; Reuter, K. *New J. Phys.* **2013**, *15*, 115004.

[166] Hansen, C. The Three Dimensional Solubility Parameter and Solvent Diffusion Coefficient and Their Importance in Surface Coating Formulation. Ph.D. thesis, Technical Univeristy of Denmark, 1967.

[167] Barrer, R.; Davies, J.; Rees, L. *J. Inorg. Nucl. Chem.* **1969**, *31*, 2599.

[168] Barrer, R.; Davies, J.; Rees, L. *J. Inorg. Nucl. Chem.* **1968**, *30*, 3333.

[169] Gaines Jr, G. L.; Thomas, H. C. *J. Chem. Phys.* **1953**, *21*, 714.

[170] Liu, X.; Li, H.; Du, W.; Tian, R.; Li, R.; Jiang, X. *J. Phys. Chem. C* **2013**, *117*, 6245.

[171] Sherry, H. S. *J. Phys. Chem.* **1966**, *70*, 1158.

[172] Lee, C.; Yang, W.; Parr, R. G. *Phys. Rev. B* **1988**, *37*, 785.

[173] Stephens, P. J.; Devlin, F. J.; Chabalowski, C. F.; Frisch, M. J. *J. Phys. Chem.* **1994**, *98*, 11623.

[174] Becke, A. *J. Chem. Phys.* **1993**, *98*, 5648.

[175] Rassolov, V. A. *J. Comput. Chem.* **2001**, *22*, 976.

[176] Hariharan, P. C.; Pople, J. A. *Mol. Phys.* **1974**, 209.

[177] Andrae, D.; Häßermann, U.; Dolg, M.; Stoll, H.; Preuß, H. *Theor. Chim. Acta* **1990**, *77*, 123–141.

[178] Bergner, A.; Dolg, M.; Küchle, W.; Stoll, H.; Preuß, H. *Mol. Phys.* **1993**, 1431.

[179] Tonigold, M.; Tu, Y.; Bredenkötter, B.; Rieger, B.; Bahnmüller, S.; Hitzbleck, J.; Langstein, G.; Volkmer, D. *Angew. Chem. Int. Ed.* **2009**, *48*, 7546.

[180] Bloch, E. D.; Murray, L. J.; Queen, W. L.; Chavan, S.; Maximoff, S. N.; Bigi, J. P.; Krishna, R.; Peterson, V. K.; Grandjean, F.; Long, G. J.; Smit, B.; Bordiga, S.; Brown, C. M.; Long, J. R. *J. Am. Chem. Soc.* **2011**, *133*, 14814.

[181] Xiao, D. J. et al. *Nat. Chem.* **2014**, *6*, 590.

[182] Denysenko, D.; Grzywa, M.; Jelic, J.; Reuter, K.; Volkmer, D. *Angew. Chem. Int. Ed.* **2014**, *53*, 5832.

[183] Fleischer, R.; Freitag, S.; Pauer, F.; Stalke, D. *Angew. Chem. Int. Ed.* **1996**, 204.

[184] Fleischer, R.; Stalke, D.; Wu, D. *Organometallics* **1998**, *7333*, 832.

[185] Less, R. J.; Naseri, V.; Wright, D. S. *Organometallics* **2009**, *28*, 3594.

[186] Ma, S.; Yuan, D.; Chang, J. S.; Zhou, H. C. *Inorg. Chem.* **2009**, *48*, 5398.

[187] Haider, G. J.; Chapman, K. W.; Neville, S. M.; Moubaraki, B.; Murray, K. S.; Letard, J. F.; Kepert, C. J. *J. Am. Chem. Soc.* **2008**, *130*, 17552.

[188] Gütlich, P.; Bill, E.; Trautwein, A. X. *Mössbauer Spectroscopy and Transition Metal Chemistry Fundamentals and Applications*; Springer-Verlag: Berlin, Heidelberg, 2011.

[189] Rancourt, D.; Ping, J. *Nucl. Instruments Methods Phys. Res. Sect. B* **1991**, *58*, 85.

[190] Neese, F. *Inorganica Chim. Acta* **2002**, *337*, 181.

[191] Blume, M.; Tjon, J. *Phys. Rev.* **1968**, *165*, 446.

[192] Tjon, J.; Blume, M. *Phys. Rev.* **1968**, *165*, 456.

[193] Lindley, D.; Debrunner, P. *Physical Review* **1966**, *146*, 199–209.

[194] Edwards, P. R. *J. Chem. Phys.* **1967**, *47*, 2074.

[195] Fitzsimmons, B. W.; Marshall, W. G. *J. Chem. Soc. Dalt. Trans.* **1992**, 73.

[196] Fitzsimmons, B. W.; Hume, A. R. *J. Chem. Soc. Dalt. Trans.* **1980**, 180.

[197] Neese, F. *Orca 2.9.1*, version 2.9.1.

[198] Dhakshinamoorthy, A.; Opanasenko, M.; Čejka, J.; Garcia, H. *Adv. Synth. Catal.* **2013**, 247.

[199] Cozzolino, A. F.; Brozek, C. K.; Palmer, R. D.; Yano, J.; Li, M.; Dincă, M. *J. Am. Chem. Soc.* **2014**, *136*, 3334.

[200] Fu, Y.; Sun, D.; Chen, Y.; Huang, R.; Ding, Z.; Fu, X.; Li, Z. *Angew. Chem. Int. Ed.* **2012**, *51*, 3364.

[201] Dan-Hardi, M.; Serre, C.; Frot, T.; Rozes, L.; Maurin, G.; Sanchez, C.; Férey, G. *J. Am. Chem. Soc.* **2009**, *131*, 10857.

[202] Murray, L. J.; Dincă, M.; Yano, J.; Chavan, S.; Bordiga, S.; Brown, C. M.; Long, J. R. *J. Am. Chem. Soc.* **2010**, *132*, 7856.

[203] Wei, W.; Xia, Z.; Wei, Q.; Xie, G.; Chen, S.; Qiao, C.; Zhang, G.; Zhou, C. *Micropor. Mesopor. Mater.* **2013**, *165*, 20.

[204] Li, H.; Shi, W.; Zhao, K.; Li, H.; Bing, Y.; Cheng, P. *Inorg. Chem.* **2012**, *51*, 9200.

[205] Drago, R. S. *Physical Methods for Chemists*, 2nd ed.; Saunders (W.B.) Co Ltd: Philadelphia, 1992; p 750.

[206] Ganesan, R.; Viswanathan, B. *J. Mol. Catal. A Chem.* **2004**, *223*, 21.

[207] Ravikumar, R.; Komatsu, R.; Ikeda, K.; Chandrasekhar, A.; Reddy, B.; Reddy, Y.; Rao, P. *Solid State Commun.* **2003**, *126*, 251.

[208] Xiao, B.; Wheatley, P. S.; Zhao, X.; Fletcher, A. J.; Fox, S.; Rossi, A. G.; Megson, I. L.; Bordiga, S.; Regli, L.; Thomas, K. M.; Morris, R. E. *J. Am. Chem. Soc.* **2007**, *129*, 1203.

[209] Bonino, F.; Chavan, S.; Vitillo, J. G.; Groppo, E.; Agostini, G.; Lamberti, C.; Dietzel, P. D. C.; Prestipino, C.; Bordiga, S. *Chem. Mater.* **2008**, *20*, 4957.

[210] McKinlay, A. C.; Xiao, B.; Wragg, D. S.; Wheatley, P. S.; Megson, I. L.; Morris, R. E. *J. Am. Chem. Soc.* **2008**, *130*, 10440.

[211] Vimont, A.; Cortes, P. H.; Hwang, Y. K.; Ferey, G.; Daturi, M.; Chang, J.-S.; Serre, C.; Yoon, J.; VIMONT, A. *U.S. Patent 2012/0129684* **May 24, 2010**. 2010.

[212] Wu, P.; Wang, J.; He, C.; Zhang, X.; Wang, Y.; Liu, T.; Duan, C. *Adv. Funct. Mater.* **2012**, *22*, 1698.

[213] Szanyi, J.; Daturi, M.; Clet, G.; Baer, D. R.; Peden, C. H. F. *Phys. Chem. Chem. Phys.* **2012**, *14*, 4383.

[214] Enemark, J.; Feltham, R. *Coord. Chem. Rev.* **1974**, *13*, 339.

[215] Schneppensieper, T.; Finkler, S.; Czap, A.; van Eldik, R.; Heus, M.; Nieuwenhuizen, P.; Wreesmann, C.; Abma, W. *Eur. J. Inorg. Chem.* **2001**, *2001*, 491.

[216] Ray, M.; Golombek, A. P.; Hendrich, M. P.; Yap, G. P. A.; Liable-Sands, L. M.; Rheingold, Arnold, L.; Borovik, a. S. *Inorg. Chem.* **1999**, *38*, 3110.

[217] Conradie, J.; Quarless, D. A.; Hsu, H.-F.; Harrop, T. C.; Lippard, S. J.; Koch, S. A.; Ghosh, A. *J. Am. Chem. Soc.* **2007**, *129*, 10446.

[218] Maxwell, J. C.; Caughey, W. S. *Biochemistry* **1976**, *15*, 388.

[219] Clay, M. D.; Cosper, C. A.; Jenney, F. E.; Adams, M. W. W.; Johnson, M. K. *Proc. Natl. Acad. Sci. U.S.A.* **2003**, *100*, 3796.

[220] Long, R. Q.; Yang, R. T. *J. Am. Chem. Soc.* **1999**, *121*, 5595.

[221] Lee, M.; Arosio, P.; Cozzi, A.; Chasteen, N. D. *Biochemistry* **1994**, *33*, 3679.

[222] Bouma, R. J.; Teuben, J. H.; Beukema, W. R.; Bansemer, R. L.; Huffman, J. C.; Caulton, K. G. *Inorg. Chem.* **1984**, *23*, 2715.

[223] Neill, F. M. O.; Boeyens, J. C. A.; Chem, C. J. A. I. *Inorg. Chem.* **1990**, *29*, 1302.

[224] Manxzer, L. E.; Deaton, J.; Sharp, P.; Schrock, R. R. *Inorg. Synth.* **1982**, *21*, 135.

[225] Boudjouk, P.; So, J. *Inorg. Synth.* **2007**, *29*, 108.

[226] Balloch, L.; Drummond, A. M.; García-Álvarez, P.; Graham, D. V.; Kennedy, A. R.; Klett, J.; Mulvey, R. E.; O'Hara, C. T.; Rodger, P. J. A.; Rushworth, I. D. *Inorg. Chem.* **2009**, *48*, 6934.

[227] Lelieveld, J.; Crutzen, P. J. *Science* **1994**, *264*, 1759.

[228] Liu, F.; He, H.; Xie, L. *ChemCatChem* **2013**, *5*, 3760.

[229] Long, J.; Zhang, Z.; Ding, Z.; Ruan, R.; Li, Z.; Wang, X. *J. Phys. Chem. C* **2010**, *114*, 15713.

[230] Ignarro, L. J. *Nitric oxide: Biology and Pathobiology*, 2nd ed.; Academic Press: San Diego, CA, USA, 2009.

[231] Yu, A. E.; Hu, S.; Spiro, T. G.; Burstyn, J. N. *J. Am. Chem. Soc.* **1994**, *116*, 4117.

[232] Wasser, I. M.; De Vries, S.; Moënne-Loccoz, P.; Schröder, I.; Karlin, K. D. *Chem. Rev.* **2002**, *102*, 1201.

[233] Moënne-Loccoz, P. *Nat. Prod. Rep.* **2007**, *24*, 610.

[234] Varotsis, C.; Ohta, T.; Kitagawa, T.; Soulimane, T.; Pinakoulaki, E. *Angew. Chem. Int. Ed.* **2007**, *46*, 2210.

[235] Tosha, T.; Shiro, Y. *IUBMB Life* **2013**, *65*, 217.

[236] Bou-Abdallah, F.; Chasteen, N. D. *J. Biol. Inorg. Chem.* **2008**, *13*, 15.

[237] Martirosyan, G. G.; Azizyan, A. S.; Kurtikyan, T. S.; Ford, P. C. *Inorg. Chem.* **2006**, *45*, 4079.

[238] Tsai, F.-T.; Lee, Y.-C.; Chiang, M.-H.; Liaw, W.-F. *Inorg. Chem.* **2013**, *52*, 464.

[239] Tsai, F. T.; Kuo, T. S.; Liaw, W. F. *J. Am. Chem. Soc.* **2009**, *131*, 3426.

[240] Weber, B.; Käpplinger, I.; Görls, H.; Jäger, E.-G. *Eur. J. Inorg. Chem.* **2005**, *2005*, 2794.

[241] Villar-Acevedo, G.; Nam, E.; Fitch, S.; Benedict, J.; Freudenthal, J.; Kaminsky, W.; Kovacs, J. A. *J. Am. Chem. Soc.* **2011**, *133*, 1419.

[242] Ellison, M. K.; Ellison, M. K.; Schulz, C. E.; Schulz, C. E.; Scheidt, W. R.; Scheidt, W. R. *Polyhedron* **1999**, *38*, 100.

[243] Patra, A. K.; Rose, M. J.; Olmstead, M. M.; Mascharak, P. K. *J. Am. Chem. Soc.* **2004**, *126*, 4780.

[244] Tsai, F.-T.; Chen, P.-L.; Liaw, W.-F. *J. Am. Chem. Soc.* **2010**, *132*, 5290.

[245] Arulsamy, N.; Bohle, D. S.; Hansert, B.; Powell, A. K.; Thomson, A. J.; Wocaldo, S. *Inorg. Chem.* **1998**, *37*, 746.

[246] Nakamoto, K. *Infrared and Raman Spectra of Inorganic and Coordination Compounds*, 6th ed.; Wiley: Hoboken, NJ, USA, 2009.

[247] Arulsamy, N.; Bohle, D. S.; Imonigie, J. A.; Moore, R. C. *Polyhedron* **2007**, *26*, 4737.

[248] Villalba, M. E. C.; Navaza, A.; Güida, J. A.; Varetti, E. L.; Aymonino, P. J. *Inorganica Chim. Acta* **2006**, *359*, 707.

[249] Ruggiero, C. E.; Carrier, S. M.; Tolman, W. B. *Angew. Chem. Int. Ed.* **1994**, *33*, 895.

[250] Franz, K. J.; Lippard, S. J. *J. Am. Chem. Soc.* **1998**, *120*, 9034.

[251] Franz, K. J.; Lippard, S. J. *J. Am. Chem. Soc.* **1999**, *121*, 10504.

[252] Ford, P. C.; Lorkovic, I. M. *Chem. Rev.* **2002**, *102*, 993.

[253] MacNeil, J. H.; Berseth, P. A.; Bruner, E. L.; Perkins, T. L.; Wadia, Y.; Westwood, G.; Trogler, W. C. *J. Am. Chem. Soc.* **1997**, *119*, 1668.

[254] Hino, T.; Matsumoto, Y.; Nagano, S.; Sugimoto, H.; Fukumori, Y.; Murata, T.; Iwata, S.; Shiro, Y. *Science* **2010**, *330*, 1666.

[255] Wright, A. M.; Wu, G.; Hayton, T. W. *J. Am. Chem. Soc.* **2012**, *134*, 9930.

[256] Gans, P. *J. Chem. Soc. A Inorganic, Phys. Theor.* **1967**, 943.

[257] Poskrebyshev, G. A.; Shafirovich, V.; Lymar, S. V. *J. Phys. Chem. A* **2008**, *2*, 8295.

[258] Jacox, M. E.; Thompson, W. E. *J. Chem. Phys.* **1990**, *93*, 7609.

[259] Li, R.; Continetti, R. E. *J. Phys. Chem. A* **2002**, *106*, 1183.

[260] Andrews, L.; Citra, A. *Chem. Rev.* **2002**, *102*, 885.

[261] Andrews, L.; Zhou, M.; Willson, S. P.; Kushto, G. P.; Snis, A.; Panas, I. *J. Chem. Phys.* **1998**, *109*, 177.

[262] Andrews, L.; Zhou, M. *J. Chem. Phys.* **1999**, *111*, 6036.

[263] Lymar, S. V.; Shafirovich, V.; Poskrebyshev, G. A. *Inorg. Chem.* **2005**, *44*, 5212.

[264] Valiev, M.; Lymar, S. V. *J. Phys. Chem. A* **2011**, *115*, 12004.

[265] Staroverov, V. N.; Scuseria, G. E.; Tao, J.; Perdew, J. P. *J. Chem. Phys.* **2003**, *119*, 12129.

Acknowledgements

Mom, Dad, and Ali, thank you for being my greatest fans, for waiting eagerly on the other side of the phone, week after week, and for keeping your gentle reassurance nearby. Drew, from the Audi dealership, must be jealous.

Mircea, the lab's growth and scientific triumphs are owed to you challenging the group to raise above itself, demonstrating with your own restless efforts to do the same. After some initial squirming, wrestling, climbing, and eventual, glorious discovery, you never let us settle and look back. As I leave here, approaching the age you were when I first joined, I'm beginning to fully appreciate the vision you set in front of all of us. Thank you for making me a far better scientist.

I would like to thank Professors Nocera, Schock, and Cummins for all serving, during different stints over the past 5 years, as my thesis Chair, and to Professor Lippard for insightful conversations about physical methods.

This thesis would be missing many hyphens if not for the invaluable edits made by Toshiki.

Well; Natalia, Anthony, Casey, Tarun, Guillaume, Brian, Milstein III and Nima; the Lone Ranger is riding on.

He's riding past the S.S. Erie and beyond the Rubicon. Let's meet him at the Pearl for Sunday Brunch and remember not to get μ-shaped tattoos.

That idea was hajerdous.

Carl K Brozek

✉ ckbrozek@gmail.com

Education

2010–2015 **Ph.D. Chemistry**, *Massachusetts Institute of Technology*, Cambridge, MA, Advised by Prof. Mircea Dincă.

2006–2010 **S.B. Chemistry**, *University of Chicago*, Chicago, IL, Advised by Prof. Gregory Hillhouse.

Publications

14 Bellarosa, L.; **Brozek, C. K.**; Garcia-Melchior; Dincă, M.; López, N. "When the Solvent Locks the Cage: Theoretical Insight into the Transmetalation of MOF-5 Lattices and its Kinetic Limitations"
Chem. Mater. **2015**, *27*, in press.

13 **Brozek, C. K.**; Miller, J. T., Stoian, S. A.; Dincă, M. "NO Disproportionation at a Mononuclear Site-Isolated Fe^{2+} Center in Fe^{2+}-MOF-5"
submitted

12 **Brozek, C. K.**; Michaelis, V. K.; Ong, T.-C.; Bellarosa, L.; López, N.; Griffin, R. G.; Dincă, M. "MOF-5 exhibits unsaturated Zn centers"
submitted

11 Sheberla, D.; Sun, L.; Blood-Forsythe, M. A.; Er, S.; Wade, C. R.; **Brozek, C. K.**; Aspuru-Guzik, A.; Dincă, M. "High Electrical Conductivity in Ni_3(2,3,6,7,10,11-hexaiminotriphenylene)$_2$, a Semiconducting Metal-Organic Graphene Analogue"
J. Am. Chem. Soc. **2014**, *136*, 8859.

10 **Brozek, C. K.**; Dincă, M "Cation Exchange at the Secondary Building Units of Metal-organic Frameworks"
Chem. Soc. Rev. **2014**, *43*, 5456.

9 **Brozek, C. K.**; Bellarosa, L.; Soejima, T.; Clark, T. V.; Lopez, N.; Dincă, M "Solvent-Dependent Cation Exchange in Metal-organic Frameworks"
Chem.–Eur. J. **2014**, *20*, 6871.

8 Kuppuswamy, S.; Powers, T. M.; Johnson, B. M.; **Brozek, C. K.**; Krogman, J. P.; Bezpalko, M. W.; Berben, L. A.; Keith, J. M.; Foxman, B. M.; Thomas, C. M. "One-electron Oxidation Chemistry and Subsequent Reactivity of Diiron Imido Complexes"
Inorg. Chem. **2014**, *53*, 5429.

7 Cozzolino, A. F.; **Brozek, C. K.**; Palmer, R. D.; Yano, J.; Li, M.; Dincă, M. "Ligand Redox Non-innocence in the Stiochiometric Oxidation of Mn_2(2,5-dioxidoterephthalate) (Mn-MOF-74)"
J. Am. Chem. Soc. **2014**, *136*, 3334.

6 Kuppuswamy, S.; Bezpalko, M. W.; Powers, T. M.; Wilding, M. J. T.; **Brozek, C. K.**; C. K.; Foxman, B. M.; Thomas, C. M. "A Series of C_3-Symmetric Heterobimetallic Cr/M (M = Fe, Co, and Cu) Complexes"
Chem. Sci. **2014**, *5*, 1617.

5 **Brozek, C. K.**; Dincă, M. "Ti^{3+}-, $V^{2+/3+}$-, $Cr^{2+/3+}$-, Mn^{2+}-, and Fe^{2+}-Substituted MOF-5 and Redox Reactivity in Cr- and Fe-MOF-5"
J. Am. Chem. Soc. **2013**, *135*, 12886.

4 **Brozek, C. K.**; Cozzolino, A. F.; Teat, S. J.; Chen, Y.-C.; Dincă, M. "Quantification of Site-Specific Cation Exchange in Metal-organic Frameworks Using Multi-Wavelength Anomalous X-ray Dispersion"
Chem. Mater. **2013**, *25*, 2998.

3 Kuppuswamy, S.; Powers, T. M.; Johnson, B. M.; Bezpalko, M. W.; **Brozek, C. K.**; Foxman, B. M.; Berben, L. A.; Thomas, C. M. "Metal-Metal Interactions in C_3-Symmetric Diiron Imido Complexes Linked by Phosphinoamide Ligands"
Inorg. Chem. **2013**, *52*, 4802.

2 **Brozek, C. K.**; Dincă, M. "Lattice-Imposed Geometry in Metal-Organic Frameworks: Lacunary Zn_4O Clusters in MOF-5 Serve as Tripodal Chelating Ligands for Ni^{2+}"
Chem. Sci. **2012**, *3*, 2110.

1 Iluc, V. M.; Laskowski, C. K.; **Brozek, C. K.**; Harrold, N. D.; Hillhouse, G. L. "Monomeric and Dimeric Disulfide Complexes of Nickel(II)"
Inorg. Chem. **2010**, *49*, 6817.

Presentations and Posters

6 "Imbedding Reactive Fe Sites Into Metal-organic Frameworks" **Brozek, C. K.**; Stoian, Sebastian; Dincă, M *8th Annual Mössbauer Symposium*, January 2015, Northeastern University, Boston, MA
Invited Speaker

5 "MOF-5 Is Not as It Seems" **Brozek, C. K.**; Dincă, M *MOF 2014*, September 2014, Kobe, Japan

4 "MOFs as Ligands for Reactive Metal Sites" **Brozek, C. K.**; Dincă, M *Gordon Research Conference*, June 2014, University of New England, Biddeford, ME

3 "Metal-organic Frameworks as Ligands for Coordination Chemistry" **Brozek, C. K.**; Dincă, M *American Chemical Society 245th National Meeting*, April 2013, New Orleans, LA.

2 "Redox Chemistry of Sulfide and Persulfide Ligands on Ni" **Brozek, C. K.**; Hillhouse, G. L. *Arnold and Mabel Beckman Scholars Symposium*, July 2009, UC Irvine, CA.

1 "Redox Chemistry of Sulfide and Persulfide Ligands on Ni" **Brozek, C. K.**; Hillhouse, G. L. *Gordon Research Conference: Gordon-Kenan Seminar*, 20 June 2009, University of New England, Biddeford, ME.

Honors

- **Washington Research Foundation Innovation Fellowship**, 2015
- **MIT School of Science Appreciation Award**, 2015
- **National Science Foundation Graduate Research Fellowship**, 2010-2014
- **Beckman Scholars Program in Molecular Sciences Fellowship**, 2007-2009

Teaching

Intern **Research Communication Laboratory** *Museum of Science, Boston, MA* Attended weekly workshops to improve science communication through various media. Designed a prototype chemistry exhibit over the course of an internship that is currently implemented in the museum.

Mentor **Independent Research** *Massachusetts Institute of Technology* Designed novel research projects for undergraduates students and visiting high school teachers. Trained graduate and undergraduate students in basic laboratory techniques, advanced analytical methods, and data analysis. Instructed students in relevant scientific concepts.

Teaching Assistant **Physical Inorganic Chemistry** *Massachusetts Institute of Technology* Developed the syllabus, assignments, lectures and exams with Prof. Dincă for a new curriculum. Lectured collaboratively.

Teaching Assistant **General Chemistry** *Massachusetts Institute of Technology* Designed bi-weekly instruction sessions with original lecturing and assignment components. Conducted weekly meetings with students to address their academic concerns.

Teaching Assistant **Organic Chemistry** *University of Chicago* Managed weekly laboratory course and guided students in their synthetic chemistry assignments. Advised students on their academic challenges. Tailored weekly discussions with lectures and assignments according to the needs of the students.

Service

Chair **Advising Initiative** *Graduate Student Council of MIT* Negotiated with faculty, students, administrators, and institutional offices to compose and implement a Rights and Responsibilities for graduate students. Organized promotional events and other communication efforts to disseminate throughout MIT.

Tutor **Tutoring Plus of Cambridge** Tutored students between grades 4 and 12 in science topics through weekly demonstrations.

Tutor **Chemistry Department of MIT** Reviewed course material and assisted with assignments for undergraduate students in chemistry courses.

Volunteer **People Making a Difference** Volunteered at various weekly community activities, including cleaning public parks and building educational toys for children.